

**Studies on Design and Development of Multifunctional  
Reconfigurable Frequency Selective Surfaces for Advanced  
Electromagnetic Applications**

**Ph.D. Thesis**

*by*

**Patinavalasa Megh Sainadh**



**DEPARTMENT OF ELECTRICAL ENGINEERING  
INDIAN INSTITUTE OF TECHNOLOGY INDORE**

**December, 2025**



**Studies on Design and Development of Multifunctional  
Reconfigurable Frequency Selective Surfaces for Advanced  
Electromagnetic Applications**

**A THESIS**

*Submitted in partial fulfillment of the  
requirements for the award of the degree*

*of*

**Doctor of Philosophy**

*by*

**Patinavalasa Megh Sainadh**



**DEPARTMENT OF ELECTRICAL ENGINEERING  
INDIAN INSTITUTE OF TECHNOLOGY INDORE**

**December, 2025**





## INDIAN INSTITUTE OF TECHNOLOGY INDORE

### CANDIDATE'S DECLARATION

I hereby certify that the work which is being presented in the thesis entitled “**Studies on Design and Development of Multifunctional Reconfigurable Frequency Selective Surfaces for Advanced Electromagnetic Applications**”, in partial fulfillment of the requirements for the award of the degree of Doctor of Philosophy, and submitted in the Department of Electrical Engineering, Indian Institute of Technology Indore, is an authentic record of my own work carried out during the time period from August 2021 to December 2025 under the supervision of Dr. Saptarshi Ghosh, Indian Institute of Technology Indore, India.

The matter presented in this thesis has not been submitted for the award of any other degree of this or any other institute.

*Megh Sainadh*  
1/4/26

Signature of the student with date

**(Patinavalasa Megh Sainadh)**

-----

This is to certify that the above statement made by the candidate is correct to the best of my knowledge.

*Saptarshi Ghosh*

01/04/26

Signature of Thesis Supervisor(s) with date

**(Dr. Saptarshi Ghosh)**

-----

Patinavalasa Megh Sainadh has successfully given his Ph.D. Oral Examination held on 13/10/2025.

*Saptarshi Ghosh*

01/04/26

Signature of Thesis Supervisor(s) with date

**(Dr. Saptarshi Ghosh)**



# Synopsis

---

**Name of Student:** Patinavalasa Megh Sainadh      **Roll Number:** 2101102007

**Degree for which submitted:** Ph.D.      **Department:** Electrical Engineering

**Thesis Title:** *Studies on Design and Development of Multifunctional Reconfigurable Frequency Selective Surfaces for Advanced Electromagnetic Applications*

**Name of thesis supervisor:** Dr. Saptarshi Ghosh

**Month and year of submission:** December, 2025

---

Over the past few decades, research on frequency selective surfaces (FSSs) has grown rapidly because of their importance in stealth technology, radar systems, and electromagnetic (EM) shielding. An FSS is a periodic array of metallic elements that controls EM wave behavior such as transmission, reflection, and absorption, based on its geometry, polarization, and angle of incidence. Conventional FSS designs are restricted to a single fixed function, which limits their practical use. With the rapid expansion of wireless communication systems and modern radar platforms, there is a growing demand for compact and multifunctional reconfigurable frequency selective surfaces (RFSSs) that can perform various EM functions like absorption, transmission, and reflection- either simultaneously or selectively within a single structure. To realize this flexibility, FSS designs are engineered using various reconfigurable techniques, exhibiting different EM responses in real-time scenarios.

In advanced communication and sensing environments, where different EM functionalities are required across distinct frequency bands or at different time instants within the same band, such RFSS designs hold strong potential. For example, an RFSS with switchable transmission–reflection characteristics can selectively permit desired signals in the transmissive state for adaptive wireless links, while it can reject or redirect unwanted signals in the reflective state improving link security. An absorptive mode can suppress undesirable or hostile signals by dissipating incident energy, supporting stealth functionality and electromagnetic interference

(EMI) reduction. A rasorber structure- combining both absorption and transmission behaviour can simultaneously support radar cross-section (RCS) reduction and reliable communication performance. Beyond defense and wireless communication domains, multifunctional RFSS structures are also well-suited for tunable filters, EM shielding, cognitive radar systems, and intelligent reconfigurable surfaces for next-generation wireless networks. The ability to dynamically realize multiple EM responses within a single physical geometry makes the RFSS technology highly attractive for modern EM platforms, and this has been the central focus of this PhD thesis.

To achieve the RFSS designs, several methods have been investigated, including the use of MEMS switches, liquid crystals, and composite materials. These approaches often face challenges such as complex fabrication, slower switching speed, and high implementation cost. To address these limitations, the electronically reconfigurable technique is often used, employing p-i-n diodes and varactors as the constituent elements. These components provide fast, reliable, and economical control of the FSS frequency response, making them suitable for multifunctional applications. The RFSS performance mainly depends on the diode behavior. A p-i-n diode functions as a switch that alternates between a low-resistance ON state under forward bias and a high-capacitance OFF state under reverse bias. This switching enables a single structure to exhibit distinct EM responses. A varactor diode acts as a tuning element whose capacitance varies with bias voltage, allowing continuous frequency control. Integrating these diodes offers several benefits, such as fast response, low power consumption, compact integration, and simple control compared with other reconfigurable approaches.

To achieve these multifunctional responses, the designed geometries are analyzed in terms of two fundamental parameters, namely the reflection coefficient ( $S_{11}$ ) and the transmission coefficient ( $S_{21}$ ). The parameter  $S_{11}$  represents the portion of the incident EM energy that is reflected from the structure, while  $S_{21}$  represents the portion that is transmitted through it. The magnitudes of these coefficients indicate how efficiently the structure responds under different functional modes. In the transmissive mode, the structure should allow most of the energy to pass through; therefore,  $S_{21}$  must be high (typically greater than -3 dB) and  $S_{11}$  must

be low (typically less than -10 dB), ensuring minimal reflection and absorption. In the reflective mode, most of the incident energy should be reflected to the source, which requires  $S_{11}$  to remain high (typically  $> -3$  dB) and  $S_{21}$  small (typically  $< -10$  dB), confirming negligible transmission and absorption. For the absorptive mode, both reflection and transmission must be suppressed so that most of the energy is absorbed within the structure. Hence, both  $S_{11}$  and  $S_{21}$  should be below -10 dB at the resonant frequency, resulting in near-unity absorption ( $A(\omega) = 1 - |S_{11}|^2 - |S_{21}|^2$ ). In the case of a raserber, which combines a wideband absorption with a transmission window, the S-parameters vary across frequency. Within the absorption band, both  $S_{11}$  and  $S_{21}$  should be small enough to ensure high absorption, while in the transmission band, the  $S_{21}$  should be high (and  $S_{11}$  should be low), generating a distinct passband behavior. These criteria form the basis for designing RFSS structures exhibiting multifunctional responses.

Along with their geometrical characteristics, the equivalent circuit model plays a crucial role in realizing the multifunctional behavior of the proposed RFSS structures. A typical RFSS consists of metallic patterns printed on one or both sides of a dielectric substrate, with diode components embedded at strategic locations to enable switchable or tunable EM responses. Each diode-integrated metallic layer contributes a distinct electrical behavior, and the combined response of these layers governs the overall EM functionality of the structure. For instance, a parallel *RLC* network typically exhibits a bandpass response, while a series *RLC* network produces a bandstop response. Accordingly, a transmissive mode can be achieved when either or both of the metallic layers emulate a parallel *RLC* circuit. Conversely, the reflective mode operation can be obtained when the metallic layer behaves as a series *RLC* circuit or presents a high-impedance (effectively short-circuited) state. For absorptive operation, the top layer should be modeled as a parallel or series *RLC* circuit, while the bottom layer must act as a perfect reflector to suppress transmission. In the case of a raserber configuration, a suitable combination of transmission and absorption behavior must be realized by tailoring the metallic patterns at different frequency bands. Thus, the equivalent circuit model is extensively used for analyzing the multifunctional responses of all RFSS designs presented in this thesis.

The motivation for this thesis arises from the need to develop advanced RFSS

designs that can overcome the limitations of conventional structures while broadening their functional capabilities. This research follows a systematic and progressive investigation across different domains of EM wave control. It begins with the exploration of fundamental switching mechanisms using p-i-n diode configurations to realize dual-mode operations, achieving polarization-insensitive absorber/transmitter functionalities through embedded biasing networks. Building upon this foundation, the work progresses toward multifunctional systems that integrate both switching and frequency-tuning features by combining p-i-n and varactor diodes, thereby enabling simultaneous control of EM response and operational frequency. The work is further extended to multilayer architectures capable of exhibiting wideband behaviors among four distinct operating modes, including absorber (T-A), absorption, transmission, and reflection characteristics. In addition, this research addresses experimental challenges by developing a modified parallel plate waveguide (PPW) setup for wide-angle FSS characterization, providing a reliable and cost-effective approach for accurate measurement and validation. In summary, this thesis presents a structured approach that progresses from basic switching concepts to advanced multifunctional designs, supported by innovative measurement methodologies that enhance the practical realization of reconfigurable FSS technologies.

Despite these advances, several limitations remain in existing switchable RFSS designs. Most reported geometries are restricted to specific functionalities, such as reflection/transmission, reflection/absorption, and polarizer/reflector operations. Only a few studies demonstrate switching between absorption and transmission modes, and these approaches often suffer from additional issues such as multilayer arrangements, polarization sensitivity, and angular instability. Moreover, the integration of electronic control elements typically requires additional biasing networks, which further increases design complexity. To address these constraints, a single p-i-n diode configuration is considered to demonstrate basic dual-mode switching between absorption and transmission, while maintaining polarization-insensitive behavior in a single-layer substrate with simplified embedded bias networks. This motivation leads to the first contribution of this thesis.

The first contribution presents a polarization-insensitive absorptive/transmissive RFSS that employs p-i-n diodes with an integrated biasing network. The proposed

design consists of two periodic metallic patterns fabricated on opposite sides of a single FR4 substrate. The top layer contains a cross dipole surrounded by a Jerusalem cross connected to adjacent unit cells, while the bottom layer features a square slot with four symmetrically placed p-i-n diodes. The complete unit cell configuration, along with dimensional parameters, is illustrated in Figure 1.

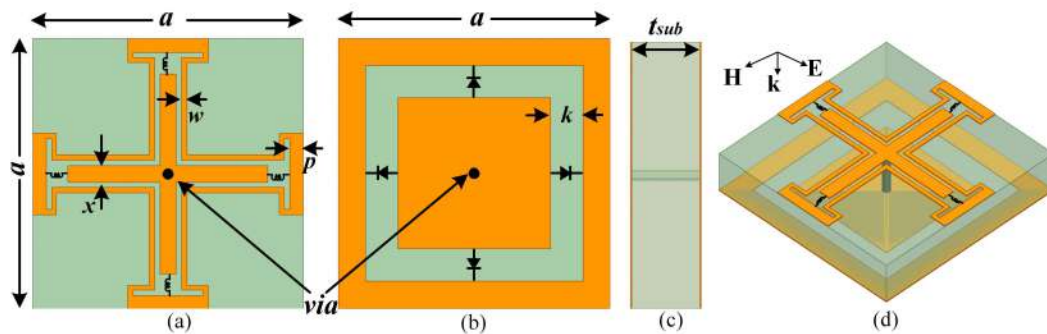


Figure 1: Proposed narrowband absorber/transmitter unit cell geometry: (a) top view, (b) bottom view, (c) side view, and (d) isometric view. The design parameters are finalized as (in mm):  $a = 10$ ,  $w = 0.2$ ,  $x = 0.6$ ,  $p = 0.5$ ,  $k = 1.2$ , and  $t_{sub} = 1.6$ .

The reconfigurable behavior is realized through a p-i-n diode positioned in the bottom layer, which switches between ON and OFF states under different biasing conditions. In the ON condition, the structure achieves strong absorption with 93.51% absorptivity at 6.93 GHz, functioning as a radar absorber. In the OFF condition, it provides transmission at 5.62 GHz with an insertion loss of 0.96 dB, operating as a bandpass filter. The embedded biasing network, consisting of vias and lumped inductors acting as RF chokes, enables polarization-insensitive behavior without degrading performance. An equivalent circuit model validates the switching mechanism and serves as a basis for further designs. The structure maintains stable performance for both TE and TM polarizations up to  $60^\circ$ , and consistency is observed across different polarization angles.

A prototype was fabricated and characterized using an in-house developed PPW measurement setup, which avoids the need for large free-space measurements while ensuring accurate validation. Figure 2 presents the fabricated sample photograph, experimental setup, and comparison between simulated and measured responses. The experimental data shows good agreement with simulations, confirming the effectiveness of the absorber/transmitter design and the suitability of the embedded

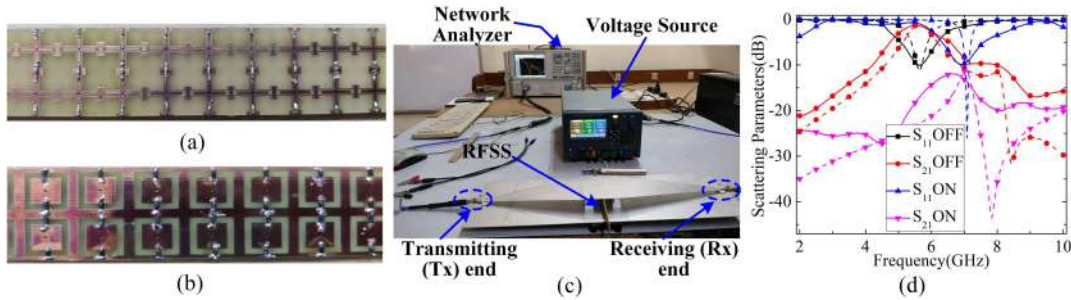


Figure 2: Photograph of the fabricated narrowband absorber/transmitter RFSS structure: (a) top layer, (b) bottom layer. (c) Measurement setup, and (d) comparison of the measured and simulated responses (solid lines represent PPW setup results, and dashed lines represent HFSS results).

biasing scheme for practical RFSS applications.

Although the first contribution establishes a basic understanding of the fundamental switching mechanism of RFSS using a single p-i-n diode configuration, the design only operates between absorption and transmission modes, which limits the number of operating modes and its functional versatility for advanced EM applications. Furthermore, the diode control mechanism in this design relies on manual biasing for switching between operational states, making it unsuitable for real-time dynamic systems. To address these limitations, the second contribution of this thesis introduces a more sophisticated architecture where two independently controlled diodes are strategically positioned on opposite sides of a single-layer dielectric substrate. This configuration simplifies both the biasing circuit design and topology implementation compared to multi-layer alternatives. Through careful selection of metallic patterns and precise placement of diode elements, this arrangement generates four distinct operating states (ON-ON, ON-OFF, OFF-ON, and OFF-OFF), with each state engineered to produce a unique EM response. This enables the structure to achieve three distinct EM behaviors such as absorption, transmission, and reflection across different modes. A field-programmable gate array (FPGA) is integrated into the diode control system to automate the switching mechanism and enable real-time operation.

In this work, the RFSS geometry is designed such that it can exhibit absorption, transmission, and reflection functionalities by employing a single-layer structure using two sets of p-i-n diodes. The design incorporates diode sets on both the top

and bottom layers of an FR4 substrate to expand the number of operating states and enhance the overall multifunctional performance of the structure. The top layer consists of a meander line connected to an inner cross-dipole through the first set of diodes ( $PD_1$ ), while the bottom layer includes an outer square loop with a  $45^\circ$  rotated inner square patch integrated with the second set of diodes ( $PD_2$ ). The schematic diagram of the proposed RFSS with FPGA control is shown in Figure 3(a), whereas Figures 3(b)-(d) depict the top layer, bottom layer, and side view, respectively, of the unit cell geometry along with all geometric dimensions.

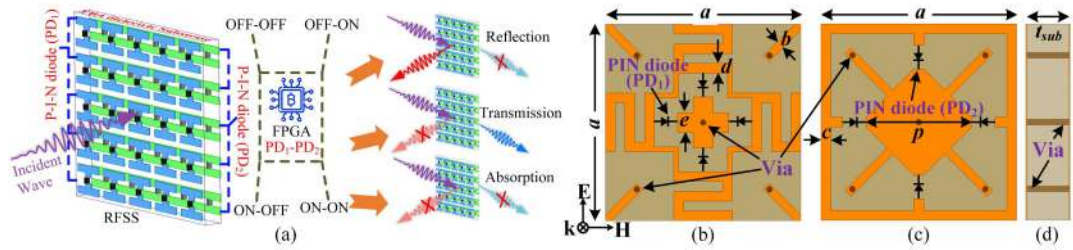


Figure 3: (a) Schematic representation of the RFSS with FPGA control. Unit cell design of the proposed narrowband absorber/transmitter/reflector RFSS: (b) top layer metallic pattern with diode set  $PD_1$ , (c) bottom layer metallic pattern with diode set  $PD_2$ , and (d) side view illustrating metallic vias. The dimensions are:  $a = 10$ ,  $b = 0.35$ ,  $c = d = 0.5$ ,  $e = 1$ ,  $p = 5.4$ ,  $t_{sub} = 1.6$  (units: mm).

The simulated results demonstrate the multifunctional behavior across all the operating modes. In the OFF-OFF mode, the structure exhibits the transmission response at 5.07 GHz with an insertion loss of 1.4 dB. The OFF-ON mode provides over 90% absorption at 5.2 GHz. The ON-OFF and ON-ON configurations produce the partial and full reflective characteristics till 6 and 8 GHz, respectively. The parallel biasing network, formed by shared metallic lines and vias, ensures independent control of both set of diodes in different layers while maintaining structural integrity. The FPGA-based controller applies a 2-bit coding sequence to regulate both sets, generating the required voltage levels for forward bias and zero voltage for reverse bias conditions. A detailed equivalent circuit model is developed to verify the underlying switching mechanism, and the design is further analyzed for polarization insensitivity and oblique-incidence stability to confirm its practical robustness.

Afterward, a one-dimensional (1-D) prototype was fabricated and experimentally validated using the in-house developed PPW measurement technique. The fab-

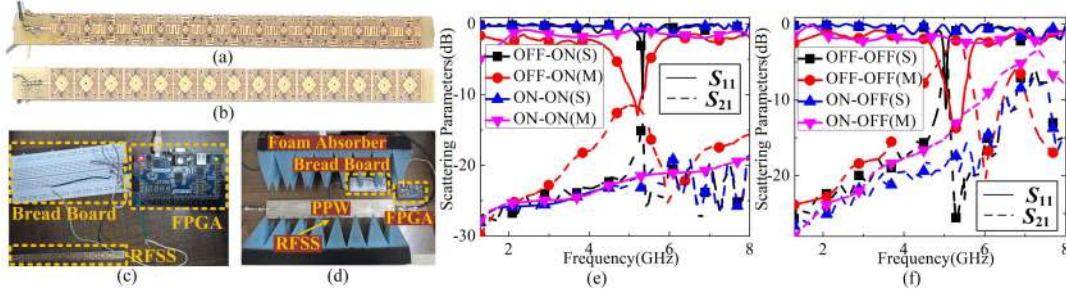


Figure 4: Fabricated prototype of the narrowband absorber/transmitter/reflector RFSS and experimental setup: (a) top layer, (b) bottom layer, (c) FPGA integration for controlling diode sets  $PD_1$  and  $PD_2$ , and (d) measurement arrangement. Comparison of simulated and measured results: (e) OFF-ON and ON-ON states, (f) OFF-OFF and ON-OFF states. S: simulation, M: measurement.

ricated prototype, FPGA-controlled measurement setup, and comparison between simulated and measured S-parameters for all four operating modes are shown in Figure 4. The FPGA-controlled measurements show close agreement with simulated results, confirming accurate switching between operational modes. The structure maintains polarization-insensitivity and angular stability across a wide range of incidence angles, demonstrating its suitability for real-time reconfigurable EM systems that require multiple operational functionalities within a single design.

The first two works of the thesis establish the principles of switching and multifunctional operation; however, both designs operate at fixed narrowband frequencies in each mode, which limits their flexibility for systems requiring tunable or dynamic EM responses. Although the second design achieves three distinct EM behaviors using two sets of p-i-n diodes, the resonant frequencies remain static once the geometric parameters are optimized. This limitation has been addressed in the third work, where varactor diodes are integrated with the existing p-i-n diode configuration, thereby enabling both mode switching and continuous frequency tuning within a single structure. This approach retains the single-layer configuration from earlier designs but introduces frequency agility by varying the capacitance of the varactor diodes under applied bias, creating a multifunctional reconfigurable RFSS capable of both discrete and continuous control.

This work develops a multifunctional reconfigurable FSS (MRFSS) that combines p-i-n and varactor diodes within a single-layer topology. The design consists of metallic patterns printed on both sides of an FR4 substrate. The top layer

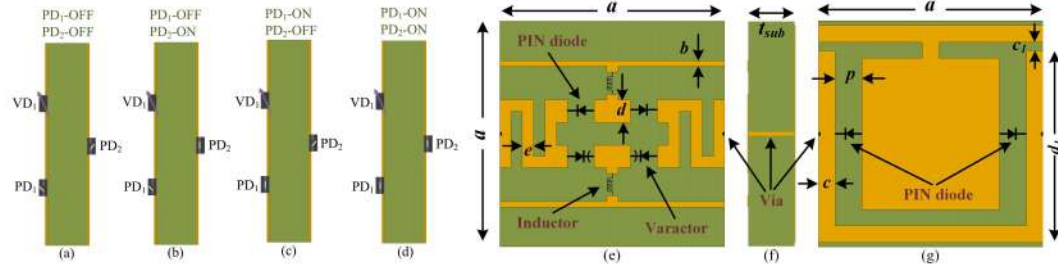


Figure 5: Illustration of the proposed switching + tuning MRFSS showing diode placement and operating states: (a) OFF-OFF, (b) OFF-ON, (c) ON-OFF, and (d) ON-ON. Unit cell geometry views of the proposed design: (e) top view, (f) side view, and (g) bottom view. The dimensions of different parts of the geometry are mentioned as  $a = 10$  mm,  $b = 0.25$  mm,  $c = 0.75$  mm,  $d = 1$  mm,  $e = 0.5$  mm,  $c_1 = 0.375$  mm,  $d_1 = 8.5$  mm,  $p = 1.2$  mm, and  $t_{sub} = 2$  mm.

features a meander line loaded with parallel-mounted varactors and p-i-n diodes, while the bottom layer includes a central metallic patch with connecting lines and an additional set of p-i-n diodes. Unlike earlier designs that operate at fixed frequencies, this structure allows frequency tuning within each mode by controlling the reverse bias voltage applied to the varactor diodes. Figures 5(a)-(d) illustrate the proposed MRFSS across all operating states, showing the placement of varactor and p-i-n diodes. Figures 5(e)-(g) present the unit cell geometry with top, bottom, and side views, including all dimensional parameters. The reconfigurable behavior is achieved by operating both types of diodes, producing four distinct operational states with frequency tunability in each mode. In the OFF-OFF condition, the structure provides a tunable bandpass transmission response from 1.68 to 2.56 GHz, with an insertion loss ranging between 1.8 and 2.9 dB. In the OFF-ON condition, the absorption response tunes from 1.84 to 2.85 GHz, achieving absorptivity between 84.3% and 96.5%. The ON-ON state demonstrates reflection tuning from 2.55 to 4.62 GHz, while the ON-OFF state exhibits selective reflection from 2.48 to 4.43 GHz. The biasing network is designed to independently control all diode elements using only four terminals, significantly reducing circuit complexity compared to conventional approaches. A comprehensive equivalent circuit analysis has been performed to support the multifunctional and tunable behavior, and the structure exhibits stable performance for both TE and TM polarizations under oblique incidence.

A  $20 \times 20$  unit cell array was fabricated and tested using free-space measurement

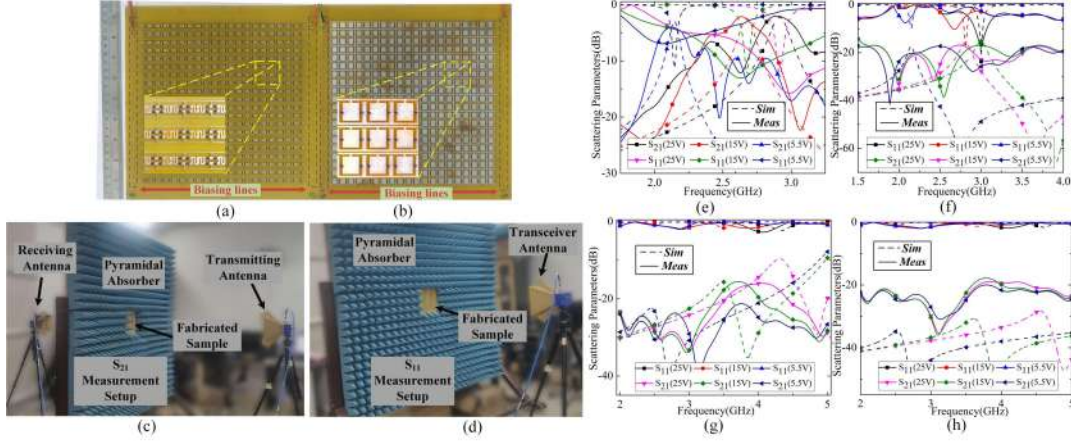


Figure 6: Fabricated prototype of proposed switching + tuning MRFSS and measurement setup: (a) top layer, (b) bottom layer, (c)  $S_{21}$  measurement setup, (d)  $S_{11}$  measurement setup. Comparison of measured and simulated responses for different modes: (e) transmission, (f) absorption, (g) selective-reflection, and (h) full reflection.

techniques. The independent DC power supplies regulate the bias voltages for both p-i-n and varactor diodes. The fabricated prototype photograph, free-space measurement setup, and comparison between simulated and measured frequency tunable responses across all four operating modes are presented in Figure 6. The measured results validate frequency tunability by varying the reverse bias voltage from 5.5 V to 25 V, confirming accurate switching and tuning performance. The equivalent circuit model supports the theoretical understanding of the multifunctional behavior, while angular stability analysis verifies reliable operation for incident angles up to  $60^\circ$ . This design effectively integrates both switching and frequency tuning functions within a compact single-layer structure, marking an important advancement in reconfigurable FSS development.

Although this third work demonstrates both switching and frequency tuning capabilities, all operating modes remain narrowband. The limited absorption bandwidth, restricted transmission passband, and confined reflection range reduce its suitability for wideband applications. To overcome these bandwidth limitations, the fourth contribution of this thesis introduces a multilayer architecture that integrates two dielectric layers separated by an air spacer. This configuration enables wideband operation across four distinct EM functions. In addition, lumped resistors are incorporated along with p-i-n diodes to broaden the absorption response, while four-

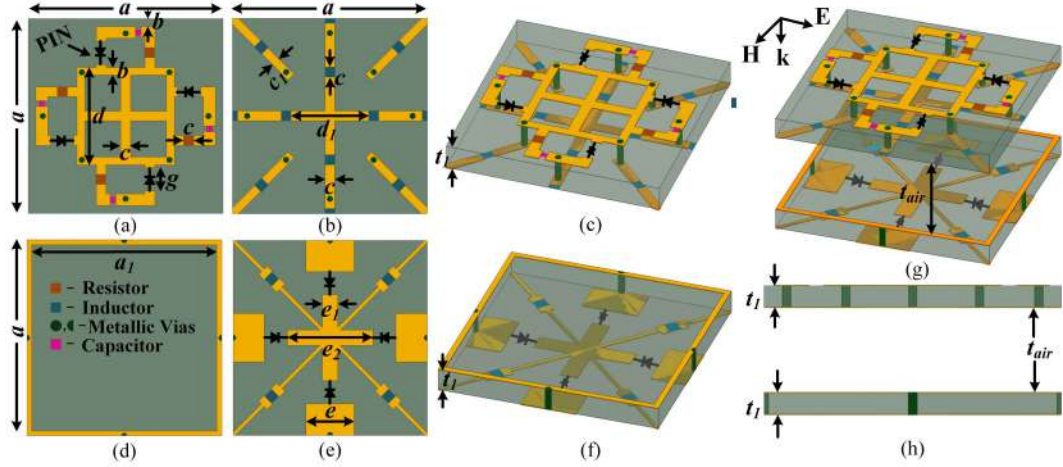


Figure 7: Proposed wideband raserber/absorber/transmitter/reflector RFSS unit cell geometry: Layer 1: (a) top view, (b) bottom view, (c) isometric view; Layer 2: (d) top view, (e) bottom view, (f) isometric view; Overall unit cell: (g) isometric view, (h) side view. The optimized dimensions of the design (in mm):  $a = 10$ ,  $a_1 = 9.5$ ,  $b = 0.4$ ,  $c = 0.5$ ,  $c_1 = 0.42$ ,  $d = 5$ ,  $d_1 = 4$ ,  $g = 1.2$ ,  $e = 2.5$ ,  $e_1 = 4.4$ ,  $e_2 = 0.8$ ,  $t_1 = 1$ , and  $t_{air} = 4$ .

fold symmetric geometries across the substrate layers ensure polarization-insensitive performance.

The fourth contribution presents a wideband reconfigurable FSS capable of four EM functionalities: raserber (transmission-absorption), absorption, transmission, and reflection. The proposed structure employs two FR4 substrate layers (layer 1-top and layer 2 - bottom) separated by a 4 mm air gap. Layer 1 includes a modified square loop with four symmetric dipole arms, each integrated with a p-i-n diode and a  $30 \Omega$  lumped resistor connected through bias lines. Layer 2 consists of a square loop linked to rectangular patches through vias, where p-i-n diodes are positioned between the cross-dipole and rectangular sections. The unit cell geometry with complete dimensional parameters and all layer configurations is shown in Figure 7.

The broadband reconfigurable behavior is obtained through an independent control of the two sets of p-i-n diodes presented in both layers. In the OFF-OFF mode, the structure exhibits raserber characteristics with transmission at 2.67 GHz (insertion loss of 2.1 dB) and broadband absorption from 4.76-6.37 GHz, corresponding to a 28.5% fractional bandwidth. The OFF-ON state produces broadband absorption from 3.25- 6.05 GHz, achieving a 60.21% fractional bandwidth with absorptivity exceeding 80%. In the ON-OFF mode, the structure provides broadband transmission

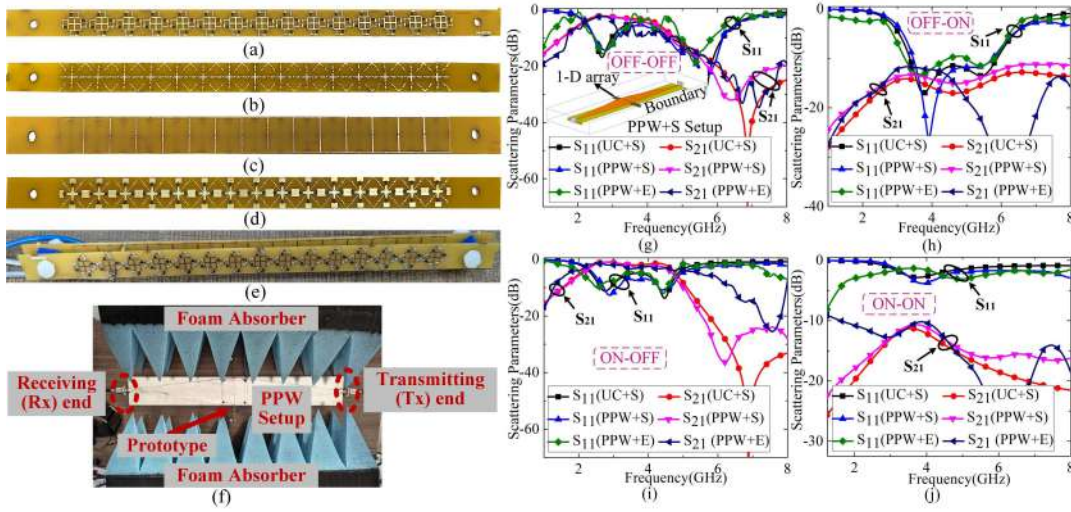


Figure 8: Fabricated prototype of the proposed wideband rasorber/absorber/transmitter/reflector RFSS and measurement setup: Layer 1: (a) top view, (b) bottom view; Layer 2: (c) top view, (d) bottom view; (e) complete sample; (f) PPW experimental setup for  $S_{11}$  and  $S_{21}$  measurements. Comparison of measured and simulated responses: (g) rasorber mode, (h) absorption mode, (i) transmission mode, (j) reflection mode. The inset figure shows the simulated PPW setup in HFSS.

from 2.41 to 4.49 GHz with a 60.28% fractional bandwidth and an insertion loss below 2 dB, while the ON-ON mode delivers full reflection ( $S_{11} < 2.8$  dB) across the entire operating band. The multilayer arrangement with an air spacer enhances the bandwidth while maintaining angular stability and polarization insensitivity through its symmetric design. The proposed wideband configuration is thoroughly validated through equivalent circuit modeling, polarization, and oblique-incidence analyses, ensuring reliable operation across all designed modes.

A 1-D prototype, comprising  $15 \times 1$  unit cells, was fabricated and validated using a custom-built PPW measurement setup capable of oblique incidence testing. The fabricated prototype photograph, PPW measurement setup, and comparison between simulated and measured wideband responses for all four modes are presented in Figure 8. The measured results closely match simulations across all four operational modes, confirming wideband performance and reliable reconfigurability. The angular stability analysis shows consistent operation up to  $45^\circ$  for TE polarization and similar stability for TM modes. This multilayer design demonstrates a significant improvement in bandwidth while maintaining compactness and polarization insensitivity, marking another important step toward practical broadband

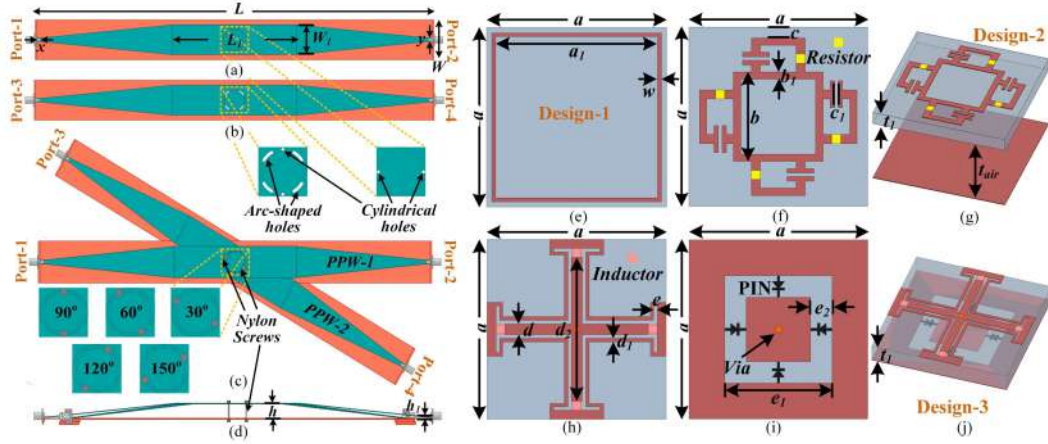


Figure 9: Modified PPW setup and unit cell designs: PPW configurations: (a) PPW-1 with cylindrical apertures, (b) PPW-2 with cylindrical and arc-shaped apertures, overall PPW setup: (c) top view, and (d) side view. Unit cell geometries: Design-1: (e) top view; Design-2: (f) top view, (g) isometric view; Design-3: (h) top view, (i) bottom view, (j) isometric view. The optimized dimensions for PPW and unit cell geometries (in mm):  $L = 800$ ,  $W = 80$ ,  $W_1 = 60$ ,  $L_1 = 250$ ,  $x = 8$ ,  $y = 7$ ,  $h = 10$ ,  $h_1 = 1.5$ ,  $a = 10$ ,  $a_1 = 9$ ,  $w = 0.2$ ,  $b = 5$ ,  $b_1 = 0.4$ ,  $c = d = 0.6$ ,  $c_1 = 0.2$ ,  $t_1 = 1$ ,  $t_{air} = 4$ ,  $d_1 = e = 0.25$ ,  $d_2 = 8$ ,  $e_1 = 6$ , and  $e_2 = 1.2$ .

reconfigurable FSS solutions for advanced EM applications.

While the four contributions collectively establish a complete framework for reconfigurable FSS advancement, experimental validation of such designs remains a challenge due to the limitations of existing measurement techniques. Traditional free-space measurements require large prototypes, wideband horn antennas, and anechoic chambers, which increase cost and complexity, especially for structures incorporating DC biasing networks. Although the PPW technique was used for validation in previous works, conventional PPW systems are restricted to normal incidence characterization and cannot evaluate wide-angle performance. This limitation motivated the development of a modified PPW system capable of accurate wide-angle characterization of FSS structures.

The fifth contribution of this thesis introduces a modified PPW setup designed for precise measurement of 1-D arrays of FSS prototypes under both normal and oblique incidence conditions. The system consists of two parallel metallic plates engineered with varying geometry, with an increased central height to accommodate 1-D FSS arrays and tapered ends for wideband impedance matching with coaxial connectors. The tapered structure minimizes edge radiation and leakage, ensuring

measurement accuracy across the 1-8 GHz range. For wide-angle testing, two PPW sections with different apertures are mechanically joined at adjustable angles, allowing controlled angular excitation from  $30^\circ$  to  $150^\circ$  while maintaining electrical continuity and mechanical alignment. Figure 9 illustrates the modified PPW configurations used for oblique incidence measurements. Figures 9(a)-(d) show the individual setups, including PPW-1 with cylindrical apertures, PPW-2 with cylindrical and arc-shaped apertures, and the combined top and side views of the measurement arrangement. Figures 9(e)-(j) present the unit cell designs of the three proposed structures, showing the top, bottom, and isometric views along with all optimized dimensional parameters.

The system achieves wide-angle measurement capability through a dual-section PPW configuration. During oblique incidence testing, one section remains stationary while the other rotates about its axis, enabling the incident transverse electromagnetic (TEM) wave to strike the FSS at angle  $\theta$  and exit at the complementary angle  $2\theta$  without distortion. The cylindrical and arc-shaped apertures at the junction ensure smooth rotation and alignment. The calibration is performed using two references: a copper plate for reflection ( $S_{11}$ ) and an empty setup for transmission ( $S_{21}$ ). The simulated calibration results indicate low insertion loss, below 3 dB for normal incidence and between 5-7 dB for oblique incidence, confirming the accuracy and reliability of the system, which will be presented in detail in the subsequent sections of the thesis.

To validate its effectiveness, three FSS prototypes were fabricated and tested using the developed setup: a bandstop filter, a two-layer broadband absorber, and a switchable absorber/transmitter. Each prototype consists of a 15 unit-cell 1-D array measuring  $150 \times 10$  mm, fabricated using PCB etching with appropriate lumped components and p-i-n diodes. The fabricated FSS prototypes, complete measurement setup with angular adjustment mechanism, and measured results under both normal and oblique incidence conditions are presented in Figure 10. The experimental results in comparison with simulated results, including frequency deviations and electric field distributions under normal and oblique incidence, are discussed in detail in the subsequent sections of the thesis. This modified PPW configuration eliminates the need for large free-space prototypes and anechoic chamber setups while

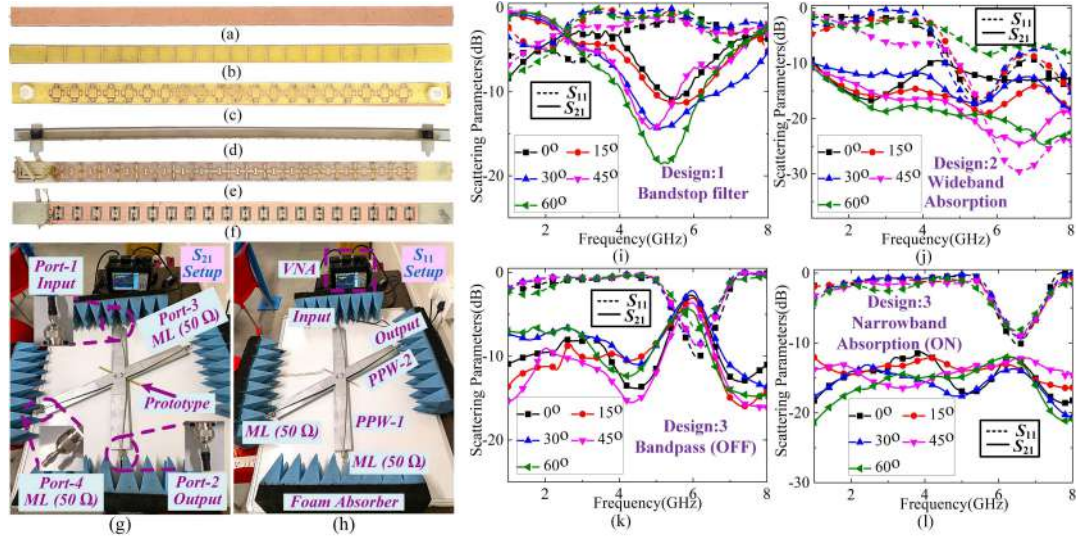


Figure 10: FSS prototypes, modified PPW experimental setup, and measured responses: (a) copper reference sample, (b) bandstop filter; wideband absorber: (c) top view, (d) side view; RFSS: (e) top view, (f) bottom view; PPW Oblique incidence measurement setup: (g)  $S_{21}$ , (h)  $S_{11}$ . Measured responses under normal and oblique incidences: (i) bandstop filter, (j) wideband absorber, and RFSS: (k) OFF state, (l) ON state.

providing a cost-effective and precise approach for wide-angle FSS characterization, establishing a reliable measurement method for RFSS geometries.

In summary, this thesis presents a systematic and comprehensive investigation into the design, analysis, and experimental validation of multifunctional RFSS structures. The research begins with the development of a basic single-layer RFSS configuration that demonstrates dual-mode switching between absorption and transmission, establishing the foundation for understanding the role of p-i-n diodes in achieving reconfigurable EM behavior. The work is subsequently extended by incorporating two diode sets independently controlled through an FPGA-based system to realize three distinct functionalities, namely transmission, reflection, and absorption, within a single structure. Building on these concepts, the work introduces a hybrid design that integrates p-i-n and varactor diodes to simultaneously achieve switching among different operating states and tuning within each state, thereby achieving a tunable-switchable multifunctional RFSS capable of dynamic operation. To further improve bandwidth and multifunctional stability, a multilayer architecture is then proposed, which achieves wideband absorber, absorber, transmission, and reflection characteristics along with improved polarization and angular stability. All these

proposed designs are supported by detailed design methodologies, equivalent circuit modeling, full-wave simulations, and experimental validations. Beyond the structural development, the thesis also addresses practical implementation challenges by introducing a modified PPW measurement setup capable of wide-angle characterization, offering a cost-effective and accurate alternative to conventional free-space measurement systems. Overall, these contributions advance the state of RFSS technology by realizing compact, multifunctional, and frequency-agile RFSS structures that combine versatility with real-time reconfiguration. The unified framework developed in this thesis demonstrates strong applicability for a wide range of modern EM platforms, including stealth systems, RCS reduction, wireless communication, and EM shielding.

## Acknowledgment

My PhD journey begins with the belief that choosing *Dr. Saptarshi Ghosh* as my supervisor would be the right decision, which later proved to be one of the best decisions of my life. As a young researcher, I have started this journey with a few expectations; however, with his guidance, encouragement, and support, it has become far more meaningful and productive than I have anticipated. I could not have asked for anything more. Our discussions on technical insights play a crucial role in improving the quality of my research work. Beyond academic mentorship, I am deeply impressed by his qualities as a person, which inspire me even more. These interactions strengthen our bond by allowing me to understand and share my thoughts more deeply. I can confidently say that I begin this journey as a stranger in a purely professional relationship, which gradually evolved into one of the most meaningful personal bonds of my life.

I also express my sincere gratitude to my PSPC members: *Prof. Srivathsan Vasudevan* (IIT Indore), *Prof. Gourab Sil* (IIT Indore), and *Prof. Saikat Sarkar* (IIT Delhi), for their constructive feedback and valuable suggestions. Their insights have refined my presentation skills and helped me to communicate research ideas effectively to both technical experts and a broader audience. I am also grateful to *Prof. Abhirup Datta* (IIT Indore) for kindly providing access to the vector network analyzer and other essential components whenever required for my research.

I am thankful to the senior members of our laboratory, especially the *postdoctoral fellows*, who share their valuable experiences and offer insightful guidance that helped me shape my research direction and future career plans. I am equally grateful to my *fellow PhD scholars*, both seniors and juniors, for creating a supportive and motivating research environment. It is a truly enriching experience sharing the professional space with them.

I also acknowledge the *M.Tech/MS (R)* research students for their assistance in carrying out the FSS measurements and for their help with several non-technical tasks. Working with the *junior research fellows* in our laboratory is a great experience, during which I share many memorable moments. Their research work often encourages me to explore new ideas.

I further acknowledge the *B.Tech students and interns* with whom I have had the opportunity to interact and whom I have had the privilege of guiding through their final-year projects and internships. Mentoring these young minds is both challenging and fulfilling, and it greatly enhances my confidence and appreciation for the joy of academic guidance and student interaction.

---

I am grateful to my collaborators and co-authors: *Dr. Aditi Sharma, Dr. Soumendu Ghosh, and Dr. Laxmikant Dewangan*, for their valuable collaboration, teamwork, and insightful discussions that greatly enrich our research work.

I further acknowledge the laboratory staff of the Department of Electrical Engineering, IIT Indore, especially *Mr. Raghvendra Hanswal*, for his relentless effort, precision, and patience in soldering all the RF components used in the fabricated prototypes. I am also thankful to the *office and administrative staff* of the Department of Electrical Engineering and IIT Indore for efficiently handling financial and administrative matters, making my PhD journey smooth and hassle-free.

I gratefully acknowledge the financial support provided by the *Ministry of Human Resource Development (MHRD)* and sincerely thank *IIT Indore* for offering an enriching academic environment and one of the most rewarding experiences of my doctoral journey.

I express my sincere thanks to my closest friend at IIT Indore, *Mr. Shubhanshu Bishwash*, who has always been there to listen to me and make me feel comfortable sharing anything at any time without any judgment. He has provided unwavering moral support whenever required. I also extend my gratitude to *Dr. Hemapriya Raju, Mr. Y. Venu Gopal, Mr. Abhishek Srivastava, Ms. Manopriya Samtham, Mr. P. J. S. Rama Krishna, and Mr. Shivaji Cheepurapalli* for their constant encouragement and support.

I also thank my *school, college, and B.Tech friends*, who have remained close to me and provided continuous support and encouragement during the challenging phases of my PhD journey. I am equally grateful to the educational institutions that shape my academic path, beginning with my school education, followed by my undergraduate studies at the University College of Engineering, JNTU Kakinada, and my postgraduate studies at the National Institute of Technology, Surathkal, Karnataka. These institutions provide a strong academic foundation and lay the essential building blocks for this doctoral journey.

Finally, I would like to express my heartfelt gratitude to my parents, who have stood by me through every challenge with unwavering support. Their unconditional love, wholehearted blessings, and constant care are a guiding strength throughout my life. Without their support, I would not be able to experience this beautiful and enriching journey.

Patinavalasa Megh Sainadh

*Dedicated*  
*to*  
*my grandparents*  
*and*  
*parents*



# Contents

<b>List of Figures</b>	<b>ix</b>
<b>List of Tables</b>	<b>xviii</b>
<b>List of Abbreviations/Acronyms</b>	<b>xx</b>
<b>List of Symbols</b>	<b>xxiii</b>
<b>1 Introduction</b>	<b>1</b>
1.1 Overview of FSS . . . . .	5
1.2 Need for Reconfigurability in FSS . . . . .	9
1.3 Working Principle of Electronic Diodes . . . . .	10
1.4 Basic Mechanisms of EM Operation . . . . .	11
1.4.1 Reflection Mechanism . . . . .	12
1.4.2 Transmission Mechanism . . . . .	14
1.4.3 Absorption Mechanism . . . . .	15
1.4.4 Resorber Mechanism . . . . .	17
1.5 Literature Survey on RFSS Structures . . . . .	19
1.5.1 Switchable RFSS Structures . . . . .	20
1.5.2 Tunable RFSS Structures . . . . .	28
1.5.3 Switchable-Tunable MRFSS Structures . . . . .	31
1.5.4 Measurement Techniques for RFSS Structures . . . . .	33
1.6 Motivation of Thesis . . . . .	36
1.7 Organization of Thesis . . . . .	39
<b>2 Polarization-Insensitive Narrowband Absorptive/ Transmissive RFSS</b>	<b>43</b>
2.1 Introduction . . . . .	43
2.2 Design and Analysis . . . . .	44
2.2.1 Unit Cell Geometry . . . . .	45
2.2.2 Equivalent Circuit Modeling . . . . .	48
2.2.3 Polarization-Insensitivity and Angular Stability . . . . .	51
2.3 Fabrication and Measurement . . . . .	52
2.3.1 Embedded Biasing Circuitry . . . . .	52
2.3.2 Fabrication of the RFSS Prototype . . . . .	54
2.3.3 PPW Measurement Setup and Experimental Results . . . . .	54
2.4 Conclusion . . . . .	56

<b>3</b>	<b>Polarization-Insensitive Narrowband Multifunctional RFSS with FPGA Control</b>	<b>59</b>
3.1	Introduction . . . . .	59
3.2	Design and Analysis . . . . .	61
3.2.1	Unit Cell Geometry . . . . .	61
3.2.2	Simulated Responses . . . . .	62
3.2.3	Equivalent Circuit Modeling . . . . .	65
3.2.4	Polarization Insensitivity and Angular Stability . . . . .	67
3.3	Fabrication and Measurement . . . . .	70
3.3.1	Biasing, Fabrication, and Hardware Integration . . . . .	70
3.3.2	Measurement using PPW Setup . . . . .	72
3.4	Conclusion . . . . .	75
<b>4</b>	<b>Switchable and Tunable Narrowband Multifunctional RFSS</b>	<b>79</b>
4.1	Introduction . . . . .	79
4.2	Design and Analysis . . . . .	81
4.2.1	Design Methodology of the Unit Cell . . . . .	82
4.2.2	Equivalent Circuit Modeling . . . . .	86
4.3	Fabrication and Experimental Verification . . . . .	92
4.3.1	Parallel Biasing Technique . . . . .	92
4.3.2	Fabrication and Measurement . . . . .	94
4.3.3	Analysis of Response Deviations . . . . .	97
4.4	Conclusion . . . . .	100
<b>5</b>	<b>Wideband Polarization-Insensitive RFSS-based Risorber/ Absorber/ Transmitter/ Reflector</b>	<b>103</b>
5.1	Introduction . . . . .	103
5.2	Design and Analysis . . . . .	105
5.3	Simulation Results . . . . .	113
5.4	Fabrication And Experimental Verification . . . . .	118
5.4.1	Biasing Framework . . . . .	118
5.4.2	Fabrication of 1-D Prototype . . . . .	119
5.4.3	PPW Measurement Setup . . . . .	120
5.4.4	Validation of Measurement Results . . . . .	122
5.5	Conclusion . . . . .	125
<b>6</b>	<b>Wide-Angle RFSS Characterization using Modified Parallel-Plate Waveguide</b>	<b>127</b>
6.1	Introduction . . . . .	127
6.2	PPW Design and Characterization . . . . .	130
6.2.1	PPW Design . . . . .	130
6.2.2	FSS unit cell designs and simulation results . . . . .	132
6.3	Modified PPW for Oblique Incidence . . . . .	135
6.3.1	Calibration of the Modified PPW Setup: . . . . .	136
6.3.2	Comparison of Unit-Cell (PBC) and PPW Simulation Results for Modified PPW Setup . . . . .	137
6.3.3	Electric Field Distribution Analysis . . . . .	139
6.4	Fabrication and Experimental Setup . . . . .	140
6.4.1	Fabrication of FSS Prototypes . . . . .	140

6.4.2	Fabrication of the Modified PPW Setup . . . . .	141
6.4.3	Measurement Setup . . . . .	142
6.4.4	Measured Results . . . . .	142
6.5	Conclusion . . . . .	143
<b>7</b>	<b>Conclusion and Future Scope</b>	<b>147</b>
7.1	Summary of Research . . . . .	147
7.2	Scope of Future Work . . . . .	151



# List of Figures

1	Proposed narrowband absorber/transmitter unit cell geometry: (a) top view, (b) bottom view, (c) side view, and (d) isometric view. The design parameters are finalized as (in mm): $a = 10$ , $w = 0.2$ , $x = 0.6$ , $p = 0.5$ , $k = 1.2$ , and $t_{sub} = 1.6$ . . . . .	vii
2	Photograph of the fabricated narrowband absorber/transmitter RFSS structure: (a) top layer, (b) bottom layer. (c) Measurement setup, and (d) comparison of the measured and simulated responses (solid lines represent PPW setup results, and dashed lines represent HFSS results). . . . .	viii
3	(a) Schematic representation of the RFSS with FPGA control. Unit cell design of the proposed narrowband absorber/transmitter/reflector RFSS: (b) top layer metallic pattern with diode set $PD_1$ , (c) bottom layer metallic pattern with diode set $PD_2$ , and (d) side view illustrating metallic vias. The dimensions are: $a = 10$ , $b = 0.35$ , $c = d = 0.5$ , $e = 1$ , $p = 5.4$ , $t_{sub} = 1.6$ (units: mm). . . . .	ix
4	Fabricated prototype of the narrowband absorber/transmitter/reflector RFSS and experimental setup: (a) top layer, (b) bottom layer, (c) FPGA integration for controlling diode sets $PD_1$ and $PD_2$ , and (d) measurement arrangement. Comparison of simulated and measured results: (e) OFF-ON and ON-ON states, (f) OFF-OFF and ON-OFF states. S: simulation, M: measurement. . . . .	x
5	Illustration of the proposed switching + tuning MRFSS showing diode placement and operating states: (a) OFF-OFF, (b) OFF-ON, (c) ON-OFF, and (d) ON-ON. Unit cell geometry views of the proposed design: (e) top view, (f) side view, and (g) bottom view. The dimensions of different parts of the geometry are mentioned as $a = 10$ mm, $b = 0.25$ mm, $c = 0.75$ mm, $d = 1$ mm, $e = 0.5$ mm, $c_1 = 0.375$ mm, $d_1 = 8.5$ mm, $p = 1.2$ mm, and $t_{sub} = 2$ mm. . . . .	xi
6	Fabricated prototype of proposed switching + tuning MRFSS and measurement setup: (a) top layer, (b) bottom layer, (c) $S_{21}$ measurement setup, (d) $S_{11}$ measurement setup. Comparison of measured and simulated responses for different modes: (e) transmission, (f) absorption, (g) selective-reflection, and (h) full reflection. . . . .	xii

- 7 Proposed wideband rasorber/absorber/transmitter/reflector RFSS unit cell geometry: Layer 1: (a) top view, (b) bottom view, (c) isometric view; Layer 2: (d) top view, (e) bottom view, (f) isometric view; Overall unit cell: (g) isometric view, (h) side view. The optimized dimensions of the design (in mm):  $a = 10$ ,  $a_1 = 9.5$ ,  $b = 0.4$ ,  $c = 0.5$ ,  $c_1 = 0.42$ ,  $d = 5$ ,  $d_1 = 4$ ,  $g = 1.2$ ,  $e = 2.5$ ,  $e_1 = 4.4$ ,  $e_2 = 0.8$ ,  $t_1 = 1$ , and  $t_{air} = 4$ . . . . . xiii
- 8 Fabricated prototype of the proposed wideband rasorber/absorber/transmitter/reflector RFSS and measurement setup: Layer 1: (a) top view, (b) bottom view; Layer 2: (c) top view, (d) bottom view; (e) complete sample; (f) PPW experimental setup for  $S_{11}$  and  $S_{21}$  measurements. Comparison of measured and simulated responses: (g) rasorber mode, (h) absorption mode, (i) transmission mode, (j) reflection mode. The inset figure shows the simulated PPW setup in HFSS. . . . . xiv
- 9 Modified PPW setup and unit cell designs: PPW configurations: (a) PPW-1 with cylindrical apertures, (b) PPW-2 with cylindrical and arc-shaped apertures, overall PPW setup: (c) top view, and (d) side view. Unit cell geometries: Design-1: (e) top view; Design-2: (f) top view, (g) isometric view; Design-3: (h) top view, (i) bottom view, (j) isometric view. The optimized dimensions for PPW and unit cell geometries (in mm):  $L = 800$ ,  $W = 80$ ,  $W_1 = 60$ ,  $L_1 = 250$ ,  $x = 8$ ,  $y = 7$ ,  $h = 10$ ,  $h_1 = 1.5$ ,  $a = 10$ ,  $a_1 = 9$ ,  $w = 0.2$ ,  $b = 5$ ,  $b_1 = 0.4$ ,  $c = d = 0.6$ ,  $c_1 = 0.2$ ,  $t_1 = 1$ ,  $t_{air} = 4$ ,  $d_1 = e = 0.25$ ,  $d_2 = 8$ ,  $e_1 = 6$ , and  $e_2 = 1.2$ . . . . . xv
- 10 FSS prototypes, modified PPW experimental setup, and measured responses: (a) copper reference sample, (b) bandstop filter; wideband absorber: (c) top view, (d) side view; RFSS: (e) top view, (f) bottom view; PPW Oblique incidence measurement setup: (g)  $S_{21}$ , (h)  $S_{11}$ . Measured responses under normal and oblique incidences: (i) bandstop filter, (j) wideband absorber, and RFSS: (k) OFF state, (l) ON state. . . . . xvii
- 1.1 Evolution of FSS concepts: From the 1919 Marconi & Franklin wire-grid reflector [47] through WWII mesh reflectors [51, 52], planar dipole/slot arrays of the 1960s–1980s, and compact miniaturized unit cells developed after 2000. . . . . 7
- 1.2 Applications of multifunctional FSS/RFSS: (a) adaptive radome for in-band transmission and stealth [59], (b) multifunctional surface for radar-communication coexistence [60], and (c) intelligent surface for secure, reconfigurable wireless control [61]. . . . . 8
- 1.3 Equivalent circuit models of p-i-n diode in the ON and OFF states and varactor diode illustrating voltage-controlled junction capacitance. 10
- 1.4 Basic mechanisms of RFSS: (a) representative single dielectric structure with p-i-n diodes, (b)-(d) schematic depiction of reflection, transmission, and absorption operations, and (e) equivalent circuit model illustrating common impedance representation for all modes. . . . . 12

1.5	(a) Representative dual-layer RFSS structure with p-i-n diodes, (b) schematic depiction of rasorber operation, and (c) equivalent circuit model illustrating common impedance representation. . . . .	17
1.6	Active annular ring FSS: (a) unit cell configuration, (b) p-i-n diode equivalent circuits, (c) simulated ON-state response, and (d) simulated OFF-state response. [Courtesy: P. S. Taylor, E. A. Parker, and J. C. Batchelor, "An active annular ring frequency selective surface," <i>IEEE Trans. Antennas Propag.</i> , vol. 59, no. 9, pp. 3265–3271, Sept. 2011.] . . . . .	20
1.7	Switchable metamaterial reflector/absorber: (a) schematic layout, (b) fabricated sample, (c) Row A ON/OFF states, and (d) Row B ON/OFF states. [Courtesy: B. Zhu, Y. Feng, J. Zhao, C. Huang, and T. Jiang, "Switchable metamaterial reflector/absorber for different polarized electromagnetic waves," <i>Appl. Phys. Lett.</i> , vol. 97, no. 5, p. 051906, 2010.] . . . . .	21
1.8	Active absorption/transmission FSS using diodes: (a) front view, (b) back view, and (c) simulated reflection and transmission characteristics for ON and OFF states. [Courtesy: S. Kitagawa, R. Suga, K. Araki, and O. Hashimoto, "Active absorption/transmission FSS using diodes," <i>IEEE Asia-Pacific Microwave Conference</i> , 2015.] . . . . .	22
1.9	Switchable linear/circular polarization converter: (a) unit cell geometry, (b) side view, (c) $S_{11}$ for co- and cross-polarization, and (d) polarization conversion ratio (PCR). [Courtesy: Y. Li, Q. Cao, and Y. Wang, "A switchable reflection-type linear/circular polarizers based on active metasurface," <i>2019 IEEE International Symposium on Antennas and Propagation and USNC-URSI Radio Science Meeting</i> , Atlanta, GA, USA, 2019.] . . . . .	23
1.10	Dual-layer FSS-based switchable rasorber/absorber: (a) structure schematic with resistive elements, (b) surface current distributions for diode OFF and ON states, and (c) simulated $S$ -parameters showing rasorber and absorber modes. [Courtesy: Y. Han, W. Che, X. Xiu, W. Yang, and C. Christopoulos, "Switchable low-profile broadband frequency-selective rasorber/absorber based on slot arrays," <i>IEEE Trans. Antennas Propag.</i> , vol. 65, no. 12, pp. 6998–7008, Dec. 2017.] . . . . .	24
1.11	Dual-layer p-i-n diode-based polarization-independent switchable FSS: (a) 3D schematic, (b) cross-sectional view, (c) biasing network layout, and (d)–(g) simulated transmission responses for different diode bias states under TE and TM polarizations. [Courtesy: H. Li, Q. Cao, and Y. Wang, "A novel 2-B multifunctional active frequency selective surface for LTE-2.1 GHz," <i>IEEE Trans. Antennas Propag.</i> , vol. 65, no. 6, pp. 3084–3092, Jun. 2017.] . . . . .	25
1.12	Multifunctional reconfigurable AFSS: (a)–(b) top and bottom unit cells, and (c)–(f) simulated $S$ -parameters for four switching states. [Courtesy: R. Phon, S. Ghosh, and S. Lim, "Novel multifunctional reconfigurable active frequency selective surface," <i>IEEE Trans. Antennas Propag.</i> , vol. 67, no. 3, pp. 1709–1719, 2019.] . . . . .	26

- 1.13 Varactor-tunable convoluted dipole FSS: (a)–(b) upper and lower metallization layers with varactor diodes and resistors, and (c) simulated transmission response demonstrating tunability. [Courtesy: C. Mias, “Varactor-tunable frequency selective surface with resistive-lumped-element biasing grids,” *IEEE Microw. Wireless Compon. Lett.*, vol. 15, no. 9, pp. 570–572, 2005.] . . . . . 28
- 1.14 Tunable high-impedance surface with reduced varactors: (a)–(b) structure and feeding network with a single-diode configuration, and (c)–(d) simulated and measured reflection responses for different diode capacitances and resistances. [Courtesy: F. Costa, A. Monorchio, and G. P. Vastante, “Tunable high-impedance surface with a reduced number of varactors,” *IEEE Antennas Wireless Propag. Lett.*, vol. 10, pp. 11–13, 2011.] . . . . . 29
- 1.15 Varactor-tunable second-order bandpass FSS: (a)–(b) three-dimensional and cross-sectional views showing the multilayer structure and vias, and (c) simulated transmission response for different bias voltages. [Courtesy: A. Ebrahimi, Z. Shen, W. Withayachumnankul, S. F. Al-Sarawi, and D. Abbott, “Varactor-tunable second-order bandpass frequency-selective surface with embedded bias network,” *IEEE Trans. Antennas Propag.*, vol. 64, no. 5, pp. 1672–1680, 2016.] . . . . . 30
- 1.16 Improved multifunctional active FSS: (a) three-dimensional and top–bottom layer views, and (b)–(e) simulated transmission coefficients for TE and TM modes under different capacitance values, demonstrating switching, polarization selection, and frequency-tuning functions. [Courtesy: H. Li, Q. Cao, L. Liu, and Y. Wang, “An improved multifunctional active frequency selective surface,” *IEEE Trans. Antennas Propag.*, vol. 66, no. 4, pp. 1854–1862, Apr. 2018.] . . . . . 31
- 1.17 Polarization-insensitive AFSS for switchable and tunable operation: (a) top and bottom unit cells with biasing and diode placement, and (b)–(c) simulated transmission and absorption characteristics under ON and OFF modes. [Courtesy: R. Phon, S. Ghosh, and S. Lim, “Active frequency selective surface to switch between absorption and transmission band with additional frequency tuning capability,” *IEEE Trans. Antennas Propag.*, vol. 67, no. 9, pp. 6059–6067, Sept. 2019.] . . . . . 32
- 1.18 Experimental setup and validation of a switchable FSS: (a)–(c) fabricated prototype and measurement arrangements, (d) test setup, and (e)–(f) measured results for TE and TM polarizations under different incidence angles. [Courtesy: G. I. Kiani, K. L. Ford, L. G. Olsson, K. P. Esselle, and C. J. Panagamuwa, “Switchable frequency selective surface for reconfigurable electromagnetic architecture of buildings,” *IEEE Trans. Antennas Propag.*, vol. 58, no. 2, pp. 581–584, 2010.] . . . . . 34
- 1.19 Waveguide prototype and tunability measurement of a miniaturized-element FSS: (a) fabricated loop-wire FSS sample, (b) WR90 waveguide measurement setup, and (c) measured transmission response. [Courtesy: F. Bayatpur and K. Sarabandi, “Tuning performance of metamaterial-based frequency selective surfaces,” *IEEE Trans. Antennas Propag.*, vol. 57, no. 2, pp. 590–592, 2009.] . . . . . 35

1.20	Adjustable parallel-plate waveguide (PPW) setup: (a) three-dimensional schematic, (b) two test FSS absorbers, (c)–(d) fabricated samples and experimental setup, and (e)–(f) comparison of simulated, free-space, and PPW–TRL measured reflection results. [Courtesy: M. I. Hos-sain, N. Nguyen-Trong, and A. M. Abbosh, “Calibrated parallel-plate waveguide technique for low-frequency and broadband absorptivity measurement,” <i>IEEE Antennas Wireless Propag. Lett.</i> , vol. 19, no. 9, pp. 1541–1545, 2020.] . . . . .	36
2.1	Schematic diagram of the proposed RFSS structure under different working states. . . . .	44
2.2	Geometry of the proposed RFSS structure: (a) top layer, (b) bottom layer, (c) isometric view, and (d) side view. The design parameters of the RFSS structure are finalized as: $a = 10$ mm, $w = 0.2$ mm, $x = 0.6$ mm, $p = 0.5$ mm, $k = 1.2$ mm, and $t_{\text{sub}} = 1.6$ mm. . . . .	45
2.3	Simulated scattering responses of the bottom layer (+ dielectric) for different diode biasing conditions: (a) ON mode, and (b) OFF mode. . . . .	46
2.4	Simulated scattering parameters for different top-layer configurations: (a) simple cross-dipole, and (b) jerusalem-cross-loaded geometry. . . . .	47
2.5	(a) Equivalent circuit of the proposed RFSS. Comparison of scattering parameters (solid and dashed lines represent plots from HFSS and ADS, respectively): (b) ON mode, and (c) OFF mode. The optimized circuit parameters: $L_1 = 7.5$ nH, $L_2 = 8.5$ nH, $L_3 = 1.01$ nH, $L_4 = 1.25$ nH, $R_1 = 18$ $\Omega$ , $R_2 = 6$ $\Omega$ , $R_3 = R_4 = 3$ $\Omega$ , $C_1 = 55$ fF, $C_2 = 44.5$ fF, $L_{\text{via}} = 0.01$ nH. . . . .	48
2.6	Surface current distributions of the RFSS structure: at 5.62 GHz under OFF state (a) top layer, (b) via, (c) bottom layer, and at 6.93 GHz under ON state (d) top layer, (e) via, and (f) bottom layer. . . . .	49
2.7	Simulated scattering parameters for different polarization angles at normal incidence. TE polarization: (a) ON mode, and (b) OFF mode. TM polarization: (c) ON mode, and (d) OFF mode. . . . .	50
2.8	Simulated scattering parameters for different angles of incidence under TM polarization: (a) ON state, and (b) OFF state. . . . .	51
2.9	Simulated scattering parameters for different angles of incidence under TE polarization: (a) ON state, and (b) OFF state. . . . .	52
2.10	Schematic diagram of the biasing network in the proposed RFSS: (a) top layer, and (b) bottom layer. . . . .	53
2.11	Photographs of the fabricated prototype: (a) top surface and (b) bottom surface. PPW simulation setups: (c) top view, and (d) side view. The waveguide dimensions are: $L_1 = 500$ mm, $W_1 = 150$ mm, $P_1 = 80$ mm, $R_1 = 212.5$ mm, and $h_1 = 20$ mm. (e) Measurement setup photograph. (f) Comparison between the measured and simulated responses of the proposed RFSS structure (solid and dashed lines represent results from the PPW setup and HFSS, respectively). . . . .	55
3.1	Schematic diagram of the proposed RFSS structure under different working states. . . . .	61

3.2	Geometry of the proposed RFSS structure: (a) top layer, (b) bottom layer, and (c) side view. The dimensions are: $a = 10$ mm, $b = 0.35$ mm, $c = d = 0.5$ mm, $e = 1$ mm, $p = 5.4$ mm, and $t_{\text{sub}} = 1.6$ mm.	62
3.3	Simulated scattering responses of the bottom layer (+ dielectric) for different diode biasing conditions: (a) OFF mode, and (b) ON mode.	63
3.4	Simulated scattering parameters of the top layer (+ dielectric) for different diode biasing conditions: (a) OFF mode, and (b) ON mode.	63
3.5	Comparison of simulated responses of the proposed RFSS geometry in HFSS and ADS software: (a) transmission mode, (b) absorption mode, (c) selective reflection mode, and (d) full reflection mode. The optimized values are: $L_1 = 0.08$ nH, $L_2 = 0.8$ nH, $L_3 = 1.43$ nH, $L_4 = 1.7$ nH, $L_5 = 4.5$ nH, $C_1 = 2$ pF, $R_3 = 0.6 \Omega$ , $R_1 = R_2 = R_4 = R_5 = 0.01 \Omega$ .	65
3.6	Equivalent circuit model of the proposed unit cell geometry.	66
3.7	Simulated scattering parameters for orthogonal polarization angles at normal incidence: (a) transmission mode, (b) absorption mode, (c) selective reflection mode, and (d) full reflection mode.	67
3.8	Simulated scattering parameters for different angles of incidence under TE polarization: (a) transmission mode, (b) absorption mode, (c) selective reflection mode, and (d) full reflection mode.	68
3.9	Simulated scattering parameters for different angles of incidence under TM polarization. (a) Transmission mode, (b) absorption mode, (c) selective reflection mode, and (d) full reflection mode.	69
3.10	Biasing mechanism of the proposed AFSS: (a) top layer, (b) bottom layer. Fabricated prototype: (c) top layer, (d) bottom layer. (e) Integration of FPGA with the fabricated prototype to regulate the diodes ( $PD_1$ and $PD_2$ ).	70
3.11	(a) Measurement setup. (b) 1-D array simulation arrangement.	72
3.12	Comparison of simulated and measured data: (a) transmission mode, (b) absorption mode, (c) selective reflection mode, and (d) full reflection mode. S: Simulation, M: Measured.	73
3.13	(a) Conceptual diagram showing the oblique incidence measurement in the PPW setup. Electric field distribution of the proposed metasurfaces in PPW setup: (b) absorption mode at 5.06 GHz, (c) transmission mode at 5.14 GHz, and (d) reflection mode at 5 GHz.	74
3.14	Oblique incidence responses of the proposed RFSS geometry in PPW setup: (a) transmission mode, (b) absorption mode, (c) selective reflection mode, and (d) full reflection mode.	75
4.1	Schematic view of the proposed MRFSS geometry: (a) OFF–OFF state, (b) OFF–ON state, (c) ON–OFF state, and (d) ON–ON state.	81
4.2	Design of the proposed MRFSS unit cell geometry: (a) top view, (b) Side view, (c) bottom view, and (d) isometric view.	82
4.3	Schematic conceptualization to achieve different operating modes from the proposed MRFSS geometry: (a) transmission mode, (b) absorption mode, and (c) reflection mode.	84
4.4	Simulated scattering parameters of the bottom layer (+ dielectric) under (a) OFF state, and (b) ON state.	85

4.5	Simulated scattering parameters of the top layer (+ dielectric): (a) OFF state, and (b) ON state. . . . .	86
4.6	Equivalent circuit modeling of the proposed MRFSS geometry. . . . .	87
4.7	Simulated scattering parameters of the proposed MRFSS geometry: (a) transmission mode, (b) absorption mode, (c) selective-reflection mode, and (d) reflection mode. . . . .	88
4.8	Scattering parameters of the proposed MRFSS geometry at a reverse-bias voltage of 6.2 V using HFSS and ADS software for all the modes: (a), (b) $+z$ direction and (c), (d) $-z$ direction. The optimized circuit parameter values are: $L_1 = 9$ nH, $R_1 = 0.01 \Omega$ , $L_2 = 1.3$ nH, $R_2 = 0.31 \Omega$ , $C_2 = 0.11$ pF, $L_3 = 2.5$ nH, $R_3 = 0.01 \Omega$ , $L_4 = 2$ nH, $R_4 = 0.01 \Omega$ , $L_5 = 0.01$ nH, $R_5 = 0.01 \Omega$ . . . . .	89
4.9	Scattering parameters of the proposed MRFSS geometry under TE polarization: (a) transmission mode, (b) absorption mode, (c) selective-reflection mode, and (d) reflection mode. . . . .	90
4.10	Biasing technique of the proposed MRFSS geometry: (a) top layer, and (b) bottom layer. Biasing conditions for different cases: (c) OFF-OFF case: ( $VT_{13} < V_{th}$ ); ( $VB_{43} < V_{th}$ ); ( $VT_{23} < V_{th}$ ). (d) OFF-ON case: ( $VT_{13} < V_{th}$ ); ( $VB_{43} > V_{th}$ ); ( $VT_{23} < V_{th}$ ). (e) ON-OFF case: ( $VT_{13} > V_{th}$ ); ( $VB_{43} < V_{th}$ ); ( $VT_{23} < V_{th}$ ). (f) ON-ON case: ( $VT_{13} > V_{th}$ ); ( $VB_{43} > V_{th}$ ); ( $VT_{23} < V_{th}$ ). [ $V_{th}$ is the threshold voltage of the diode]. . . . .	91
4.11	Fabricated photographs along with enlarged views of the proposed MRFSS geometry: (a) top layer, and (b) bottom layer. . . . .	93
4.12	Measurement setup for the proposed MRFSS geometry: (a) $S_{21}$ response (normal incidence), (b) $S_{11}$ response (normal incidence), and (c) $S_{11}$ response (oblique incidence). . . . .	94
4.13	Measured scattering parameters of the proposed MRFSS geometry: (a) transmission mode, (b) absorption mode, (c) selective-reflection mode, and (d) reflection mode. . . . .	95
4.14	The measured oblique incidence responses for the proposed MRFSS structure: (a) transmission mode, (b) absorption mode, (c) selective-reflection mode, and (d) reflection mode. Two different bias voltages (5.5 V and 25 V) have been considered under each mode. . . . .	96
4.15	Effect of parasitic resistance on the proposed MRFSS geometry: (a) transmission mode, (b) absorption mode, (c) selective-reflection mode, and (d) reflection mode. . . . .	98
4.16	Effect of loss tangent of the dielectric substrate on the proposed MRFSS geometry: (a) transmission mode, (b) absorption mode, (c) selective-reflection mode, and (d) reflection mode. . . . .	99
5.1	Conceptual diagram illustrating four distinct EM operations of the proposed RFSS geometry. . . . .	105
5.2	Layer 2 of the proposed RFSS geometry: (a) top view, (b) bottom view, (c) equivalent circuit, and (d) simulation results. The optimized dimensions are: $a = 10$ mm, $a_1 = 9.5$ mm, $e = 2.5$ mm, $e_1 = 4.4$ mm, and $e_2 = 0.8$ mm. . . . .	106

- 5.3 Layer 1 of the proposed RFSS geometry: (a) top view, and (b) bottom view. Only Layer-1: (c) equivalent circuit, and (d) simulation results. Layer 1 along with ground plane: (e) equivalent circuit, and (f) simulation responses. The optimized dimensions are:  $a = 10$  mm,  $b = 0.4$  mm,  $c = 0.5$  mm,  $c_1 = 0.42$  mm,  $d = 5$  mm,  $d_1 = 4$  mm,  $g = 1.2$  mm. . . . . 108
- 5.4 Design of the proposed RFSS geometry. Isometric view of: (a) layer 1, and (b) layer 2. Overall structure: (c) isometric view, and (d) side view. (e) Equivalent circuit model. The dimensions are:  $t_1 = 1$  mm and  $t_{\text{air}} = 4$  mm. . . . . 109
- 5.5 Simulated scattering parameters of the proposed wideband RFSS geometry: (a) transmission-absorption (T-A) mode, (b) absorption mode, (c) transmission mode, and (d) reflection mode. The inset top and bottom views of layers 1 and 2 represent operating modes. . . . . 111
- 5.6 Comparison of the proposed wideband RFSS geometry scattering responses in HFSS and ADS software: (a) transmission-absorption (T-A) mode, (b) absorption mode, (c) transmission mode, and (d) reflection mode. The optimized parameter values are  $L_1 = L_3 = L_5 = 0.01$  nH,  $L_2 = 10$  nH,  $L_4 = 3.65$  nH,  $L_6 = 4.95$  nH,  $L_7 = 1.52$  nH,  $L_8 = 9$  nH,  $C_1 = 0.3$  pF,  $C_2 = 0.03$  pF,  $C_3 = 0.1$  pF,  $R_1 = 5 \Omega$ ,  $R_2 = R_3 = R_4 = R_7 = 0.01 \Omega$ ,  $R_5 = 2.5 \Omega$ ,  $R_6 = 3.5 \Omega$ ,  $R_8 = 1 \Omega$ ,  $R_{\text{ON}}^1 = 0.85 \Omega$ ,  $C_{\text{OFF}}^1 = 0.17$  pF,  $R_{\text{ON}}^2 = 0.56 \Omega$ ,  $C_{\text{OFF}}^2 = 0.35$  pF, and  $R_L = 65 \Omega$ . . . . . 112
- 5.7 Scattering parameters of the proposed wideband RFSS geometry for different polarization angles under normal incidence: (a) transmission-absorption (T-A) mode, (b) absorption mode, (c) transmission mode, and (d) reflection mode. . . . . 114
- 5.8 Scattering parameters of the proposed wideband RFSS geometry for different incidence angles under TE polarization: (a) transmission-absorption (T-A) mode, (b) absorption mode, (c) transmission mode, and (d) reflection mode. . . . . 115
- 5.9 Scattering parameters of the proposed wideband RFSS geometry for different incidence angles under TM polarization: (a) transmission-absorption (T-A) mode, (b) absorption mode, (c) transmission mode, and (d) reflection mode. . . . . 116
- 5.10 Biasing technique for four different operating states, viz. OFF-OFF ( $V_{21} < V_{\text{th}1}$ ,  $V_{43} < V_{\text{th}2}$ ), OFF-ON ( $V_{21} < V_{\text{th}1}$ ,  $V_{43} > V_{\text{th}2}$ ), ON-OFF ( $V_{21} > V_{\text{th}1}$ ,  $V_{43} < V_{\text{th}2}$ ), and ON-ON ( $V_{21} > V_{\text{th}1}$ ,  $V_{43} > V_{\text{th}2}$ ) of the proposed RFSS geometry: (a) top side of layer 1, (b) bottom side of layer 1, (c) top side of layer 2, and (d) bottom side of layer 2. (e) Bias voltage conditions to operate the diodes. . . . . 117
- 5.11 Fabricated prototype and measurement setup photographs of the proposed wideband RFSS geometry: (a)–(d) individual layer photographs, (e) overall sample photographs, (f)–(i) enlarged views of the unit cell, and (j) PPW experimental setup for  $S_{11}$  and  $S_{21}$  characteristics. . . . . 120

5.12	Comparison of measured responses with unit-cell simulation results and 1-D array PPW simulation setup results for the proposed wideband RFSS geometry: (a) transmission-absorption (T-A) mode, (b) absorption mode, (c) transmission mode, and (d) reflection mode. The inset figures show the simulation and experimental PPW setups.	121
5.13	Oblique incidence responses and electric field distribution of the proposed wideband RFSS geometry in the PPW setup: rasorber mode – E-field at (a) 2.75 GHz and (b) 5 GHz, and (c) scattering parameters; absorption mode – (d) scattering parameters and (e) E-field at 4 GHz; transmission mode – (f) E-field at 4 GHz and (g) scattering parameters; reflection mode – (h) scattering parameters and (i) E-field at 3.85 GHz. The inset shows the oblique incidence setup in the PPW device.	122
6.1	Schematic representation of the proposed PPW structure: (a) top view, (b) side view, and (c) isometric view.	130
6.2	Simulated results of the PPW: (a) with a copper sheet placed at the center, and (b) without any test structure.	131
6.3	Unit cell designs. Design-1: (a) top view. Design-2: (b) top view, and (c) isometric view. Design-3: (d) top view, (e) bottom view, and (f) isometric view. The optimized dimensions (in mm) are: $a = 10$ , $a_1 = 9$ , $w = 0.2$ , $b = 5$ , $b_1 = 0.4$ , $c = d = 0.6$ , $c_1 = 0.2$ , $t_1 = 1$ , $t_{\text{air}} = 4$ , $d_1 = e = 0.25$ , $d_2 = 8$ , $e_1 = 6$ , and $e_2 = 1.2$ .	133
6.4	Comparison of unit cell (UC) and PPW simulations under normal incidences of the proposed designs: (a) bandstop filter, (b) wideband absorber, and RFSS: (c) OFF case, (d) ON case.	134
6.5	Modified PPW configuration for oblique incidence measurement: (a) PPW-1 (with cylindrical apertures); (b) PPW-2 (with both cylindrical and arc-shaped apertures). Combined measurement setup integrating both PPWs: (c) top view and (d) side view.	136
6.6	Simulated results of the modified PPW: (a) with a copper sheet placed at the center, and (b) without any test structure. ML: Matched Load.	137
6.7	Comparison of unit cell and full wave PPW simulations under normal and oblique incidences of the proposed designs: (a) bandstop filter, (b) wideband absorber, and RFSS: (c) OFF case, (d) ON case.	138
6.8	Electric field distributions of the proposed designs in the modified PPW simulations for the 90° configuration: (a) bandstop filter at 5.00 GHz, (b) wideband absorber at 5.27 GHz, and (c) RFSS at 5.68 GHz under OFF state.	139
6.9	FSS prototypes and modified PPW experimental setup for 60° arrangement: (a) copper with the same dimensions as FSS samples, (b) bandstop filter (Design-1), wideband absorber (Design-2): (c) top view, (d) side view, and RFSS (Design-3): (e) top view, (f) bottom view.	140
6.10	Modified PPW measurement setup for: (a) $S_{21}$ , (b) $S_{11}$ .	141
6.11	Measured responses in the modified PPW setup under normal and oblique incidences of the proposed designs: (a) bandstop filter, (b) wideband absorber, and RFSS: (c) OFF case, (d) ON case.	143



# List of Tables

2.1	Comparison with other RFSS Designs . . . . .	56
3.1	Coding Sequence by FPGA for Different Operating Modes . . . . .	71
3.2	Comparison with Existing Literature . . . . .	76
4.1	Varactor Diode Voltage versus Capacitance Values . . . . .	83
4.2	Circuitual Requirement in the Proposed MRFSS Geometry . . . . .	84
4.3	Comparison with other RFSS Designs . . . . .	100
5.1	Realization of Wideband Multifunctional Responses in the Proposed RFSS . . . . .	110
5.2	Comparison with other Existing Designs . . . . .	124
6.1	Comparison with Existing Literature . . . . .	144



# List of Abbreviations/Acronyms

**A-T** Absorption–Transmission.

**A-T-A** Absorption–Transmission–Absorption.

**ADS** Advanced Design System.

**DC** Direct Current.

**DUT** Device Under Test.

**ECM** Equivalent Circuit Model.

**ELC** Electric-LC Resonators.

**EM** Electromagnetic.

**EMI** Electromagnetic Interference.

**FPGA** Field-Programmable Gate Array.

**FSRs** Frequency Selective Resonators.

**FSS** Frequency Selective Surfaces.

**HFSS** High-Frequency Structure Simulator.

**HIS** High-Impedance Surface.

**MRFSs** Multifunctional Reconfigurable Frequency Selective Surfaces.

**PBC** Periodic Boundary Conditions.

**PCB** Printed Circuit Board.

**PPW** Parallel Plate Waveguide.

**RCS** Radar Cross-Section.

**RFSSs** Reconfigurable Frequency Selective Surfaces.

**SOLT** Short-Open-Load-Through Method.

**T-A** Transmission–Absorption.

**TEM** Transverse Electromagnetic.

**TRL** Through-Reflect-Line.

**VNA** Vector Network Analyzer.

# List of Symbols

Symbol	Description
A	Absorption
T	Transmission
Ref	Reflection
Ras	Rasorber
C	Capacitance
E	Electric field
H	Magnetic field
k	Electromagnetic wave vector
L	Inductance
R	Resistance
$f_c$	Centre frequency of the operating band
$f_r$	Resonance frequency
$S_{11}$	Reflection coefficient
$S_{21}$	Transmission coefficient
$Y_{in}$	Input admittance
$Y_d$	Dielectric admittance
$Y_0$	Free space admittance
$Z_{in}$	Input impedance
$Z_d$	Dielectric impedance
$Z_0$	Free space impedance
$\epsilon_0$	Permittivity of free space
$\epsilon_r$	Permittivity of the dielectric
$\mu_0$	Permeability of free space
$\mu_r$	Permeability of the dielectric
$\tan \delta$	Loss tangent of the dielectric
$\alpha$	Attenuation constant
$\beta$	Propagation constant
$\sigma$	Conductivity of metal
$\omega$	Angular frequency
$\lambda_g$	Guided wavelength
$\lambda_0$	Free space wavelength
$\phi$	Polarization angle
$\theta$	Incident angle



# Chapter 1

## Introduction

Over the past few decades, research on frequency selective surfaces (FSS) grows rapidly because of their importance in stealth technology, radar systems, and electromagnetic (EM) shielding. An FSS is a periodic array of metallic elements that exhibits different EM wave behaviors such as transmission, reflection, and absorption, based on its geometric dimensions, material properties, and interaction with the incident EM wave. These structures act as spatial filters, allowing selective passage or blocking of EM waves at specific frequencies. They are widely used in the designs of radomes, antennas, absorbers, polarizers, and shielding applications in microwave and millimeter-wave regimes [1–5]. Conventional FSS designs are restricted to a single fixed function, which limits their practical use. With the rapid expansion of wireless communication systems and modern radar platforms, there is a growing demand for compact and reconfigurable frequency selective surfaces (RFSSs) that can perform various EM functions like absorption, transmission, and reflection, either simultaneously or selectively in a single structure. To realize this flexibility, FSS designs are engineered using various reconfigurable techniques, exhibiting different EM responses in real-time scenarios [6–10].

In advanced communication and sensing environments, where different EM functionalities are required across distinct frequency bands or at different time instants in the same band, such RFSS designs hold strong potential. For example, an RFSS with switchable transmission-reflection characteristics can selectively permit desired signals in the transmissive state for adaptive wireless links, while it can reject or redirect unwanted signals in the reflective state, improving link security [11–13].

An absorptive mode can suppress undesirable or hostile signals by dissipating incident energy, supporting stealth functionality and electromagnetic interference (EMI) reduction [14–17]. A rasorber structure combining both absorption and transmission behaviors can simultaneously support radar cross-section (RCS) reduction and reliable communication performance [18–21]. Beyond defense and wireless communication domains, multifunctional RFSS (MRFSS) structures are also well-suited for tunable filters, EM shielding, cognitive radar systems, and intelligent reconfigurable surfaces for next-generation wireless networks [22–25]. The ability to dynamically realize multiple EM responses in a single physical geometry makes the RFSS technology highly attractive for modern EM platforms, and this remains the central focus of this PhD thesis.

To achieve the RFSS designs, several methods are investigated, including the use of MEMS switches, liquid crystals, and composite materials [26–30]. These approaches often face challenges such as complex fabrication, slower switching speed, and high implementation cost. To address these limitations, the electronically reconfigurable technique is often used, employing p-i-n diodes and varactors as the constituent elements [31–35]. These components provide fast, reliable, and economical control of the FSS frequency response, making them suitable for multifunctional applications. The RFSS performance mainly depends on the diode behavior. A p-i-n diode functions as a switch that alternates between a low-resistance ON state under forward bias and a high-capacitance OFF state under reverse bias. This switching allows a single structure to exhibit distinct EM responses. A varactor diode acts as a tuning element whose capacitance varies with bias voltage, allowing continuous frequency control. Integrating these diodes offers several benefits, such as fast response, low power consumption, compact integration, and simple control over other approaches.

To achieve the multifunctional responses, the designed geometries are analyzed based on their EM responses and geometrical characteristics such that they can exhibit transmission, reflection, and absorption performance [36–38]. Along with their geometrical characteristics, the equivalent circuit model plays a crucial role in realizing the multifunctional behavior of the proposed RFSS structures. These geometries typically consist of metallic patterns printed on one or both sides of a dielectric sub-

strate, with diode components embedded at strategic locations to enable switchable or tunable EM responses. Each diode-integrated metallic layer contributes a distinct electrical behavior, and the combined response of these layers governs the overall EM functionality of the structure. For instance, a parallel  $RLC$  network generally exhibits a bandpass filter response, while a series  $RLC$  network produces a bandstop response. Accordingly, a transmissive mode can be achieved when either or both of the metallic layers emulate a parallel  $RLC$  circuit. Conversely, the reflective mode operation can be obtained when the metallic layer behaves as a series  $RLC$  circuit or presents a high-impedance (effectively short-circuited) state. For absorptive operation, the top layer should be modeled as a parallel or series  $RLC$  circuit, while the bottom layer must act as a perfect reflector to suppress transmission. In the case of a rasorber configuration, a suitable combination of transmission and absorption behavior must be realized by tailoring the metallic patterns at different frequency bands. Thus, the equivalent circuit model is extensively used for analyzing the multifunctional responses of all RFSS designs presented in this thesis.

Despite these advances, several limitations persist in existing switchable RFSS designs. Most reported geometries remain restricted to specific functionalities such as reflection/transmission [11–13], reflection/absorption [39–41], and polarizer/ reflector [42–44] operations. Only a few studies demonstrate switching between absorption and transmission modes, and these approaches often suffer from additional issues such as multilayer arrangements, polarization sensitivity, and angular instability [45, 46]. Moreover, the integration of electronic control elements typically requires additional biasing networks, which further increases design complexity. To address these constraints and establish a foundational understanding of reconfigurable mechanisms, a single p-i-n diode-based configuration with an embedded biasing network is explored to demonstrate basic dual-mode switching between absorption and transmission, while maintaining polarization-insensitive behavior in a single-layer substrate.

Although this initial work establishes the fundamental switching mechanism, it operates between only two modes and relies on manual biasing for switching between operational states, making it unsuitable for real-time dynamic systems. Building upon this foundation, the work progresses toward enhanced multifunctionality by

introducing two independently controlled diode sets to generate multiple operating states. This configuration expands the number of operating modes and allows the structure to achieve three distinct EM behaviors: absorption, transmission, and reflection. To realize automated switching and real-time operation, a field-programmable gate array (FPGA)-based control system is integrated to regulate the diode sets.

While the previous designs achieve multiple distinct EM behaviors using p-i-n diodes, the resonant frequencies remain fixed once the geometric parameters are optimized. To overcome this limitation and introduce frequency agility, varactor diodes are integrated with the existing p-i-n diode configuration, realizing both mode switching and continuous frequency tuning in a single structure. This approach combines discrete switching and continuous tuning capabilities, where the capacitance variation of varactor diodes under applied bias provides frequency control across different operating modes. The structure demonstrates switchable and tunable characteristics with multiple operational states.

Despite demonstrating both switching and frequency-tuning capabilities, all the previous designs operate at narrowband frequencies in each mode, which limits their flexibility for systems requiring wideband EM responses. To address these bandwidth limitations, a multilayer architecture is developed by integrating two dielectric layers separated by an air spacer. In addition, lumped resistors are incorporated along with p-i-n diodes to broaden the absorption response, while symmetric geometries across the substrate layers ensure polarization-insensitive performance. This configuration realizes wideband operation across multiple distinct EM functions, including absorber, absorption, transmission, and reflection characteristics.

While the design contributions establish a framework for RFSS development, experimental validation of such designs remains challenging due to limitations of existing measurement techniques. Traditional free-space measurements require large prototypes, wideband horn antennas, and anechoic chambers, which increase cost and complexity, especially for structures incorporating direct current (DC) biasing networks. Although the parallel plate waveguide (PPW) technique is employed for validation, conventional PPW systems are restricted to normal incidence characterization and cannot evaluate wide-angle performance. This limitation motivates

the development of a modified PPW measurement system capable of accurate characterization under both normal and oblique incidence conditions. The modified configuration consists of mechanically adjustable sections that allow controlled angular excitation while maintaining electrical continuity. Different FSS prototypes are fabricated and tested to validate the effectiveness of this measurement approach.

Thus, the motivation for this thesis arises from the need to develop advanced RFSS designs that overcome the limitations of conventional structures while broadening their functional capabilities. In summary, the research follows a systematic and progressive investigation across different domains of EM wave control. It begins with the exploration of fundamental switching mechanisms using p-i-n diode configurations to realize dual-mode operations, achieving polarization-insensitive absorber/transmitter functionalities through embedded biasing networks. Building upon this foundation, the work progresses toward multifunctional systems that integrate both switching and frequency-tuning features by combining p-i-n and varactor diodes, thereby realizing simultaneous control of EM response and operational frequency. The work is further extended to multilayer architectures capable of exhibiting wideband behaviors among four distinct operating modes, including absorber, absorption, transmission, and reflection characteristics. In addition, the research addresses experimental challenges by developing a modified parallel plate waveguide setup for wide-angle FSS characterization, providing a reliable and cost-effective approach for accurate measurement and validation. In summary, this thesis presents a structured approach that progresses from basic switching concepts to advanced multifunctional designs, supported by innovative measurement methodologies that enhance the practical realization of RFSS technologies.

## 1.1 Overview of FSS

The idea of controlling EM waves through engineered periodic structures emerged more than a century ago. In the early twentieth century, pioneers such as Marconi and Franklin demonstrated that wire grids can behave as reflective surfaces when the lengths of individual wires are tuned to resonate at particular frequencies [1–3]. Their 1919 patent documents these resonant metallic arrays, establishing the foun-

dation for what later becomes known as frequency selective surfaces (FSS) [47]. The concept remains largely theoretical until the mid-twentieth century, when the rapid growth of radar technology during World War II highlights the need for structures capable of filtering and manipulating EM energy [48]. The increasing demand for RCS reduction and efficient microwave filtering encourages extensive research on thin metallic sheets patterned with periodic resonant elements.

As radar and microwave technologies advance, FSS structures begin to take practical form. Early implementations are based on metallic dipole/mesh arrays in radome applications, where frequency transparency is required for selected radar bands while suppressing unwanted frequencies. Subsequent investigations introduce the complementary configurations, such as patch-type and slot-type elements, inspired by Babinet's principle, which exhibit opposite EM behaviours. Patch arrays act as capacitive surfaces that support low-frequency transmission, whereas slot arrays behave as inductive structures that favor high-frequency propagation [1–3]. The combination of these complementary effects enables diverse filtering characteristics such as low-pass, high-pass, band-pass, and band-stop responses, firmly establishing the fundamental filtering role of FSS in EM design.

Structurally, an FSS consists of a periodic array of metallic elements whose dimensions are a small fraction of the operating wavelength. The overall structure typically comprises one or more patterned metallic layers printed on dielectric substrates, forming a periodic network. The geometry and periodicity of the elements determine the equivalent inductance and capacitance of the surface, which in turn dictate its resonance frequency. When an EM wave impinges on the structure at its resonance frequency, a strong interaction occurs, leading to selective transmission or reflection. Therefore, these surfaces act as two-dimensional analogues of lumped-element filters that operate in the spatial domain [49, 50].

Building on this foundation, modern FSS designs evolve toward compact and multifunctional geometries. The contemporary unit-cell configurations include dipole, cross, loop, ring, meander line, Jerusalem cross, and fractal pattern. The evolution of FSS is illustrated in Figure 1.1, showing their progression from early wire-grid reflectors [47] to compact and miniaturized geometries. Each geometry produces a unique current distribution and localized field pattern that modifies how EM

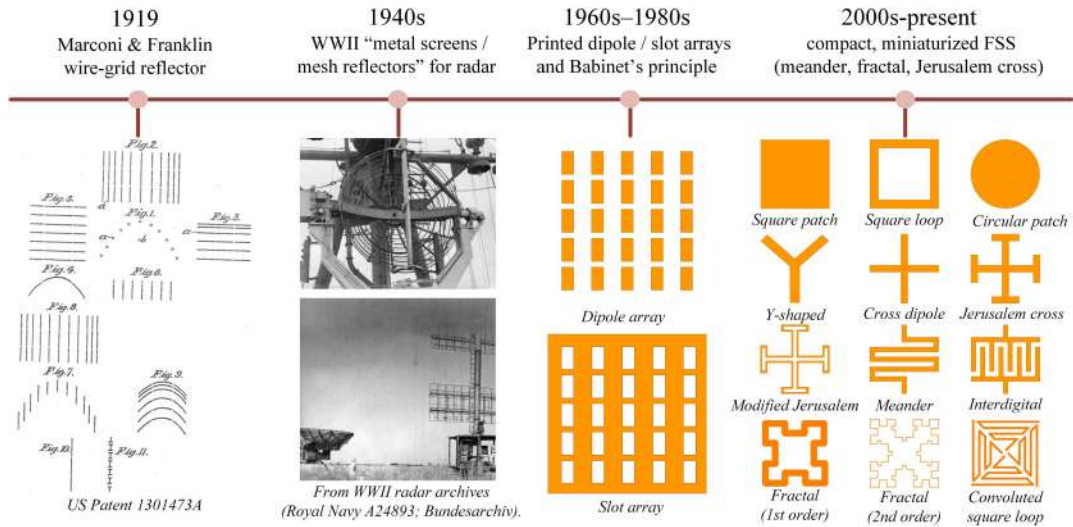


Figure 1.1: Evolution of FSS concepts: From the 1919 Marconi & Franklin wire-grid reflector [47] through WWII mesh reflectors [51, 52], planar dipole/slot arrays of the 1960s–1980s, and compact miniaturized unit cells developed after 2000.

energy interacts with the surface. The conductive path length primarily influences the inductive response, while the gap spacing and dielectric constant determine the capacitive coupling. This interplay allows precise control over resonance position, bandwidth, and strength. Moreover, coupling between adjacent unit cells affects frequency stability and angular performance, shaping the overall electromagnetic behavior of the surface.

Beyond transmission and reflection control, FSS can also be engineered to exhibit absorption characteristics, significantly extending their functionality. When properly configured, an FSS can minimize both reflection and transmission at specific frequencies, causing most of the incident energy to dissipate as heat. This behavior is achieved by incorporating resistive or lossy components into the periodic array to ensure impedance matching with free space. The principle of EM absorption traces back to Salisbury screens and Dallenbach layers, which use resistive sheets backed by conductive plates to cancel reflections through destructive interference. With advances in fabrication, these bulky absorbers evolve into compact, lightweight FSS-based absorbers that combine frequency selectivity with energy dissipation, providing effective solutions for stealth and EMI-shielding applications [53–55].

As research advances, the scope of FSS extends even further toward multifunctional control. Many modern radar and communication systems require simultane-

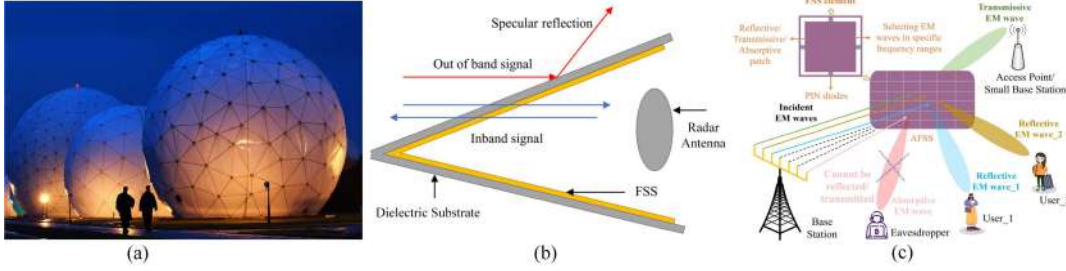


Figure 1.2: Applications of multifunctional FSS/RFSS: (a) adaptive radome for in-band transmission and stealth [59], (b) multifunctional surface for radar-communication coexistence [60], and (c) intelligent surface for secure, reconfigurable wireless control [61].

ous management of transmission and absorption, giving rise to frequency selective rasorbers (FSRs). These hybrid structures merge the principles of filtering and absorption to achieve selective in-band transmission while attenuating or absorbing out-of-band signals. Depending on the spectral arrangement of these bands, FSRs are generally classified into transmission-absorption (T-A), absorption-transmission (A-T), or absorption-transmission-absorption (A-T-A) configurations [56–58]. This combination of filtering and absorbing behaviors makes FSRs indispensable for advanced radome and stealth technologies where both transparency and suppression are required in a single, compact design.

The overall performance of an FSS depends on several interrelated parameters, including resonant frequency, impedance bandwidth, angular stability, and polarization response. The resonant frequency is primarily determined by the equivalent inductance and capacitance of the unit cell, following the resonance condition

$$f_r = \frac{1}{2\pi\sqrt{LC}}. \quad (1.1)$$

The bandwidth represents the frequency range over which the transmission or reflection coefficients remain in the desired limits and is typically measured at the  $-3$  dB points. Angular stability ensures that the frequency response remains nearly invariant under oblique incidence, while polarization insensitivity guarantees consistent behavior for both transverse electric (TE) and transverse magnetic (TM) polarizations. Together, these parameters define the operational reliability of an FSS and form the foundation for advanced multifunctional and reconfigurable struc-

tures. Such multifunctional FSSs are increasingly vital in adaptive systems requiring dynamic control of electromagnetic behavior. These surfaces enable selective transmission, reflection, or absorption according to operational requirements, supporting emerging technologies such as reconfigurable radomes, integrated communication radar platforms, and intelligent wireless environments [59–61], as depicted in Figure 1.2.

## 1.2 Need for Reconfigurability in FSS

Conventional FSS are passive structures whose EM responses depend solely on their geometry and material composition. Once fabricated, these parameters remain fixed, resulting in a single operational mode and limited functionality. However, modern radar, communication, and sensing systems operate in dynamic environments, where the required EM behavior can vary in real time. To meet these demands, RFSSs have been developed that can tune or switch their EM response without physical modification [62–65]. This capability enhances design flexibility, broadens operational bandwidth, and reduces fabrication cost and time.

To realize such adaptability, various control mechanisms have been proposed for implementing reconfigurability in FSSs. The most common approaches include mechanical, magnetic, and electronic tuning methods [66–70]. Mechanical tuning involves physically altering the structure through movements such as rotation, translation, or deformation of the resonant elements. Although this approach offers wide tuning ranges, it suffers from slow response times, high wear, and complex actuation mechanisms. Magnetically reconfigurable designs employ ferrite or magneto-optic materials that alter their permeability or permittivity under external magnetic fields. While these methods allow contactless control, they generally require bulky biasing setups and high magnetic fields. In contrast, electronically reconfigurable FSSs utilize components such as p–i–n diodes, varactors, MEMS switches, liquid crystals, or graphene layers. These components modify the equivalent circuit parameters—primarily resistance, inductance, and capacitance—under applied bias conditions, enabling real-time tuning of the resonance frequency or switching between different EM states. Compared with mechanical and magnetic techniques, electronic

approaches offer faster response, compact integration, and simpler biasing networks, making them the most suitable choice for practical RFSS implementations.

Among various electronic methods, the use of p–i–n diodes and varactors is particularly widespread due to their robustness, low cost, and reliable operation over wide frequency ranges [71–73]. MEMS- and liquid-crystal-based FSSs, although functional, often suffer from complex fabrication processes and limited switching speed. In contrast, p–i–n diodes provide instantaneous binary switching between resistive and capacitive states, while varactors enable continuous tuning of capacitance under variable bias voltage. This complementary behavior allows both discrete and analog control of the EM response in a single design. Consequently, electronically reconfigurable FSSs employing these diodes achieve high adaptability with low power consumption and minimal hardware overhead.

### 1.3 Working Principle of Electronic Diodes

The electronic diodes, viz., p–i–n diode and varactor diode, operate under two different principles. A p–i–n diode functions as a discrete switch that alternates between two electrical states (ON state and OFF state). Under forward bias, it behaves as a low-resistance element, effectively creating a conductive path across the connected resonators. Under reverse bias, it acts as a high-impedance capacitor, interrupting the current flow. The equivalent circuit representation of a p–i–n diode consists of a series resistance ( $R_{ON}$ ) and a parasitic inductance ( $L_{ON}$ ) in the ON state, and a series combination of capacitance ( $C_{OFF}$ ) and inductance ( $L_{OFF}$ ) in the OFF state. The transition between these two states provides rapid switching between different EM modes such as reflection, transmission, and absorption. The relationship between the stored charge and the carrier lifetime in the intrinsic region determines the switching speed, which is typically on the order of nanoseconds.



Figure 1.3: Equivalent circuit models of p–i–n diode in the ON and OFF states and varactor diode illustrating voltage-controlled junction capacitance.

A varactor diode, in contrast, operates as a voltage-controlled capacitor. When a reverse-bias voltage  $V_r$  is applied, the depletion width of the junction changes, leading to a variable junction capacitance  $C(V_r)$ . The capacitance is inversely related to the applied voltage and is generally expressed as

$$C(V_r) = \frac{C_0}{\left(1 + \frac{V_r}{V_j}\right)^m}, \quad (1.2)$$

where  $C_0$  is the zero-bias junction capacitance,  $V_j$  is the built-in potential, and  $m$  is the grading coefficient (typically 0.3–0.5 for abrupt junctions).

This nonlinear voltage–capacitance relationship allows continuous tuning of the resonant frequency according to

$$f_r = \frac{1}{2\pi\sqrt{LC(V_r)}}. \quad (1.3)$$

By adjusting  $V_r$ , the resonance of the FSS unit cell can be shifted over a wide frequency range without altering its geometry. When used in combination with p–i–n diodes, varactors provide an additional degree of freedom by enabling simultaneous switching and tuning operations in the same structure. The integration of these electronic components in an FSS transforms the traditionally static surface into an intelligent, adaptive interface capable of multiple EM functionalities. The combined use of p–i–n and varactor diodes enables both discrete state transitions and continuous frequency tunability, with the help of equivalent circuit modeling, as shown in Figure 1.3. These advantages make electronically reconfigurable FSSs particularly suitable for next-generation applications in RCS reduction, adaptive filtering, beam steering, and dynamic communication systems that demand real-time control and multifunctional performance.

## 1.4 Basic Mechanisms of EM Operation

The EM operations of an FSS depend on its periodic metallic patterns and their interactions with the incident EM waves. Depending on the electrical boundary conditions and equivalent impedance relationships, the structure can exhibit reflec-

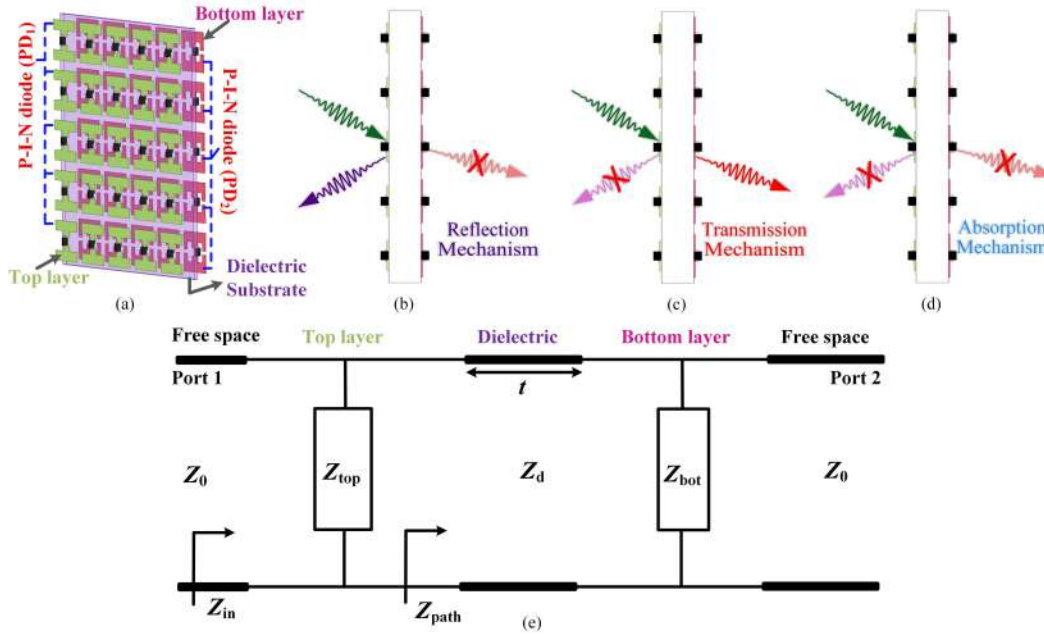


Figure 1.4: Basic mechanisms of RFSS: (a) representative single dielectric structure with p-i-n diodes, (b)-(d) schematic depiction of reflection, transmission, and absorption operations, and (e) equivalent circuit model illustrating common impedance representation for all modes.

tion, transmission, absorption, rasorber (transmission combined with absorption), or other types of EM behaviors, as shown in Figure 1.4. The interaction of the incident field with the patterned metallic layer, dielectric substrate, and bottom layer determines the power distribution among various characteristics. These effects are governed primarily by the impedance matching conditions between the FSS and free space. When the impedance of the structure differs significantly from that of free space, reflection dominates. When the impedances are matched, transmission or absorption occurs, depending on whether the transmitted wave is allowed to pass or is attenuated in the surface.

### 1.4.1 Reflection Mechanism

The reflection mechanism in FSSs originates from the impedance mismatch that occurs between the surface and the surrounding medium. When the incident EM wave encounters the periodic metallic surface, the induced surface current on the pattern re-radiates the energy toward the source instead of allowing it to transmit through. This re-radiation process becomes dominant whenever the input impedance

of the surface,  $Z_{\text{in}}$ , differs from the free-space impedance,  $Z_0$ . A highly mismatched condition, either  $Z_{\text{in}} \gg Z_0$  or  $Z_{\text{in}} \ll Z_0$ , leads to strong reflection and negligible transmission. The extent of this reflection is represented by the reflection coefficient  $S_{11}$ , given by

$$S_{11} = \frac{Z_{\text{in}} - Z_0}{Z_{\text{in}} + Z_0}. \quad (1.4)$$

To obtain  $Z_{\text{in}}$ , the periodic surface is modeled as a parallel impedance network consisting of the top patterned sheet, the dielectric substrate, and the bottom conducting surface, as illustrated in Figure 1.4(e). The dielectric and bottom combination presents an impedance  $Z_{\text{path}}$ , expressed as

$$Z_{\text{path}} = \frac{Z_d (Z_{\text{bot}} + jZ_d \tan(\beta t))}{Z_d + jZ_{\text{bot}} \tan(\beta t)}. \quad (1.5)$$

The overall input impedance is therefore

$$Z_{\text{in}} = \left( \frac{1}{Z_{\text{top}}} + \frac{1}{Z_{\text{path}}} \right)^{-1}. \quad (1.6)$$

When the imaginary part of  $Z_{\text{in}}$  is not equal to zero, that is, when  $\text{Im}(Z_{\text{in}}) \neq 0$ , the structure behaves as a reactive surface. The stored electric or magnetic energy oscillates between the layers without being radiated, leading to strong reflection. This typically occurs away from the resonant frequency of the surface, where the pattern behaves either as a capacitive or an inductive sheet. For example, when the periodic elements contain narrow gaps or small apertures, capacitive coupling becomes dominant and  $Z_{\text{in}}$  decreases, causing a reflection band at lower frequencies. Conversely, when the pattern contains long current paths such as dipoles or slots, inductive effects dominate, shifting the reflection band to higher frequencies.

In reconfigurable structures, reflection can be dynamically controlled by adjusting the surface impedance through p-i-n diodes. When these diodes are forward biased, the conductive path across the gaps becomes continuous, effectively reducing  $Z_{\text{top}}$  to a small resistive value. The resulting mismatch with free space generates a high reflection coefficient, switching the surface into a reflective state, as shown in Figure 1.4(b). By modifying the biasing condition or replacing p-i-n diodes with varactors, the equivalent inductive and capacitive parameters can be tuned, thereby

shifting the resonant frequency and adjusting the reflection bandwidth [74, 75].

### 1.4.2 Transmission Mechanism

Transmission through an FSS occurs when the overall input impedance matches the free-space impedance, allowing the incident EM energy to propagate through the structure with minimal reflection. The transmission coefficient  $S_{21}$  can be derived from the impedance relationship as

$$S_{21} = \frac{2Z_{\text{in}}}{Z_{\text{in}} + Z_0}. \quad (1.7)$$

The structure reaches the transmission condition when  $Z_{\text{in}} \approx Z_0$  and  $S_{11} \approx 0$ . In this state, the reactive components of the top and bottom layers cancel each other, resulting in a purely resistive impedance that supports power flow across the dielectric substrate. The dielectric medium of thickness  $t$  introduces a phase delay, while the top and bottom patterns control the electric and magnetic field distributions, respectively. Transmission maxima occur when the phase difference between the waves reflected from both interfaces satisfies the constructive interference condition

$$2\beta t = n\pi, \quad (1.8)$$

where  $\beta$  is the propagation constant in the dielectric and  $n$  is an integer. Under this condition, the reflections from successive layers cancel each other, and the net transmitted wave achieves maximum amplitude.

The top and bottom metallic patterns behave as resonant  $LC$  networks, with inductance arising from current paths and capacitance from inter-element gaps. The resonance frequency of each surface can be approximately expressed as

$$f_r = \frac{1}{2\pi\sqrt{LC}}, \quad (1.9)$$

where  $L$  and  $C$  represent the effective inductance and capacitance, respectively, in each unit cell.

In reconfigurable structures, the reverse-bias condition in p-i-n diodes introduces a junction capacitance that forms a resonant circuit with the inductance of

the unit-cell geometry. However, the resonance frequency remains fixed by the diode capacitance. To enable dynamic frequency variation, varactor diodes are employed, where the reverse bias continuously alters the junction capacitance  $C_v$ . This tunability allows real-time adjustment of the EM response, enabling adaptive transparency across multiple frequency bands [76–78]. Consequently, the transmission behavior of an FSS is governed by the EM coupling between patterned layers, substrate thickness, and the effective reactance of the embedded diodes, allowing the surface to operate as a spatial band-pass filter that transmits desired signals while suppressing unwanted frequencies.

### 1.4.3 Absorption Mechanism

In absorber configurations, the goal is to suppress both reflection and transmission simultaneously so that the incident EM energy is dissipated in the surface. This phenomenon occurs when the input impedance of the structure matches the free-space impedance, thereby eliminating the reflection, while the bottom surface prevents any transmitted power. A typical structure used for such absorption behavior consists of a top resistive layer, a dielectric substrate of finite thickness, and a bottom metallic sheet or patterned surface. The top layer introduces a lossy impedance that contributes to energy dissipation, while the dielectric substrate provides a phase delay to ensure destructive interference between direct and reflected fields. The bottom layer acts either as a perfect conductor or as a reactive impedance that controls the reflected field strength.

The equivalent impedance and the  $S_{11}$  of such a single-layer absorber can be expressed using the parallel input impedance model ( $Z_{\text{in}}$ ), as discussed in the reflector mechanism. Under perfect absorption,  $S_{21} = 0$  and  $Z_{\text{in}} = Z_0$ , resulting in  $S_{11} = 0$  and maximum energy dissipation. The absorptivity of the surface is calculated as

$$A(\omega) = 1 - |S_{11}|^2 - |S_{21}|^2, \quad (1.10)$$

which simplifies to

$$A(\omega) = 1 - |S_{11}|^2 \quad (1.11)$$

for ground-backed configurations.

The key design objective is to tune  $Z_{\text{top}}$ ,  $Z_d$ , and  $Z_{\text{bot}}$  such that the real part of  $Z_{\text{in}}$  equals  $Z_0$  and its imaginary part is minimized, thereby ensuring complete impedance matching. When these two conditions are satisfied simultaneously, the reflected and re-radiated fields interfere destructively, causing the incident energy to dissipate through the resistive elements or lossy substrate.

To realize this condition practically, the top layer is designed as a lossy series or parallel *RLC* network, where the resistor controls the absorption strength, while the inductor and capacitor represent the distributed effects of the patterned elements. The dielectric substrate introduces phase compensation so that the effective impedance presented to the incident wave becomes purely resistive at resonance. For normal incidence, when the top sheet is modeled as  $Z_{\text{top}} = R + jX$ , the absorption condition is satisfied if the substrate parameters obey

$$\beta t \approx \frac{n\pi}{2}, \quad (1.12)$$

producing a quarter-wave-like resonance that cancels the reactive part of  $Z_{\text{in}}$ . The bottom impedance  $Z_{\text{bot}}$  determines the reflection boundary: when  $Z_{\text{bot}} \rightarrow 0$ , it behaves as a perfect conductor, while a finite or reactive  $Z_{\text{bot}}$  can be used to broaden the absorption bandwidth or tailor the frequency response. By carefully balancing  $Z_{\text{top}}$ ,  $Z_d$ , and  $Z_{\text{bot}}$ , the input impedance of the surface can be matched to  $Z_0$  over a wide frequency range, producing near-unity absorption.

In reconfigurable absorber configurations, the absorption performance can be dynamically adjusted by controlling the impedance components  $Z_{\text{top}}$ ,  $Z_d$ , and  $Z_{\text{bot}}$  through bias-dependent elements. When p-i-n diodes are integrated across the gaps of the top pattern, their switching state modifies the effective resistance and reactance of  $Z_{\text{top}}$ . Under forward bias, the diodes provide a low-resistance path, enhancing energy dissipation and increasing absorption. In contrast, the reverse-biased state introduces a junction capacitance that alters the resonance frequency and shifts the absorption band. Varactors offer continuous tuning capability by varying their junction capacitance with applied bias voltage, enabling real-time adjustment of the absorption magnitude and bandwidth. By tuning these impedance parameters, the overall input impedance  $Z_{\text{in}}$  can be matched to  $Z_0$  across different bias states, allowing dynamic control of the absorption characteristics [79–82].

### 1.4.4 Rasorber Mechanism

A rasorber represents an advanced form of FSS that combines both absorbing and transmitting characteristics in a single geometry. Unlike conventional absorbers that suppress all frequencies, a rasorber selectively absorbs out-of-band frequencies while allowing in-band transmission. This dual functionality is achieved by carefully adjusting the surface impedances of the top and bottom layers such that the structure behaves as an absorber in one frequency range and as a transmitter in another. A typical rasorber configuration consists of two dielectric substrates separated by an air spacer. The top substrate supports a lossy FSS pattern that includes resistive elements in series with an equivalent parallel  $LC$  circuit, while the bottom substrate carries a reactive FSS layer modeled by a parallel  $LC$  network. The air spacer between these two substrates behaves like a quarter-wavelength transmission line, introducing a necessary phase shift between the layers. The multilayer FSS configuration presented in Figure 1.5 demonstrates the interaction between the dielectric and air-spacer layers required to achieve the rasorber response.

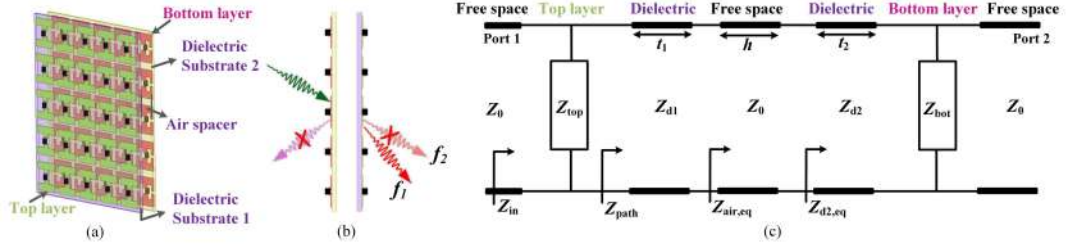


Figure 1.5: (a) Representative dual-layer RFSS structure with p-i-n diodes, (b) schematic depiction of rasorber operation, and (c) equivalent circuit model illustrating common impedance representation.

Using the same parallel-impedance framework discussed earlier, the overall input impedance at the top surface can be expressed as

$$Z_{path} = \frac{Z_{d1} (Z_{air,eq} + jZ_{d1} \tan(\beta_1 t_1))}{Z_{d1} + jZ_{air,eq} \tan(\beta_1 t_1)}, \quad (1.13)$$

where the equivalent impedance of the air spacer backed by the bottom substrate is

$$Z_{air,eq} = \frac{Z_{air} (Z_{d2,eq} + jZ_{air} \tan(\beta_0 h))}{Z_{air} + jZ_{d2,eq} \tan(\beta_0 h)}, \quad (1.14)$$

and the impedance of the second dielectric substrate terminated by the bottom FSS is given by

$$Z_{d2,\text{eq}} = \frac{Z_{d2} (Z_{\text{bot}} + jZ_{d2} \tan(\beta_2 t_2))}{Z_{d2} + jZ_{\text{bot}} \tan(\beta_2 t_2)}. \quad (1.15)$$

Here,  $Z_{\text{top}}$  represents the impedance of the top resistive layer,  $Z_{d1}$  and  $Z_{d2}$  are the characteristic impedances of the two dielectric substrates with thicknesses  $t_1$  and  $t_2$ , respectively,  $Z_{\text{air}}$  corresponds to the impedance of the air spacer of height  $h$ , and  $Z_{\text{bot}}$  denotes the impedance of the bottom reactive FSS layer. The overall input impedance seen from free space is then obtained as

$$Z_{\text{in}} = \left( \frac{1}{Z_{\text{top}}} + \frac{1}{Z_{\text{path}}} \right)^{-1}. \quad (1.16)$$

At the absorption frequencies, the bottom FSS behaves like a low-impedance reflector, resulting in a small  $Z_{\text{path}}$ , while the lossy top sheet is designed such that  $Z_{\text{in}} = Z_0$ . This condition ensures minimal reflection and transmission, forcing most of the incident energy to dissipate in the resistive elements of the top surface. In the transmission band, the reactive bottom FSS exhibits a parallel-resonant band-pass response and effectively transforms into a high-impedance surface ( $Z_{\text{path}} \rightarrow \infty$ ). Under this condition, the total admittance at the input plane becomes nearly zero, i.e.,

$$Y_{\text{in}} = \frac{1}{Z_{\text{top}}} + \frac{1}{Z_{\text{path}}} \approx 0, \quad (1.17)$$

allowing the electromagnetic wave to pass through the structure with minimal reflection. Consequently, the rasorber alternates between two impedance states: a matched lossy state for absorption and a parallel-resonant open state for transmission.

Depending on the spectral ordering of these bands, rasorbers can be categorized as absorption–transmission–absorption (A–T–A), transmission–absorption (T–A), or absorption–transmission (A–T) types. By adjusting the impedance values of  $Z_{\text{top}}$  and  $Z_{\text{bot}}$  using p–i–n diodes or varactors, the resonance and loss characteristics can be dynamically tuned [83–85]. By modifying the diode bias states, the equivalent circuit parameters ( $R$ ,  $L$ , and  $C$ ) in the surface impedance expressions are dynamically adjusted, enabling real-time switching between reflection, transmission, absorption, and rasorber states in a single structure.

## 1.5 Literature Survey on RFSS Structures

In this section, a brief description of earlier reported electronically controlled RFSS structures has been presented. These reconfigurable designs can be broadly classified into switchable structures, tunable structures, switchable-tunable multifunctional structures, and measurement approaches developed for their experimental verification.

A switchable structure operates by altering its EM response through discrete changes in bias states of active elements such as p-i-n diodes. Depending on the applied bias, the structure can exhibit distinct modes such as absorption, reflection, or transmission. These designs are simple to implement and provide clear functional switching, though their operating frequencies remain fixed once fabricated.

A tunable structure achieves continuous variation in frequency response by employing elements like varactor diodes. Such configurations allow adjustment of resonant frequencies under varying bias conditions, providing frequency agility. However, their functional states are generally limited to a single operational mode.

A switchable-tunable multifunctional structure integrates both switching and tuning mechanisms in a single configuration. This combination enables multiple operational modes along with frequency flexibility, thereby extending the adaptability of the surface for multifunctional applications. Although this approach increases control capability, it also demands careful biasing and circuit optimization.

Apart from structural development, significant efforts have been devoted to improving measurement approaches for accurate characterization of these reconfigurable structures. Traditional free-space setups often require large samples and precise alignment, whereas the PPW technique provides compact, repeatable, and cost-effective alternatives for validating multifunctional FSS responses.

A brief overview of these switchable, tunable, and switchable-tunable structures, along with the relevant measurement methodologies, has been presented in the subsequent sections.

### 1.5.1 Switchable RFSS Structures

Switchable FSS represents the earliest class of electronically reconfigurable designs, which include p-i-n diodes that operate with two different characteristics under forward bias and reverse bias conditions. The concept of introducing electronic switches into FSS unit cells emerged in the early 1990s, marking a shift from fixed passive filters toward dynamically controllable structures. Among the various electronic components, the p-i-n diode has become the most widely adopted due to its fast switching speed, compact size, and ease of integration in periodic metallic patterns. In recent years, several switchable FSS configurations have been explored to achieve multifunctional operations such as transmission, reflection, absorption, polarization, and rasorber through simple diode control mechanisms. These designs collectively demonstrate how the integration of a single electronically controlled element, such as a p-i-n diode, can tune the surface response to realize various EM functionalities depending on the structural configuration and biasing state.

#### Single p-i-n diode-based Switchable RFSS Structures

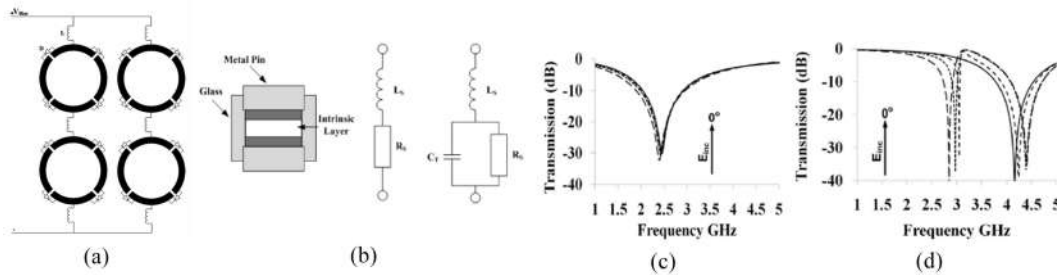


Figure 1.6: Active annular ring FSS: (a) unit cell configuration, (b) p-i-n diode equivalent circuits, (c) simulated ON-state response, and (d) simulated OFF-state response. [Courtesy: P. S. Taylor, E. A. Parker, and J. C. Batchelor, “An active annular ring frequency selective surface,” *IEEE Trans. Antennas Propag.*, vol. 59, no. 9, pp. 3265–3271, Sept. 2011.]

Initially, single-band switchable transparent/reflector configurations are reported, where the transition between transmission and reflection is achieved by controlling the electrical connection in the resonant geometry. In [6], an active annular ring FSS is proposed in which the structure can dynamically switch between transparent and reflective states by biasing p-i-n diodes, as shown in Figure 1.6. The sur-

face comprises annular rings segmented at orthogonal positions, and the ON and OFF states of the diodes determine whether the surface behaves as an inductive or capacitive grid. When the diodes are forward biased, the conductive paths are connected, restoring the fundamental resonance that produces a reflection peak at 2.45 GHz. Conversely, when the diodes are reverse biased, the current paths are interrupted, leading to a transparent state with minimal transmission loss, as shown in Figure 1.6. This mechanism illustrates that by modifying the electrical continuity of the resonator through the diode bias, the structure can effectively switch between high-reflection and high-transmission modes, providing the foundation for switchable FSS geometries.

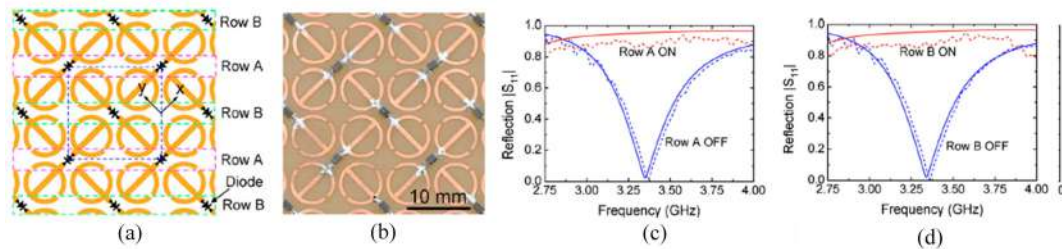


Figure 1.7: Switchable metamaterial reflector/absorber: (a) schematic layout, (b) fabricated sample, (c) Row A ON/OFF states, and (d) Row B ON/OFF states. [Courtesy: B. Zhu, Y. Feng, J. Zhao, C. Huang, and T. Jiang, “Switchable metamaterial reflector/absorber for different polarized electromagnetic waves,” *Appl. Phys. Lett.*, vol. 97, no. 5, p. 051906, 2010.]

Later, the concept is extended to switchable absorber/reflector configurations, demonstrating the ability to control EM dissipation characteristics. In [86], a metamaterial absorber/reflector is developed using an array of electric-LC (ELC) resonators integrated with p–i–n diodes, as presented in Figure 1.7. The design enables control of EM operation through capacitive or inductive coupling between resonant elements, which is determined by the diode bias state. When the diodes are in the OFF condition, the ELC elements are capacitively coupled, resulting in strong electric and magnetic resonances that match the impedance of free space and lead to near-perfect absorption at 3.34 GHz. When the diodes are switched ON, the coupling becomes inductive, canceling charge accumulation across the resonators and converting the surface into a reflective state. Moreover, by arranging two orthogonal sets of ELCs, the surface achieves polarization-selective absorption

or reflection. This study reveals that simple bias control can tailor the coupling mechanism in resonant inclusions to achieve switchable absorber/reflector behavior with good polarization selectivity.

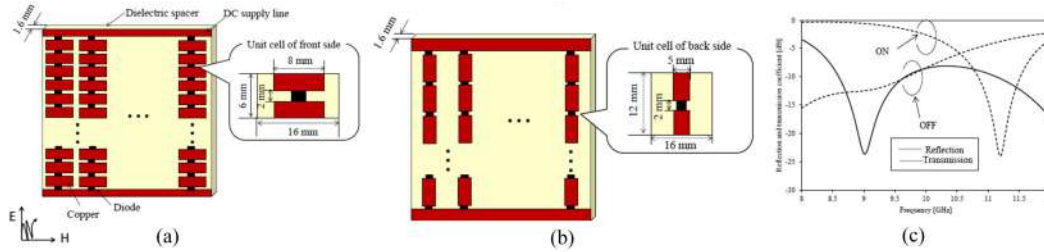


Figure 1.8: Active absorption/transmission FSS using diodes: (a) front view, (b) back view, and (c) simulated reflection and transmission characteristics for ON and OFF states. [Courtesy: S. Kitagawa, R. Suga, K. Araki, and O. Hashimoto, “Active absorption/transmission FSS using diodes,” *IEEE Asia-Pacific Microwave Conference*, 2015.]

Building upon these principles, several other designs focus on absorber/transmitter operations. These configurations aim to achieve absorption and transmission characteristics in the same structure by partially modifying the ground plane or introducing openings that allow EM wave propagation under different bias conditions. In [45], a diode-controlled FSS is proposed in which p–i–n diodes provide EM coupling in the resonant structure to alternate between narrowband absorption and transmission characteristics, as depicted in Figure 1.8. When the diodes are reverse-biased, the capacitive nature of the circuit supports strong resonance, enabling effective absorption of incident energy. Conversely, in the forward-biased state, the diodes provide an inductive path that suppresses resonance and permits EM wave propagation through the surface. This configuration highlights the role of active switching in dynamically modifying impedance matching and resonance suppression, demonstrating the transition between absorber and transmitter functions in a single planar design.

Subsequently, another important category of switchable FSSs is introduced to achieve polarization and reflection operations using diode-controlled geometries. In [44], a switchable reflection-type linear/circular polarization converter is proposed, where the FSS transforms a linearly polarized incident wave into either a cross-polarized or a circularly polarized reflected wave depending on the diode bias

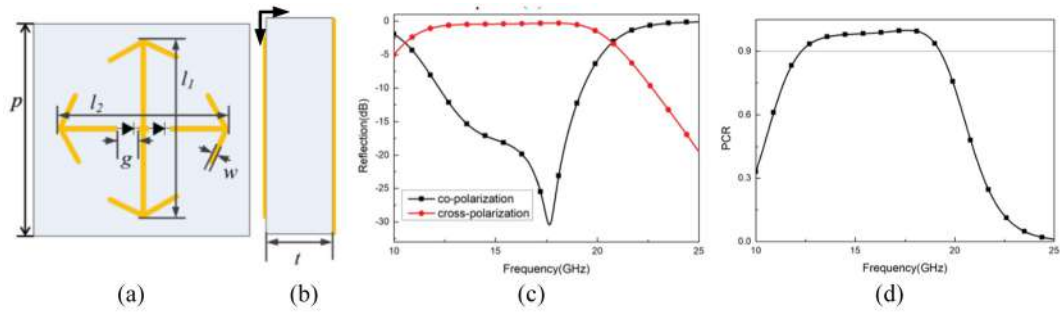


Figure 1.9: Switchable linear/circular polarization converter: (a) unit cell geometry, (b) side view, (c)  $S_{11}$  for co- and cross-polarization, and (d) polarization conversion ratio (PCR). [Courtesy: Y. Li, Q. Cao, and Y. Wang, “A switchable reflection-type linear/circular polarizers based on active metasurface,” *2019 IEEE International Symposium on Antennas and Propagation and USNC-URSI Radio Science Meeting*, Atlanta, GA, USA, 2019.]

state. The structure employs a cross double-head arrow configuration with two p-i-n diodes integrated along one arm. In the OFF state, one arm of the arrow is electrically isolated, enabling the other arm to function as a linear polarizer that converts co-polarized reflection into cross-polarization through anisotropic current distribution. When the diodes are switched ON, the two arms are electrically connected, resulting in a symmetric structure that supports equal magnitudes of orthogonal linear polarization components with a  $90^\circ$  phase shift, thereby generating circularly polarized reflection, as shown in Figure 1.9. This work demonstrates polarization manipulation through dynamic reconfiguration of current distribution and resonator symmetry using simple diode biasing.

After discussing the polarization/reflector configuration, which demonstrates bias-controlled polarization conversion between linear and circular reflections, another advancement in switchable FSSs is introduced through the design of rasorber/absorber structures. These configurations represent an extended form of multifunctional FSSs in which both absorption and transmission characteristics coexist in a cascading manner, providing more sophisticated EM control. In [87], a low-profile broadband frequency-selective rasorber/absorber based on slot arrays loaded with switching diodes is proposed, as presented in Figure 1.10. The rasorber acts as a hybrid between an absorber and a bandpass FSS, allowing transmission in a defined frequency window while absorbing out-of-band EM energy.

The physical mechanism underlying this design relies on the coupling between

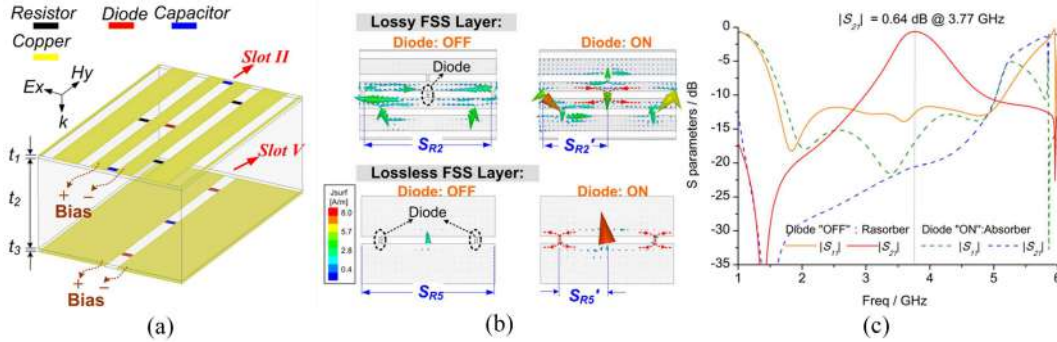


Figure 1.10: Dual-layer FSS-based switchable rasorber/absorber: (a) structure schematic with resistive elements, (b) surface current distributions for diode OFF and ON states, and (c) simulated  $S$ -parameters showing rasorber and absorber modes. [Courtesy: Y. Han, W. Che, X. Xiu, W. Yang, and C. Christopoulos, “Switchable low-profile broadband frequency-selective rasorber/absorber based on slot arrays,” *IEEE Trans. Antennas Propag.*, vol. 65, no. 12, pp. 6998–7008, Dec. 2017.]

lossy and lossless FSS layers. The lossy layer, composed of resistively loaded slots, primarily determines the absorption regions, while the lossless slot layer introduces the transmission window. The equivalent circuit model demonstrates that the rasorber operates with three distinct frequency bands: lower absorption, transmission, and upper absorption regions. When the embedded p–i–n diodes are in the OFF state, the structure maintains its resonant slot lengths, allowing a passband in the absorption band. In this condition, the incident wave partially transmits through the structure due to impedance matching between the lossy and lossless layers. However, when the diodes are forward biased (ON state), the effective resonant length of the lossless slots decreases, shifting the passband out of the absorption band. This eliminates the transmission window and transforms the structure into a full absorber. Thus, the device dynamically transitions between the rasorber and absorber states through bias control.

The inclusion of a single p–i–n diode not only governs the resonance coupling between the layers but also determines the effective impedance seen by the incident wave, enabling broadband absorption or selective transmission. Such mechanisms illustrate the evolution of single-diode-controlled FSSs from simple absorber/reflector or transmitter/reflector configurations to advanced hybrid devices, thereby forming the physical foundation for multifunctional RFSS designs.

From the above-discussed works, it is evident that a single p–i–n diode can

effectively govern one or two specific EM operations depending on the resonator geometry and bias-dependent impedance behavior. Several existing studies have further examined such single-diode-based FSS configurations, reporting a range of switchable responses that are limited to a small set of operational modes due to the availability of only two bias states [88–92]. However, achieving all these functionalities simultaneously in a single structure requires a higher degree of control. This can be realized by integrating multiple diodes in the unit cell. For instance, the use of two p–i–n diodes introduces four possible biasing combinations (OFF–OFF, OFF–ON, ON–OFF, and ON–ON), thereby enabling multiple functional states in a single design. These additional switching combinations allow the FSS to achieve extended multifunctionality in a single reconfigurable geometry.

### Dual p–i–n diode based Switchable RFSS Structures

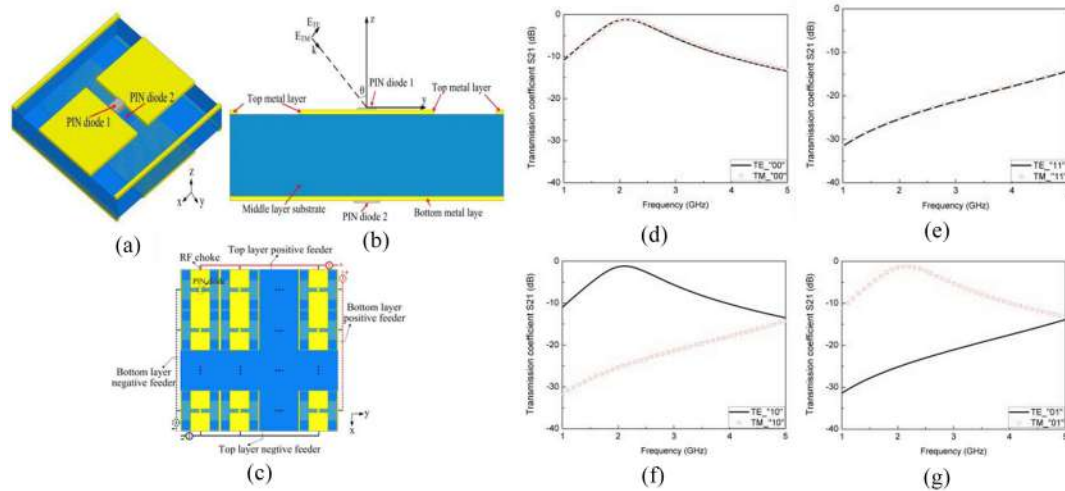


Figure 1.11: Dual-layer p–i–n diode-based polarization-independent switchable FSS: (a) 3D schematic, (b) cross-sectional view, (c) biasing network layout, and (d)–(g) simulated transmission responses for different diode bias states under TE and TM polarizations. [Courtesy: H. Li, Q. Cao, and Y. Wang, “A novel 2-B multifunctional active frequency selective surface for LTE-2.1 GHz,” *IEEE Trans. Antennas Propag.*, vol. 65, no. 6, pp. 3084–3092, Jun. 2017.]

To proceed with further developments in multifunctional FSS geometries, two independently controlled p–i–n diodes are employed on the top and bottom layers of a dielectric substrate. This two-layered approach enables independent tuning of the surface impedance at each layer, thereby allowing four possible bias combinations

that result in distinct EM operations in a single structure. In [93], a dual-layer RFSS is designed in which both layers contribute complementary EM functionalities through bias-controlled transitions between capacitive and inductive coupling, as shown in Figure 1.11. The top layer is primarily responsible for establishing the transmission behavior, whereas the bottom layer determines reflection or absorption depending on its diode state.

When both diodes are in the OFF state, the structure exhibits dual-band transmission due to capacitive resonance coupling between the two layers. When both diodes are ON, the conductive paths are connected, forming continuous current loops that suppress resonance and result in a broadband reflective state. Under asymmetric biasing conditions, the surface exhibits hybrid functionalities such as TE-pass/TM-stop and TM-pass/TE-stop, demonstrating independent polarization control from each layer. The physical mechanism underlying these states is governed by variations in surface reactance and interlayer coupling, where each diode state modifies the resonance strength and electric-field distribution across the substrate. This enables precise manipulation of the frequency-selective response in a single multifunctional RFSS configuration.

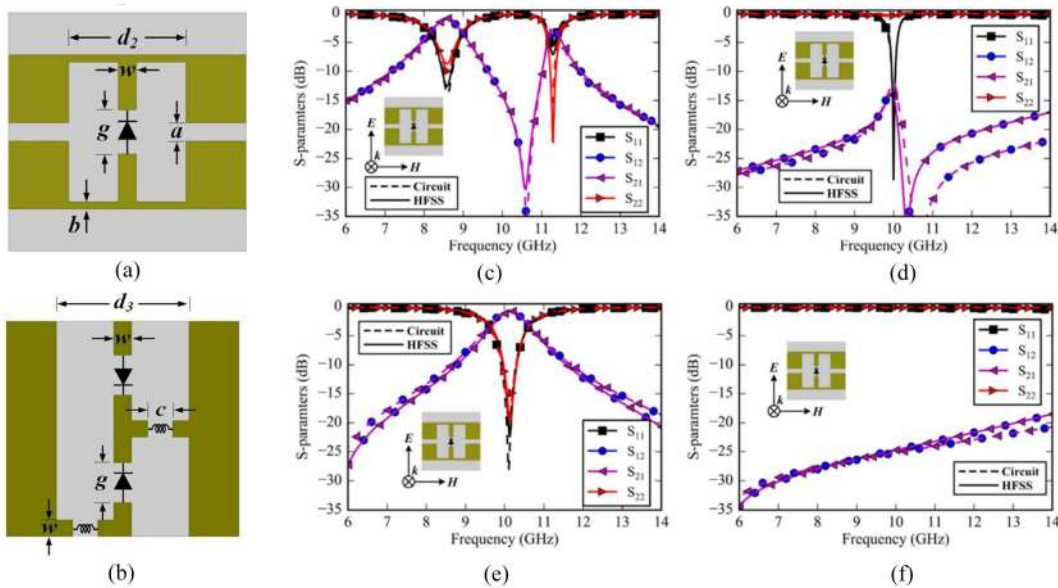


Figure 1.12: Multifunctional reconfigurable AFSS: (a)–(b) top and bottom unit cells, and (c)–(f) simulated  $S$ -parameters for four switching states. [Courtesy: R. Phon, S. Ghosh, and S. Lim, “Novel multifunctional reconfigurable active frequency selective surface,” *IEEE Trans. Antennas Propag.*, vol. 67, no. 3, pp. 1709–1719, 2019.]

A subsequent configuration extends this concept by modifying the resonator topology of the two layers to realize even broader multifunctional characteristics. In [94], both layers are patterned with distinct metallic geometries such that the overall surface response can be tuned to obtain dual-band transmission, narrowband absorption, single-band transmission, or broadband reflection, depending on the diode bias combinations. The OFF–OFF state provides simultaneous resonance on both layers, leading to dual-band transmission. When the top diode is ON, and the bottom remains OFF, the top layer acts as a reflector while the bottom layer continues to transmit, resulting in a single transmission band.

Conversely, when the top diode is OFF and the bottom diode is ON, strong resonant coupling between the lossy and reflective layers produces a narrowband absorption response. When both diodes are ON, the system achieves high reflectivity over a wide frequency range due to the suppression of both transmission and absorption mechanisms, as illustrated in Figure 1.12. These behaviors are well explained through equivalent circuit representations and field analysis, revealing how independent electrical control of two diodes dynamically adjusts impedance matching and interlayer coupling to obtain four distinct EM operations in a single FSS configuration.

These studies clearly demonstrate that employing two p–i–n diodes in dual-layer FSS geometries enables a significantly expanded control mechanism compared with single-diode designs. Several subsequent works have further explored multifunctional RFSS configurations, introducing a variety of switchable layouts capable of providing reflection, transmission, absorption, and hybrid responses in similar structural frameworks [95]. While these switchable configurations allow transitions among multiple functionalities, the corresponding resonant frequencies remain fixed. To enable dynamic frequency control, the next evolution in RFSS design involves tunable structures, in which the integration of continuously variable components such as varactor diodes provides frequency agility through voltage-controlled capacitance variation. This tunability enhances adaptability by enabling real-time adjustment of the resonance position without altering the physical geometry, thereby extending operation over wider spectral regions.

### 1.5.2 Tunable RFSS Structures

One of the earliest implementations of this concept utilizes a varactor-tunable convoluted dipole FSS structure in which each dipole element incorporates a varactor diode connected through resistive lumped-element biasing grids [96]. These grids serve a dual function: providing the biasing path for the diodes and suppressing parasitic resonances that often degrade the frequency response, as shown in Figure 1.13. The resistive biasing network, realized using surface-mounted resistors, effectively mitigates microwave current coupling in the grids and improves the low-pass performance of the filter. In this configuration, reverse biasing of the varactors continuously alters their capacitance, thereby shifting the band-stop frequency of the FSS. As the bias voltage increases, the capacitance decreases, resulting in an upward shift in the resonant frequency. The design achieves a stable tuning response with minimal voltage drop across the biasing grids, ensuring uniform diode excitation across the array. Thus, this work demonstrates that resistively biased varactor-loaded FSS structures can achieve continuous frequency tuning.

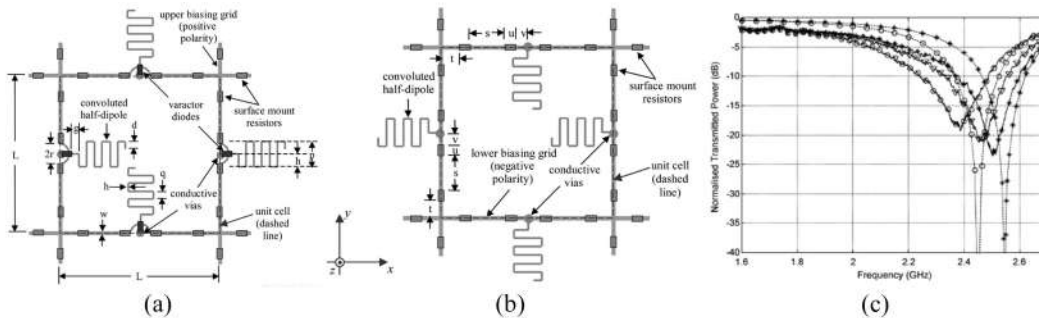


Figure 1.13: Varactor-tunable convoluted dipole FSS: (a)–(b) upper and lower metallization layers with varactor diodes and resistors, and (c) simulated transmission response demonstrating tunability. [Courtesy: C. Mias, “Varactor-tunable frequency selective surface with resistive-lumped-element biasing grids,” *IEEE Microw. Wireless Compon. Lett.*, vol. 15, no. 9, pp. 570–572, 2005.]

Another significant contribution toward tunable FSS development is the realization of a high-impedance surface (HIS) with a reduced number of varactor diodes [97], addressing the complexity and cost issues of conventional designs, as illustrated in Figure 1.14. Typically, each unit cell requires one or more varactors, leading to a dense biasing network. This limitation is overcome by introducing a feeding network behind the ground plane, which is connected to the FSS elements

through metallized vias, allowing a single varactor to control a group of unit cells. The tuning mechanism of this shared varactor follows the same principle described earlier, where varying the reverse bias alters the equivalent capacitance, thereby shifting the resonance frequency and reflection phase. The feeding lines are designed to ensure electrical equivalence, preserving the desired tunable response with minimal amplitude degradation. The reduced varactor count simplifies the overall design and biasing network without compromising the tuning range or phase linearity. The losses primarily arise from the substrate rather than the tuning mechanism, indicating that the use of low-loss dielectric materials can further enhance performance. This approach establishes a cost-effective and practical foundation for tunable high-impedance FSSs suitable for integration with low-profile antenna systems.

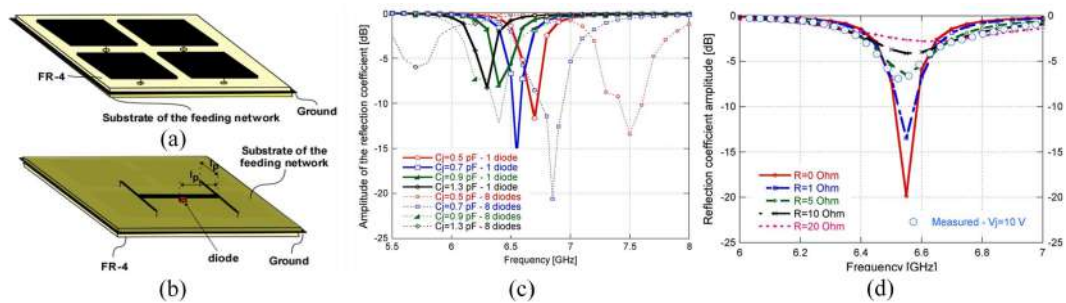


Figure 1.14: Tunable high-impedance surface with reduced varactors: (a)–(b) structure and feeding network with a single-diode configuration, and (c)–(d) simulated and measured reflection responses for different diode capacitances and resistances. [Courtesy: F. Costa, A. Monorchio, and G. P. Vastante, “Tunable high-impedance surface with a reduced number of varactors,” *IEEE Antennas Wireless Propag. Lett.*, vol. 10, pp. 11–13, 2011.]

Building upon this concept, a more advanced tunable design introduces a varactor loaded second-order bandpass FSS employing embedded bias networks for seamless electrical control, as presented in Figure 1.15 [98]. This configuration incorporates three metallic layers separated by thin dielectric spacers, where the top and bottom layers contain miniaturized meandered cross-shaped resonators and the middle layer consists of inductive wire grids connected through metallic vias. Varactor diodes placed between the cross resonators and the wire grids provide voltage-controlled capacitance, thereby adjusting the center frequency of the filter. The key innovation in this design lies in the integrated biasing approach, in

which all varactors are biased in parallel through the metallic grids, eliminating the need for external bias lines, resistors, or capacitors that typically disturb RF performance. The equivalent circuit model reveals a second-order coupled-resonator system, where variation of the varactor capacitance continuously shifts the passband while maintaining a nearly constant fractional bandwidth. Experimental results confirm frequency tuning from 5.2 GHz to 3.7 GHz with minimal insertion loss and stable operation under both TE and TM polarizations over wide incidence angles. The physical mechanism underlying this tunability is the controlled modification of inter-resonator capacitances and inductive coupling in the multilayer structure, enabling dynamic impedance matching through applied bias control.

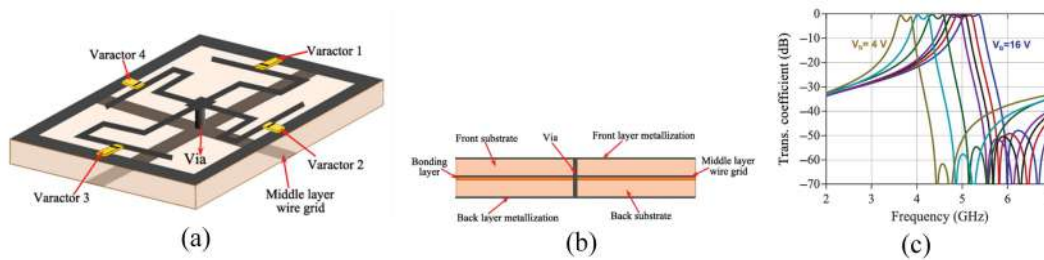


Figure 1.15: Varactor-tunable second-order bandpass FSS: (a)–(b) three-dimensional and cross-sectional views showing the multilayer structure and vias, and (c) simulated transmission response for different bias voltages. [Courtesy: A. Ebrahimi, Z. Shen, W. Withayachumnankul, S. F. Al-Sarawi, and D. Abbott, “Varactor-tunable second-order bandpass frequency-selective surface with embedded bias network,” *IEEE Trans. Antennas Propag.*, vol. 64, no. 5, pp. 1672–1680, 2016.]

Following the discussion on tunable structures, it is evident that while varactor-based designs successfully enable continuous frequency adjustment, they remain limited to a single electromagnetic (EM) function, such as transmission or absorption. Several studies in the existing literature have further expanded on these tunable configurations, demonstrating a wide range of continuously adjustable FSS responses achieved through different varactor placements, loading schemes, and unit-cell geometries [99–102]. In contrast, switchable structures based solely on p–i–n diodes can realize multiple operational modes such as reflection, transmission, and absorption, but cannot dynamically alter their operating frequencies once fabricated. Therefore, to achieve simultaneous multifunctionality and frequency agility, researchers have progressively integrated both p–i–n diodes and varactors in a single

FSS. This hybrid approach provides discrete mode switching through p–i–n diodes while enabling continuous frequency tuning via varactors, resulting in a versatile and highly controllable FSS design that combines the advantages of both mechanisms.

### 1.5.3 Switchable-Tunable MRFSS Structures

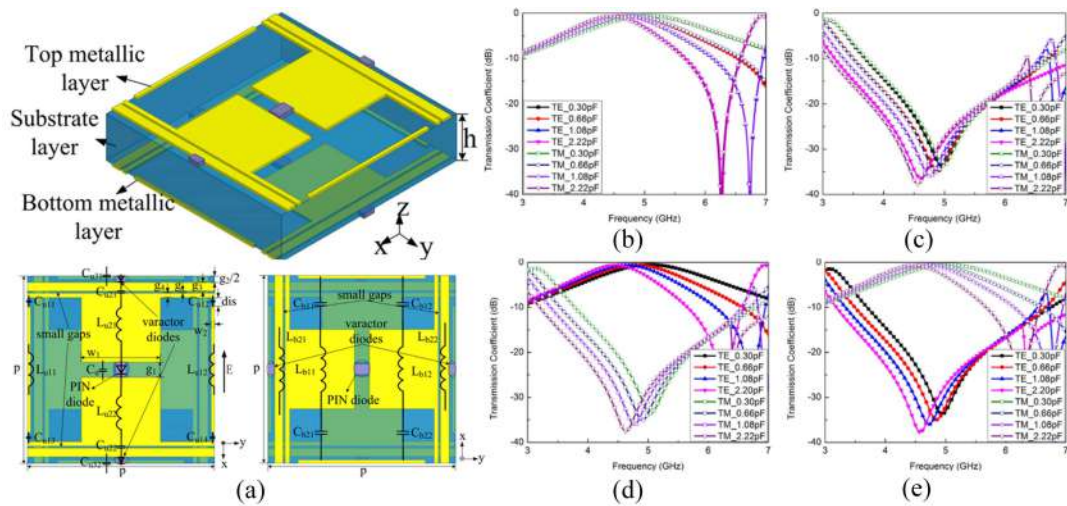


Figure 1.16: Improved multifunctional active FSS: (a) three-dimensional and top–bottom layer views, and (b)–(e) simulated transmission coefficients for TE and TM modes under different capacitance values, demonstrating switching, polarization selection, and frequency-tuning functions. [Courtesy: H. Li, Q. Cao, L. Liu, and Y. Wang, “An improved multifunctional active frequency selective surface,” *IEEE Trans. Antennas Propag.*, vol. 66, no. 4, pp. 1854–1862, Apr. 2018.]

In [65], an multifunctional reconfigurable FSS is presented, comprising two metallic layers separated by a dielectric substrate, with both p–i–n and varactor diodes incorporated into a parallel-feed configuration. The design offers three independent and controllable EM functions, switching, polarization selection, and frequency tuning, in a single compact architecture, as shown in Figure 1.16. The inclusion of varactors enables continuous adjustment of the resonant frequency from 4.48 GHz to 5.05 GHz under different bias voltages, while the p–i–n diodes support discrete state switching between transmission, reflection, and polarization-selective operations. The structure maintains stable performance for both TE and TM polarizations up to  $45^\circ$  oblique incidence and achieves efficient biasing without external feed lines by integrating the bias network into the FSS geometry itself. Experimental validation confirms strong agreement between simulated and measured responses,

verifying that the combined switching and tuning mechanisms significantly enhance operational flexibility and angular stability.

Similarly, in [103], a polarization-insensitive active FSS is developed capable of switching between absorption and transmission modes while simultaneously providing frequency tuning. The design employs p–i–n diodes on the bottom layer for mode switching and varactors on the top layer for frequency control, as depicted in Figure 1.17. The proposed geometry achieves a tunable transmission band from 3.70 to 4.27 GHz with an insertion loss of 1.96–4.30 dB, along with an adjustable absorption band from 4.28 to 5.12 GHz exhibiting 78–91% absorptivity. By introducing a parallel bias configuration, the structure effectively minimizes power consumption and response time while ensuring angular and polarization stability. Equivalent-circuit and full-wave analyses confirm that integrating both reactive components in a single multilayer configuration provides enhanced reconfigurability, compactness, and control over EM responses.

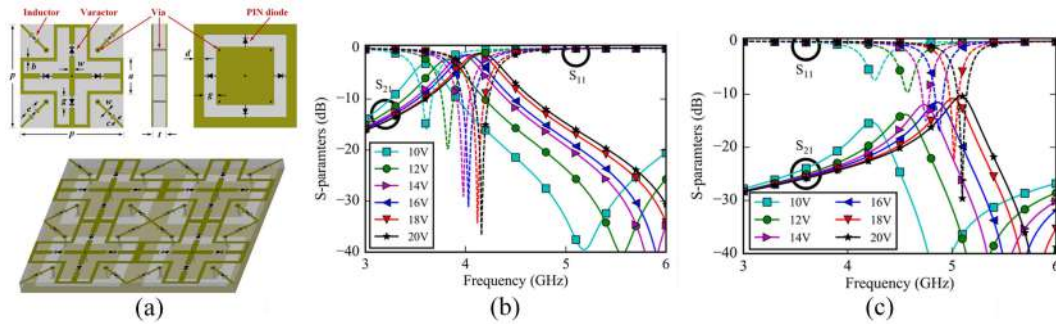


Figure 1.17: Polarization-insensitive AFSS for switchable and tunable operation: (a) top and bottom unit cells with biasing and diode placement, and (b)–(c) simulated transmission and absorption characteristics under ON and OFF modes. [Courtesy: R. Phon, S. Ghosh, and S. Lim, “Active frequency selective surface to switch between absorption and transmission band with additional frequency tuning capability,” *IEEE Trans. Antennas Propag.*, vol. 67, no. 9, pp. 6059–6067, Sept. 2019.]

Despite the significant advancements reported in switchable–tunable multifunctional FSS designs, several challenges persist that continue to limit their practical implementation and accurate characterization. Most reported designs remain restricted to limited functionalities, operating only between two or three states such as transmission, reflection, and absorption [104, 105]. Many of these structures exhibit polarization sensitivity and angular instability. Additionally, the tuning range achieved is relatively narrow, limiting adaptability across broader frequency bands.

In several cases, the biasing networks employed for diode control are complex and intrusive, resulting in increased parasitic effects and performance degradation. Furthermore, while simulation-based analyses provide valuable insights into multifunctional behavior, experimental realization and measurement of these responses require equally robust and precise characterization frameworks. This necessity extends the discussion from the design domain to the measurement perspective, where various techniques, ranging from free-space setups to waveguide and parallel-plate configurations, are explored to accurately evaluate the EM performance of FSS structures under realistic conditions.

#### 1.5.4 Measurement Techniques for RFSS Structures

To validate RFSS behaviors experimentally, multiple measurement methodologies are adopted depending on the target response, frequency range, and sample size. Free-space systems emulate plane-wave illumination and are typically used for transmission and reflection characterization under realistic far-field conditions [106–108]. On the other hand, the rectangular-waveguide technique provides precise and low-cost  $S$ -parameter extraction for periodic samples sized to the waveguide aperture, ensuring controlled boundary conditions in a defined frequency band [109–111]. PPW setups offer a compact alternative, supporting TEM wave propagation and allowing repeatable measurements on smaller samples while reducing chamber and alignment requirements [112–114]. The following sections discuss each approach in the context of reconfigurable structures, emphasizing the measurement flow, instrumentation, calibration strategy, and practical considerations.

In [71], a free-space measurement setup is employed for the characterization of an RFSS structure. The setup consists of a pair of horn antennas positioned in an anechoic environment, with the sample mounted at the center to ensure minimal reflection interference. The incident and transmitted waves are captured using a vector network analyzer (VNA), allowing the extraction of  $S$ -parameters across the desired frequency band. The VNA is first calibrated using standard through–reflect–line (TRL) or short–open–load–through (SOLT) techniques to remove the effects of cables and connectors, thereby ensuring accurate measurement of the reflection ( $S_{11}$ ) and transmission ( $S_{21}$ ) parameters. During testing, time-domain gating is

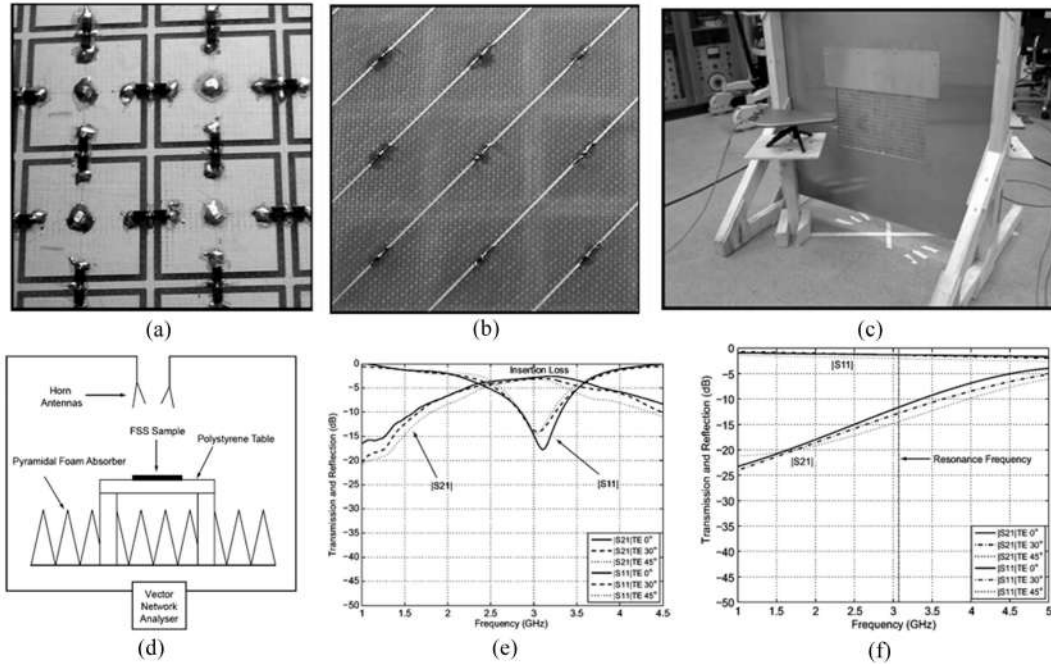


Figure 1.18: Experimental setup and validation of a switchable FSS: (a)–(c) fabricated prototype and measurement arrangements, (d) test setup, and (e)–(f) measured results for TE and TM polarizations under different incidence angles. [Courtesy: G. I. Kiani, K. L. Ford, L. G. Olsson, K. P. Esselle, and C. J. Panagamuwa, “Switchable frequency selective surface for reconfigurable electromagnetic architecture of buildings,” *IEEE Trans. Antennas Propag.*, vol. 58, no. 2, pp. 581–584, 2010.]

applied to eliminate unwanted reflections from nearby objects. Measurements are performed for both normal and oblique incidences by adjusting the orientation of the sample with respect to the antennas. This approach provides a reliable assessment of transmission and reflection responses under different polarization and biasing conditions. However, as illustrated in Figure 1.18, free-space setups typically require large sample sizes, precise alignment, and well-calibrated absorber surroundings to minimize measurement uncertainties. Despite these challenges, this method remains one of the most versatile techniques for broadband studies, offering direct insight into the real-time behavior of reconfigurable surfaces under far-field conditions.

In [99], a rectangular waveguide measurement technique is utilized to evaluate the performance of an RFSS, as shown in Figure 1.19. In this approach, a portion of the periodic surface is placed at the open aperture of a standard waveguide connected to a vector network analyzer (VNA). The confined propagation environment in the waveguide allows accurate determination of reflection and transmission

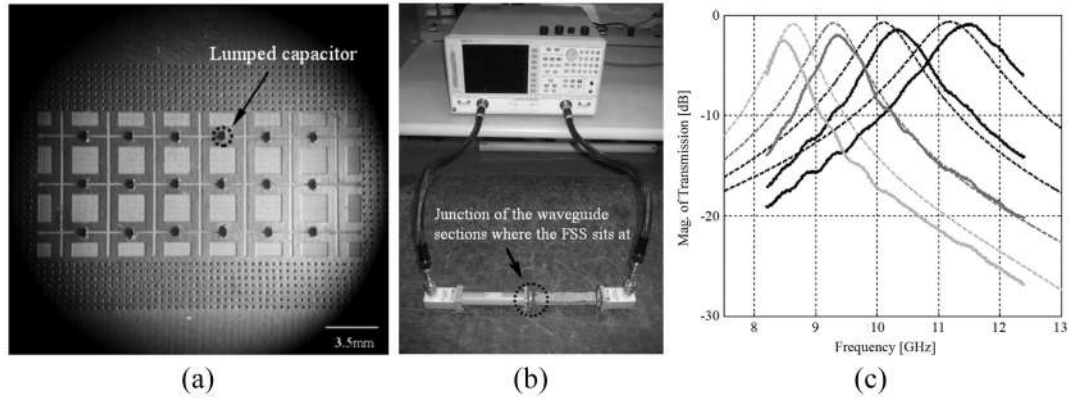


Figure 1.19: Waveguide prototype and tunability measurement of a miniaturized-element FSS: (a) fabricated loop-wire FSS sample, (b) WR90 waveguide measurement setup, and (c) measured transmission response. [Courtesy: F. Bayatpur and K. Sarabandi, “Tuning performance of metamaterial-based frequency selective surfaces,” *IEEE Trans. Antennas Propag.*, vol. 57, no. 2, pp. 590–592, 2009.]

coefficients under normal incidence. Prior to measurement, the VNA is calibrated using the through–reflect–line (TRL) method specific to the waveguide band, ensuring that the measurement plane corresponds exactly to the waveguide aperture and thereby eliminating systematic phase and magnitude errors. During the measurement, the reflection coefficient  $S_{11}$  is obtained directly from the reflected signal at the waveguide port, while the transmission coefficient  $S_{21}$  is derived when a second waveguide section is employed for transmission analysis. This method provides high measurement repeatability and does not require large prototype dimensions, making it well suited for testing unit-cell-based reconfigurable designs. This configuration enables precise control of boundary conditions and minimizes external electromagnetic (EM) interference. However, its primary limitation lies in its narrow operating frequency band and fixed incidence angle, restricting its applicability for wideband or oblique-incidence characterization. Nonetheless, this technique offers an efficient and compact alternative to large-scale free-space measurements for bias-controlled FSS validation.

To overcome the limitations associated with free-space and waveguide-based techniques, PPW measurements are gaining prominence as a compact and accurate alternative. The PPW setup is developed to measure broadband absorption characteristics, as presented in Figure 1.20. The system comprises two parallel conducting plates forming a TEM propagation environment, which ensures controlled

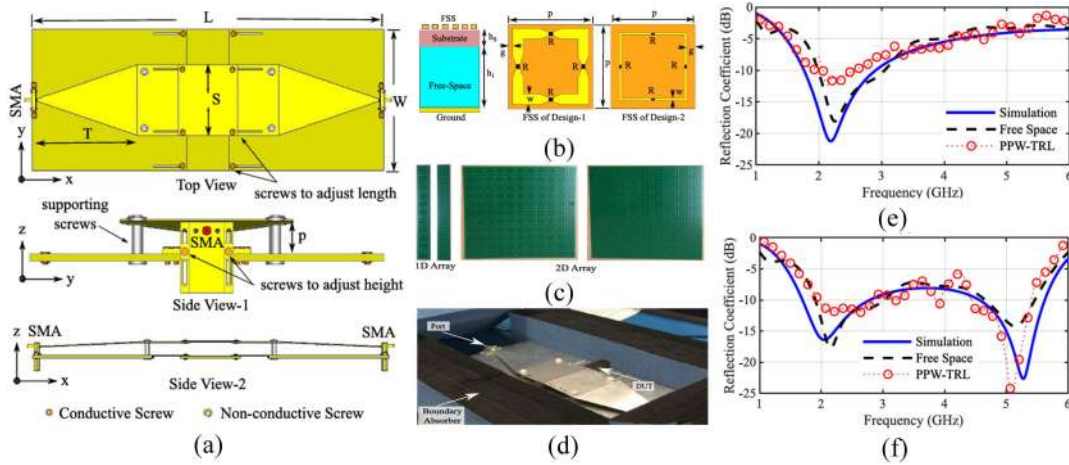


Figure 1.20: Adjustable parallel-plate waveguide (PPW) setup: (a) three-dimensional schematic, (b) two test FSS absorbers, (c)–(d) fabricated samples and experimental setup, and (e)–(f) comparison of simulated, free-space, and PPW–TRL measured reflection results. [Courtesy: M. I. Hossain, N. Nguyen-Trong, and A. M. Abbosh, “Calibrated parallel-plate waveguide technique for low-frequency and broadband absorptivity measurement,” *IEEE Antennas Wireless Propag. Lett.*, vol. 19, no. 9, pp. 1541–1545, 2020.]

field distribution and minimal edge-diffraction effects. In this approach, VNA calibration is performed using the TRL technique implemented in the PPW section, where the through, reflect, and line standards are realized using reference metal plates and precisely machined spacers to ensure consistent phase referencing. After calibration, the reflection and transmission coefficients,  $S_{11}$  and  $S_{21}$ , are measured directly by connecting coaxial probes at both ends of the PPW structure. This method requires only a small sample size and achieves high measurement accuracy over a wide frequency range. As discussed in [115], the PPW configuration effectively replicates free-space conditions in a compact form factor, demonstrating strong correlation between PPW measurements and conventional anechoic-chamber results. Consequently, the PPW approach represents a reliable measurement technique for characterizing reconfigurable and multifunctional FSS structures under normal-incidence conditions.

## 1.6 Motivation of Thesis

Electromagnetic surfaces that can dynamically manipulate incident waves in terms of reflection, transmission, and absorption play a crucial role in the development of

next-generation communication, sensing, and stealth systems. Among these, FSSs have emerged as one of the most versatile platforms due to their inherent ability to exhibit filter characteristics in the spatial domain. However, conventional FSSs are inherently static and operate only at predetermined frequencies once fabricated, thereby restricting their adaptability to dynamically changing EM environments. To overcome this limitation, reconfigurable or active FSSs have been introduced by integrating semiconductor or tunable components, enabling control over their spectral responses. Such RFSSs are capable of dynamically switching between functional states or continuously tuning their resonant frequencies, thereby providing significant flexibility in EM manipulation. The motivation of this thesis arises from the need to design and experimentally validate multifunctional RFSSs that can alter their EM responses to realize absorption, reflection, transmission, and rasorber characteristics, while maintaining structural compactness, polarization stability, and practical feasibility.

Early RFSS structures primarily focused on switchable configurations using p-i-n diodes as electronically controlled elements. By altering the diode bias state between ON and OFF, discrete transitions among reflection, transmission, and absorption modes were achieved. While these designs demonstrated clear functional switching, they suffered from limited operational bandwidth and fixed resonance frequencies. Furthermore, most reported switchable FSSs exhibited polarization sensitivity and operated effectively only for specific polarizations or incidence directions. The complexity of biasing networks also imposed constraints on large-scale implementations, as each diode required separate bias control lines that introduced unwanted parasitic effects and fabrication challenges. Addressing these issues, the present research focuses on developing polarization-insensitive switchable metasurfaces with simplified biasing arrangements that independently control EM functionalities through compact and symmetrically distributed configurations. In particular, the concept of parallel biasing is emphasized to replace traditional series networks, enabling uniform voltage distribution and improved switching stability over wide incidence angles.

In parallel with switchable designs, significant effort has been directed toward achieving continuous frequency tunability. Varactor-loaded FSSs have been exten-

sively investigated for their capability to shift the resonant frequency by varying the applied reverse-bias voltage. Although such tunable designs introduce frequency agility, they are typically limited to a single functional state, such as reflection or transmission. Moreover, the tuning range of most reported designs remains narrow due to limited capacitance variation and parasitic coupling effects in practical layouts. To address these limitations, this thesis introduces tunable RFSS configurations with enhanced tuning range and improved stability by optimizing inter-resonator coupling and employing efficient bias isolation strategies. The resulting tunability enables dynamic frequency adaptation without modifying the structural geometry, thereby laying the foundation for frequency-agile EM surfaces.

A further step in the evolution of RFSSs involves switchable–tunable multifunctional architectures, in which both p–i–n and varactor diodes are integrated in the same structure. This hybrid integration enables discrete switching between functional states through p–i–n diodes while simultaneously allowing continuous frequency tuning via varactors. Such designs combine the advantages of switchable and tunable structures in a single configuration, providing superior adaptability and control. However, many existing hybrid designs still exhibit narrow tuning ranges, polarization-dependent responses, and complex multilayer arrangements. The present work addresses these challenges by developing multifunctional hybrid metasurfaces capable of realizing multiple EM states, including reflection, transmission, and absorption, over tunable frequency bands using simplified single-layer geometries. The proposed design strategies focus on achieving independent control of each electronically controlled element, thereby maximizing the number of operational combinations without compromising structural compactness.

While considerable research has focused on the design of RFSSs, experimental characterization remains a critical requirement for validating theoretical predictions and numerical simulations. Various measurement approaches have been reported in the literature, including free-space setups, rectangular waveguide techniques, and PPW methods. Free-space systems allow simultaneous measurement of reflection and transmission coefficients under realistic plane-wave excitation but require large prototypes, precise alignment, and costly anechoic facilities. Rectangular waveguide measurements provide compact and accurate  $S$ -parameter extraction but are

inherently limited by single-mode operation and fixed incidence angles. To overcome these limitations, the PPW measurement technique has emerged as an efficient alternative, enabling characterization under controlled TEM-mode propagation with smaller sample sizes and facilitating angle-dependent studies through mechanical reconfiguration. The present thesis extends this methodology by proposing a modified PPW setup capable of wide-angle characterization of multifunctional FSS prototypes, offering improved repeatability and reduced measurement uncertainty compared to conventional techniques.

Thus, the motivation of this thesis is driven by the need to address the key challenges identified in existing literature, namely polarization sensitivity, limited tunability, complex biasing networks, and the lack of efficient measurement techniques, and to develop a comprehensive framework for the design, fabrication, and experimental evaluation of multifunctional reconfigurable frequency selective surfaces. The investigations presented in this work aim to establish a pathway toward intelligent EM surfaces capable of adaptive and multifunctional operation, which are essential for next-generation communication, sensing, and stealth applications.

## 1.7 Organization of Thesis

The thesis is organized into seven chapters. **Chapter 1** provides an introduction to FSSs and RFSSs, presenting a brief overview of their fundamental concepts. The limitations of existing RFSS designs are discussed, followed by the motivation and objectives of the present research.

**Chapter 2** presents a polarization-insensitive absorptive/transmissive RFSS employing a single p-i-n diode configuration. The design consists of metallic patterns fabricated on opposite sides of a single dielectric substrate, where reconfigurable behavior is achieved by switching the p-i-n diode between ON and OFF states under different biasing conditions. An embedded biasing network incorporating vias and lumped inductors enables polarization-insensitive operation without performance degradation. The proposed structure is fabricated and experimentally validated using an in-house developed PPW measurement setup. This work has been published in *IEEE Antennas and Wireless Propagation Letters* (2023), as listed in the

Publications section.

While the structure presented in **Chapter 2** operates between two modes, it relies on manual biasing and is therefore unsuitable for real-time applications. To address this limitation, **Chapter 3** introduces a multifunctional RFSS employing two independently controlled diode sets to achieve three distinct EM behaviors: absorption, transmission, and reflection. The configuration generates four operating states through careful selection of metallic patterns and precise placement of diode elements. An FPGA-based control system is integrated to automate the switching mechanism and enable real-time operation. The structure is experimentally validated and demonstrates multifunctional performance while maintaining polarization insensitivity and angular stability. This work has been accepted for publication in *IEEE Microwave And Wireless Technology Letters* (2026), as listed in the Publications section.

Following the switchable RFSS designs discussed in earlier chapters, **Chapter 4** focuses on the integration of frequency-tuning capability along with switching functionality. In this chapter, a multifunctional RFSS is designed by incorporating varactor diodes together with p-i-n diodes in a single-layer topology. Unlike earlier fixed-frequency designs, this structure enables frequency tuning in each operational mode by controlling the reverse-bias voltage applied to the varactor diodes. The design demonstrates both discrete mode switching and continuous frequency control, yielding four operational states with tunability in each mode. The structure is fabricated and tested using free-space measurement techniques. This work has been published in *IEEE Transactions on Antennas and Propagation* (2024), as listed in the Publications section.

Although the RFSS designs presented in the preceding chapters demonstrate switching and tuning capabilities, their operating modes remain narrowband, limiting flexibility for broadband applications. To overcome this limitation, **Chapter 5** is dedicated to wideband RFSS design. A multilayer architecture is developed by integrating two dielectric layers separated by an air spacer. Lumped resistors are incorporated alongside p-i-n diodes to broaden the absorption response, while symmetric geometries ensure polarization-insensitive performance. The proposed structure exhibits four distinct EM functionalities: absorber operation with com-

bined transmission and absorption, broadband absorption, broadband transmission, and full reflection under different operating modes. The design is fabricated and validated using a custom-built PPW measurement setup. This work has been published in *IEEE Antennas and Wireless Propagation Letters* (2025), as listed in the Publications section.

Since all RFSS designs require experimental validation, **Chapter 6** focuses on the development of a modified PPW measurement system for wide-angle FSS characterization. The system consists of two parallel metallic plates with tapered ends to provide wideband impedance matching. For oblique-incidence testing, two PPW sections with different apertures are mechanically joined at adjustable angles, enabling controlled angular excitation while maintaining electrical continuity and mechanical alignment. Various FSS prototypes, including bandstop filters, broadband absorbers, and switchable structures, are fabricated and measured to validate the effectiveness of the proposed measurement approach. This work has been accepted for publication in *IEEE Antennas and Wireless Propagation Letters* (2026), as listed in the Publications section.

Finally, **Chapter 7** presents the conclusions of the thesis and outlines potential directions for future research.



# Chapter 2

## Polarization-Insensitive Narrowband Absorptive/ Transmissive RFSS

### 2.1 Introduction

Since the last few decades, FSSs have been extensively used in various EM applications such as radomes, stealth technology, EMI mitigation, and wireless communication systems. Depending on the operational requirements, these structures are designed to realize specific functionalities namely reflection, transmission, or absorption in the microwave regime. In several practical scenarios, narrowband absorption is required for detector-based systems like bolometers or pixel sensors, while in other cases, selective transmission becomes important for adaptive radomes and stealth configurations. Integrating absorption and transmission operations in a single structure will attract several applications.

In the previous chapter, a broad overview of different switchable reconfigurable frequency selective surfaces (RFSSs) configurations has been discussed, capable of achieving absorption/reflection, reflection/transmission, transmission/absorption, and polarization/reflection operations. Although these earlier studies establish the fundamental concepts of diode-based switching, most of these structures suffer from various practical limitations such as multilayer arrangements, polarization sensitivity, and complicated biasing networks, which reduce their suitability for real EM

platforms. This highlights the need for a compact structure that maintains symmetry, supports stable TE and TM performance, and offers clear switching between functional states.

This chapter introduces a polarization-insensitive RFSS that provides both absorptive and transmissive operation using electronically switched p-i-n diodes. The structure uses a single-layer design and switches between the two operations by adjusting the diode bias conditions. An integrated biasing network with metallic vias and RF inductors ensures proper diode control without disturbing the EM response, allowing stable performance under both TE and TM polarization conditions. The following sections of this chapter describe the design topology, explain the equivalent circuit and operating mechanism, and discuss fabrication and measurement using a parallel-plate waveguide setup. Finally, the measured results validate the proposed design and demonstrate its suitability for adaptive radomes, sensing applications, and low-observable systems.

## 2.2 Design and Analysis

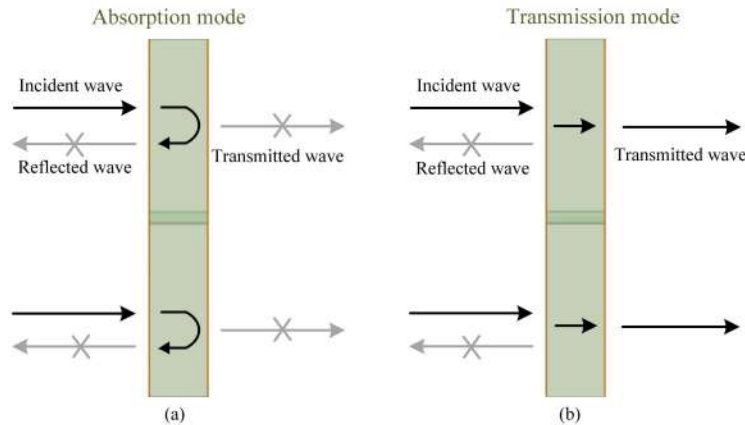


Figure 2.1: Schematic diagram of the proposed RFSS structure under different working states.

The RFSS is designed to achieve two distinct EM responses, such as absorption and transmission, through bias-controlled switching of p-i-n diodes. To clearly explain the operating principle, the schematic representation of the structure under different working states is first illustrated in Figure 2.1. This figure illustrates the interaction

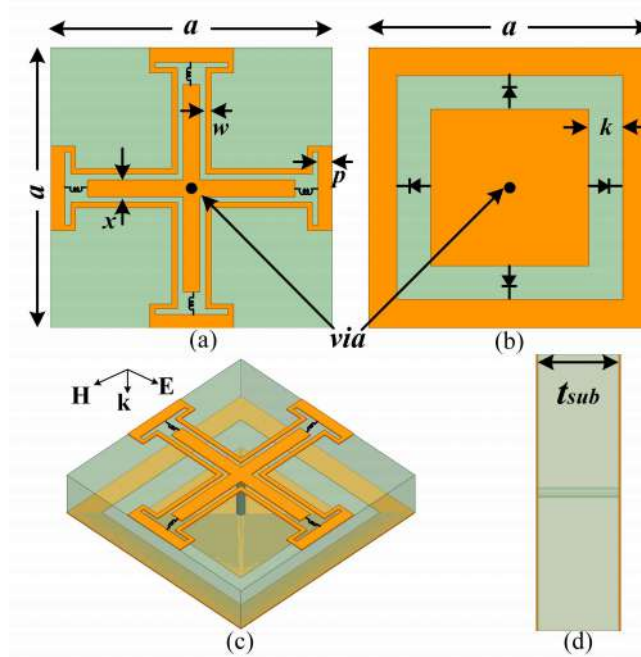


Figure 2.2: Geometry of the proposed RFSS structure: (a) top layer, (b) bottom layer, (c) isometric view, and (d) side view. The design parameters of the RFSS structure are finalized as:  $a = 10$  mm,  $w = 0.2$  mm,  $x = 0.6$  mm,  $p = 0.5$  mm,  $k = 1.2$  mm, and  $t_{\text{sub}} = 1.6$  mm.

between the incident EM wave and the RFSS in both ON and OFF conditions of the diodes. Under forward bias, the geometry provides a narrowband absorption response, whereas reverse bias results in a selective transmission band. This schematic overview establishes the conceptual basis for the subsequent structural design.

### 2.2.1 Unit Cell Geometry

Following the schematic explanation, the complete unit-cell geometry of the proposed RFSS is shown in Figure 2.2. The structure consists of two periodic metallic patterns printed on either side of an FR4 dielectric substrate ( $\epsilon_r = 4.4$ ,  $\tan \delta = 0.02$ ) of thickness 1.6 mm. The top layer incorporates a cross-dipole resonator enclosed by a Jerusalem-cross framework, where the outer region connects to adjacent unit cells to ensure periodic continuity. The bottom layer employs a square-slot topology, across which four p-i-n diodes are symmetrically placed. An embedded biasing network is implemented using a centrally located metallic via in each unit cell, enabling proper regulation of the diodes without disturbing the EM response. To prevent RF leakage into the bias lines, lumped inductors are inserted across the top-layer gaps,

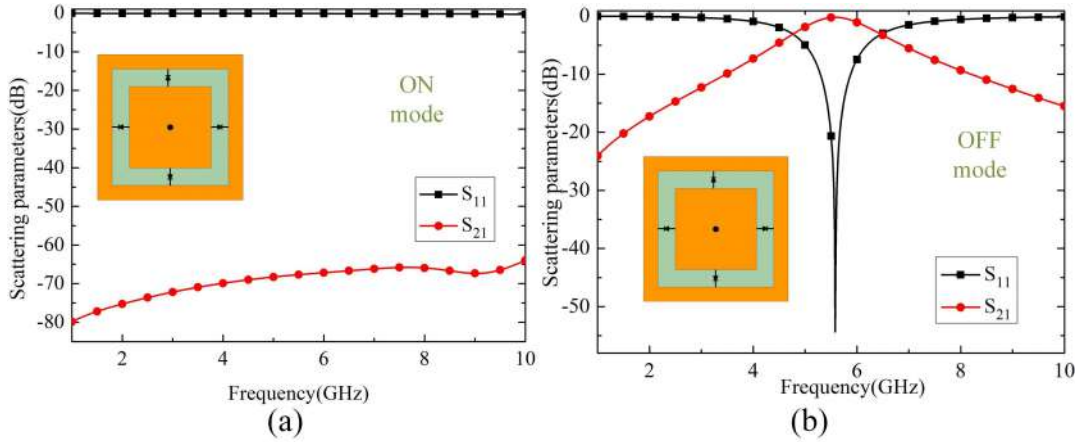


Figure 2.3: Simulated scattering responses of the bottom layer (+ dielectric) for different diode biasing conditions: (a) ON mode, and (b) OFF mode.

functioning as RF chokes. The overall configuration is compact, symmetric, and inherently suitable for polarization-insensitive operation. The optimized dimensions are mentioned in the caption of Figure 2.2.

To understand the switching behaviour governed by the diode elements, the bottom metallic pattern along with the supporting dielectric substrate is analyzed independently, as shown in Figure 2.3. This simplified configuration provides a clear insight into the diode-controlled resonance mechanism. When the diodes are forward biased, they behave as low-resistance elements, resulting in negligible capacitive coupling across the slot and producing a strong reflection response. Under reverse bias, the diodes introduce a capacitance that generates a bandpass behaviour at 5.62 GHz. This bottom-layer response serves as the basis for the transmission/reflection states in the complete RFSS.

Once the behavior of the bottom-layer slot topology is established, the top layer metallic pattern is introduced on the top side of the substrate whose bottom side is loaded with the switchable layer. The overall combination, based on the resonant behavior originating from the top layer and switching characteristic resulting from the bottom layer, helps in achieving the desired absorption/transmission switching response. The underlying concept behind this mechanism is that the absorption becomes maximum when both reflection and transmission from a structure can be minimized simultaneously. Thus, when the bottom layer behaves as a reflector (during forward biasing condition of the diodes), the transmission from the overall

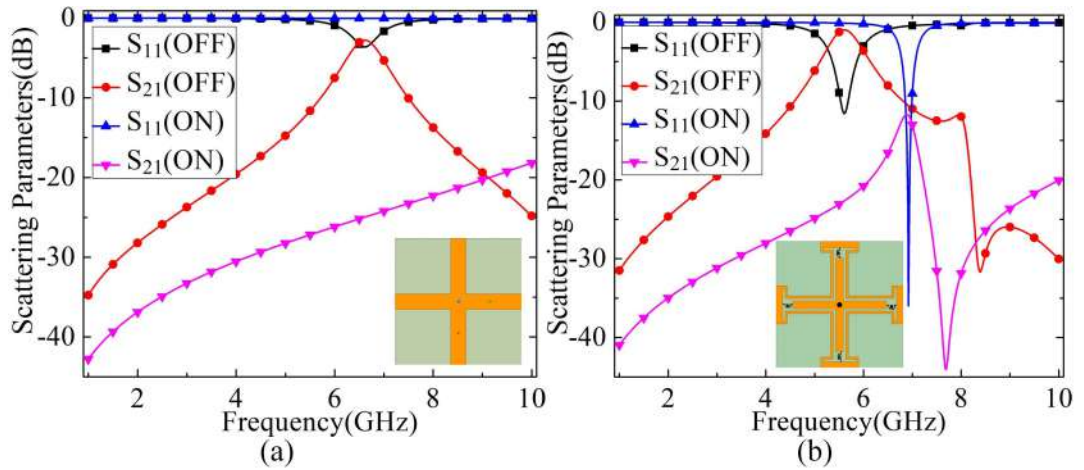


Figure 2.4: Simulated scattering parameters for different top-layer configurations: (a) simple cross-dipole, and (b) jerusalem-cross-loaded geometry.

structure is highly attenuated, while the top layer further reduces the reflection at the same frequency, thereby resulting in the absorption response. In contrast, when the bottom layer behaves as a transmitter (during reverse bias condition), then the overall configuration will combinedly allow a specific frequency band for transmission.

Initially, a simple cross-dipole resonator is used as the top layer metallic pattern, and the corresponding scattering characteristics are shown in Figure 2.4(a). Although this configuration exhibits a resonant behavior, the response predominantly consists of lossy transmission and weak reflection, and it does not generate a distinct bandstop feature. Since the absorption mechanism requires a stopband feature to be produced by the top layer, the simple cross-dipole does not provide sufficient resonance strength.

To overcome this limitation, the top-layer geometry is modified by surrounding the cross-dipole with a Jerusalem-cross structure, as illustrated in Figure 2.4(b). The additional metallic arms increase the distributed capacitance of the top layer, which results in a prominent bandstop behavior at 6.93 GHz. In the ON state, the diodes act as low-resistance elements, causing the bottom layer to function as a reflective surface. The resulting minima in both reflection and transmission at this frequency produces the narrowband absorption in the forward-biasing condition. In contrast, the diodes present a capacitive response under the OFF state, allowing the bottom layer to support a transmission band at 5.62 GHz. Since the top layer does

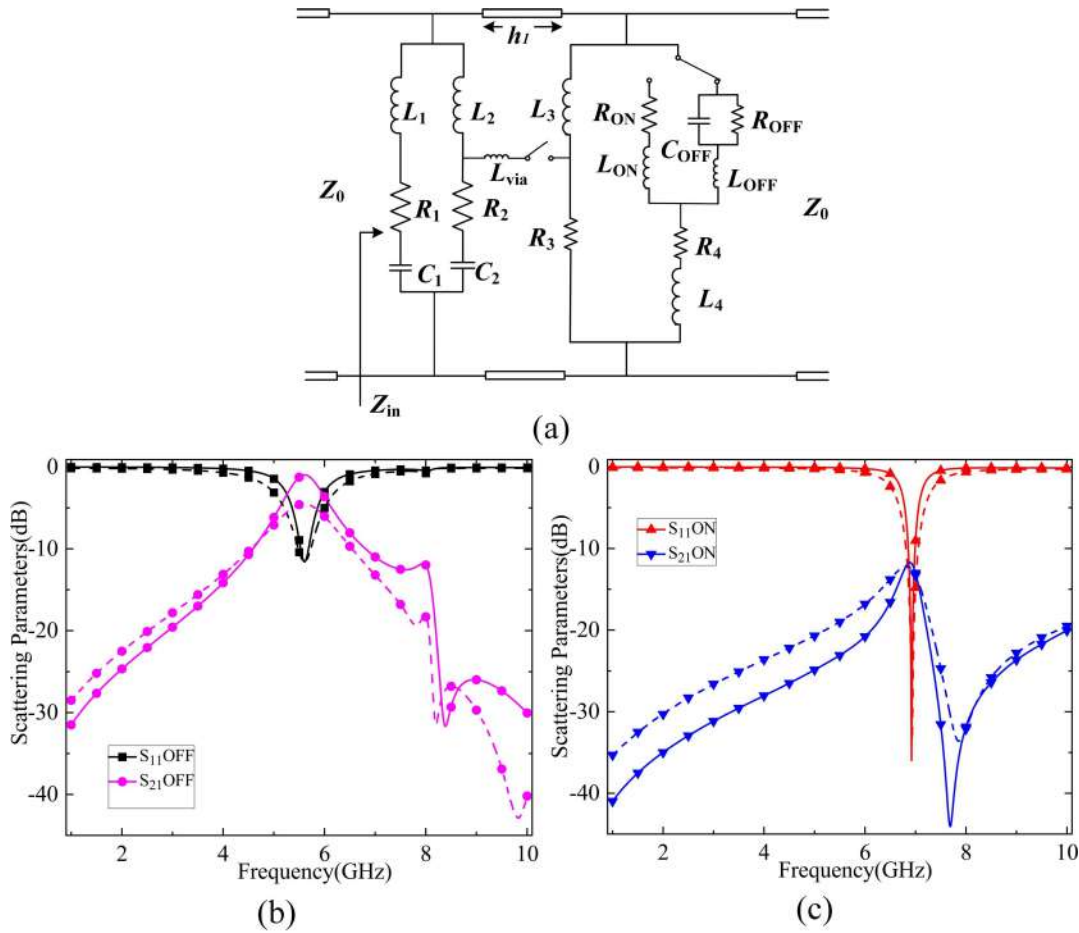


Figure 2.5: (a) Equivalent circuit of the proposed RFSS. Comparison of scattering parameters (solid and dashed lines represent plots from HFSS and ADS, respectively): (b) ON mode, and (c) OFF mode. The optimized circuit parameters:  $L_1 = 7.5$  nH,  $L_2 = 8.5$  nH,  $L_3 = 1.01$  nH,  $L_4 = 1.25$  nH,  $R_1 = 18 \Omega$ ,  $R_2 = 6 \Omega$ ,  $R_3 = R_4 = 3 \Omega$ ,  $C_1 = 55$  fF,  $C_2 = 44.5$  fF,  $L_{\text{via}} = 0.01$  nH.

not introduce any attenuation at this frequency, the overall configuration results in a high-transmission state. Thus, the optimized RFSS geometry exhibits the desired switching characteristics.

## 2.2.2 Equivalent Circuit Modeling

To further interpret the operation of the proposed structure, an equivalent circuit model (ECM) is developed and is presented in Figure 2.5(a). The top-layer metallic pattern is represented by a series-parallel combination of  $RLC$  networks, where the  $R_1-L_1-C_1$  and  $R_2-L_2-C_2$  branches correspond to the inner cross-dipole and outer Jerusalem-cross sections, respectively. The bottom-layer slot topology is modeled

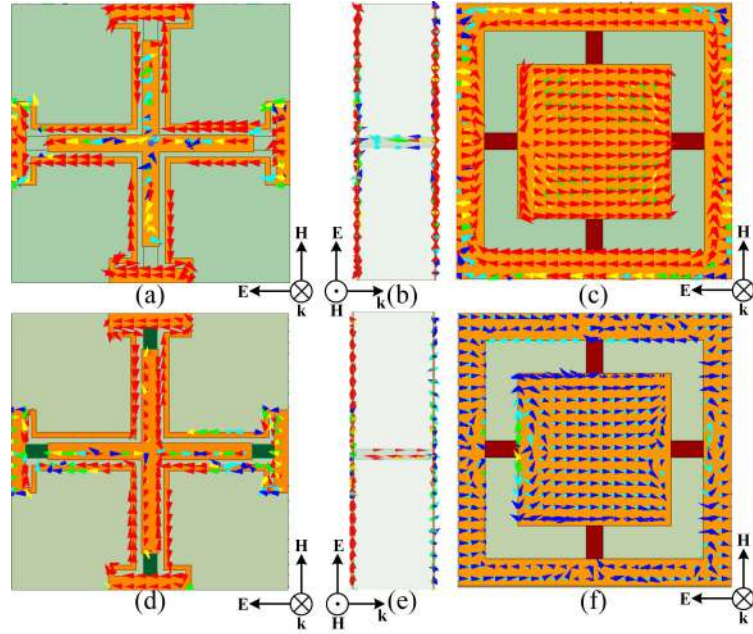


Figure 2.6: Surface current distributions of the RFSS structure: at 5.62 GHz under OFF state (a) top layer, (b) via, (c) bottom layer, and at 6.93 GHz under ON state (d) top layer, (e) via, and (f) bottom layer.

as a parallel combination of  $R_3 - L_3$  and  $R_4 - L_4$ , which are connected to the p-i-n diodes. The dielectric substrate is modeled using a transmission-line section, while the metallic via is represented by an inductive element that behaves as a short circuit under the ON state and an open circuit under the OFF state.

Based on the diode datasheet, a small resistance of  $1 \Omega$  ( $R_{\text{ON}}$ ) is assigned to the diode in the forward-biased condition, whereas a capacitance of  $0.21 \text{ pF}$  ( $C_{\text{OFF}}$ ) in parallel with a large resistance of  $1 \text{ M}\Omega$  ( $R_{\text{OFF}}$ ) is assigned in the reverse-biased condition. A small parasitic inductance of  $0.7 \text{ nH}$  ( $L_{\text{ON}} = L_{\text{OFF}}$ ) is also included in both biasing states. The distributed circuit parameter values are determined from the works in [116, 117]. The scattering parameters obtained from the ECM are calculated using Advanced Design System (ADS) and compared with the full-wave simulated responses extracted from HFSS. The comparison, shown in Figures 2.5(b) and 2.5(c) demonstrate good agreement for ON and OFF states respectively, thereby validating the accuracy of the circuit representation and confirming the physical operation of the proposed RFSS.

To better understand the operating mechanism of the proposed RFSS, the surface current distributions for both ON and OFF states are examined, as shown

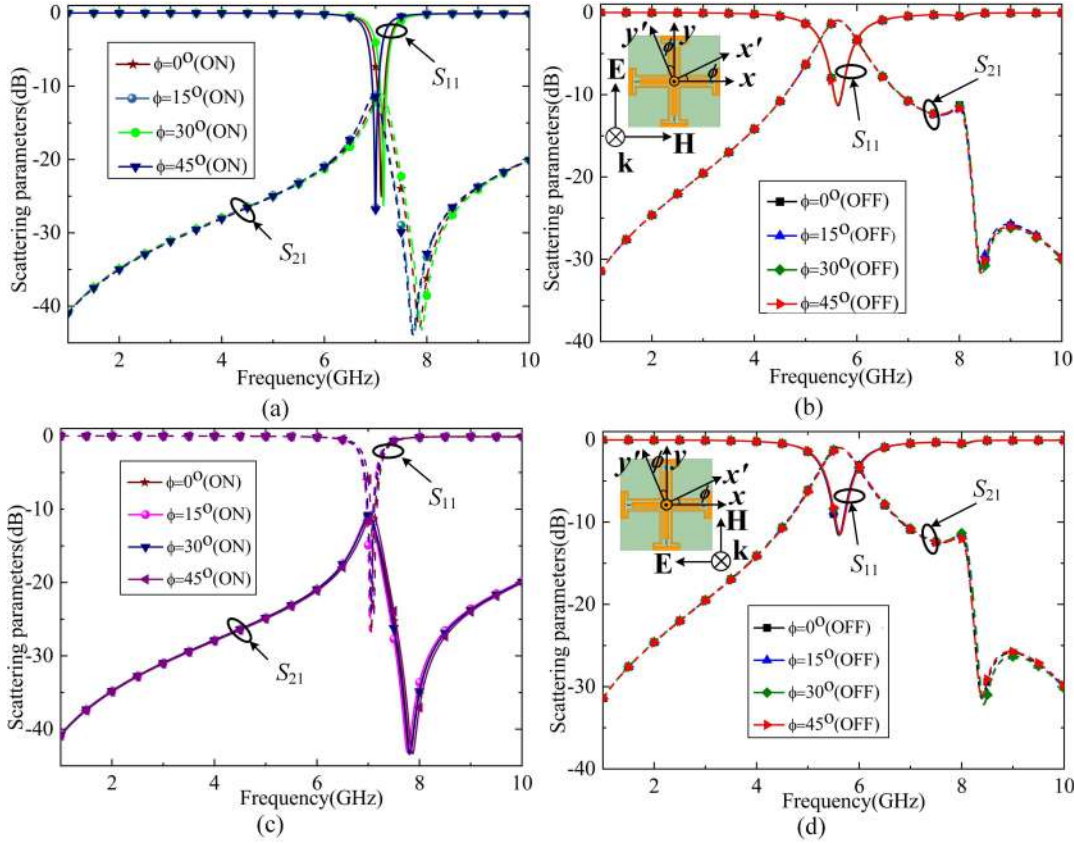


Figure 2.7: Simulated scattering parameters for different polarization angles at normal incidence. TE polarization: (a) ON mode, and (b) OFF mode. TM polarization: (c) ON mode, and (d) OFF mode.

in Figure 2.6. In the OFF state, a large portion of current is concentrated on the bottom layer, as seen in Figures 2.6(a)–(c). This confirms that the bottom layer supports a transmission band around 5.62 GHz, and energy mainly propagates through the slot region. The top layer exhibits minimal current, consistent with the high-transmission behavior observed in the scattering response.

In contrast, under the ON state, the current becomes strongly localized on the top-layer metallic pattern, as illustrated in Figures 2.6(d)–(f). The concentration of current around the cross-dipole and jerusalem-cross sections demonstrates the resonant behavior at 6.93 GHz, thereby forming the narrowband absorption. When the current path through the metallic via is observed, a strong current appears during the ON state, while it nearly disappears during the OFF state. This behavior confirms the conduction/open-circuit switching nature of the via under different diode biasing conditions. Additionally, under forward bias, a unidirectional current

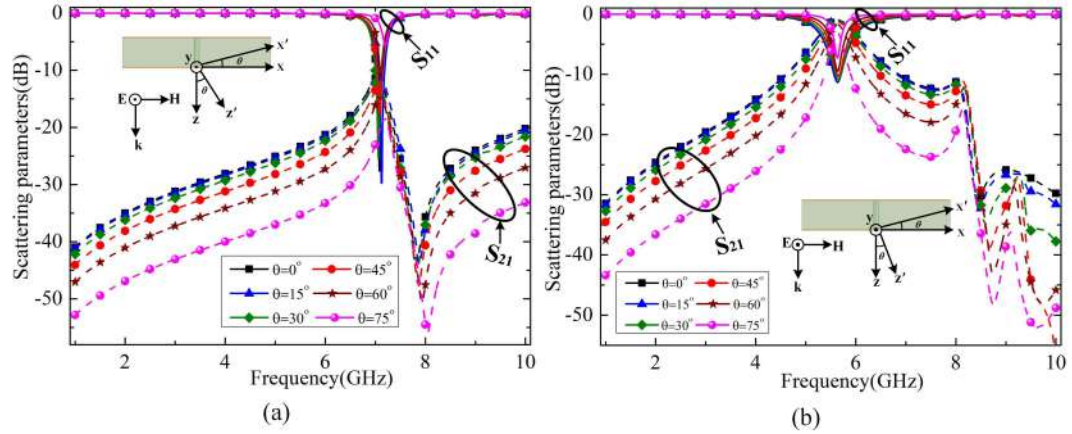


Figure 2.8: Simulated scattering parameters for different angles of incidence under TM polarization: (a) ON state, and (b) OFF state.

flows through the bottom layer and subsequently completes the loop via the metallic via into the top layer, reinforcing the resonant absorption mechanism.

### 2.2.3 Polarization-Insensitivity and Angular Stability

The polarization-insensitivity of the RFSS is investigated by varying the electric-field polarization angle  $\phi$  while maintaining the wave propagation direction constant. The corresponding scattering parameters during the normal incidence condition for the absorption (ON) and transmission (OFF) states are presented in Figure 2.7. The simulated results show that the structure exhibits almost identical responses for all polarization angles ranging from  $\phi = 0^\circ$  to  $45^\circ$  in both ON and OFF states. For the ON state, as the absorption peak at 6.93 GHz remains stable, and both  $S_{11}$  and  $S_{21}$  curves overlap closely for all  $\phi$  values under both TE and TM polarizations, as depicted in Figures 2.7(a) and 2.7(c), respectively. Similarly, in the OFF state, as shown in Figures 2.7(b) and 2.7(d), the transmission band at 5.62 GHz remains unaffected by the polarization rotation. These results confirm that the embedded biasing network and the symmetric top-layer geometry do not disturb the polarization-dependent current paths, and therefore the RFSS can be regarded as polarization-insensitive.

The angular stability of the RFSS is observed for oblique incidence under both TE and TM polarizations. For TM polarization, the structure maintains stable behavior for incident angles up to  $75^\circ$ , as shown in Figure 2.8. Both the absorption

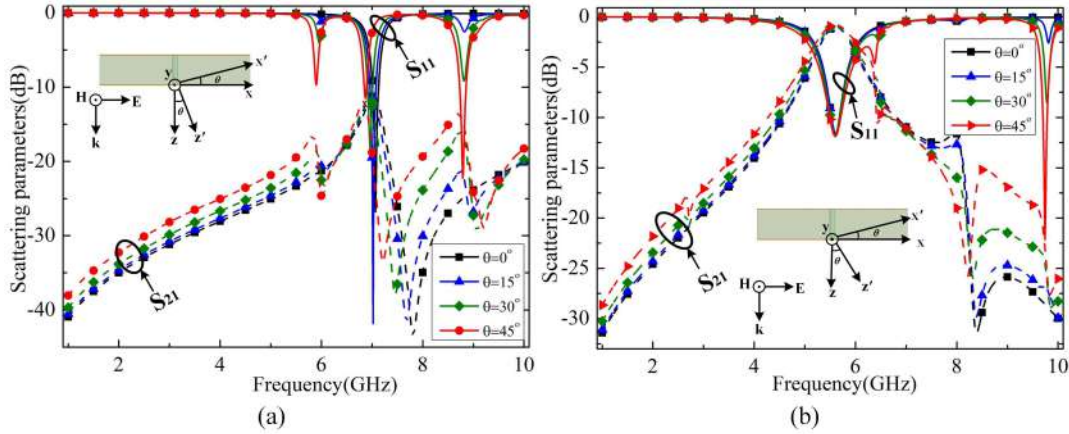


Figure 2.9: Simulated scattering parameters for different angles of incidence under TE polarization: (a) ON state, and (b) OFF state.

peak in the ON state and the transmission band in the OFF state remain nearly invariant across  $\theta = 0^\circ$  to  $75^\circ$ . This indicates that the magnetic-field alignment under TM excitation does not significantly alter the resonant paths of the structure.

For TE polarization, the responses are shown in Figure 2.9. The structure exhibits stable behavior for angles up to  $45^\circ$ . However, at higher angles, an additional resonance appears near the absorption band during the ON state. This can be attributed to increased mutual inductance introduced by the metallic via under oblique TE excitation. Although this effect can be mitigated using a multi-layer or via-less biasing circuit, such approaches increase fabrication complexity. Despite this, the RFSS still maintains stable performance for a sufficiently wide range of angles, particularly at the operating frequencies associated with the desired ON and OFF states.

## 2.3 Fabrication and Measurement

### 2.3.1 Embedded Biasing Circuitry

A diode-based RFSS structure requires appropriate biasing circuitry to enable independent operation of the diodes within the geometry. The bias lines must be carefully designed such that no interference occurs in the EM operation, while ensuring that the DC voltage is properly applied across the electronic components. To remotely regulate the p-i-n diodes integrated in the bottom metallic layer, an addi-

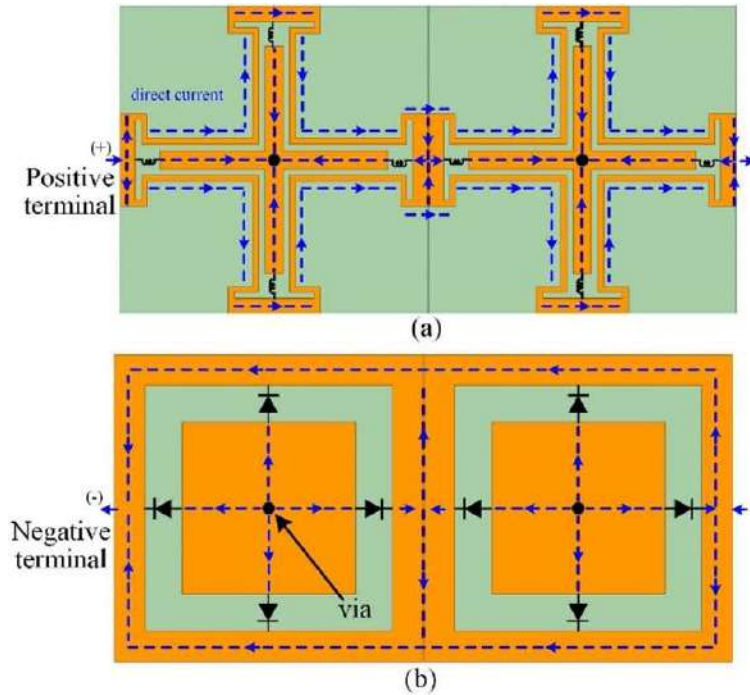


Figure 2.10: Schematic diagram of the biasing network in the proposed RFSS: (a) top layer, and (b) bottom layer.

tional biasing mechanism is required. In many conventional RFSS designs, external bias lines or surface-mounted bias networks deteriorate the EM response by introducing undesired current leakage and parasitic radiation. To avoid these issues, a parallel embedded biasing technique is often preferred over a serial biasing method, as it allows for lower voltage supply, reduced ohmic losses, and a faster switching response. A schematic diagram illustrating two unit cells arranged in a single row is shown in Figure 2.10. When the positive and negative terminals of a DC voltage source are connected to the top and bottom metallic layers, respectively, the current in the top layer flows toward the metallic via through the outer Jerusalem-crossing ring, the lumped inductors, and the inner cross-dipole arms. The metallic via then carries the current to the bottom layer, where it is routed through the p-i-n diodes and finally reaches the negative terminal of the source. By regulating the external voltage, the diodes can be switched between the ON and OFF states, thereby enabling the required reconfigurable EM operation.

To prevent RF leakage through the biasing paths, lumped inductors of 4.3 nH are placed at appropriate locations along the top-layer bias line. These inductors act as RF chokes and ensure that the bias network does not interfere with the operational

frequencies of the RFSS. Since the entire biasing arrangement is embedded inside the geometry, the presence of electronically controlled components produces negligible perturbation in the overall EM behavior of the structure.

### **2.3.2 Fabrication of the RFSS Prototype**

After finalizing the biasing network, the RFSS prototype is fabricated using a standard printed circuit board (PCB) process using an LDK ProtoMat S104 prototyping machine, as shown in Figures 2.11(a) and 2.11(b). The structure consists of two metallic patterns printed on opposite sides of an FR4 substrate of thickness 1.6 mm. The bottom layer contains the square slot with four p-i-n diodes, whereas the top layer contains the capacitively loaded cross-dipole and outer Jerusalem-cross geometry. For diode integration, BAR-63-02V devices from Infineon Technologies are used because their ON resistance and OFF capacitance closely match the simulated parameters. The surface-mounted 4.3 nH inductors are placed on the top layer to implement the biasing network. All components are soldered using an SMD reflow process to maintain consistency and minimize parasitic variations.

To enable practical measurement in a waveguide environment, a one-dimensional sample is created by arranging 20 unit cells in two parallel rows, forming a sample strip with an overall width of 20 mm and length of 150 mm. This geometry aligns with the requirements of the PPW measurement setup and ensures proper TEM-mode propagation during testing.

### **2.3.3 PPW Measurement Setup and Experimental Results**

A PPW setup is used for the experimental characterization of the fabricated 1-D array, offering a compact and economical alternative to conventional 2-D free-space measurements. The PPW geometry is first designed and optimized using full-wave simulation, as presented in Figures 2.11(c) and 2.11(d), consisting of the aluminium PPW structure, pyramidal RF absorbers, the RFSS sample, and a VNA. This arrangement eliminates the need for horn antennas or anechoic chambers, providing reasonable accuracy with significantly reduced cost and setup complexity.

The structure consists of two metallic plates with constant separation, except at the feeding ends where tapered transitions are introduced for wideband impedance

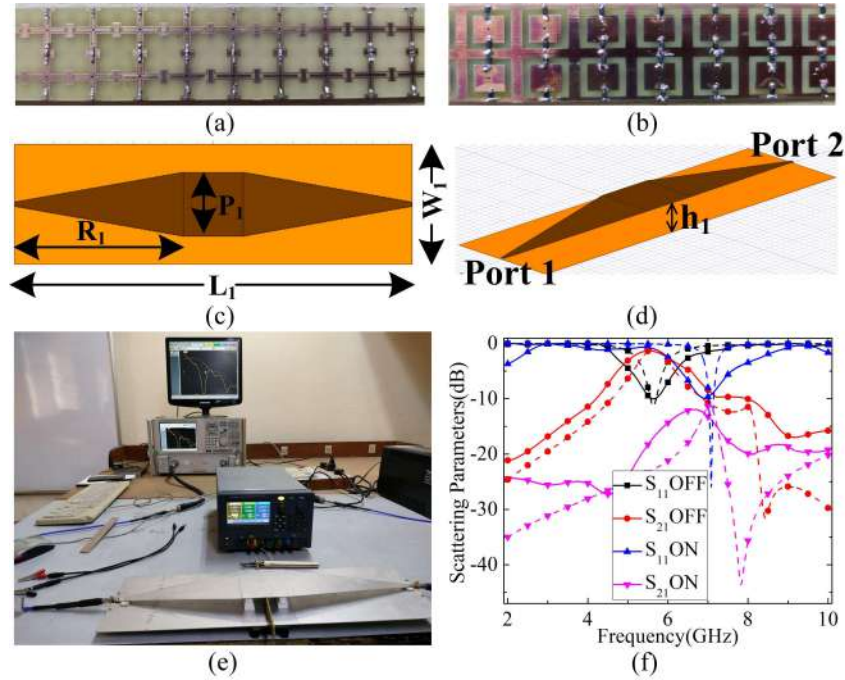


Figure 2.11: Photographs of the fabricated prototype: (a) top surface and (b) bottom surface. PPW simulation setups: (c) top view, and (d) side view. The waveguide dimensions are:  $L_1 = 500$  mm,  $W_1 = 150$  mm,  $P_1 = 80$  mm,  $R_1 = 212.5$  mm, and  $h_1 = 20$  mm. (e) Measurement setup photograph. (f) Comparison between the measured and simulated responses of the proposed RFSS structure (solid and dashed lines represent results from the PPW setup and HFSS, respectively).

matching. This ensures minimal reflection at the ports and stable propagation characteristics across the operational band. The calibration is performed using two reference configurations: For  $S_{11}$  calibration, a copper sheet with identical dimensions to the FSS sample is placed at the center of the PPW. The measured response represents total reflection, and this trace is later subtracted from the measured reflection of the prototype to obtain the actual  $S_{11}$ . For  $S_{21}$  calibration, the copper sheet is removed, and the empty PPW is measured. The resulting transmission trace represents the baseline  $S_{21}$ , which is later used to normalize the measured transmission of the prototype. Thus, this calibration method ensures that the final extracted S-parameters represent only the EM behavior of the RFSS sample and not the inherent PPW response. The measurement setup is configured such that only the transverse electromagnetic (TEM) mode propagates inside the waveguide up to 9 GHz, while higher-order modes begin to appear beyond this frequency. Since the proposed RFSS operates below 9 GHz, the prototype placed inside the waveguide is

Table 2.1: Comparison with other RFSS Designs

References	Number of Working modes	Working Functions			Polarization-insensitive	Angular Stability	Biasing Circuitry	Unit cell thickness (in terms of $\lambda$ )	Absorptivity (%) / Insertion loss (dB)
		Absorption	Transmission	Reflection					
[6]	2	No	Yes	Yes	No	N.A.	Parallel	6.0 mm ( $\lambda/4$ )	N.A./< 1
[45]	2	Yes	No	Yes	No	N.A.	Series-Parallel	10.45 mm ( $\lambda/4$ )	95.00/1.1
[74]	2	Yes	Yes	No	No	N.A.	Series-Parallel	1.6 mm ( $\lambda/20$ )	94.50/0.6
[86]	2	Yes	No	Yes	Yes	$\leq 45^\circ$	Series-Parallel	9.0 mm ( $\lambda/5$ )	93.69/N.A.
[94]	3	Yes	Yes	Yes	No	$\leq 45^\circ$	Parallel	1.0 mm ( $\lambda/25$ )	94.00/2.36, 2.76
<b>This Work</b>	<b>2</b>	<b>Yes</b>	<b>Yes</b>	<b>No</b>	<b>Yes</b>	<b><math>\leq 60^\circ</math></b>	<b>Embedded</b>	<b>1.6 mm (<math>\lambda/35</math>)</b>	<b>93.51/0.96</b>

Note: N.A. Not available;  $\lambda$ : Wavelength corresponding to lowest operating frequency.

characterized exclusively for TEM-mode propagation, thereby ensuring consistency with the conditions assumed in the full-wave simulation analysis.

The complete measurement setup is shown in Figure 2.11(e). A vector network analyzer (Anritsu S820E) is used to record the scattering parameters. For the measurements, Port 1 of the VNA is connected to Port 1 of the PPW, and Port 2 of the VNA is connected to Port 2 of the PPW. The reflection coefficient  $S_{11}$  is measured at Port 1, while the transmission coefficient  $S_{21}$  is measured between Ports 1 and 2. For the reconfigurable design, an external DC supply is used to bias the p-i-n diodes. Under forward bias, a small voltage is applied to achieve low-resistance conduction, enabling the absorption mode. Under reverse bias, no voltage is applied, and the diodes exhibit high impedance, enabling the transmission mode.

Under forward bias (ON state), a narrowband absorption response is observed around 6.23 GHz, which aligns well with the simulated absorption band. Under reverse bias (OFF state), a bandpass response is obtained at 5.98 GHz with low insertion loss. The measured scattering parameters closely match the PPW-simulated results, with a frequency deviation of only  $\pm 0.2$  GHz, as shown in Figure 2.11(f). This deviation is primarily attributed to fabrication tolerances, finite sample size, and parasitic effects of the lumped components. These results confirm the effectiveness of the embedded biasing method and demonstrate the suitability of the PPW-based characterization setup for measuring reconfigurable FSS structures.

## 2.4 Conclusion

This chapter presents a polarization-insensitive absorptive and transmissive RFSS realized on a single dielectric layer with an embedded biasing network. By integrat-

ing p-i-n diodes within a square-slot topology, the structure successfully achieves two distinct electromagnetic behaviours. In the diode ON state, the geometry behaves as a narrowband absorber with near-unity absorptivity, while in the OFF state, it exhibits a bandpass transmission response with low insertion loss. The embedded biasing arrangement ensures proper diode regulation without introducing parasitic paths, which helps maintain the stability under different angles of polarization and incidence. In addition to this, the electric field and surface current distribution plots clearly demonstrate how the structure supports absorption and transmission in the two switching conditions.

The equivalent circuit model provides a clear understanding of the switching mechanism and validates the operating principles observed in full-wave simulations. The fabricated prototype is evaluated using the PPW measurement technique, where the measured results closely match the simulated responses and confirm the dual-mode performance. A comparison table is also presented with the existing literature, highlighting the improvements achieved in the proposed design in terms of functionality, simplicity, and polarization stability, as shown in Table 2.1. Overall, the structure establishes a simple yet effective switching methodology that forms the foundation for more advanced multifunctional designs involving additional diode combinations, tunable elements, and wideband operation, which are addressed in the subsequent chapters of this thesis.



# Chapter 3

## Polarization-Insensitive Narrowband Multifunctional RFSS with FPGA Control

### 3.1 Introduction

The previous chapter establishes the fundamental switching mechanism of RFSS structures, switching between two states by using a single set of p-i-n diodes mounted in each unit cell. The design achieves narrowband absorption and transmission responses while maintaining polarization insensitivity and a compact single-layer profile. Although this dual-mode behavior provides the foundational understanding of electronically controlled switching operation in RFSS structures, the functionality remains limited to two states, and the biasing process relies on manual control. This restricts its applicability in practical EM environments that require multiple operating modes with an autonomous real-time control.

To address these limitations and extend the scope of the previous design, this chapter develops an advanced switching framework by integrating two independently controlled sets of p-i-n diodes in a single-layer RFSS geometry. By strategically placing diode sets on the top and bottom layers, the structure generates four different combinations (OFF-OFF, OFF-ON, ON-OFF, ON-ON), among which three combinations produce distinct EM functionalities such as absorption, transmission, and reflection. This progression represents an extension of the previous chapter,

allowing for the support of multifunctional operations without increasing the structural complexity or footprint. These multifunctional responses are useful for various applications such as adaptive radomes, electromagnetic interference mitigation, and frequency-selective filtering in wireless communication environments. The narrowband absorption can support detector-based microwave systems where the incident energy at a particular frequency needs to be efficiently absorbed, whereas narrowband transmission enables controlled propagation of desired frequency channels while suppressing unwanted signals. The reflective states can further enhance electromagnetic shielding and signal rejection.

A key advancement introduced in this chapter is the use of a field-programmable gate array (FPGA)-based control system that automatically regulates diode states. Instead of manual biasing, digital control signals from the FPGA determine the ON and OFF conditions of each diode set. This real-time programmability allows the structure to switch between operating modes rapidly and reliably, enabling deployment in dynamic EM environments such as intelligent radomes, adaptive shielding platforms, and sensing-assisted microwave systems. The FPGA-based switching also eliminates human dependency and ensures precise and repeatable biasing control, which is essential for stable multifunctional behavior.

In addition to the switching improvements, the RFSS geometry in this chapter is engineered to maintain polarization-insensitivity and consistent performance under oblique incidence. A parallel biasing network embedded within the metallic layers ensures independent control of both diode sets without introducing external biasing paths. The design is supported by an equivalent circuit model that explains the role of each layer and diode state in shaping the EM response. The structure is additionally validated using a PPW setup.

The remaining sections of this chapter describe the complete development of the multifunctional RFSS. The design and analysis section explains the unit cell configuration, metallic pattern arrangement, diode placement, and switching mechanism with circuit based interpretation. This is followed by the fabrication and hardware integration section, where the FPGA control system and embedded biasing network are detailed. The chapter concludes with experimental validation using the PPW setup and a comparison between simulated and measured responses, demonstrating

that the proposed design achieves reliable absorption, transmission, and reflection states with automatic real time control.

## 3.2 Design and Analysis

The fundamental idea of the proposed multifunctional RFSS can be understood from the schematic illustration shown in Figure 3.1. The diagram represents the overall framework in which the incident wave interacts with the patterned metallic structure, and the resulting EM behavior is regulated electronically. The RFSS is biased through an embedded parallel biasing network and is driven externally using an FPGA platform, enabling real-time switching between different EM functionalities. The schematic does not focus on individual bias-dependent outcomes; instead, it emphasizes the broader concept that the RFSS behaves as a programmable surface whose transmission, reflection, or absorption characteristic can be modified through electronic reconfiguration. The FPGA-enabled control allows the surface to operate dynamically under different scenarios, thereby offering multifunctionality in a compact and single-layer configuration. This conceptual representation establishes the foundation for the subsequent geometric design and provides an intuitive understanding of the electronically switchable behavior of the proposed structure.

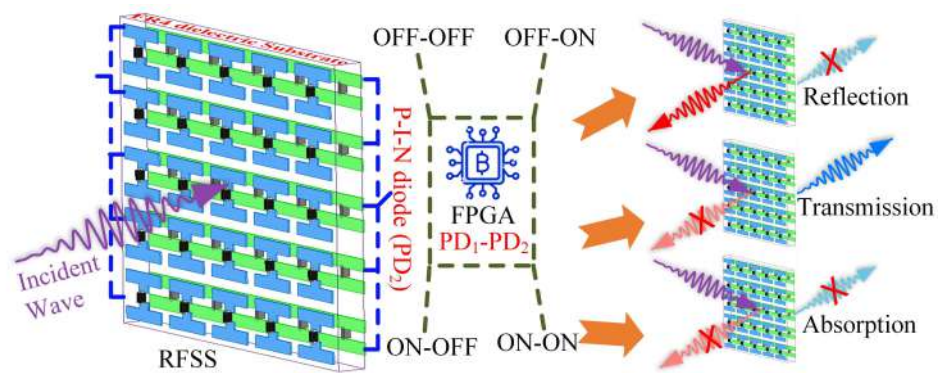


Figure 3.1: Schematic diagram of the proposed RFSS structure under different working states.

### 3.2.1 Unit Cell Geometry

Based on the conceptual analysis, the unit cell geometry is designed and presented in Figure 3.2. The top layer is made of a meander line segment connected to an inner

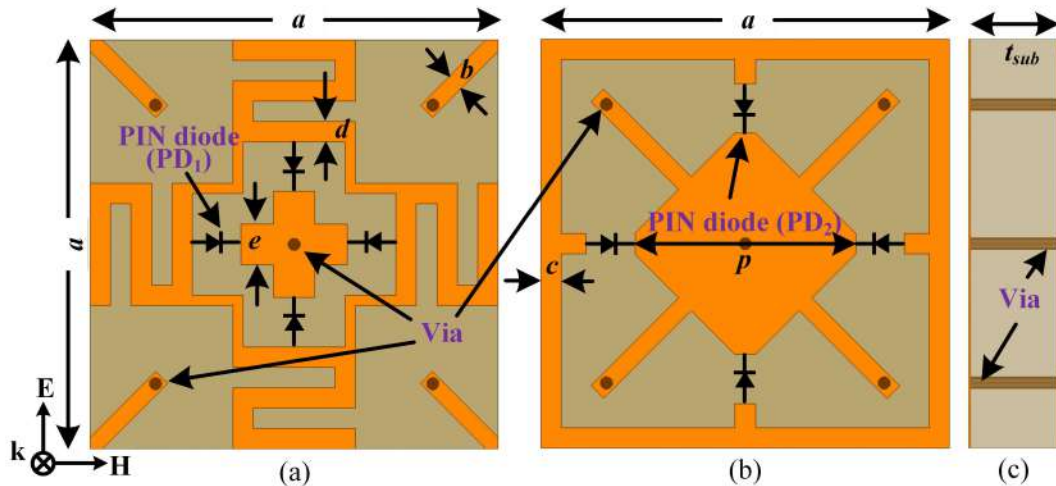


Figure 3.2: Geometry of the proposed RFSS structure: (a) top layer, (b) bottom layer, and (c) side view. The dimensions are:  $a = 10$  mm,  $b = 0.35$  mm,  $c = d = 0.5$  mm,  $e = 1$  mm,  $p = 5.4$  mm, and  $t_{\text{sub}} = 1.6$  mm.

cross-dipole through p-i-n diodes ( $\text{PD}_1$ ). The bottom layer consists of an outer square loop and a  $45^\circ$  rotated inner square patch, integrated with another set of p-i-n diodes ( $\text{PD}_2$ ). To facilitate biasing, four shared metallic lines are incorporated into both layers and connected through metallic vias across the substrate. FR4 is used as the constituent dielectric with  $\epsilon_r = 4.4$  and  $\tan \delta = 0.02$ . Two different diode models are used in the simulation:  $\text{PD}_1$  has an equivalent resistance ( $R_{\text{ON}}$ ) of  $3 \Omega$  in the forward bias and a capacitance ( $C_{\text{OFF}}$ ) of  $0.15$  pF in the reverse bias, along with a series inductance ( $L_{\text{ON}} = L_{\text{OFF}}$ ) of  $0.6$  nH in both states. The corresponding values for  $\text{PD}_2$  are  $0.56 \Omega$ ,  $0.4$  pF, and  $0.6$  nH, respectively. The geometrical dimensions of the unit cell are presented in the caption of Figure 3.2.

### 3.2.2 Simulated Responses

To understand the diode-controlled switching mechanism, the bottom metallic pattern is analyzed independently together with the supporting dielectric substrate. This approach illustrates the effects of the bottom-layer resonant structure, and explains the behavior of the  $\text{PD}_2$  diode states that govern the bandpass and reflective responses. In the reverse-biased condition, the diodes introduce a small junction capacitance ( $C_{\text{OFF1}}$ ), causing the inner rotated patch and the outer loop to form a parallel  $LC$  resonant circuit. This parallel  $RLC$  configuration results in a dis-

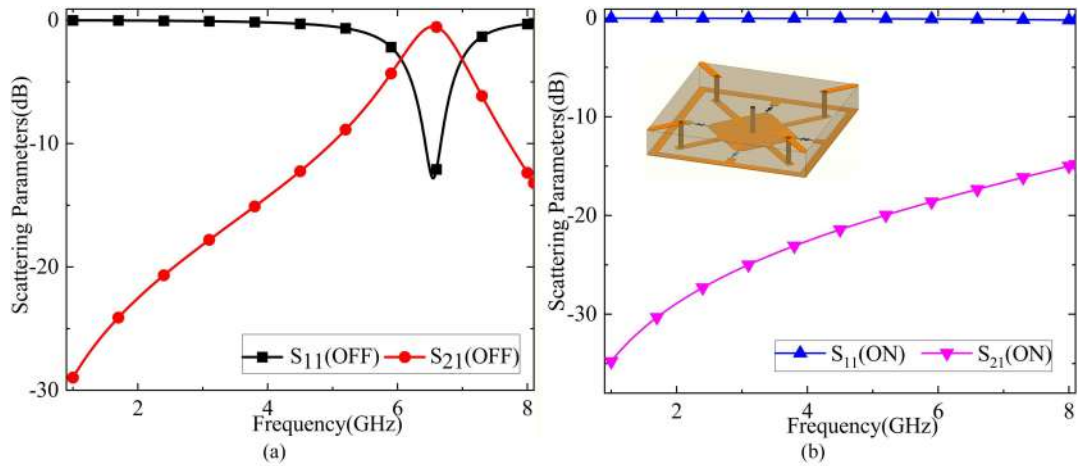


Figure 3.3: Simulated scattering responses of the bottom layer (+ dielectric) for different diode biasing conditions: (a) OFF mode, and (b) ON mode.

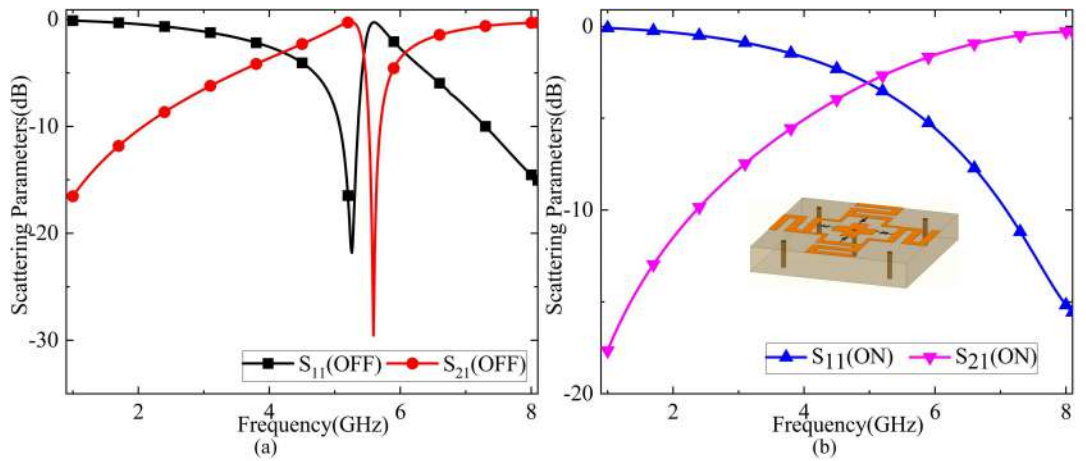


Figure 3.4: Simulated scattering parameters of the top layer (+ dielectric) for different diode biasing conditions: (a) OFF mode, and (b) ON mode.

tinct bandpass behavior centered around 6.5 GHz along an insertion loss of about 0.5 dB, as observed in Figure 3.3(a). The capacitive coupling across the diode gaps is responsible for generating this resonance, enabling selective transmission while suppressing unwanted frequency components. When forward biased, PD<sub>2</sub> behaves as a low-resistance element ( $R_{ON1}$ ) with a small series inductance ( $L_{ON1}$ ), effectively short-circuiting the inner patch to the outer loop. Under this condition, the bottom layer becomes almost a continuous conductive surface, thereby acting as an adaptive ground plane that reflects incident EM wave over a broad frequency range, as shown in Figure 3.3(b).

After establishing the behavior of the bottom layer, the top metallic pattern is analyzed independently to determine the operation of the PD<sub>1</sub> diode. The top surface consists of a combination of a meander line, a cross-dipole resonator, and interconnecting metallic strips. The meander line contributes significant series inductance ( $L_1$ ) and creates multiple current pathways, while the cross-dipole provides capacitive loading ( $C_1$ ) necessary for shaping the resonant behavior. When PD<sub>1</sub> is in the reverse-biased, the diode capacitance ( $C_{\text{OFF}}$ ) isolates the meander line from the central cross-dipole, forming a hybrid series-parallel  $LC$  network. This configuration exhibits two distinct resonances: a bandpass response near 5.26 GHz and a bandstop response near 5.59 GHz, as shown in Figure 3.4(a). The combination of these resonances is crucial for producing selective behavior in the transmission and absorption modes.

When PD<sub>1</sub> is forward biased, the diodes provide a conductive path of low resistance ( $R_{\text{ON}}$ ) and small inductance ( $L_{\text{ON}}$ ), connecting the outer meander sections directly to the cross-dipole. Under this condition, the overall structure behaves like a high-pass filter, reflecting low frequencies while allowing higher frequencies to propagate, as presented in Figure 3.4(b). This behavior contributes significantly towards the reflection modes.

When both top-layer and bottom-layer metallic patterns are simultaneously analyzed in the proposed geometry, the switching characteristic of each layer (ON and OFF state) is coupled with the other layer, thereby producing four different combinations (OFF-OFF, OFF-ON, ON-OFF, and ON-ON), triggering multifunctional EM responses, as depicted in Fig. 3.5. When the diode in the bottom layer (PD<sub>2</sub>) is forward biased, the metallic pattern behaves as an adaptive ground plane. In this condition, the RFSS operates in either the OFF-ON or ON-ON modes. In the OFF-ON mode, the top layer exhibits bandpass and bandstop characteristics, resulting in a narrowband absorption at 5.2 GHz with an absorptivity exceeding 90%. In contrast, when PD<sub>1</sub> is in the ON state, the top layer provides a high-pass response, and therefore the ON-ON mode yields full reflection across the entire frequency band. Consequently, when PD<sub>2</sub> is set to the OFF state, the bottom layer exhibits a bandpass response. In the OFF-OFF mode, this bandpass behavior combines with the bandpass-bandstop characteristics of the top layer, producing a narrowband

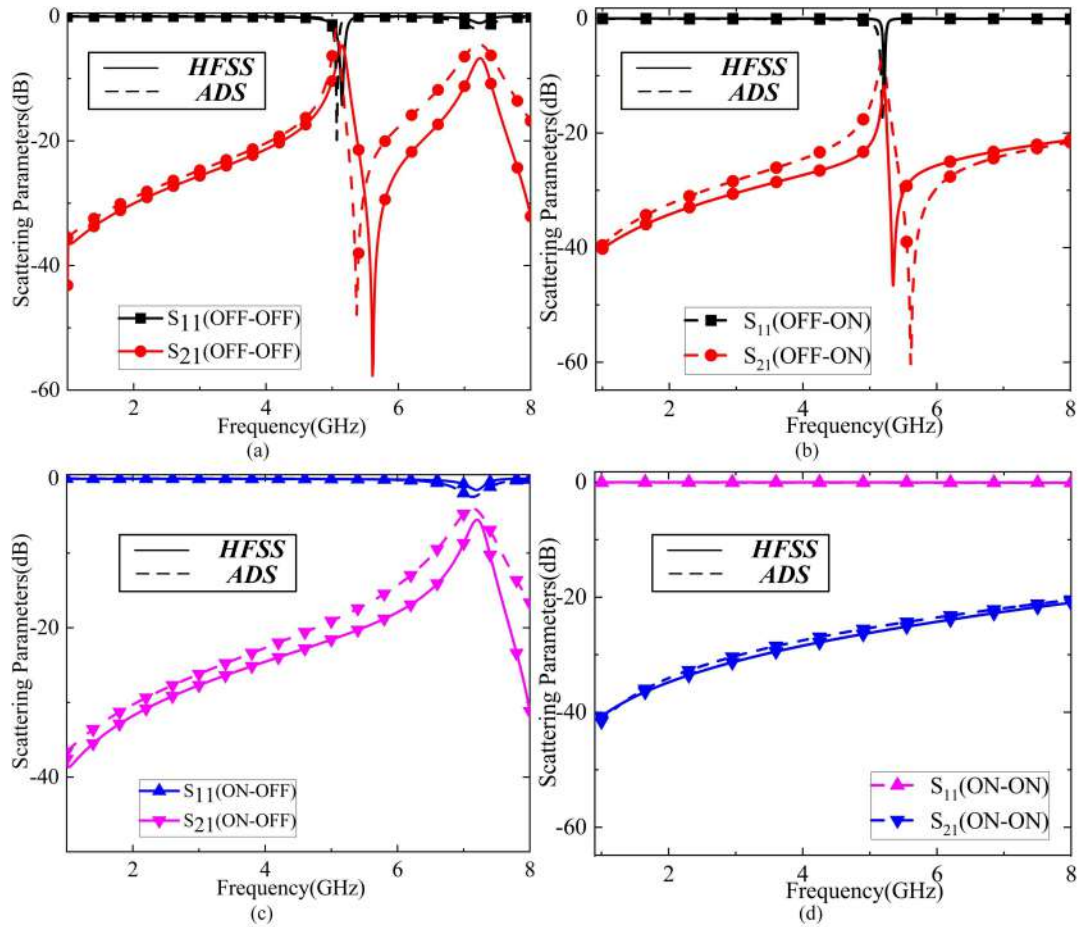


Figure 3.5: Comparison of simulated responses of the proposed RFSS geometry in HFSS and ADS software: (a) transmission mode, (b) absorption mode, (c) selective reflection mode, and (d) full reflection mode. The optimized values are:  $L_1 = 0.08$  nH,  $L_2 = 0.8$  nH,  $L_3 = 1.43$  nH,  $L_4 = 1.7$  nH,  $L_5 = 4.5$  nH,  $C_1 = 2$  pF,  $R_3 = 0.6$   $\Omega$ ,  $R_1 = R_2 = R_4 = R_5 = 0.01$   $\Omega$ .

transmission at 5.07 GHz with an insertion loss of 1.4 dB. In the ON-OFF mode, the overall response is predominantly reflective up to 6 GHz, followed by a weak bandpass feature near 7 GHz. However, this mode is considered redundant due to the presence of desirable EM operations in the other three modes.

### 3.2.3 Equivalent Circuit Modeling

The EM behavior of the proposed RFSS is further interpreted using an equivalent circuit model, illustrated in Figure 3.6. The complete unit cell is represented through a distributed  $RLC$  framework that captures the resonant interactions contributed by the metallic patterns, diode elements, and substrate. On the top layer, the

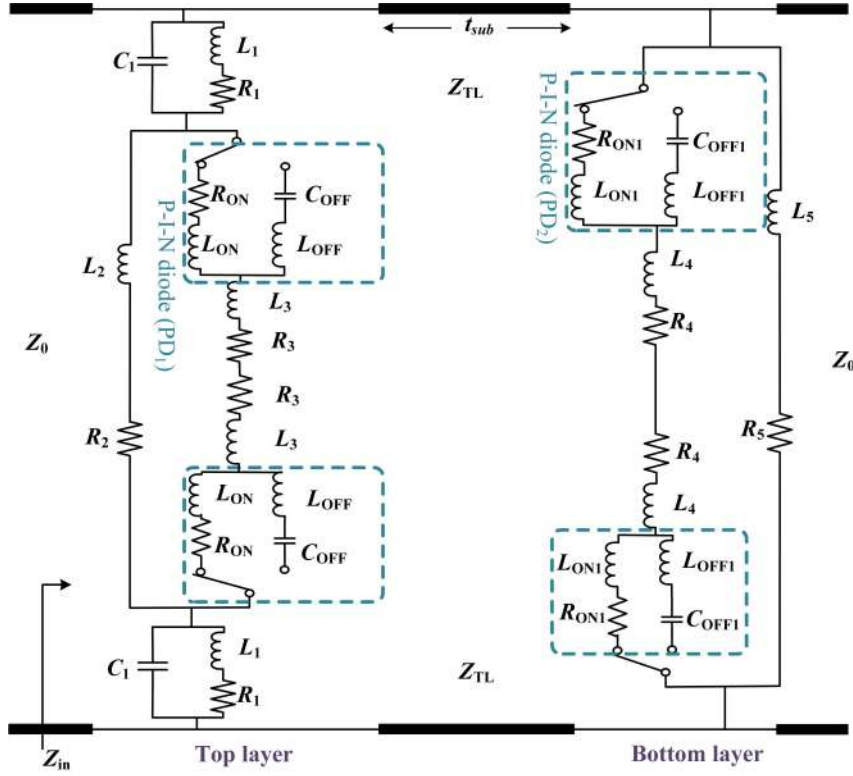


Figure 3.6: Equivalent circuit model of the proposed unit cell geometry.

meander line is modeled using a parallel combination of inductance ( $L_1$ ), capacitance ( $C_1$ ), and resistance ( $R_1$ ), while the connecting metallic strips introduce additional inductive and resistive elements ( $L_2$  and  $R_2$ ). The central cross-dipole is represented by a pair of inductance and resistance components ( $L_3$ ,  $R_3$ ), forming the dominant mid-band resonance of the upper surface. The p-i-n diode  $PD_1$  is represented by its ON-state series pair consisting of resistance and inductance ( $R_{ON}$ ,  $L_{ON}$ ) and its OFF-state equivalent pair consisting of capacitance and inductance ( $C_{OFF}$ ,  $L_{OFF}$ ), accurately reflecting its switching influence on the conduction path.

The bottom layer is modeled in a similar manner, where the rotated square patch is denoted by a series combination of inductance and resistance ( $L_6$ ,  $R_6$ ), and the surrounding loop by inductance–resistance pair ( $L_7$ ,  $R_7$ ). The metallic via contributes an inductance ( $L_5$ ) and a resistance ( $R_5$ ), while the peripheral vias are represented through another pair of inductance and resistance ( $L_4$ ,  $R_4$ ). The substrate is modeled as a transmission-line segment of characteristic impedance  $Z_{TL}$  and electrical thickness  $t_{sub}$ . This circuit arrangement effectively captures the overall impedance of diode sets and provides a circuit-level understanding for interpreting

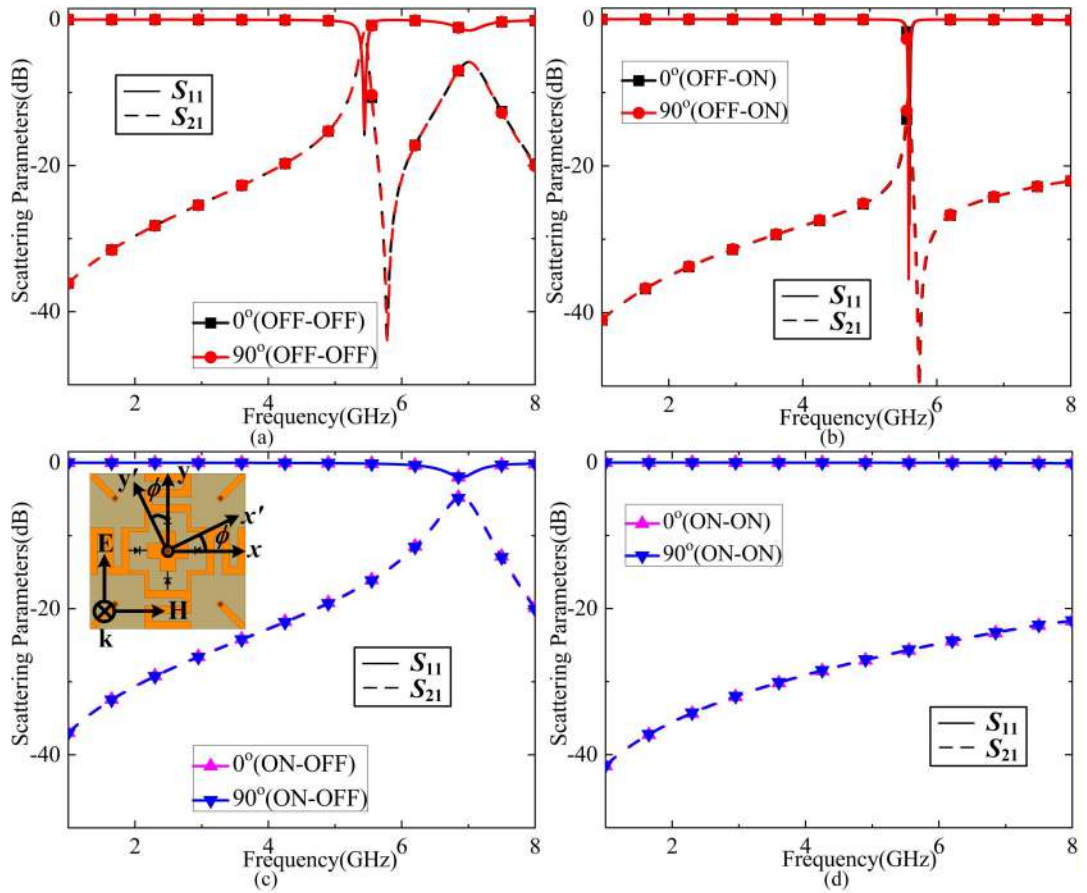


Figure 3.7: Simulated scattering parameters for orthogonal polarization angles at normal incidence: (a) transmission mode, (b) absorption mode, (c) selective reflection mode, and (d) full reflection mode.

the RFSS's multifunctional behavior.

The initial circuit parameters are derived using analytical expressions [116, 117], and the simulated responses are validated by comparing them with the numerically computed scattering parameters using Advanced Design System (ADS) software. As shown in Figure 3.5, the equivalent-circuit-based predictions and full-wave simulation results exhibit strong agreement across all diode states, confirming the accuracy of the adopted design methodology and the validity of the circuit model.

### 3.2.4 Polarization Insensitivity and Angular Stability

The RFSS exhibits polarization-independent performance owing to its four-fold symmetric topology and symmetric diode placement across the unit cell geometry. The simulations performed for orthogonal polarization angles, namely  $0^\circ$  and  $90^\circ$ , show

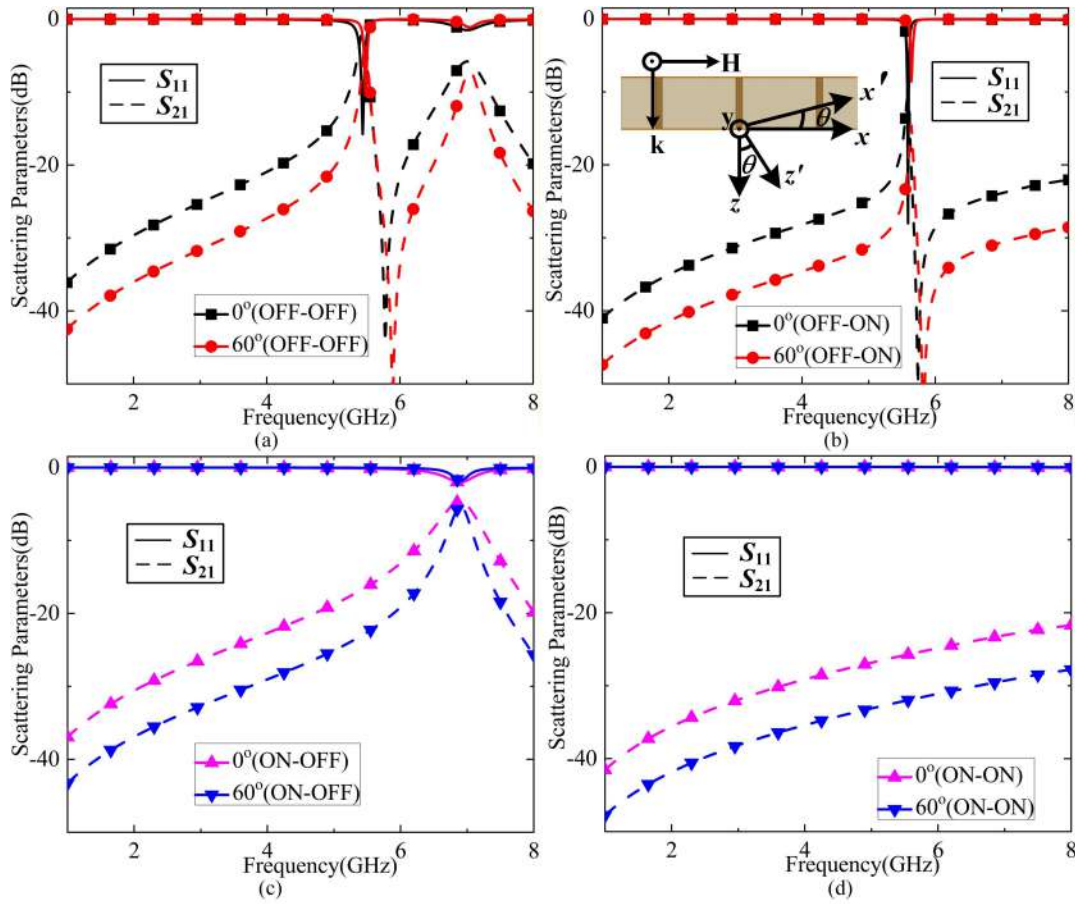


Figure 3.8: Simulated scattering parameters for different angles of incidence under TE polarization: (a) transmission mode, (b) absorption mode, (c) selective reflection mode, and (d) full reflection mode.

nearly identical resonance frequencies and scattering magnitudes for all four operational configurations. For the transmission state (OFF–OFF), the operating band near 5 GHz remains unchanged under polarization rotation, while the absorption (OFF–ON) and reflection states (ON–OFF and ON–ON) also maintain their magnitude responses with minimal deviation. The geometrical symmetry ensures that the induced surface currents follow equivalent characteristics for both orientations of the incident electric field, thereby preserving stable EM behaviour. These characteristics, illustrated in Figure 3.7, confirm that the proposed RFSS maintains its multifunctional performance irrespective of the polarization angle.

The angular robustness of the RFSS is further evaluated under both TE and TM excitations in Figures 3.8 and 3.9, respectively, for incident angles extending up to 60°. Under TE incidence, all three operation states, OFF–ON (absorption mode),

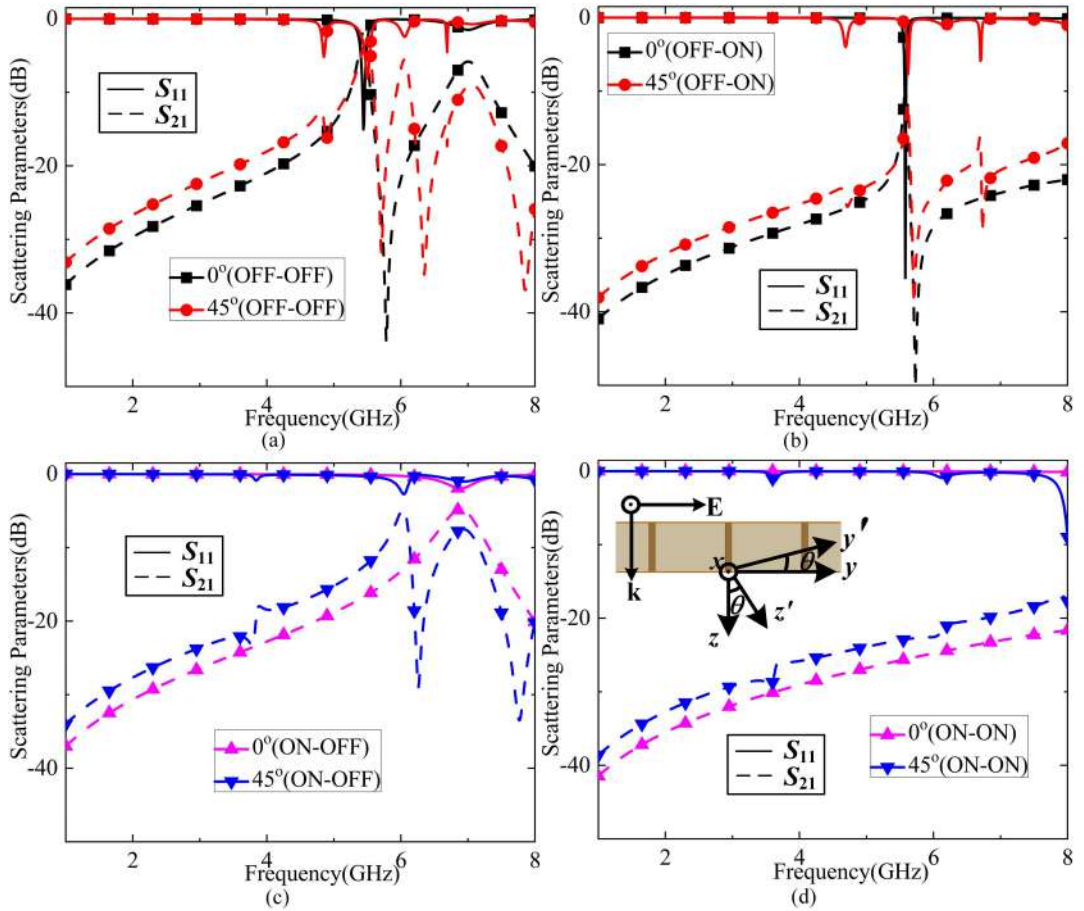


Figure 3.9: Simulated scattering parameters for different angles of incidence under TM polarization. (a) Transmission mode, (b) absorption mode, (c) selective reflection mode, and (d) full reflection mode.

ON–ON (reflection mode), and ON–OFF (reflection mode), retain their resonance positions with only negligible degradation even at  $60^\circ$ , demonstrating strong angular stability. The transmission mode (OFF–OFF) also maintains stable behavior; however, a slight frequency deviation is observed at  $60^\circ$ , attributed to enhanced EM coupling through the metallic vias. Under TM excitation, the OFF–ON (absorption mode) and ON–ON (reflection mode) remain highly stable up to  $45^\circ$ , while the OFF–OFF (transmission mode) and ON–OFF (reflection mode) configurations exhibit additional resonant peaks at higher angles, attributed to increased interaction between the obliquely incident electric field and the biasing networks that include metallic vias. These detailed TE/TM responses demonstrate that the functional frequency bands remain well preserved, validating the angular stability of the proposed RFSS geometry.

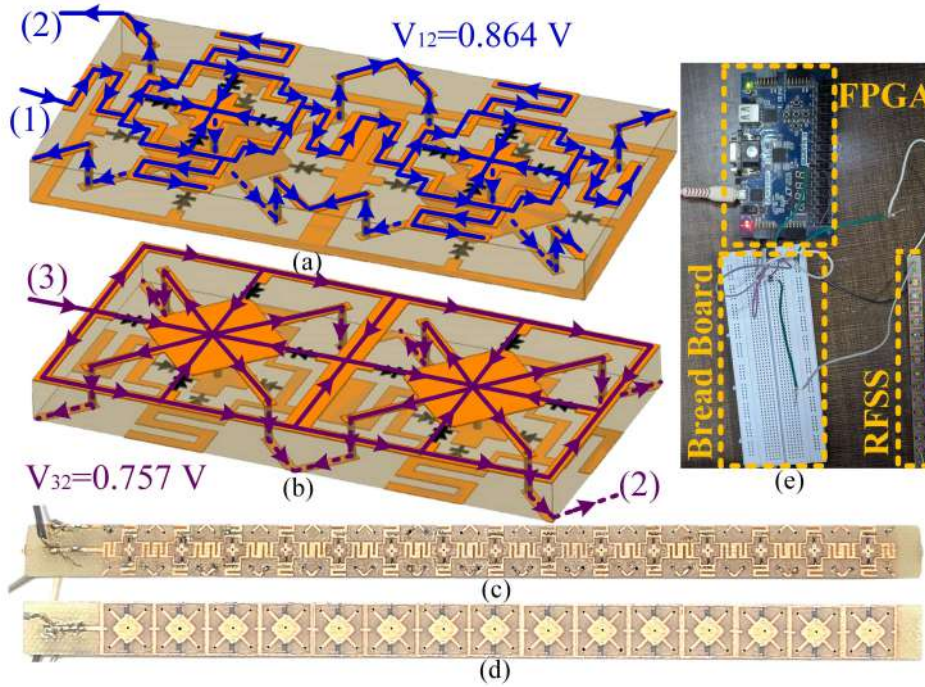


Figure 3.10: Biasing mechanism of the proposed AFSS: (a) top layer, (b) bottom layer. Fabricated prototype: (c) top layer, (d) bottom layer. (e) Integration of FPGA with the fabricated prototype to regulate the diodes ( $PD_1$  and  $PD_2$ ).

### 3.3 Fabrication and Measurement

#### 3.3.1 Biasing, Fabrication, and Hardware Integration

A diode-based RFSS structure requires appropriate biasing circuitry to enable independent operation of the diodes within the geometry. The bias lines must be carefully designed such that no interference occurs in the EM operation, while ensuring that the DC voltage is properly applied across the electronic components. A parallel biasing technique is often preferred over a serial biasing method, as it allows for lower voltage supply, reduced ohmic losses, and a faster switching response.

The proposed RFSS integrates two diode sets,  $PD_1$  and  $PD_2$ , where each set requires two terminals for DC voltage supply, resulting in a total of four terminals. To reduce complexity, one terminal (ground) is made common, reducing the total number of terminals to three for independent biasing to realize the intended multifunctional responses. As illustrated in Figures 3.10(a) and 3.10(b), terminals 1 and 3 are connected to the anode ends of the top-layer diodes ( $PD_1$ ) and bottom-

Table 3.1: Coding Sequence by FPGA for Different Operating Modes

Modes	V <sub>1</sub>	V <sub>2</sub>	V <sub>3</sub>	Modes	V <sub>1</sub>	V <sub>2</sub>	V <sub>3</sub>
OFF-OFF	0	0	0	OFF-ON	0	0	1
ON-OFF	1	0	0	ON-ON	1	0	1

*Note:* V<sub>1</sub>: Voltage at terminal 1; V<sub>2</sub>: Voltage at terminal 2; V<sub>3</sub>: Voltage at terminal 3. Digital logic depiction: 0 = Zero voltage; 1 = V<sub>12</sub> = 0.86 V and V<sub>32</sub> = 0.75 V.

layer diodes (PD<sub>2</sub>), respectively, whereas terminal 2 provides a common path to the cathode terminals of both diodes through the embedded metallic vias. The incorporation of shared metallic biasing lines ensures that adjacent unit cells receive identical DC bias levels, allowing the applied voltage to propagate uniformly across the array even when supplied from a remote location.

The current-flow patterns across the top and bottom layers under forward bias are shown in Figures 3.10(a) and 3.10(b), confirming that the bias network efficiently distributes the supply voltage to all diode elements. As observed, the diodes are regulated through a parallel basing method, thereby requiring a minimal voltage to simultaneously regulate all the diodes while reducing the chance of measurement error due to diode malfunction. Following the bias circuit design, a one-dimensional prototype composed of 15 cascaded unit cells in a single row is fabricated on an FR4 substrate using a standard PCB etching technique. The overall dimensions of the fabricated sample are 190 × 10 mm<sup>2</sup>, and the individual metallic patterns of the respective layers are presented in Figures 3.10(c) and 3.10(d). The p-i-n diode models BAR 64-02 V [118] and BAR 65-02 V [119] from Infineon Technologies are used as PD<sub>1</sub> and PD<sub>2</sub>, respectively, ensuring consistency between simulated and hardware parameters.

Once the prototype is manufactured, an FPGA [120] is employed to apply independent forward-bias voltages to both diode sets, eliminating the need for multiple DC supplies. PD<sub>1</sub> and PD<sub>2</sub> require maximum forward biases of 0.864 V (V<sub>12</sub>) and 0.757 V (V<sub>32</sub>), respectively, while a zero-volt condition establishes the reverse-bias state. The FPGA module applies a 2-bit logic sequence across terminals 1, 2, and 3 to configure the desired diode states, as illustrated in Figure 3.10(e). Terminal 2 is maintained at a logic “0” (0 V), while logic “1” corresponds to 0.864 V at terminal 1

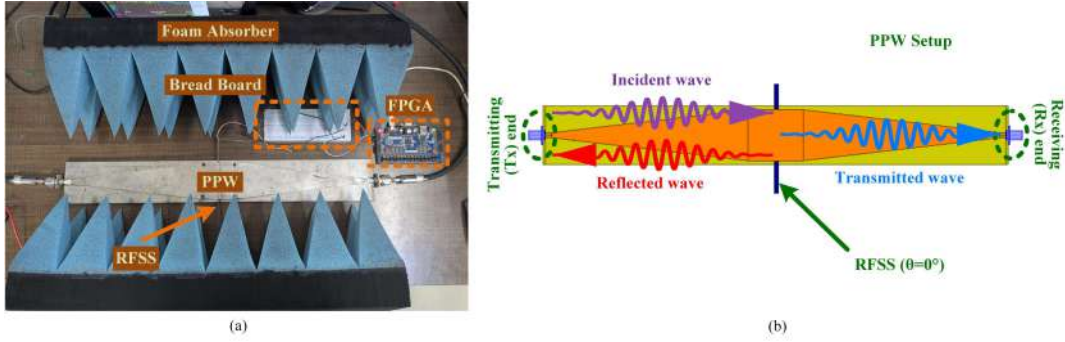


Figure 3.11: (a) Measurement setup. (b) 1-D array simulation arrangement.

and 0.757 V at terminal 3.

A consolidated summary of the applied coding scheme is provided in Table 3.1, indicating how each binary combination translates to the respective diode bias conditions. This digital control mechanism enables rapid and repeatable switching between different EM operation states, ensuring real-time reconfigurability of the RFSS during measurements.

### 3.3.2 Measurement using PPW Setup

A PPW setup is used for the experimental characterization of the fabricated 1-D array, offering a compact and economical alternative to conventional 2-D free-space measurements [121]. The complete experimental layout is shown in Figure 3.11(a), consisting of the aluminium PPW structure, pyramidal RF absorbers, the RFSS sample, the FPGA control board, and a VNA. This arrangement eliminates the need for horn antennas or anechoic chambers, providing reasonable accuracy with significantly reduced cost and setup complexity.

To ensure reliable results, a two-step calibration procedure is followed. First, the reflection ( $S_{11}$ ) reference level is established by inserting a metallic plate of identical dimensions at the centre of the PPW. Second, the transmission ( $S_{21}$ ) reference is obtained by measuring the empty PPW structure without the RFSS sample. After calibration, the fabricated RFSS array is placed inside the waveguide, and the FPGA applies the required bias voltages to activate each operation state. The calibrated S-parameters are extracted by subtracting the reference measurements from the measured data. The foam absorbers surrounding the PPW minimize edge-diffraction effects and suppress unwanted scattering, thereby improving the reliability of the

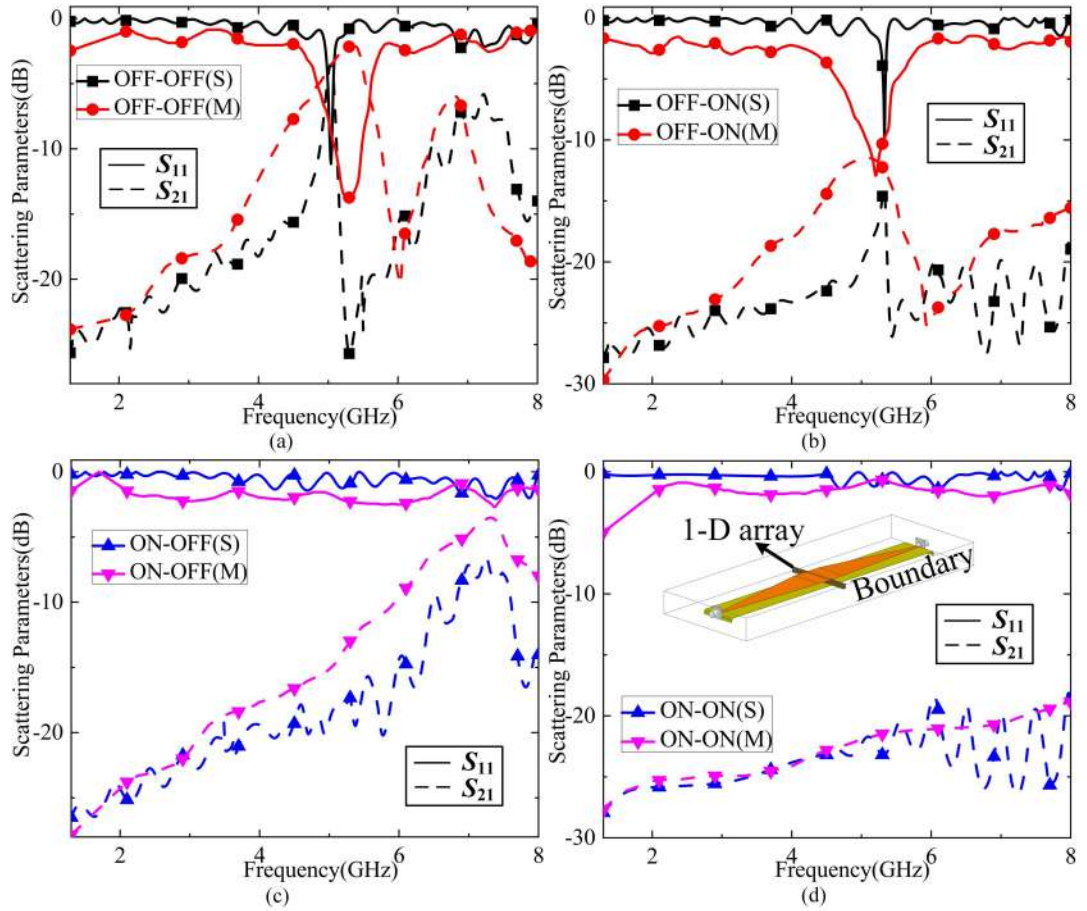


Figure 3.12: Comparison of simulated and measured data: (a) transmission mode, (b) absorption mode, (c) selective reflection mode, and (d) full reflection mode. S: Simulation, M: Measured.

measurements. A corresponding PPW simulation environment is also implemented, as depicted in Figure 3.11(b), to facilitate direct comparison between measured and simulated scattering parameters.

The fabricated prototype is evaluated under four different biasing conditions using the FPGA. In the OFF–OFF state (0–0–0 coding), a clear transmission behavior is observed, exhibiting an insertion loss of approximately 1.6 dB at 5.14 GHz. For the OFF–ON state (0–0–1), a narrowband absorption exceeding 90% is recorded at 5.06 GHz. When both diodes are forward biased (ON–ON; 1–0–1), the sample demonstrates a continuous reflective response across the entire 2–8 GHz band. Under the ON–OFF condition (1–0–0), a reflection-dominated response is observed up to 6 GHz, followed by a weak passband at higher frequencies.

All the measured results exhibit close correspondence with the simulated results

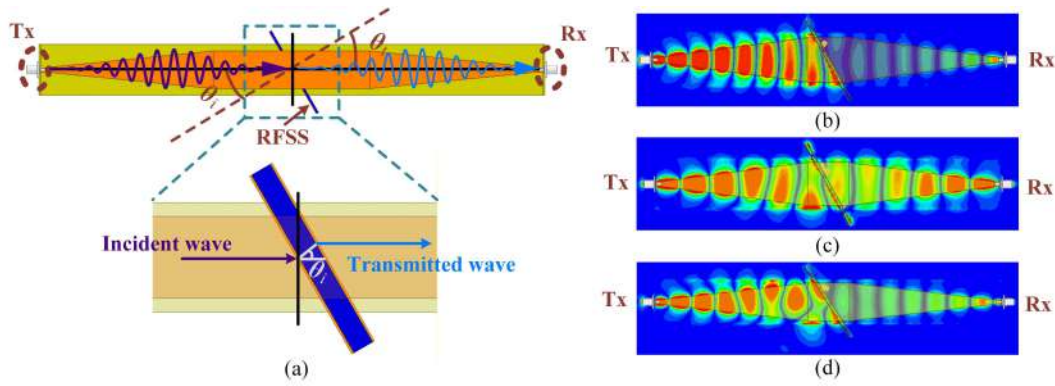


Figure 3.13: (a) Conceptual diagram showing the oblique incidence measurement in the PPW setup. Electric field distribution of the proposed metasurfaces in PPW setup: (b) absorption mode at 5.06 GHz, (c) transmission mode at 5.14 GHz, and (d) reflection mode at 5 GHz.

obtained from the PPW model, as shown in Figure 3.12. Minor discrepancies arise due to fabrication tolerances and diode parasitics, but the deviation is within the limit. Thus, the agreement confirms the accuracy of the design methodology, the reliability of the biasing network, and the effectiveness of the FPGA-integrated control scheme.

To realize oblique-incidence characterization, instead of altering the positions of the transmitting or receiving ports, the RFSS sample is tilted at the desired angle  $\theta$  [122]. The impinging wave then strikes the tilted surface at angle  $\theta$  and exits at angle  $-\theta$ , in accordance with Snell's law of refraction, thereby reaching the receiving port without deviation, as illustrated in Figure 3.13(a). By tilting the RFSS sample at different angles, the setup enables accurate characterization of  $S_{21}$  under oblique incidence in TE-mode propagation. It is noteworthy that the PPW setup can only be used for measuring the RFSS prototype under TE polarization; the setup cannot be used for TM mode characterization.

Figure 3.13(b) presents the electric-field distribution in the absorber mode (OFF–ON) at 5.06 GHz, confirming significant wave attenuation. Meanwhile, Figures 3.13(c) and 3.13(d) illustrate the corresponding E-field distribution in the transmission mode (OFF–OFF) at 5.14 GHz and the reflection mode (ON–ON) at 5.0 GHz, respectively, validating the wave propagation and suppression in the corresponding states. The  $S_{21}$  response is measured at different incident angles up to  $60^\circ$  across all four modes. As shown in Figures 3.14(a)–(d), the RFSS maintains consistent EM

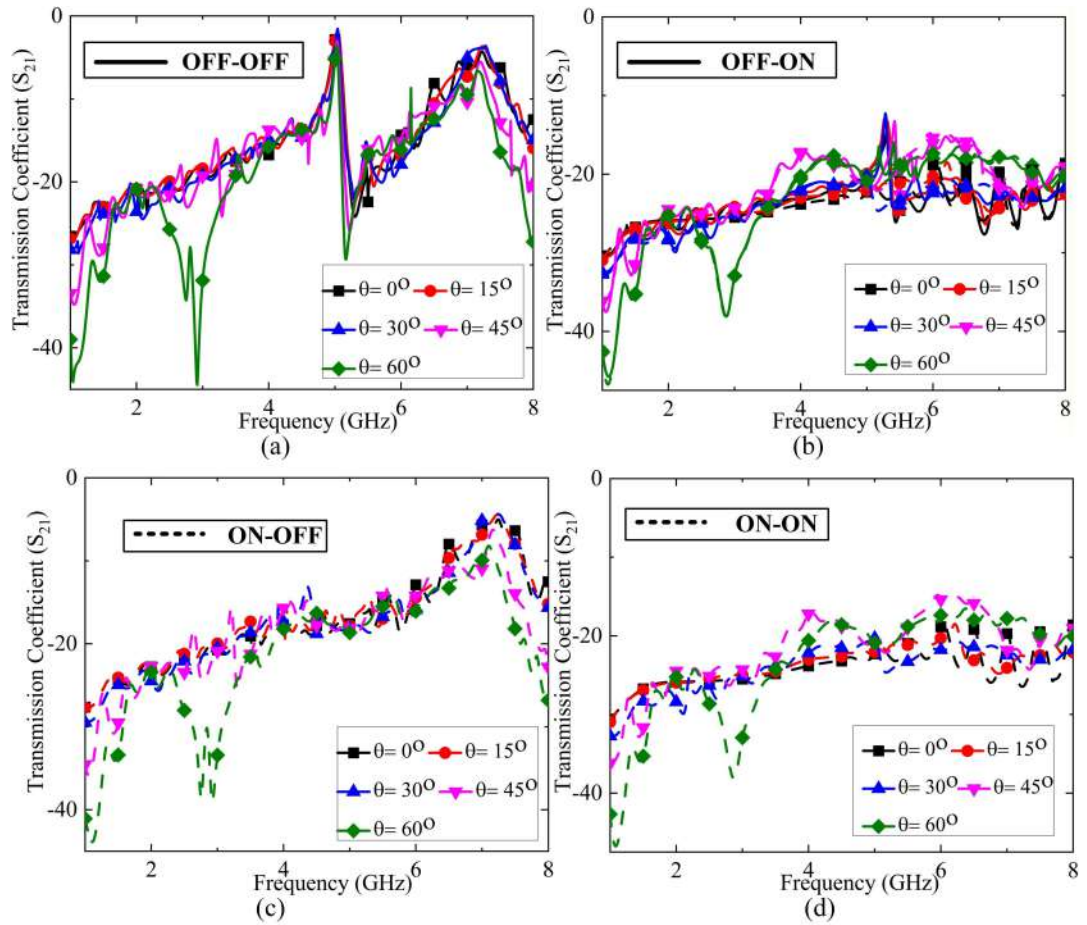


Figure 3.14: Oblique incidence responses of the proposed RFSS geometry in PPW setup: (a) transmission mode, (b) absorption mode, (c) selective reflection mode, and (d) full reflection mode.

performance under oblique incidence, demonstrating its robustness.

### 3.4 Conclusion

This chapter has presented a multifunctional RFSS that employs two independently controlled p-i-n diode sets in conjunction with an FPGA-based biasing module to realize dynamic absorption, transmission, and reflection responses within a single-layer geometry. The proposed RFSS integrates a meander-line and cross-dipole arrangement on the top layer along with a square-loop-based metallic pattern on the bottom layer, enabling four distinct diode switching states. These configurations generate multiple EM behaviours, including a narrowband transmission in the OFF-OFF mode, a near-unity absorption in the OFF-ON state, a selective reflection in

Table 3.2: Comparison with Existing Literature

Reference	Modes (A/T/R)	Polarization Insensitivity	Angular Stability	Number of Layers	Biasing Circuitry	Unit Cell Size (in terms of $\lambda$ )	Experimental Validation	Switching Control
[41]	Y/N/Y	Yes	45°	2	Serial	0.81 $\lambda$	Yes	Manual
[94]	Y/Y/Y	No	45°	1	Parallel	0.20 $\lambda$	Yes	Manual
[104]	Y/Y/N	Yes	N. R.	2	Serial	0.30 $\lambda$	Yes	Manual
[123]	Y/Y/Y	Yes	N. R.	3	N. R.	0.30 $\lambda$	No	Manual
[124]	Y/Y/Y	No	45°	1	Serial	0.36 $\lambda$	Yes	Manual
[125]	Y/Y/N	No	60°	2	N. A.	0.29 $\lambda$	No	Manual
<b>Proposed</b>	<b>Y/Y/Y</b>	<b>Yes</b>	<b>60°</b>	<b>1</b>	<b>Parallel</b>	<b>0.17<math>\lambda</math></b>	<b>Yes</b>	<b>FPGA</b>

*Note:*  $\lambda$  denotes the wavelength corresponding to the center frequency. A: Absorption, T: Transmission, R: Reflection; N. R.: Not reported; N. A.: Not Applicable.

the ON–OFF mode, and a full reflection in the ON–ON state, thereby demonstrating versatile EM characteristics under a compact structural footprint.

The ECM developed for this design provides a clear interpretation of the underlying switching mechanism by capturing the impedance transitions associated with the two diode sets. The close agreement between the ADS-predicted responses and HFSS full-wave simulations further confirms the accuracy of the circuit representation. Additionally, the structure exhibits stable performance under varying polarization angles and oblique incidence conditions, which is attributed to its symmetrical metallic configuration and embedded parallel biasing network.

A key contribution of this work is the hardware realization using an FPGA-controlled biasing module, which enables real-time switching among the four operational states using a two-bit coding sequence. The fabricated 1-D array prototype is evaluated using the in-house PPW measurement setup, and the measured scattering parameters closely match the simulated results across all modes under normal and oblique incidence setups. These experimental validations confirm the reliability of the biasing scheme, the robustness of the FPGA-based control mechanism, and the practical feasibility of achieving transitions between different EM functionalities.

Additionally, a comparison with the existing literature, summarized in Table 3.2, highlights the advancements achieved in this work. Unlike earlier designs that require multilayer structures, manual tuning, or complex biasing networks, the proposed RFSS offers a compact single-layer multifunctional structure with programmable switching. The simplified biasing approach and FPGA-based automation enhance scalability, making the design suitable for real-time EM applications.

Overall, this work extends the first research outcome by advancing from a dual-mode absorptive/transmissive structure to a tri-functional RFSS capable of reflection, absorption, and transmission using two different sets of diode switching with real-time hardware control. Although the design achieves multifunctional operation, the resonance frequencies of each mode remain fixed after fabrication. This limitation motivates further development toward frequency reconfigurability. The next chapter addresses this by incorporating varactor diodes along with p-i-n switching to realize a tunable-switchable multifunctional RFSS offering both discrete mode selection and continuous frequency tuning.



# Chapter 4

## Switchable and Tunable Narrow-band Multifunctional RFSS

### 4.1 Introduction

The earlier chapters of this thesis establish the foundation for RFSSs by showing how the diode-based switching mechanism can modify EM behaviors of different geometries. The first study introduces a single p-i-n diode-based switching operation, enabling the RFSS to alternate between two EM responses, as presented in Chapter 2. While this work confirms the basic feasibility of electronic reconfiguration, its functionality remains limited to dual-mode operation with no ability to adjust operating frequencies.

The subsequent work extends this concept by employing two independently driven sets of p-i-n diodes, creating four different switching states that support three distinct EM functions, as discussed in Chapter 3. The incorporation of FPGA-based digital control removes the need for manual biasing and enables automatic state selection. However, this design, like the first, exhibits fixed resonant frequencies determined solely by the unit cell geometry and diode conditions. As a result, both structures, though successfully exhibit switchable responses, lack the frequency tunability feature needed in environments where dynamic spectral control is essential.

To address this limitation, the present chapter introduces a multifunctional RFSS (MRFSS) that integrates switching and frequency tuning within a single-layer topology. This design incorporates varactor diodes alongside two sets of p-i-n diodes,

enabling the surface to not only switch among multiple EM states but also continuously tune its operating frequencies within each state. By modulating the reverse-bias voltage of the varactors, the structure achieves substantial frequency flexibility without any modification to its physical configuration. This advancement elevates the RFSS from a state-selective device to a frequency-agile platform suitable for cognitive radio systems, tunable radome applications, and adaptive EM wave manipulation.

The proposed MRFSS realizes this combined switching–tuning behavior through complementary metallic patterns printed on both sides of an FR4 substrate. The top layer integrates a meander-based resonant path loaded with a parallel arrangement of p-i-n diodes and varactors, enabling tunable transmission and absorption characteristics. The bottom layer employs another set of p-i-n diodes that toggle its behavior between bandpass and reflective modes. Together, these layers generate four diode combinations, such as OFF–OFF, OFF–ON, ON–OFF, and ON–ON, each supporting distinct EM functions. The varactor-controlled reactance offers a continuous tuning range for each of these functions, allowing transmission, absorption, selective reflection, and full reflection to shift across broad frequency intervals. A detailed ECM is formulated to interpret the combined effects of layered *RLC* interactions, switching states, and tunable capacitances on the EM response.

Beyond circuit-level analysis, this chapter thoroughly investigates the MRFSS under normal and oblique incidence to confirm stability across different angles of polarization and incidence. A prototype is fabricated using standard PCB processes, and dedicated bias networks are developed to independently regulate the p-i-n and varactor diodes. The structure is experimentally characterized using a free-space measurement setup, and the measured responses closely follow the simulated trends, validating its tuning range and multifunctional capabilities.

The remaining sections of this chapter present the complete development of the proposed switchable and tunable MRFSS. The design and analysis section details the unit-cell architecture, diode integration methodology, biasing configuration, and circuit interpretation. This is followed by the fabrication and measurement of the prototype. The chapter concludes with a comprehensive comparison with the earlier reported works, demonstrating that the proposed MRFSS successfully achieves dy-

namic, multifunctional behavior and frequency agility within a compact single-layer structure.

## 4.2 Design and Analysis

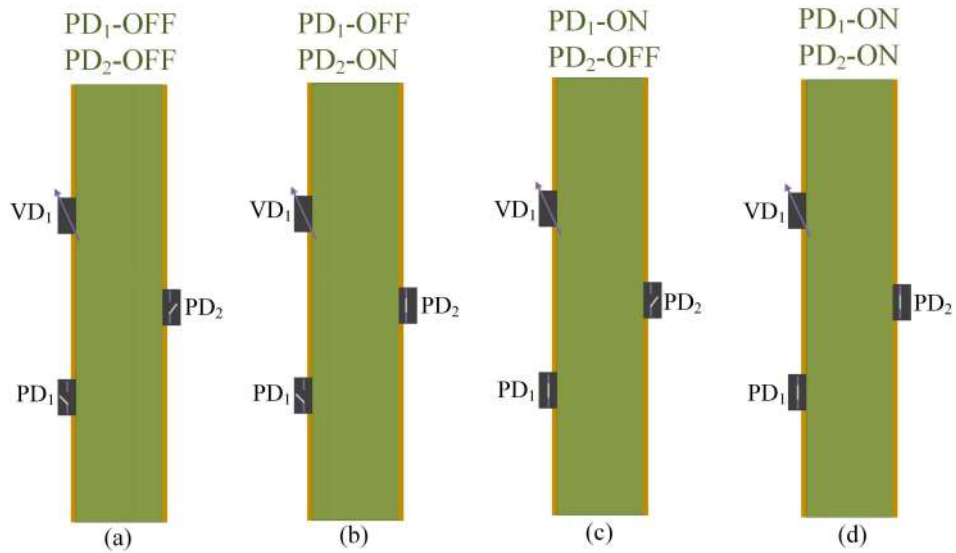


Figure 4.1: Schematic view of the proposed MRFSS geometry: (a) OFF-OFF state, (b) OFF-ON state, (c) ON-OFF state, and (d) ON-ON state.

A switchable EM geometry with two different operating states can be realized by using a single p-i-n diode in each unit cell. However, achieving three or more EM functionalities generally requires the integration of multiple diodes. These switching elements may be mounted either on a single dielectric substrate or on multiple substrates separated by an air gap. Implementing one set of diodes on the top surface and another set on the bottom surface of a single-layer dielectric substrate offers practical advantages in terms of biasing simplicity and geometric flexibility. This configuration produces four distinct diode combinations: ON (top)-ON (bottom), ON-OFF, OFF-ON, and OFF-OFF. With an appropriate choice of metallic patterns and strategic placement of the diode components, each state can be engineered to exhibit a different EM behavior such as transmission, reflection, or absorption. Furthermore, introducing a varactor diode into the geometry enables continuous frequency tunability within each of these switching states. As a result, the combined arrangement of two p-i-n diodes and one varactor forms a multifunctional structure

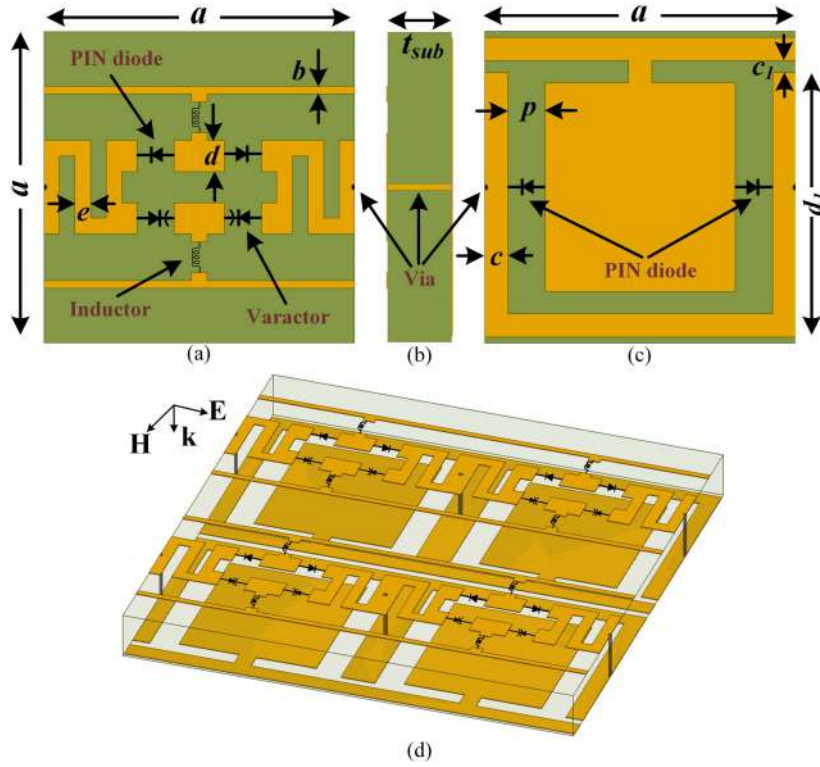


Figure 4.2: Design of the proposed MRFSS unit cell geometry: (a) top view, (b) Side view, (c) bottom view, and (d) isometric view.

capable of both switching and tuning operations. A schematic representation of the proposed configuration is shown in Fig. 4.1.

#### 4.2.1 Design Methodology of the Unit Cell

To attain the aforementioned operating modes in a single-layer structure, two different metallic patterns are considered in the proposed MRFSS design. The top layer comprises a meander-line configuration along with a set of varactors and p-i-n diodes placed in parallel with each other. The associated biasing lines are also included on either side of the pattern and are connected through lumped inductors. The geometry employed on the bottom side consists of a central patch and surrounding metal lines connected through another set of p-i-n diodes. A metallic via is inserted through the dielectric substrate to short the top meander line and the bottom metallic patch, thereby establishing a common biasing node. Figure 4.2 illustrates the individual layers with different views. The intermediate medium is an FR4 substrate ( $\epsilon_r = 4.4$ , and  $\tan \delta = 0.02$ ). The dimensions of the geometry are:

Table 4.1: Varactor Diode Voltage versus Capacitance Values

S.no	Voltage (V)	Capacitance (pF)
1	5.5	1.95
2	6.2	1.60
3	7.5	1.26
4	10	0.93
5	15	0.71
6	20	0.60
7	25	0.55

$a = 10$  mm,  $b = 0.25$  mm,  $c = 0.75$  mm,  $d = 1$  mm,  $e = 0.5$  mm,  $c_1 = 0.375$  mm,  $d_1 = 8.5$  mm,  $p = 1.2$  mm, and  $t_{\text{sub}} = 2$  mm.

To execute the reconfigurable characteristics, one set of p-i-n diodes and one set of varactors are mounted on the top side, whereas another group of p-i-n diodes is mounted on the bottom side. Each set consists of two electronic elements, thereby counting a total of 6 components per unit cell geometry. However, each of the diodes is used two times with back-to-back orientation, with an aim to realize the biasing circuitry in a simpler way. The p-i-n diode considered in the design exhibits a small resistance ( $R_{ON}$ ) of  $4.5 \Omega$  in series with a parasitic inductance ( $L_{ON}$ ) of  $0.6$  nH under the ON state, and a capacitance ( $C_{OFF}$ ) of  $0.15$  pF in series with the same parasitic inductance ( $L_{ON} = L_{OFF}$ ) under the OFF state. The varactor diode provides a nonlinear, voltage-dependent capacitance ( $C_V$ ) that varies between  $0.55$  pF and  $1.95$  pF, as detailed in Table 4.1. The bottom-layer topology contains an embedded biasing network, while two external bias lines are printed on the top layer to independently regulate the p-i-n diodes and varactors. Inductors of appropriate values are employed to isolate RF signals from these biasing paths.

To design an MRFSS structure capable of supporting different EM operations (transmission, absorption, and reflection), the working mechanism of each response is studied first, followed by the formulation of suitable layer topologies. To realize a bandpass transmissive behavior in a single-layer geometry comprising top- and bottom-side metallic patterns, the incident EM wave must be able to propagate through both layers at a designated frequency. A parallel  $RLC$  network typically provides a bandpass resonance and can therefore be utilized on both layers (e.g.,

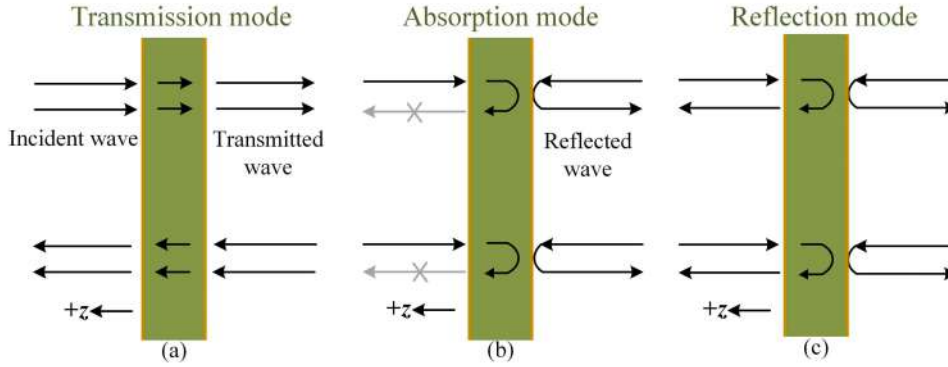


Figure 4.3: Schematic conceptualization to achieve different operating modes from the proposed MRFSS geometry: (a) transmission mode, (b) absorption mode, and (c) reflection mode.

Table 4.2: Circuitual Requirement in the Proposed MRFSS Geometry

Operating States	Top layer (for switching)	Bottom layer (for switching)	Top layer (for tuning)
Transmitter	Parallel $RLC$ circuit	Parallel $RLC$ circuit	Series $RL$ circuit with varactor capacitance ( $C_V$ )
Absorber	Series or parallel $RLC$ circuit	Reflection (no resonance)	Series $RL$ circuit with varactor capacitance ( $C_V$ )
Reflector	Reflection (no resonance)	Reflection (no resonance)	Series $RL$ circuit with varactor capacitance ( $C_V$ )

$R_1-L_1-C_1$  on the top side and  $R_2-L_2-C_2$  on the bottom side).

An absorptive operation requires simultaneous suppression of reflection and transmission. To achieve near-unity absorption, the bottom layer is configured as a reflector (preventing transmission), while the top layer incorporates a series or parallel  $RLC$  circuit designed to minimize reflection at a target frequency. Hence, a switchable mechanism is necessary on the bottom layer to toggle its response between bandpass and reflective states, while the top layer may use either the same parallel  $RLC$  model or a series configuration to produce the desired absorption.

A reflective behavior can be obtained either by engineering the top layer as a reflector (selective-reflection mode) or by configuring both layers to operate as reflectors (full-reflection mode). Hence, the top layer should be equipped with a switching concept to disable the resonance feature and enable the reflecting mode. The bottom layer can use the previous reflective circuit condition to ensure complete reflection from the overall geometry.

To dynamically regulate each operating mode, a tunable  $RLC$  network must be integrated, preferably in the top layer, and controlled independently. By varying the capacitance of this tunable network, the resonance frequency of the structure can be shifted, thereby enabling frequency agility across different EM states. Figure 4.3

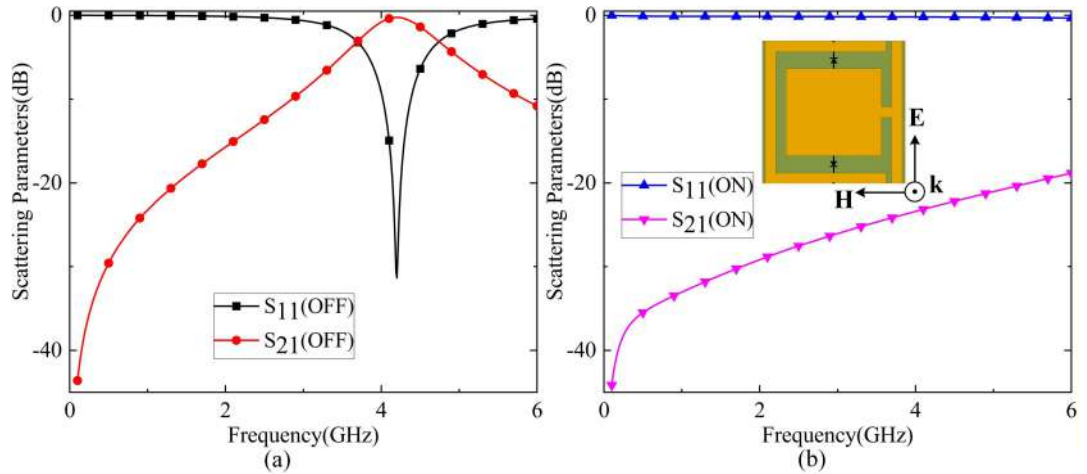


Figure 4.4: Simulated scattering parameters of the bottom layer (+ dielectric) under (a) OFF state, and (b) ON state.

illustrates the schematic representation of the operating principle, while Table 4.2 summarizes the corresponding circuit requirements.

The bottom-side topology is designed first with the aim of achieving the desired conditions, i.e., a transmission and a reflection through switching activity. A central patch along with surrounding metal lines is considered in the bottom layer, and two p-i-n diodes are inserted across the slots. Under the forward-bias condition, the diodes establish a continuous electrical connection between the metal traces, whereas a parallel  $RLC$  circuit is realized under the reverse-bias condition. Figure 4.4 illustrates the simulated response of this geometry (bottom layer + dielectric), exhibiting a bandpass characteristic at 4.2 GHz with an insertion loss of 0.24 dB in the OFF state, and a complete reflection across the entire operating range in the ON state.

On the contrary, the top layer consists of three functional segments: a parallel  $RLC$  circuit, a switching unit, and a tuning element, with the switching and tuning sections arranged in parallel. A meander-line structure is used to realize the parallel  $RLC$  response, while the p-i-n diodes and varactor diodes are positioned alongside this path, as depicted in Fig. 4.2(a). When the p-i-n diode is reverse biased, the combined structure (top layer + dielectric) exhibits a bandpass transmissive response attributed to the meander segment, along with a bandstop behavior arising from the series  $RLC$  circuit of the switching unit, as shown in Fig. 4.5(a).

With the incorporation of the tuning element, both the bandpass and bandstop responses can be dynamically adjusted. The bandpass response spans from 1.64 GHz

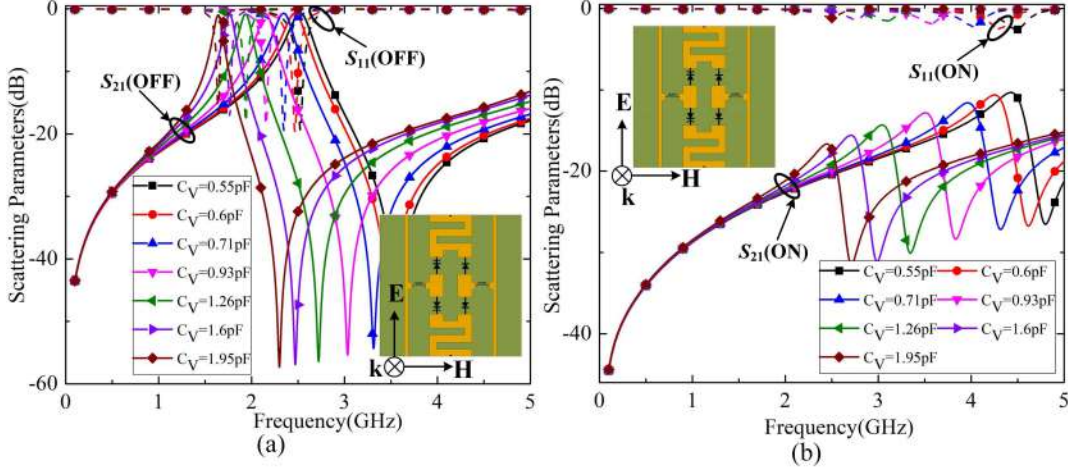


Figure 4.5: Simulated scattering parameters of the top layer (+ dielectric): (a) OFF state, and (b) ON state.

to 2.53 GHz, with an insertion loss ranging from 0.71 dB to 0.93 dB, corresponding to a varactor tuning voltage variation from 5.5 V to 25 V. When the p-i-n diode is forward biased, a continuous conductive path is established, bypassing the capacitive behavior and thereby generating a reflective response. Over the aforementioned tuning range, a reflection amplitude greater than  $-2.5$  dB is observed within the frequency interval of 2.49 GHz to 4.48 GHz.

#### 4.2.2 Equivalent Circuit Modeling

The equivalent circuit model is presented in Fig. 4.6, supporting the operation mechanism described above. The top layer contains a combination of parallel and series circuit branches: a parallel  $R_2$ - $L_2$ - $C_2$  network arising from the meander structure, and a set of varactors and p-i-n diodes mounted in series branches ( $L_3$ - $R_3$ ), which are connected in parallel with one another. The varactor diode provides a tunable capacitance  $C_V$  controlled by the applied reverse-bias voltage, while the p-i-n diode is modeled as a small resistance  $R_{ON}$  in series with a parasitic inductance  $L_{ON}$  in the ON state, and as a high capacitance  $C_{OFF}$  in series with a parasitic inductance  $L_{OFF}$  in the OFF state. The bias line in the top layer is represented by a series combination of resistance and inductance ( $R_1$ - $L_1$ ).

The bottom layer includes two series networks,  $R_4$ - $L_4$  and  $R_5$ - $L_5$ , corresponding to the surrounding metal lines and the central patch, respectively. The p-i-n diode in

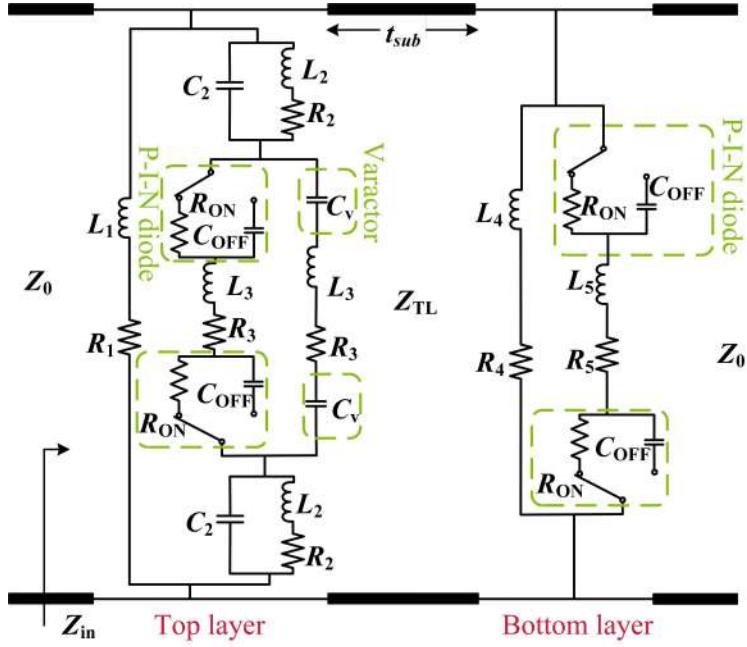


Figure 4.6: Equivalent circuit modeling of the proposed MRFSS geometry.

this layer is modeled identically to the top layer, following the SPICE representation:  $R_{ON}$  in series with  $L_{ON}$  under the ON state, and  $C_{OFF}$  in series with  $L_{OFF}$  under the OFF state. The dielectric substrate is modeled as a transmission line, while the metallic via connecting the top and bottom layers does not significantly influence RF propagation and is therefore neglected due to simplicity.

From the circuit diagram, it is evident that the bottom layer exhibits two distinct responses depending on the switching state of the p-i-n diode. In the reverse-bias condition, the topology forms a parallel  $LC$  network consisting of  $L_4$ ,  $L_5$ , and  $C_{OFF}$ , resulting in a bandpass transmission response. Conversely, under forward bias, only inductive and resistive components remain (with no capacitive contribution), thereby producing a reflective behavior.

In the top layer, the parallel  $R_2$ - $L_2$ - $C_2$  network yields a bandpass characteristic, while the series  $R_3$ - $L_3$ - $C_{OFF}$  branch introduces a bandstop response during the reverse-bias state of the p-i-n diode. Under forward bias, the diode exhibits a small resistance  $R_{ON}$ , causing the top layer to behave predominantly as a reflector. With the tunable capacitance of the varactor diode, all operational states are influenced by the  $R_3$ - $L_3$ - $C_V$  branch, enabling dynamic frequency tuning across various EM behaviors. Therefore, the proposed MRFSS topology and its corresponding circuit

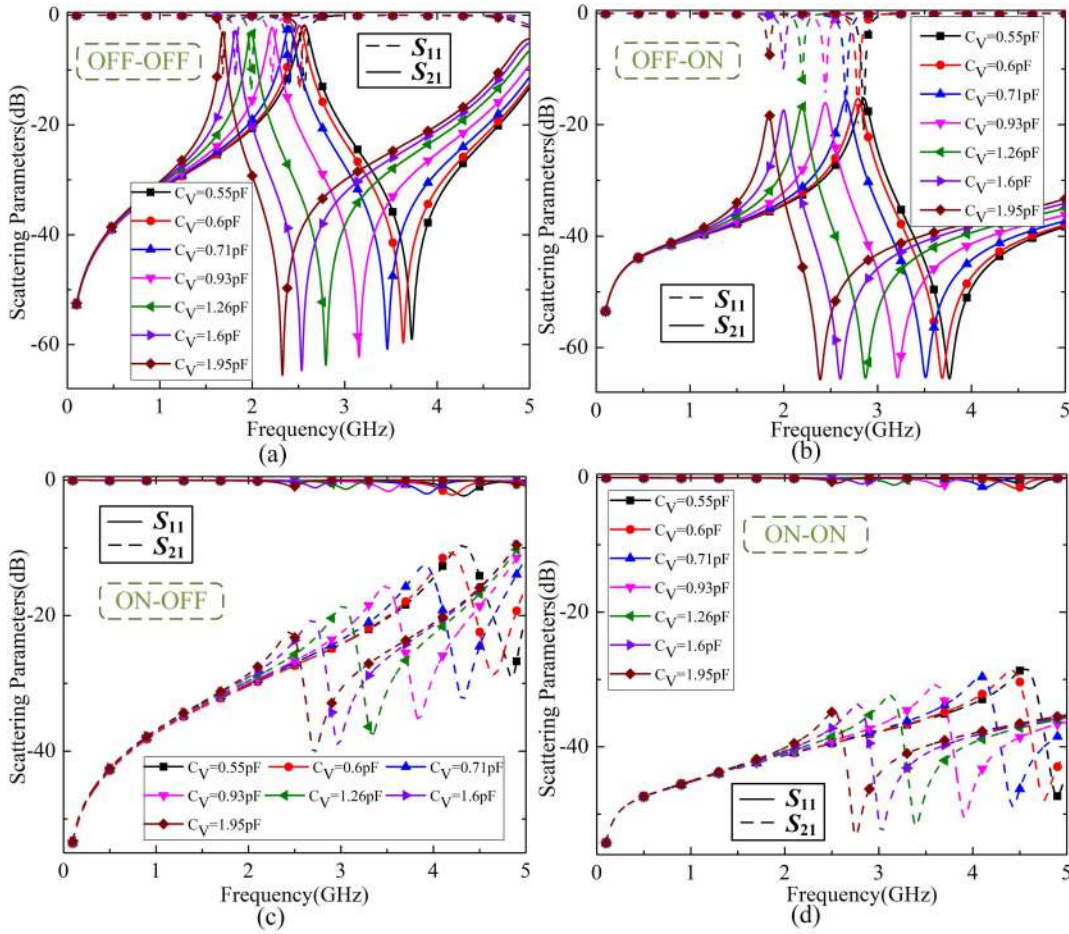


Figure 4.7: Simulated scattering parameters of the proposed MRFSS geometry: (a) transmission mode, (b) absorption mode, (c) selective-reflection mode, and (d) reflection mode.

model successfully fulfil the criteria required to achieve multiple EM responses under different switching and tuning conditions.

The complete simulation is carried out in Ansys HFSS 2020 using periodic boundary conditions. Under the OFF–OFF condition, a tunable bandpass transmission response is obtained in the frequency range of 1.68–2.56 GHz with an insertion loss of 1.8–2.9 dB, while varying the bias voltage across the varactor from 5.5 V to 25 V. The tunable capacitance of the varactor appears in parallel and series with the p-i-n diode OFF-state capacitance and the meander-line pattern, respectively, thereby enabling dynamic control for both bandstop and bandpass responses. The bottom-layer diode also exhibits a transmissive behavior under the reverse-bias state. Hence, the overall configuration yields a tunable transmission mode, as shown in Fig. 4.7(a).

Under the OFF–ON condition, the structure exhibits a tunable absorption be-

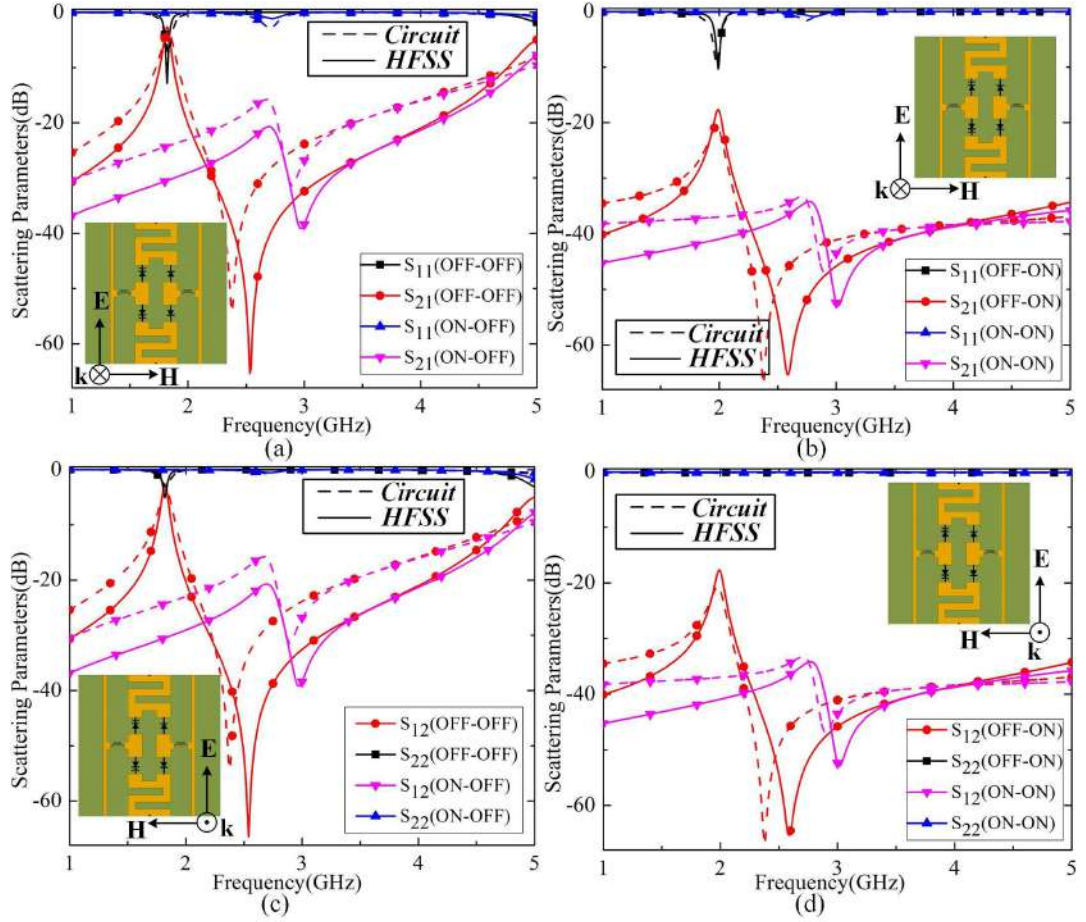


Figure 4.8: Scattering parameters of the proposed MRFSS geometry at a reverse-bias voltage of 6.2 V using HFSS and ADS software for all the modes: (a), (b)  $+z$  direction and (c), (d)  $-z$  direction. The optimized circuit parameter values are:  $L_1 = 9$  nH,  $R_1 = 0.01$   $\Omega$ ,  $L_2 = 1.3$  nH,  $R_2 = 0.31$   $\Omega$ ,  $C_2 = 0.11$  pF,  $L_3 = 2.5$  nH,  $R_3 = 0.01$   $\Omega$ ,  $L_4 = 2$  nH,  $R_4 = 0.01$   $\Omega$ ,  $L_5 = 0.01$  nH,  $R_5 = 0.01$   $\Omega$ .

havior. In the forward-bias (ON) state, the bottom layer reflects the incident EM wave due to the absence of any capacitive contribution in the circuit, effectively behaving as an adaptive ground plane. The top layer maintains the same behavior as in the OFF–OFF case. This leads to a narrowband absorption response with a tunable frequency ranging from 1.84 GHz to 2.85 GHz and an absorptivity between 84.3% and 96.5%, as depicted in Fig. 4.7(b).

The structure exhibits reflective characteristics in the remaining two switching states (ON–OFF and ON–ON), as shown in Figs. 4.7(c) and 4.7(d). In both cases, the small forward resistance  $R_{ON}$  of the top-layer p-i-n diode ensures reflection regardless of the state of the bottom-layer diode. Under the ON–OFF condition, the

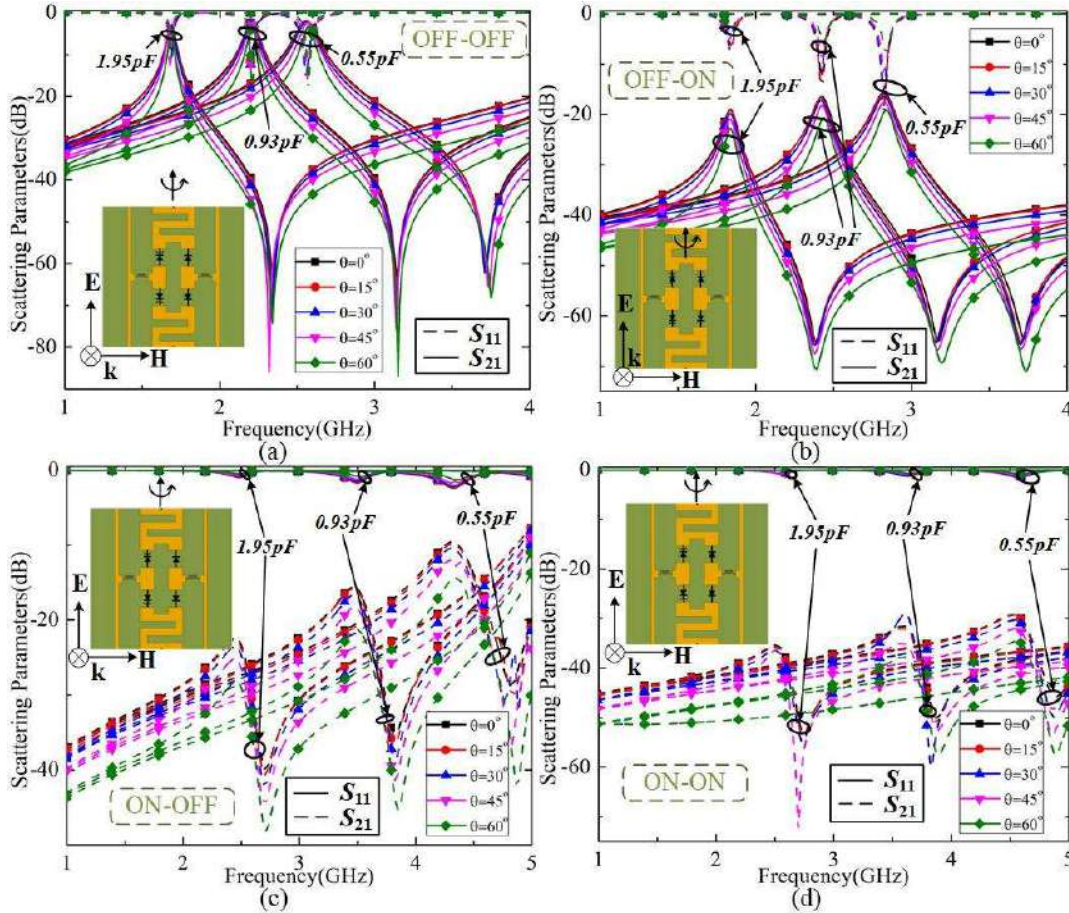


Figure 4.9: Scattering parameters of the proposed MRFSS geometry under TE polarization: (a) transmission mode, (b) absorption mode, (c) selective-reflection mode, and (d) reflection mode.

top layer demonstrates reflective behavior due to the diode being in the ON state, while the bottom layer exhibits transmission because of its parallel  $LC$  resonance. The overall geometry therefore displays a reflection response with  $S_{11}$  magnitude varying between  $-0.5$  dB and  $-2.5$  dB and a tunable frequency range of 2.48–4.43 GHz. However, as the varactor reverse-bias voltage increases (corresponding to a decrease in OFF-state capacitance), a finite  $S_{21}$  magnitude appears along with a reduction in  $S_{11}$ . Thus, for smaller bias voltages (up to 10 V), the structure exhibits a selective-reflection mode.

In the ON–ON state, the bottom layer also acts as a reflector, with significantly improved reflection characteristics as compared to the previous state. The reflection coefficient remains below  $-1.5$  dB in the frequency range of 2.55–4.62 GHz, while the transmission magnitude lies below  $-30$  dB across the entire band. All three major

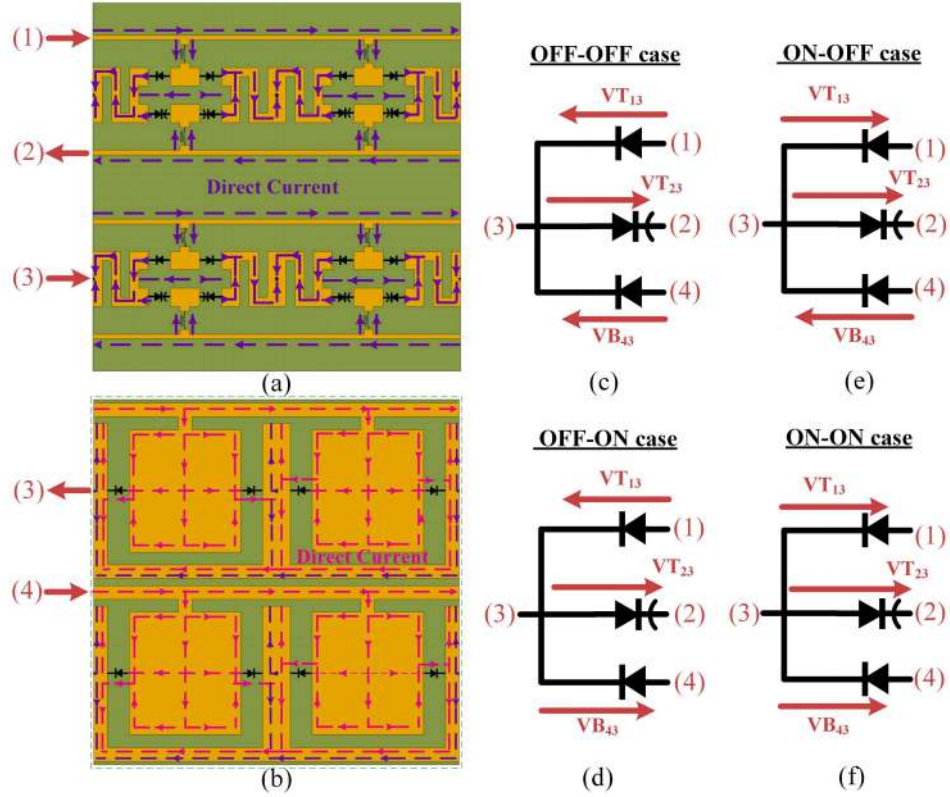


Figure 4.10: Biasing technique of the proposed MRFSS geometry: (a) top layer, and (b) bottom layer. Biasing conditions for different cases: (c) OFF-OFF case: ( $VT_{13} < V_{th}$ ); ( $VB_{43} < V_{th}$ ); ( $VT_{23} < V_{th}$ ). (d) OFF-ON case: ( $VT_{13} < V_{th}$ ); ( $VB_{43} > V_{th}$ ); ( $VT_{23} < V_{th}$ ). (e) ON-OFF case: ( $VT_{13} > V_{th}$ ); ( $VB_{43} < V_{th}$ ); ( $VT_{23} < V_{th}$ ). (f) ON-ON case: ( $VT_{13} > V_{th}$ ); ( $VB_{43} > V_{th}$ ); ( $VT_{23} < V_{th}$ ). [ $V_{th}$  is the threshold voltage of the diode].

EM functionalities, such as reflection, absorption, and transmission, are realized in the ON-ON, OFF-ON, and OFF-OFF states, respectively, while the ON-OFF state yields a tunable selective reflection. Therefore, both ON-OFF and ON-ON configurations can serve as reflective states with tunability.

It is noteworthy that most of the operating modes of the proposed MRFSS geometry function the same for incident EM waves arriving from both directions ( $+z$  and  $-z$ ), except the absorption mode. For the OFF-ON absorption case, the bottom layer acts as a reflector and the top layer provides resonance for a  $+z$  incident wave. For a  $-z$  incident wave, however, the EM wave encounters the reflective bottom layer first and does not interact with the top layer, resulting in a reflective response instead of absorption. For the remaining operating states, there is a minimal interference between the top and bottom layers regardless of wave incidence direction, and the

transmission and reflection responses remain identical. To validate the ECM, scattering parameters are extracted using ADS software and compared with full-wave HFSS simulations for all modes under both  $+z$  and  $-z$  incidence [126, 127]. The comparison is illustrated in Fig. 4.8, showing close agreement and confirming the accuracy of the proposed circuit model. The parameter values are provided in the corresponding figure caption.

The proposed MRFSS geometry is polarization-sensitive and operates for a specific electric-field orientation. When the E-field is aligned parallel to the diode elements and the meander-line pattern, the structure exhibits the desired tunable and switchable behaviors. Under the orthogonal polarization, however, the induced current cannot flow through the electronic components, and neither switching nor tuning occurs. The topology is further analyzed for various incident angles under the supported polarization (TE mode), and highly stable angular responses are observed up to an incidence angle of  $60^\circ$ , as shown in Fig. 4.9. The EM responses under TM mode are not satisfactory due to its polarization-sensitive topology.

## 4.3 Fabrication and Experimental Verification

### 4.3.1 Parallel Biasing Technique

A diode-based MRFSS structure requires appropriate biasing circuitry to enable independent operation of the diodes within the geometry. The bias lines must be carefully designed such that no interference occurs in the EM operation, while ensuring that the DC voltage is properly applied across the electronic components. A parallel biasing technique is often preferred over a serial biasing method, as it allows for lower voltage supply, reduced ohmic losses, and a faster switching response. In the proposed geometry, one varactor and one p-i-n diode are mounted on the top layer, and another p-i-n diode is placed on the bottom layer. All three components must be independently controlled. Ideally, six separate terminals would be needed; however, a novel biasing configuration is adopted such that only four terminals are required to regulate all diodes in the structure.

Figure 4.10(a) illustrates the biasing technique for the geometry. Two dedicated bias lines are printed on the top layer and connected through lumped inductors,

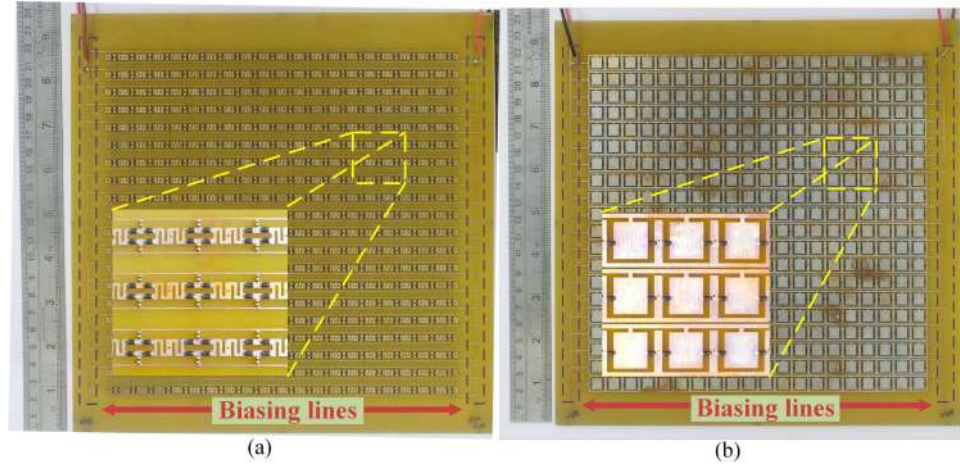


Figure 4.11: Fabricated photographs along with enlarged views of the proposed MRFSS geometry: (a) top layer, and (b) bottom layer.

while the bottom-layer topology contains embedded bias lines. Terminals 1 and 2 are located on the top layer, and terminals 3 and 4 are located on the bottom layer. Terminal 1 is connected to the anode of the top-layer p-i-n diodes, while terminal 2 is connected to the cathode of the varactors. The positive terminal of the bottom-layer p-i-n diode is connected to the central square patch, which is routed to terminal 4. Each diode component is duplicated in both layers to simplify the bias routing. A common terminal 3 (ground) is connected to the remaining ends of all diodes through a metallic via that links the top meander pattern and the bottom outer lines.

To maintain a parallel connection, terminals with identical markings are interconnected across consecutive unit cells, allowing a DC voltage applied at one edge of the prototype to reach every unit cell. Thus, a single voltage applied between terminals 1 and 3 regulates the voltage  $VT_{13}$  across the top-layer p-i-n diodes of all unit cells, while the voltage between terminals 2 and 3 provides the reverse-bias voltage  $VT_{23}$  for the top-layer varactor. In the bottom layer, the p-i-n diodes are controlled by the supply voltage  $VB_{43}$  applied between terminals 3 and 4.

In the OFF-OFF case, both top and bottom p-i-n diodes operate under reverse-bias conditions, i.e.,  $VT_{13} < V_{th}$  and  $VB_{43} < V_{th}$ , where  $V_{th}$  is the threshold voltage of the diode, resulting in a transmission response. During absorption, the top-layer diode remains reverse biased, while the bottom-layer diode is forward biased ( $VB_{43} > V_{th}$ ). Similarly, the third and fourth operating states are achieved by ap-

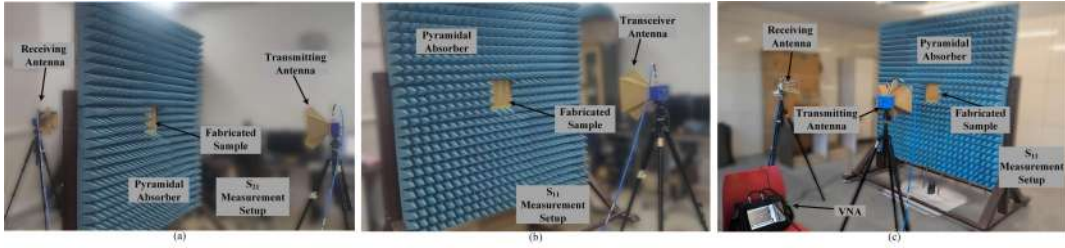


Figure 4.12: Measurement setup for the proposed MRFSS geometry: (a)  $S_{21}$  response (normal incidence), (b)  $S_{11}$  response (normal incidence), and (c)  $S_{11}$  response (oblique incidence).

appropriately regulating the bias voltages across the diodes. In all cases, the varactor operates under reverse bias with  $VT_{23}$  varying from 5.5 V to 25 V, enabling tunability. The p–i–n diodes are biased with 0.82 V for ON state (forward bias) and 0 V for OFF state (reverse bias). Figure 4.10 illustrates the schematic of biasing operations for the proposed geometry.

### 4.3.2 Fabrication and Measurement

Once the biasing circuitry is finalized, a prototype is fabricated on an FR4 substrate of thickness 2 mm. The prototype contains a periodic array of  $20 \times 20$  unit cells, resulting in an overall size of  $240 \times 240$  mm<sup>2</sup>, and is realized using a standard PCB etching process. BAR 50–02V p–i–n diodes [128] and BB 857–02V varactors [129] from Infineon Technologies are used in the structure, and the parameter values used in simulation are taken from their technical datasheets. Lumped inductors of 6.8 nH from Murata, having a self-resonant frequency of 4.5 GHz, are mounted at appropriate locations to isolate RF signals from the DC bias lines. The fabricated MRFSS sample and its enlarged views are shown in Fig. 4.11.

The experimental characterization of the prototype is performed using a free-space measurement setup [130], consisting of an Agilent E5071C VNA, horn antennas, DC power supplies, and a pyramidal foam absorber wall. Figures 4.12 (a)–(c) illustrate the measurement arrangements for obtaining the  $S_{21}$  and  $S_{11}$  responses. During normal-incidence  $S_{11}$  measurements, a single horn antenna is used as a transceiver to simultaneously transmit and receive the signal. This approach improves the accuracy of the  $S_{11}$  measurement because the field radiated from a single antenna maintains a quasi–plane-wave distribution with minimal excitation of

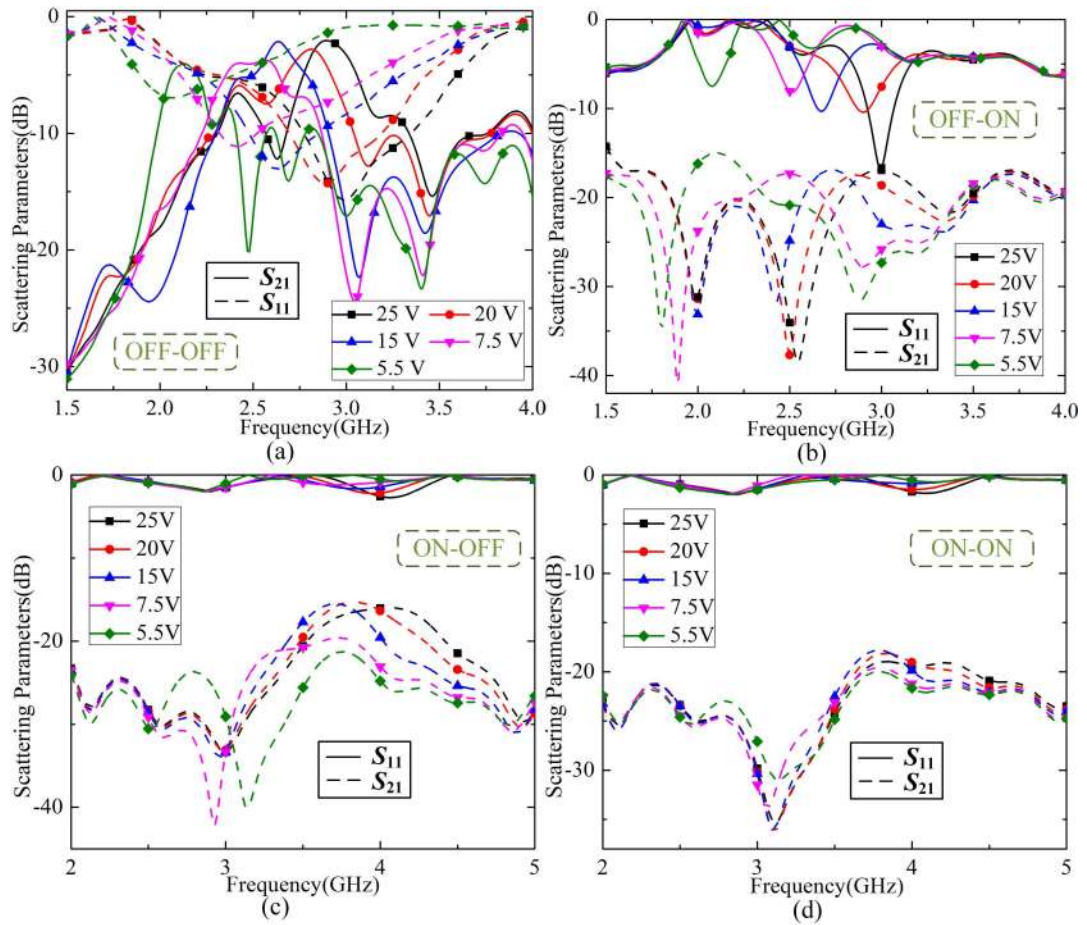


Figure 4.13: Measured scattering parameters of the proposed MRFSS geometry: (a) transmission mode, (b) absorption mode, (c) selective-reflection mode, and (d) reflection mode.

unintended TE components. In contrast, using two separate antennas for  $S_{11}$  measurement introduces additional alignment uncertainties, mutual coupling between the antennas, and non-uniform illumination across the DUT, all of which distort the reflected field. Therefore, a single horn antenna is used as a transceiver to measure  $S_{11}$  under normal incidence [75], whereas a two-antenna configuration is used for oblique incidence [130]. Three separate DC power supplies independently regulate the top-layer p-i-n diode, the bottom-layer p-i-n diode, and the top-layer varactor. FPGA control is not integrated in this design because the varactor tuning demands varying reverse-bias voltage till approximately 30 V, whereas FPGA I/O pins can provide only low-voltage digital levels and cannot directly generate the required high-voltage analog bias without complex external driver circuits.

During measurements, the device under test (DUT) is placed inside an aper-

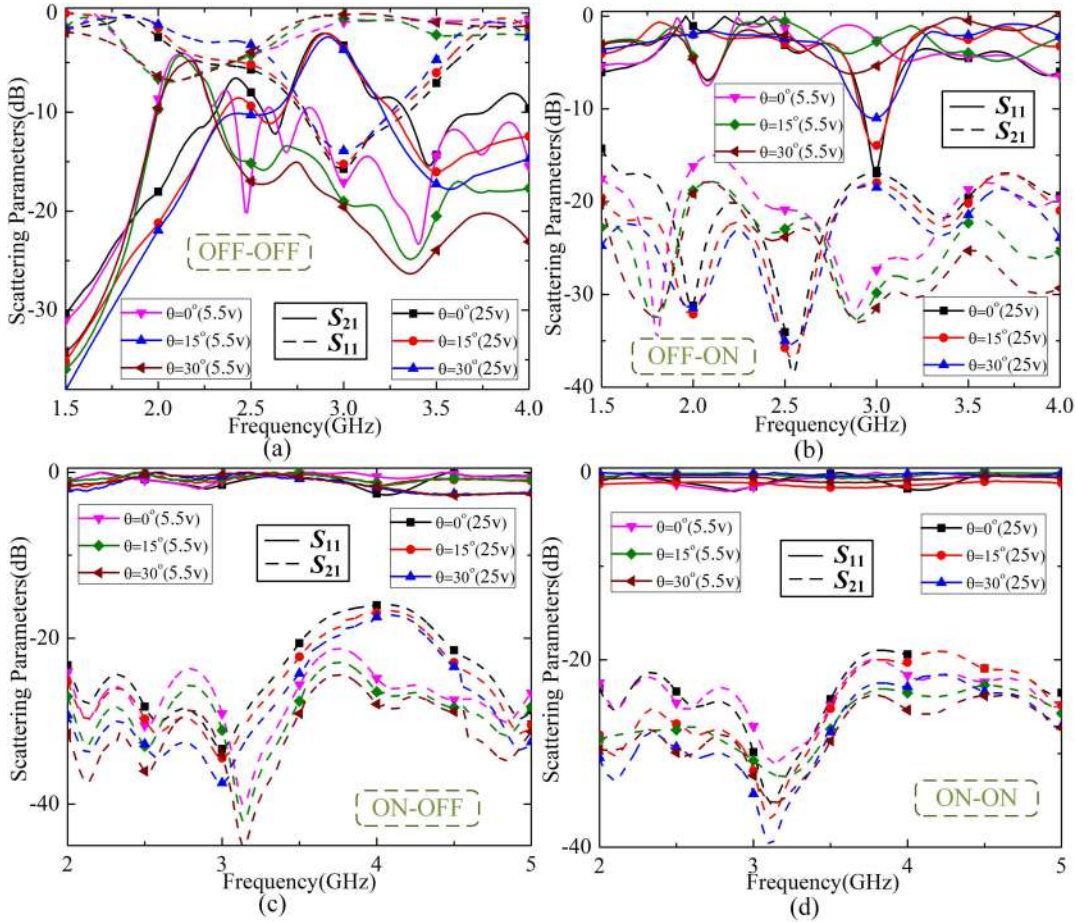


Figure 4.14: The measured oblique incidence responses for the proposed MRFSS structure: (a) transmission mode, (b) absorption mode, (c) selective-reflection mode, and (d) reflection mode. Two different bias voltages (5.5 V and 25 V) have been considered under each mode.

ture surrounded by foam absorbers to reduce finite edge effects, field dispersion, and reference-surface errors. First, the calibration is carried out by comparing the response with that of free space (for transmission) or a metal plate of identical size (for reflection). Next, the time-gating technique is applied based on the round-trip propagation delay between the antenna and the DUT. The distance between them is converted to time using the speed of light, and an appropriate time gating window (for example, around the calculated delay with a small tolerance) is applied in the VNA to suppress multipath propagation and unwanted reflections. Additional foam absorbers are placed around the DUT to reduce scattering effects. The surface resistance effects are neglected due to their negligible impact on the overall response.

The DC voltages across the p-i-n diodes are applied in two states: 1 V for

forward bias and 0 V for reverse bias. By properly applying  $VT_{13}$  for the top-layer diode and  $VB_{43}$  for the bottom-layer diode, the four switching states (OFF–OFF, OFF–ON, ON–OFF, and ON–ON) are realized. The varactor reverse-bias voltage is varied in five steps from 5.5 V to 25 V. During the tunable transmission mode, a bandpass response from 2.13 GHz to 2.98 GHz is observed, with insertion losses of 2.2–4.16 dB. In the absorption mode, absorptivity values between 80.34% and 93.83% are recorded within 2.09–3.05 GHz. In the ON–OFF and ON–ON states, the structure exhibits selective-reflection and full-reflection behavior, respectively, with reflection levels better than  $-2.6$  dB and  $-1.9$  dB over the entire measured band. The measured responses are closely aligned with the simulated results for all cases, indicating good agreement in the performance of the proposed MRFSS structure, as shown in Fig. 4.13.

The prototype is further measured for different incident angles under TE polarization. In this mode, the electric-field vector remains parallel to the diode elements and the meander path, while the magnetic field and propagation vector vary with the incidence angle. Measurements are conducted for three angles ( $0^\circ$ ,  $30^\circ$ , and  $60^\circ$ ), and the results in Fig. 4.14 indicate good angular stability.

### 4.3.3 Analysis of Response Deviations

In Chapter 2 and Chapter 3, the RFSS designs rely primarily on p–i–n diodes whose parasitic elements are relatively small and remain nearly constant across the operating band. As a result, the simulated and measured responses in those chapters show only minor deviations, and the corresponding effects are adequately accounted for within the tolerance range. However, the present chapter introduces varactor diodes to enable continuous frequency tuning, and these devices exhibit strong sensitivity to parasitic parameters, particularly the series resistance that varies with bias voltage and frequency. This resistance directly influences the resonant behaviour of the tunable behavior, causing noticeable amplitude variations and frequency shifts. Therefore, a separate detail section becomes necessary to rigorously evaluate their influence and to identify the practical limitations and design considerations specific to varactor-integrated RFSS structures.

The proposed MRFSS structure demonstrates switchable as well as tunable char-

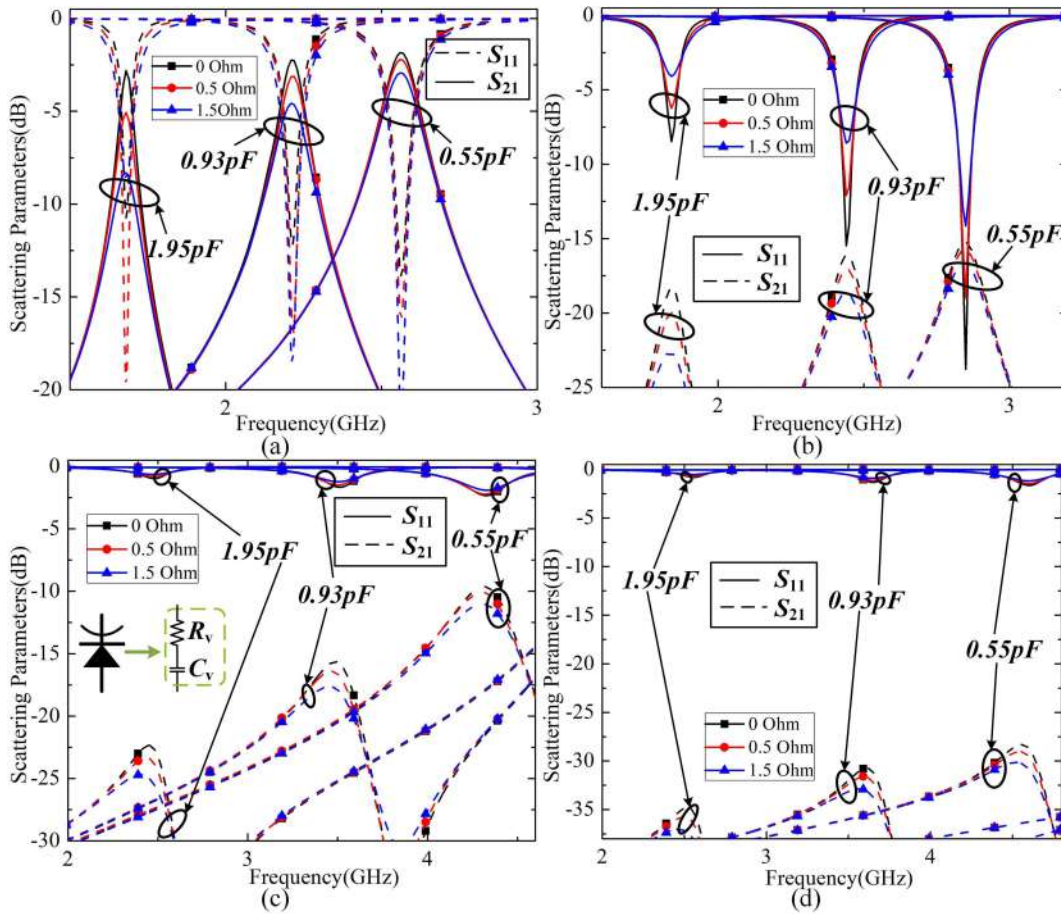


Figure 4.15: Effect of parasitic resistance on the proposed MRFSS geometry: (a) transmission mode, (b) absorption mode, (c) selective-reflection mode, and (d) reflection mode.

acteristics for different EM operations. However, minor deviations are observed in the desired responses. Ideally, under each operating mode, the structure should exhibit a tunable characteristic with nearly constant amplitude during the simulation studies. In practice, the amplitude varies within a certain range as the varactor capacitance changes, particularly for the transmission and absorption modes (for instance, the geometry shows an insertion loss ranging from 1.8 dB to 2.9 dB in the tunable transmission mode). These discrepancies can be attributed to several factors. Firstly, the unit-cell dimensions of the structure are optimized with respect to a specific frequency. Secondly, the small parasitic resistance present in the varactor diode may significantly affect the amplitude variations.

Figure 4.15 illustrates the degradation in the EM response when a parasitic resistor is added in series with the varactor capacitor. As the resistance value is

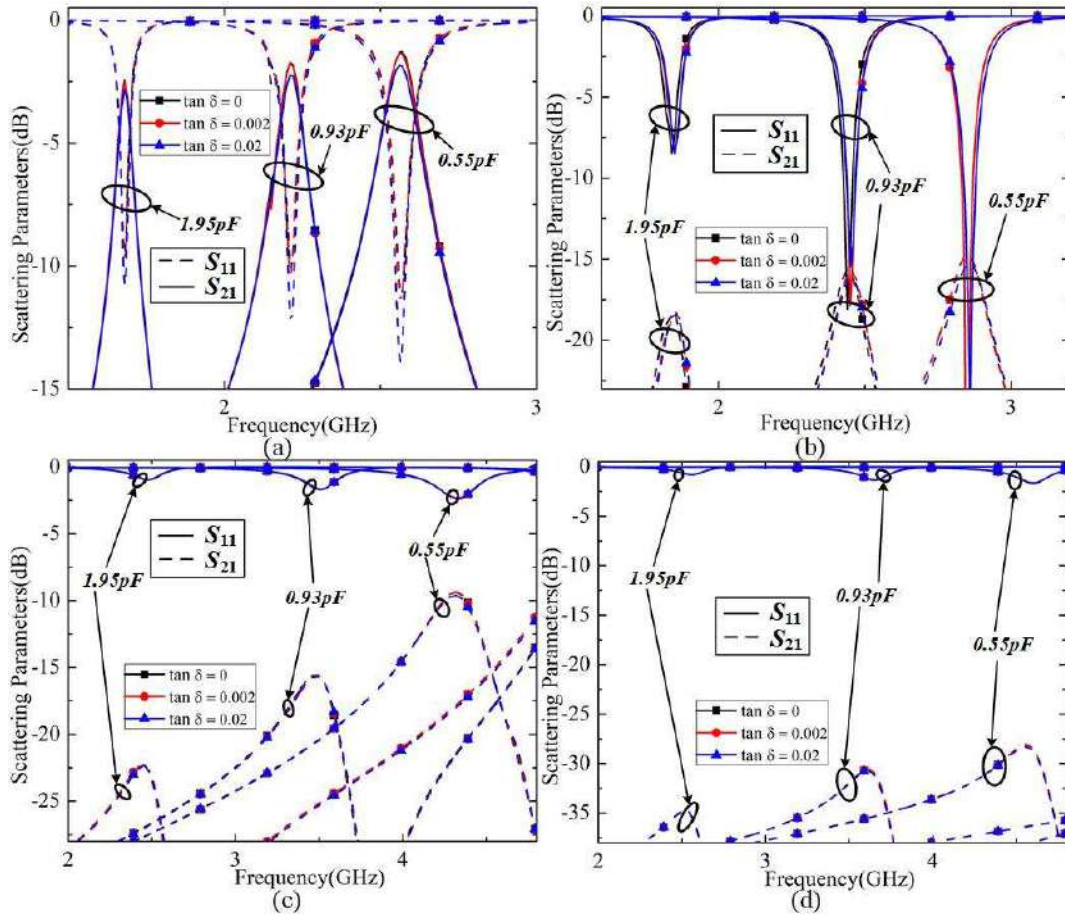


Figure 4.16: Effect of loss tangent of the dielectric substrate on the proposed MRFSS geometry: (a) transmission mode, (b) absorption mode, (c) selective-reflection mode, and (d) reflection mode.

varied from 0 to  $1.5 \Omega$ , noticeable changes in the amplitudes of the  $S_{11}$  and  $S_{21}$  responses are clearly observed, indicating one of the possible reasons behind the deviation. The potential solutions to mitigate this issue include the use of low-loss dielectric substrates and varactor diodes with lower parasitic resistance. A similar observation is made from the loss-tangent analysis, where increasing the substrate loss from  $\tan \delta = 0$  to 0.02 produces only slight deviations in both  $S_{11}$  and  $S_{21}$ , indicating that dielectric loss contributes minimally compared to the dominant parasitic-resistance effect of the varactor, as shown in Figure 4.16. Alternatively, two varactors may be connected in parallel, reducing the effective parasitic resistance, although at the cost of increased design complexity. Another approach involves designing the geometry to exhibit a wideband characteristic, wherein the tunable feature remains stable; however, such wideband structures typically require multi-

Table 4.3: Comparison with other RFSS Designs

References	Number of working modes	Operating functions	Working functions with tuning rate (%)	IL (dB)/ Ab (%)/ RA (dB)	Polarization/ Angular stability	Biasing circuitry	No. of electronic components per unit cell	Unit cell dimensions/ thickness ( $\lambda$ )
[37]	2	Switching Tuning	Bandpass (80%) Band stop (N.R.)	N.R.	Dual 40°	Series-Parallel	24	24.5 mm ( $\lambda/4$ ) 1 mm (0.01 $\lambda$ )
[65]	3	Switching Tuning	Bandpass transmission (8.94%) Bandstop transmission (5.76%) Polarization Selection (N.A.)	N.R.	Dual Dual Single 45°	Parallel	4	17.5 mm ( $\lambda/4$ ) 0.8 mm (0.01 $\lambda$ )
[94]	3	Switching	Transmission (0%) Absorption (0%) Reflection (0%)	2.36 94 > -0.5	Single 45°	Parallel	3	6.5 mm ( $\lambda/5$ ) 1 mm (0.03 $\lambda$ )
[103]	2	Switching Tuning	Transmission (13.88%) Absorption (17.87%)	1.96-4.30 78.77-90.78	Dual 60°	Parallel	8	10 mm ( $\lambda/8$ ) 1 mm (0.0125 $\lambda$ )
Proposed Work (Simulated)	3	Switching Tuning	Transmission (41.5%) Absorption (43.07%) Reflection (57.74%)	1.8-2.9 84.3-96.5 > -1.5	Single 60°	Parallel	6	10 mm ( $\lambda/10$ ) 2 mm (0.02 $\lambda$ )
Proposed Work (Measured)	3	Switching Tuning	Transmission (33.26%) Absorption (37.35%) Reflection (42.38%)	2.2-4.1 80.3-93.8 > -1.9	Single 60°	Parallel	6	10 mm ( $\lambda/10$ ) 2 mm (0.02 $\lambda$ )

*Note:* N.A.: Not applicable; N.R.: Not reported;  $\lambda$ : Wavelength corresponding to lowest operating frequency; IL (dB): Insertion loss; Ab (%): Absorptivity; RA (dB): Reflection amplitude.

layer configurations, further increasing the overall complexity.

The measured responses also show minor deviations, particularly in the form of frequency shifts compared to the simulated results. These deviations have been carefully analyzed, and several contributing factors are identified. Firstly, FR4 is a dispersive dielectric, whereas constant EM parameters are assumed during simulation. Secondly, the lumped components used in the structure possess frequency-dependent characteristics (for example, the OFF-state capacitance of the p-i-n diode varies with frequency), while constant values are used in the full-wave model. The parasitic resistance of the varactor, as previously discussed, also contributes to the observed frequency shift. Nonetheless, the deviations in both simulation and measurement remain within acceptable tolerance, confirming the reliable performance of the MRFSS geometry.

## 4.4 Conclusion

This chapter presents a compact MRFSS that combines switching and tuning capabilities using integrated p-i-n and varactor diodes. The structure employs metallic patterns on the top and bottom layers of an FR4 substrate, to realize four switching

states that support transmission, absorption, selective reflection, and full reflection. By incorporating a varactor in the top layer, the geometry provides continuous frequency tunability in each operating state without any modification of the physical configuration. The operation mechanism of the MRFSS is interpreted through a detailed ECM, which highlights the utilization of the metallic patterns, p-i-n diodes, varactors, and biasing elements. A close agreement between the ADS-based circuit responses and the full-wave HFSS simulations validates the accuracy of the proposed MRFSS geometry.

The chapter also discusses the biasing methodology, where a parallel biasing technique is employed so that the top and bottom layer p-i-n diodes and the top layer varactors are independently controlled using only four terminals across the entire array. A prototype is fabricated and characterized in a free-space measurement setup. The measured scattering parameters confirm that all characteristics are achieved with good agreement with simulations for both normal and oblique incidence. The structure maintains stable performance under TE polarization up to large oblique angles, which verifies its robustness for practical deployment.

Although dual-polarization operation is desirable in many practical applications, the proposed topology is intentionally designed to be single-polarized to avoid the complexities associated with realizing a polarization-insensitive reconfigurable structure. Such complexities include the need for multiple dielectric layers, a four-fold symmetric geometry, the careful placement of multiple p-i-n diodes and varactors in each unit cell, and the corresponding biasing networks. In addition to demonstrating the desired switching and tuning characteristics, the chapter examines practical non-idealities that influence the MRFSS performance. The discussion highlights the impact of varactor parasitic resistance and the use of low-loss dielectric substrates on the amplitude variation of the tunable responses. As a result, the proposed MRFSS operates multifunctional EM characteristics along with tunable responses in a single-layer topology, which is attractive for adaptive filtering, tunable radomes, and cognitive EM platforms.

A comparison is also presented in Table 4.3, which highlights the proposed design against existing literature structures in terms of number of operating modes, tuning range, insertion loss, absorptivity, reflection level, angular stability, biasing complex-

ity, number of components per unit cell, and electrical size. This comparison shows that the proposed MRFSS achieves a favourable compromise among multifunctional operation, tunability, and structural compactness.

Overall, this research work advances the capabilities established in the previous chapters by transitioning from fixed-frequency switchable RFSS designs to a multifunctional surface that supports both discrete-state switching and continuous frequency tuning within the same geometry. At the same time, the design intentionally remains single-polarized in order to keep the biasing and layout complexity manageable, which reveals an important tradeoff between tunability, polarization behaviour, and structural simplicity. This remaining limitation, together with the insights gained on biasing, parasitic effects, and measurement strategies, motivates the next stage of the thesis. The subsequent chapter builds on the concepts developed here and explores more advanced wideband RFSS configurations that further extend multifunctionality across the operating bands, while addressing constraints related to polarization response, operational bandwidth, and system-level integration.

# Chapter 5

## Wideband Polarization-Insensitive RFSS-based Rasorber/ Absorber/ Transmitter/ Reflector

### 5.1 Introduction

The earlier chapters of this thesis establish a progressive development of RFSS by moving from basic switching mechanisms to multifunctional and frequency-tunable platforms. The first contribution, presented in Chapter 2, introduces a single-diode configuration that provides narrowband switching between absorption and transmission responses within a compact, polarization-insensitive geometry. The second work, discussed in Chapter 3, enhances this capability by employing two independently driven p-i-n diode sets with FPGA-based digital control, enabling three distinct EM responses (absorption, transmission, and reflection) with automatic real-time switching. The third contribution, detailed in Chapter 4, further advances the concept by integrating varactor diodes alongside the p-i-n switching elements, allowing both discrete mode selection and continuous frequency tunability for each operation. Although these three works collectively demonstrate significant improvements in reconfigurable behavior, all of them operate in narrow frequency bands, which limits their applicability in wideband or broadband EM environments.

With the advent of technology, modern platforms require multifunctional EM operations such as absorbers, rasorbers, transmitters, reflectors, etc., with wide

bandwidths covering a large frequency span. Multiple systems, including cognitive radars, wideband communication networks, and stealth-aware sensing platforms, often operate over multiple spectral zones, where narrowband behavior geometries are inadequate. While the tunable RFSS from the previous chapter provides frequency agility, its operational band remains limited due to the single-layer topology and the inherent constraints of lumped-component integration, thereby making the structure less suitable for scenarios requiring broadband suppression, wideband filtering, or multi-octave EM control. These constraints motivate the need for an extended architecture that can support wideband operation while retaining reconfigurability and polarization-insensitivity characteristics.

To address these limitations, the present chapter introduces a wideband multifunctional RFSS that utilizes a multilayer configuration, resistive components, and diode-based switching technique to achieve four distinct broadband EM operations, viz., absorber, absorption, transmission, and reflection responses within a single geometry. This design employs two FR4 layers separated by an air spacer, enabling strong inter-layer coupling and enhanced bandwidth performance. The top layer integrates a modified square loop with symmetric dipole arms, each equipped with a p-i-n diode and a lumped resistor that broadens the absorption band. The bottom layer incorporates another metallic loop connected through vias to rectangular patches, along with a second set of p-i-n diodes that regulate wideband transmission and reflection characteristics. By controlling the two diode sets independently as well as carefully loading lumped resistors at strategic locations, the structure realizes four EM states with wide bandwidths.

This chapter also investigates the EM behavior of the multilayer structure using an equivalent circuit model that clarifies the individual roles of the resistive paths, capacitive slots, and switching elements behind the wideband operating ranges. The geometry is examined under different polarization and oblique-incidence conditions to confirm stable broadband performance, which is essential for practical deployment. A one-dimensional prototype of the proposed structure is fabricated using standard PCB processes and is experimentally validated using the custom-built PPW measurement setup. The measured scattering parameters closely match the simulated responses across all four operating modes, confirming the feasibility of

achieving wideband multifunctional responses in a compact multilayer RFSS.

The remaining sections of this chapter describe the complete development of the proposed wideband reconfigurable structure. The design and analysis section explains the multilayer geometry, diode placements, resistor integration, and circuit interpretations that collectively produce the wideband switchable behavior. This is followed by a detailed description of the fabrication and measurement procedures, including the normal and oblique incidence PPW characterization approach. The chapter concludes with a comparison to earlier reported works, highlighting the novelty of the proposed RFSS geometry.

## 5.2 Design and Analysis

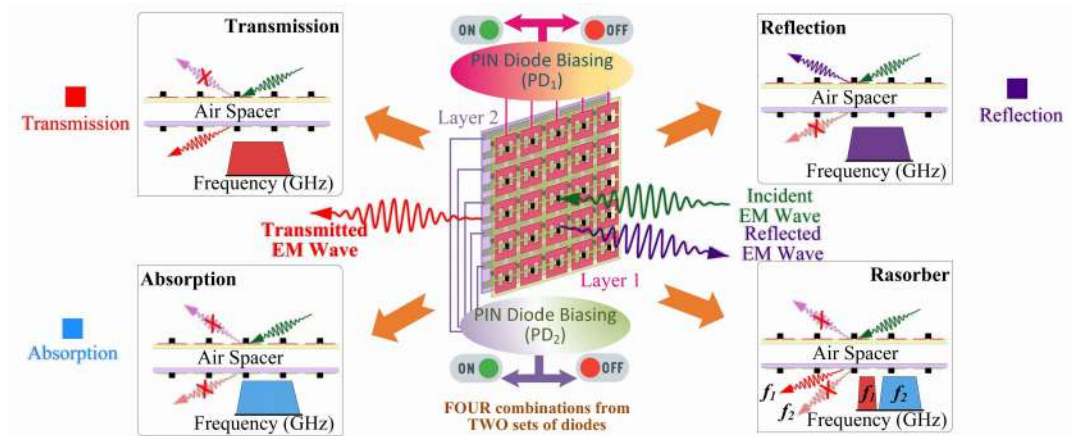


Figure 5.1: Conceptual diagram illustrating four distinct EM operations of the proposed RFSS geometry.

A switchable RFSS structure can be realized by using single or multiple p-i-n diodes (or varactors) mounted either on the same layer or in different layers to enable various EM functionalities. While a single-layer reconfigurable design offers a smaller footprint, integrating multiple diodes and their associated bias lines in the structure, especially for a polarization-insensitive topology, is highly complex. In contrast, placing diodes on separate layers provides greater flexibility as well as allows for a wider range of EM functionalities compared to the same-layer approach. Moreover, a multi-layer design can achieve a wideband response by implementing the cascaded configuration.

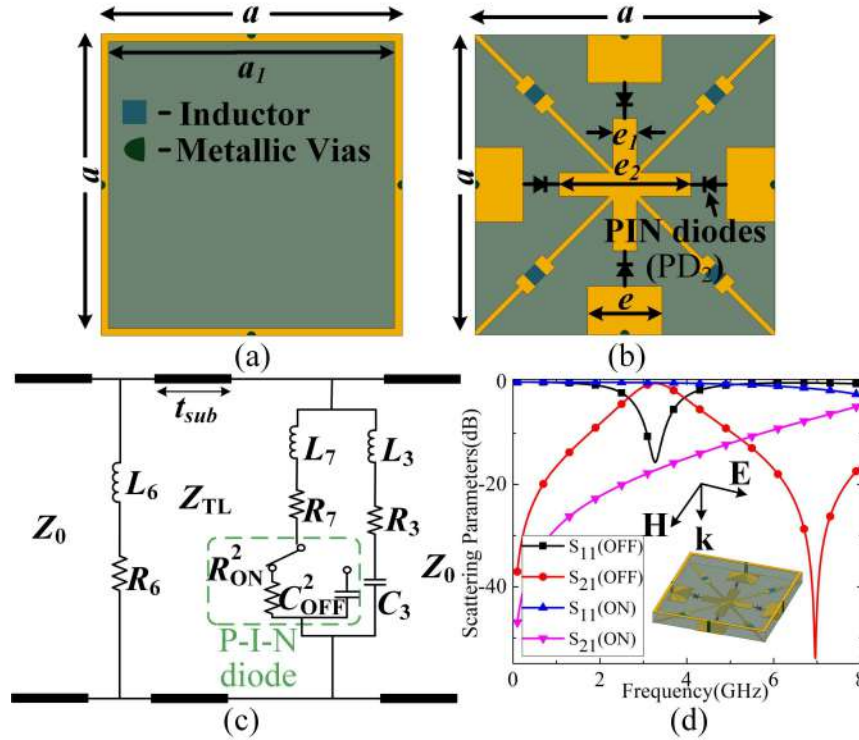


Figure 5.2: Layer 2 of the proposed RFSS geometry: (a) top view, (b) bottom view, (c) equivalent circuit, and (d) simulation results. The optimized dimensions are:  $a = 10$  mm,  $a_1 = 9.5$  mm,  $e = 2.5$  mm,  $e_1 = 4.4$  mm, and  $e_2 = 0.8$  mm.

The previous works have used single-layer configurations, but their EM responses are limited to narrowband operations only. Citing these limitations, a two-layer configuration can be adopted to widen the EM bandwidth while improving the number of EM operations. Therefore, the proposed RFSS geometry adopts a two-layer configuration, with one set of p-i-n diodes ( $PD_1$ ) on the top of layer 1 and another set ( $PD_2$ ) on the bottom of layer 2, as illustrated in Figure 5.1. By independently controlling the diode voltages, four distinct operating modes can be realized: OFF ( $PD_1$ )-OFF ( $PD_2$ ), OFF-ON, ON-OFF, and ON-ON. The diodes exhibit different constitutive parameter values (inductance, capacitance, and resistance) in different states. By integrating these components with the distributed parameters associated with the metallic patterns engraved on opposite sides of the geometry, the proposed RFSS achieves various EM characteristics, including transmission, reflection, absorption, and raserber functionality.

To realize different functionalities, each of the top and bottom layers has been separately designed with the aim of achieving specific EM features, and later com-

bined to exhibit the overall responses. The top layer is primarily designed for absorption/reflection characteristics, whereas the bottom layer is focused on switchable transmission/reflection behavior. This reconfigurability is realized by integrating a set of p–i–n diodes ( $PD_2$ ) on the bottom side of layer 2 and patterning the biasing lines on its top side. The bandpass response can be obtained from a parallel  $RLC$  circuit, whereas the bandstop behavior results from a combination of inductance and resistance. To meet these circuital requirements, the top side of layer 2 features a square-loop geometry, which is connected to the rectangular patches on the bottom side through metallic vias, as depicted in Figures 5.2(a) and (b), respectively. FR4 ( $\epsilon_r = 4.4$ ,  $\tan \delta = 0.02$ ) is used as the constituent dielectric having a thickness  $t_1 = 1$  mm. On the bottom side of the substrate, the p–i–n diodes ( $PD_2$ ) are symmetrically positioned between the rectangular patches and the cross-dipole. They have an ON-state resistance  $R_{\text{ON}}^2 = 0.56 \Omega$  and an OFF-state capacitance  $C_{\text{OFF}}^2 = 0.35$  pF. In the ON state, the diodes establish a short-circuit path, effectively transforming the structure into a continuous conductive surface that behaves as a reflective ground plane. Conversely, in the OFF state, the diodes generate a parallel  $RLC$  circuit configuration, enabling the bandpass response. The equivalent circuit model of layer 2 and its simulated responses are presented in Figures 5.2(c) and (d), respectively, displaying a complete reflection up to 7 GHz under the ON state and a transmission behavior with an insertion loss of 0.27 dB at 3.28 GHz under the OFF state.

Conversely, layer 1 requires two key elements: a switching circuit and a lossy component to achieve distinct responses under different conditions. The switching response is realized by mounting p–i–n diodes ( $PD_1$ ) on the top side, while the lossy effect is achieved by strategically placing lumped resistors in the design. The layer should independently exhibit a switchable response between a low-pass response and a lossy low-pass behavior, which, when combined with layer 2, can exhibit two different EM functionalities. To achieve a low-pass lossy filter characteristic, the top layer should be configured with a parallel  $RLC$  circuit along with a lumped resistor, where the resistance effect can be bypassed to ensure only the low-pass behavior. This can be achieved by placing the resistors in parallel with the p–i–n diodes ( $PD_1$ ), resulting in a pure low-pass response under the forward bias (ON state) of the diode.

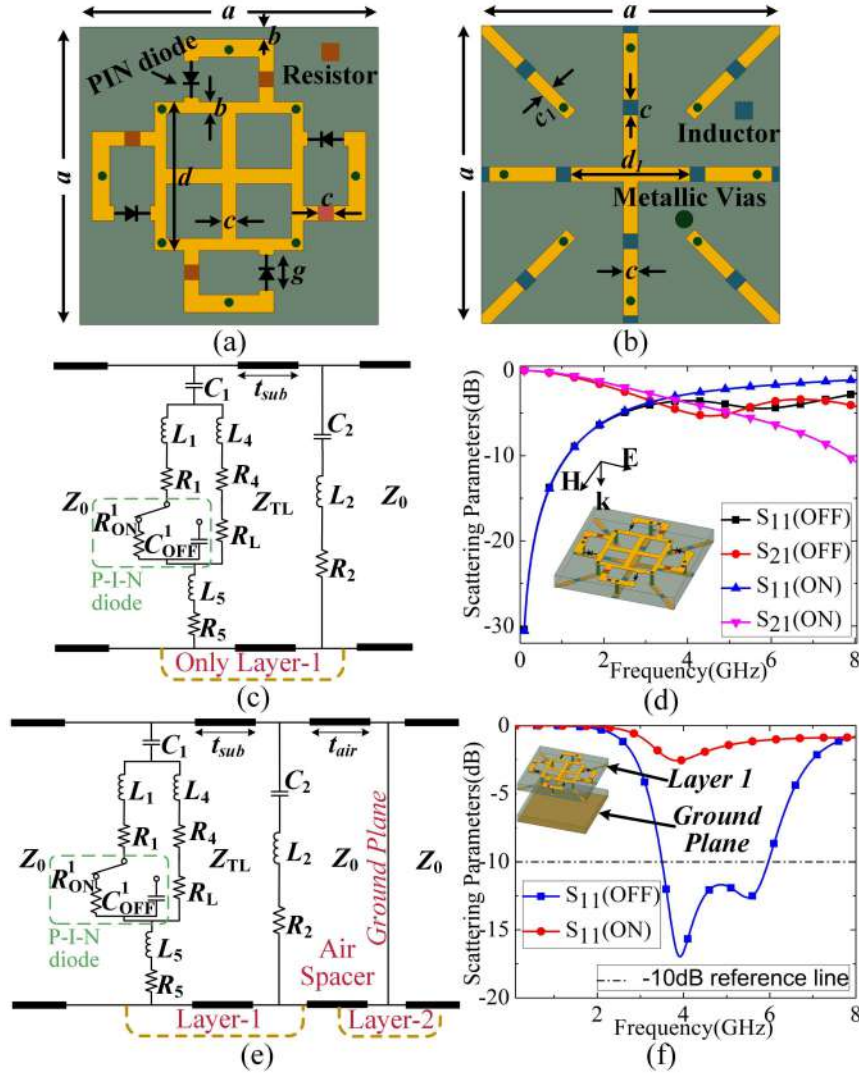


Figure 5.3: Layer 1 of the proposed RFSS geometry: (a) top view, and (b) bottom view. Only Layer-1: (c) equivalent circuit, and (d) simulation results. Layer 1 along with ground plane: (e) equivalent circuit, and (f) simulation responses. The optimized dimensions are:  $a = 10$  mm,  $b = 0.4$  mm,  $c = 0.5$  mm,  $c_1 = 0.42$  mm,  $d = 5$  mm,  $d_1 = 4$  mm,  $g = 1.2$  mm.

In the OFF state, the resistor effect becomes active, introducing a lossy response. Accordingly, the top side of layer 1 features a modified square loop integrated with four symmetric dipole arms, each containing a parallel combination of a p-i-n diode and a lumped resistor, as shown in Figure 5.3(a). The biasing circuit, along with lumped inductors, is positioned on the bottom side of layer 1, as depicted in Figure 5.3(b). FR4 is considered as the substrate for layer 1, having a thickness  $t_1 = 1$  mm.

The equivalent circuit model of layer 1 is presented in Figure 5.3(c). The diodes

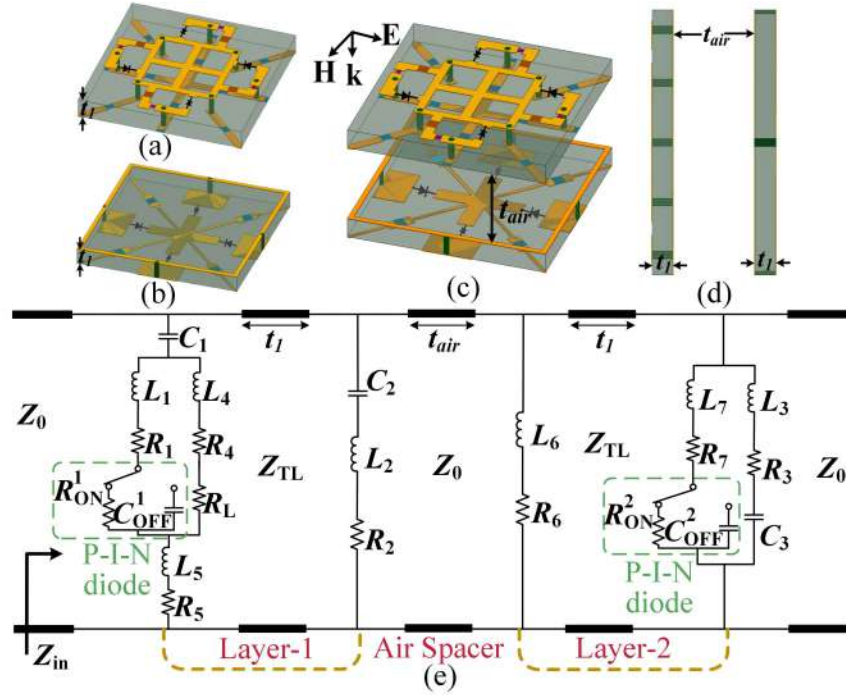


Figure 5.4: Design of the proposed RFSS geometry. Isometric view of: (a) layer 1, and (b) layer 2. Overall structure: (c) isometric view, and (d) side view. (e) Equivalent circuit model. The dimensions are:  $t_1 = 1$  mm and  $t_{air} = 4$  mm.

( $PD_1$ ) have an ON-state resistance  $R_{ON}^1 = 0.85 \Omega$  and an OFF-state capacitance  $C_{OFF}^1 = 0.17$  pF. In the ON state, the top metallic pattern forms a low-loss  $RLC$  circuit, effectively bypassing the lumped resistor  $R_L$  effect. In the OFF state, the circuit undergoes multiple resonances due to the combined effects of top and bottom layer patterns, resulting in a lossy filter characteristic. Figure 5.3(d) presents the simulated responses of layer 1, demonstrating a low-pass filter response in the ON state and a resonant lossy behavior in the OFF state. To further illustrate the contribution of the switching element and lumped resistor, a metal sheet is positioned at 4 mm ( $t_{air}$ ) below the top layer, creating a reflective ground plane at the bottom. The corresponding equivalent circuit and its simulated responses are presented in Figures 5.3(e) and (f), respectively, showing wideband absorption and near-perfect reflection under the OFF and ON states, respectively. In the OFF state, the ground plane provides the required quarter-wavelength condition with respect to the lossy top layer, thereby resulting in the wideband absorption. In the ON state, the top layer reflects most of the signal, and the overall configuration displays the reflective behavior.

Table 5.1: Realization of Wideband Multifunctional Responses in the Proposed RFSS

Working states of diodes ( $PD_1$ – $PD_2$ )	Desired characteristics of layer 1; desired parameters in $PD_1$	Desired characteristics of layer 2; desired parameters in $PD_2$	Lossy (Yes/No); Resistance effect in layer 1	Overall EM characteristics
OFF–ON	Parallel $RLC$ circuit; OFF state capacitance ( $C_{OFF}$ )	Complete reflector; ON state resistance ( $R_{ON}$ )	Lossy; High resistance ( $30 \Omega$ )	Absorber
OFF–OFF	Parallel $RLC$ circuit; OFF state capacitance ( $C_{OFF}$ )	Parallel $RLC$ circuit; OFF state capacitance ( $C_{OFF}$ )	Lossy; High resistance ( $30 \Omega$ )	Rasorber (T–A)
ON–OFF	Parallel or series $RLC$ circuit; ON state resistance ( $R_{ON}$ )	Parallel $RLC$ circuit; OFF state capacitance ( $C_{OFF}$ )	Low-loss; Resistance is bypassed	Transmitter
ON–ON	Parallel or series $RLC$ circuit; ON state resistance ( $R_{ON}$ )	Complete reflector; ON state resistance ( $R_{ON}$ )	Low-loss; Resistance is bypassed	Reflector

T–A: Transmission–Absorption;  $C_{OFF}$ : Capacitance in OFF state of the p-i-n diode;  $R_{ON}$ : Resistance in ON state of the p-i-n diode.

Once the analyses of individual layers are completed, the overall RFSS structure is configured by cascading layers 1 and 2 with an intermediate air gap, as illustrated in Figures 5.4(a)–(d). The airgap thickness ( $t_{air}$ ) is optimized at 4 mm to enable all necessary functionalities within a single geometry. By controlling the diode bias conditions ( $PD_1$  and  $PD_2$ ) based on the metallic patterns and lumped resistors, the proposed design achieves four distinct wideband EM operations, including absorption, transmission, reflection, and rasorber responses. In the OFF state of  $PD_1$ , the lumped resistors ( $R_L$ ) appear in parallel with the  $RLC$  circuit, showing a lossy characteristic from the top layer. Meanwhile, layer 2 acts as a complete reflector when  $PD_2$  is in ON state. Consequently, the overall combination (OFF–ON) produces a wideband absorption response, as described in the previous paragraph. The rasorber function, which combines wideband absorption with a transmission band, can be realized similarly to the absorber mode. However, in this case, the bottom layer must exhibit a bandpass feature at the transmission frequency while maintaining a reflective behavior during the absorption band. This requisite response is obtained from layer 2 in the OFF state of  $PD_2$ , thereby resulting in a rasorber with a transmission–absorption (T–A) feature under the OFF–OFF condition. The remaining two EM behaviors, viz., transmission and reflection, can be achieved by minimizing the lossy effect of the lumped resistor. Since  $PD_1$  is placed in parallel with the lumped resistor ( $R_L$ ) in the top layer, its low ON-state resistance ( $R_{ON}^1$ ) bypasses the lossy resistive element during the ON state. Therefore, during the ON–OFF condition, the  $RLC$  circuits from both layers generate multiple low-loss

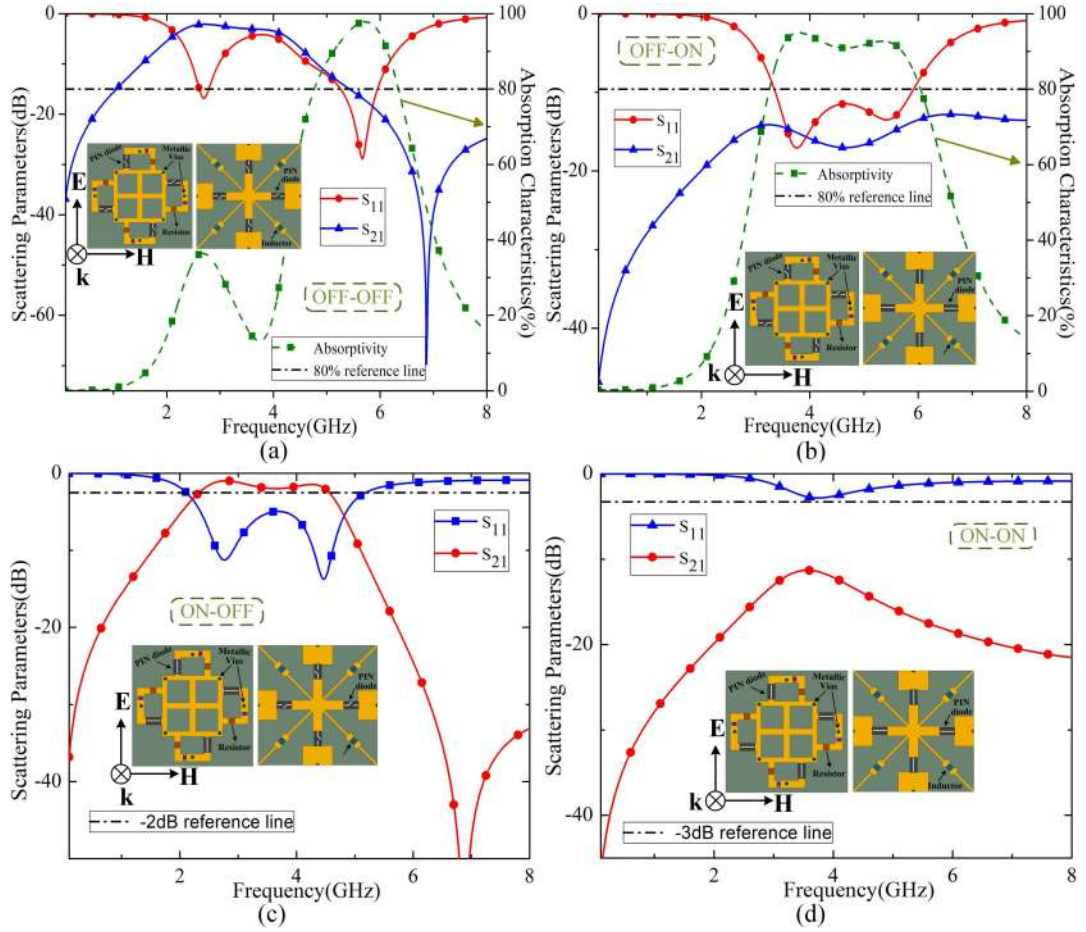


Figure 5.5: Simulated scattering parameters of the proposed wideband RFSS geometry: (a) transmission-absorption (T-A) mode, (b) absorption mode, (c) transmission mode, and (d) reflection mode. The inset top and bottom views of layers 1 and 2 represent operating modes.

resonances, which can be blended together to generate a wideband transmission response. Finally, the reflection response can be achieved by configuring one or both layers as reflectors. Layer 2 functions as a full reflector under the ON state of  $PD_2$ , while layer 1 exhibits an  $RLC$  circuit bypassing the lossy component during the ON state of  $PD_1$ , leading to an overall wideband reflection behavior. Table 5.1 provides a summary of the design methodology, outlining the above mechanisms behind each EM function in the proposed RFSS geometry.

To further validate the design, the ECM of the proposed RFSS structure is presented in Figure 5.4(e), by combining the circuit models of the individual layers. In layer 1, the top side metallic pattern exhibits a capacitance  $C_1$  due to the gap between the neighboring unit cells, while inductance  $L_1$  and resistance  $R_1$  result from

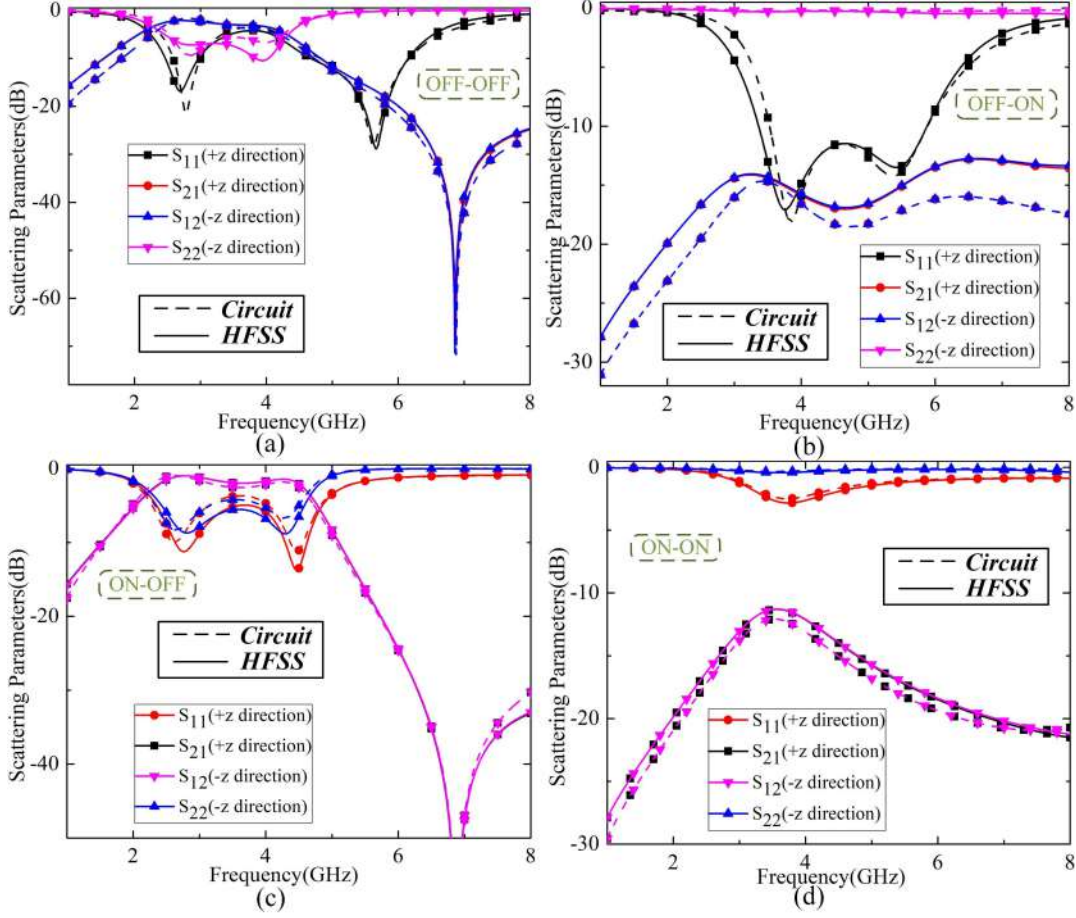


Figure 5.6: Comparison of the proposed wideband RFSS geometry scattering responses in HFSS and ADS software: (a) transmission-absorption (T-A) mode, (b) absorption mode, (c) transmission mode, and (d) reflection mode. The optimized parameter values are  $L_1 = L_3 = L_5 = 0.01$  nH,  $L_2 = 10$  nH,  $L_4 = 3.65$  nH,  $L_6 = 4.95$  nH,  $L_7 = 1.52$  nH,  $L_8 = 9$  nH,  $C_1 = 0.3$  pF,  $C_2 = 0.03$  pF,  $C_3 = 0.1$  pF,  $R_1 = 5 \Omega$ ,  $R_2 = R_3 = R_4 = R_7 = 0.01 \Omega$ ,  $R_5 = 2.5 \Omega$ ,  $R_6 = 3.5 \Omega$ ,  $R_8 = 1 \Omega$ ,  $R_{ON}^1 = 0.85 \Omega$ ,  $C_{OFF}^1 = 0.17$  pF,  $R_{ON}^2 = 0.56 \Omega$ ,  $C_{OFF}^2 = 0.35$  pF, and  $R_L = 65 \Omega$ .

the metallic patch connected to diode  $PD_1$ . Additionally,  $L_4$  and  $R_4$  arise from the metallic pattern in series with the lumped resistor  $R_L$ . During the ON state, the diode is modeled as a small resistance ( $R_{ON}^1$ ), while in the OFF state, it is represented as a high capacitance ( $C_{OFF}^1$ ). The parameters  $L_5$  and  $R_5$  correspond to the central cross dipole and square loop on the top side of layer 1. The bottom side of layer 1 is characterized by a series  $R_2$ - $L_2$ - $C_2$  circuit resulting from the bias lines designed for the diodes. The constituent FR4 substrate and the air spacer are represented by small transmission line segments, designated as  $Z_{TL}$  and  $Z_0$ , respectively. For layer 2,  $L_6$  and  $R_6$  represent the circuit parameters for the square loop present on

the top side, which serves as the biasing circuit for the diodes. The bottom side of layer 2 has a cross-dipole and rectangular patches that are similarly modeled as  $L_7$  and  $R_7$ , while the diagonal biasing lines are characterized as a series  $R_3$ – $L_3$ – $C_3$  circuit. The diode  $PD_2$  is represented as a resistance ( $R_{\text{ON}}^2$ ) and capacitance ( $C_{\text{OFF}}^2$ ) under ON and OFF states, respectively. A transmission line segment ( $Z_{\text{TL}}$ ) is similarly used for the bottom layer substrate, having the same thickness as the top layer substrate.

Upon analyzing the circuit diagram, it becomes evident that both layers 1 and 2 facilitate switching operations using the p–i–n diodes. When  $PD_2$  is in the OFF state, a bandpass response is generated due to the parallel  $RLC$  circuit formed by the inductances  $L_3$ ,  $L_6$ , and the capacitance  $C_{\text{OFF}}$ . Conversely, when  $PD_2$  is in the ON state, the absence of any resonance leads to a reflective behavior. Similarly, layer 1 is examined under different bias conditions of the diode model. When  $PD_1$  is in the OFF state, the presence of various inductances and capacitances, along with  $C_{\text{OFF}}$  and the resistive component  $R_L$ , contributes to lossy bandpass and bandstop responses. In contrast, when  $PD_1$  is in the ON state, the small resistance ( $R_{\text{ON}}^1$ ) of the diode effectively cancels the effect of  $R_L$ , resulting in a low-loss transmission response. Overall, the circuit diagram validates the concept behind the occurrence of multiple EM responses from the individual layers of the proposed geometry, highlighting the interplay between the diode states and circuit components.

### 5.3 Simulation Results

The final RFSS structure, comprising layers 1 and 2 separated by an air spacer, has been simulated using Ansys HFSS 2020. Under the OFF ( $PD_1$ )–OFF ( $PD_2$ ) condition, a rasorber (T–A) behavior is achieved, exhibiting a transmission coefficient magnitude of  $-2.1$  dB at 2.69 GHz and a wide absorption bandwidth (with  $> 80\%$  absorptivity) of 28.5% in the range of 4.76–6.34 GHz, as depicted in Figure 5.5(a). The transmission band results from the individual passband characteristics of both layers 1 and 2, while the wideband absorption is attributed to the lossy nature of layer 1 combined with the reflective characteristic of layer 2. During this condition, the diodes are modeled with OFF-state capacitances, which contribute

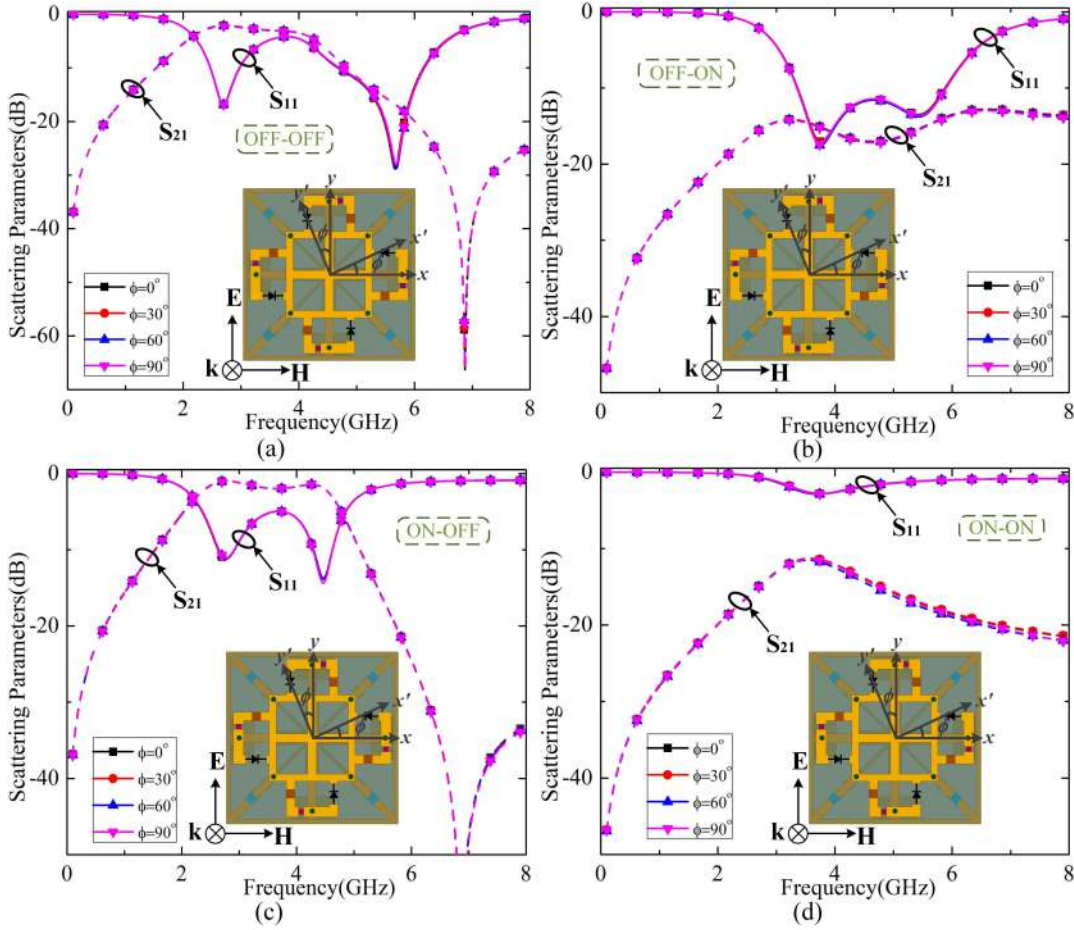


Figure 5.7: Scattering parameters of the proposed wideband RFSS geometry for different polarization angles under normal incidence: (a) transmission-absorption (T-A) mode, (b) absorption mode, (c) transmission mode, and (d) reflection mode.

to the generation of low-loss transmission and lossy absorption responses.

In the OFF–ON case, layer 1 retains its previous lossy filter characteristic, while the response of layer 2 is altered due to the change in the bias condition of  $PD_2$ . Under forward bias, the diode exhibits a low resistance value ( $R_{ON}^2$ ), allowing the bottom side of layer 2 to act as an adaptive ground plane. Consequently, the transmission band observed in the previous rasorber configuration is transformed into an absorption band at the same frequency. This leads to the merging of two absorption bands, ultimately yielding a broad absorption response in this mode. The simulated result validates the concept, exhibiting a broadband absorber with a fractional bandwidth of 60.21% (considering  $> 80\%$  absorptivity) from 3.25–6.05 GHz, as presented in Figure 5.5(b).

The other operational modes exhibit wideband transmission and reflection char-

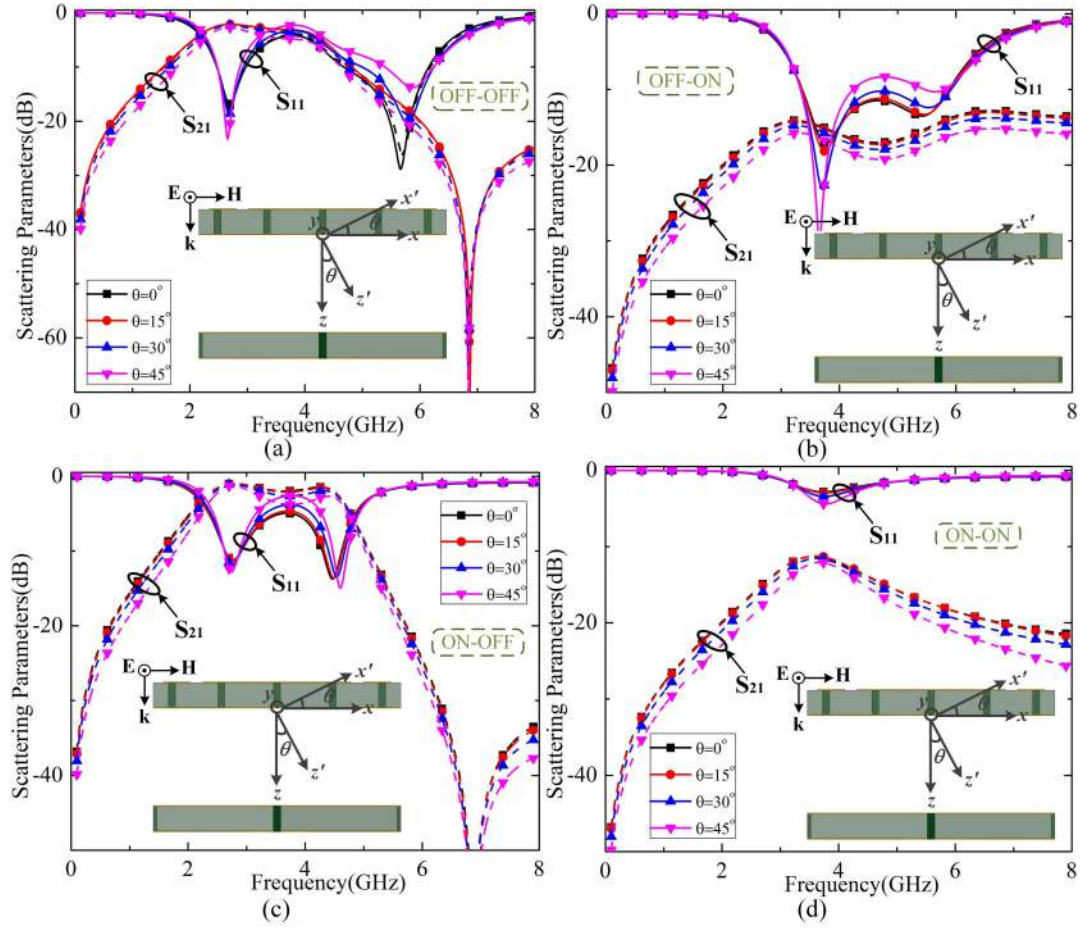


Figure 5.8: Scattering parameters of the proposed wideband RFSS geometry for different incidence angles under TE polarization: (a) transmission-absorption (T-A) mode, (b) absorption mode, (c) transmission mode, and (d) reflection mode.

acteristics during the ON–OFF and ON–ON states, respectively. In both cases, the diode in layer 1 ( $PD_1$ ) is forward-biased, resulting in a low resistance value ( $R_{ON}^1$ ) that effectively bypasses the lumped resistor  $R_L$ . This arrangement allows the incident EM wave to interact with the structure without incurring significant ohmic losses, thereby generating multiple resonance conditions. In the ON–OFF case, each layer independently exhibits a bandpass filter response, and by carefully selecting the geometric dimensions, these resonances can be combined to achieve a wideband characteristic. Consequently, the proposed topology functions as a broadband transmitter, covering a frequency range of 2.41–4.49 GHz, with a fractional bandwidth of 60.28%, as illustrated in Figure 5.5(c). The overall insertion loss remains below 2 dB, with a minimum value of 0.9 dB observed at 2.74 GHz. In the final ON–ON mode, the bottom layer p-i-n diode ( $PD_2$ ) is also forward-biased, resulting in a complete

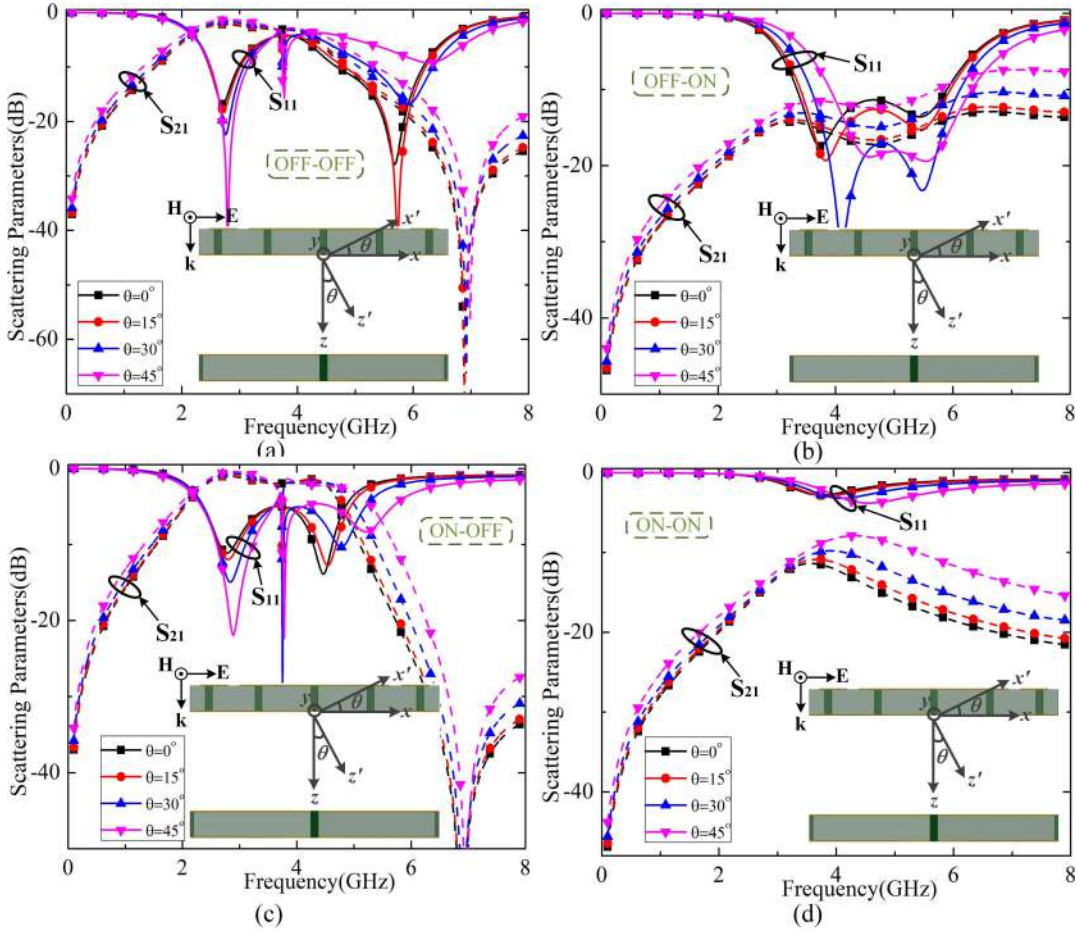


Figure 5.9: Scattering parameters of the proposed wideband RFSS geometry for different incidence angles under TM polarization: (a) transmission-absorption (T-A) mode, (b) absorption mode, (c) transmission mode, and (d) reflection mode.

reflective behavior. Layer 1 maintains the same bandpass characteristic as before; however, the transmission band of the top layer is diminished due to the reflective operation of layer 2, yielding only a minor resonance around 4 GHz. As a result, the complete structure operates as a wideband reflector, achieving a reflection loss of less than 2.8 dB across the entire operating range, as depicted in Figure 5.5(d).

To further explore the bidirectional property of the proposed RFSS, the structure has been studied for EM waves impinging from both the  $+z$  and  $-z$  directions, as illustrated in Figure 5.6. The results show that the geometry maintains consistent performance during the transmission (ON-OFF) and reflection (ON-ON) modes regardless of the wave direction. However, a notable change is observed for the absorption mode (OFF-ON): while the  $+z$ -directed wave results in absorption, the structure behaves as a complete reflector when the wave is incident from the

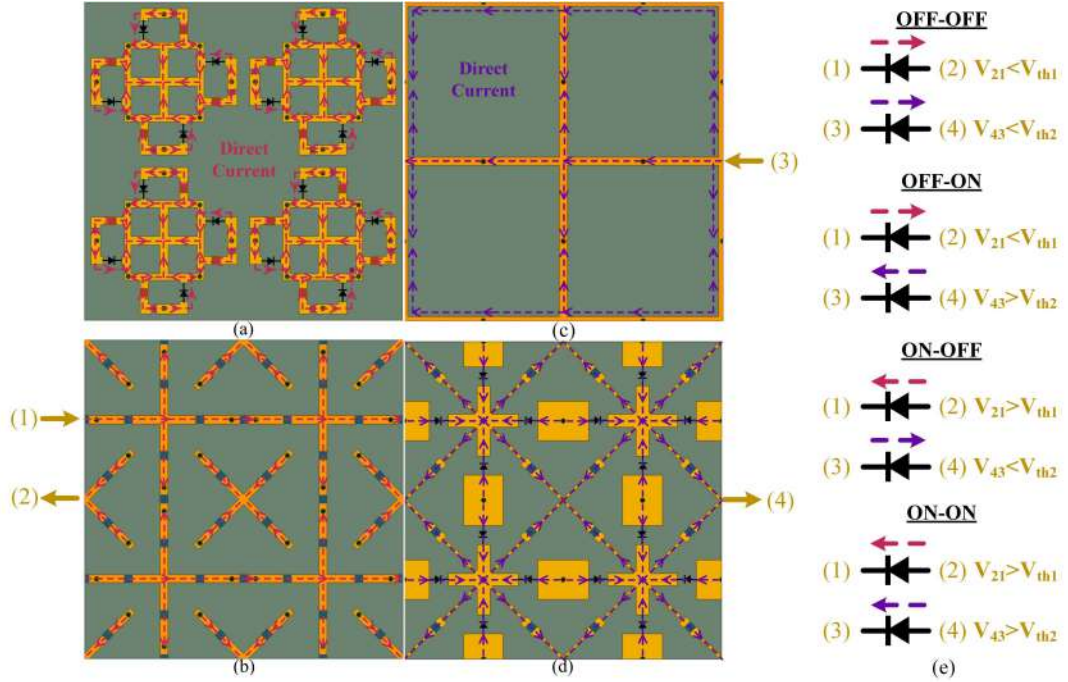


Figure 5.10: Biasing technique for four different operating states, viz. OFF–OFF ( $V_{21} < V_{th1}$ ,  $V_{43} < V_{th2}$ ), OFF–ON ( $V_{21} < V_{th1}$ ,  $V_{43} > V_{th2}$ ), ON–OFF ( $V_{21} > V_{th1}$ ,  $V_{43} < V_{th2}$ ), and ON–ON ( $V_{21} > V_{th1}$ ,  $V_{43} > V_{th2}$ ) of the proposed RFSS geometry: (a) top side of layer 1, (b) bottom side of layer 1, (c) top side of layer 2, and (d) bottom side of layer 2. (e) Bias voltage conditions to operate the diodes.

$-z$  direction. This phenomenon arises from the absorber mechanism, where layer 1 exhibits resonance behavior and layer 2 functions as a ground plane. When the incident wave arrives from the  $-z$  direction, the electric field first interacts with layer 2, leading to a reflection response independent of the top-layer behavior. Similarly, during the absorber (T–A) operation in the OFF–OFF mode, the transmission response remains unchanged with direction, but the absorption level significantly diminishes for the  $-z$ -directed wave, resulting in a multi-band transmission response from the overall structure. The distributed parameter values have also been extracted using the curve-fitting method in ADS, and the results closely match the full-wave HFSS simulations, as summarized in Figure 5.6. This strong correlation between ADS-based parameters and full-wave outcomes further validates the design and the equivalent circuit model across various operational states.

Next, the structure has been analyzed for various polarization angles ( $\phi$ ) under normal EM wave incidence, and the results are plotted in Figure 5.7. Owing to the four-fold symmetric arrangement of the metallic patterns, bias lines, and elec-

tronic components, the proposed geometry preserves its EM characteristics across all operating modes even as the polarization angle varies from  $0^\circ$  to  $90^\circ$ .

The RFSS geometry has also been investigated for different incident angles ( $\theta$ ) under both TE and TM polarizations. In the TE mode, the responses across all switching states remain stable up to an incident angle of  $45^\circ$ , as observed in Figure 5.8. In the TM mode, angular stability is maintained in the absorption (OFF–ON) and reflection (ON–ON) states. However, for the OFF–OFF and ON–OFF states, an additional resonance peak appears near the transmission band, especially at larger incident angles ( $\theta \geq 30^\circ$ ), as shown in Figure 5.9. This extra resonance arises due to the interaction between the electric field orientation and the metallic vias in the bottom layer, which enhances the surface current distribution under oblique incidence.

## 5.4 Fabrication And Experimental Verification

### 5.4.1 Biasing Framework

Since the proposed geometry incorporates multiple diodes in each layer, with an intent to regulate them independently, dedicated biasing lines should be carefully designed to supply the required DC voltage to each diode and achieve the desired EM responses. In addition, a parallel biasing network is preferred due to low power consumption and fast response time [72]. As the structure consists of one set of p-i-n diodes on the top side of layer 1 and another set of diodes on the bottom side of layer 2, four separate terminals are considered to regulate these diodes effectively.

Figures 5.10(a)–(d) illustrate the biasing configuration and the current flow directions in the proposed RFSS. In layer 1, the p-i-n diodes ( $PD_1$ ) are symmetrically arranged on the top side, while the bias lines are printed on the bottom side, connecting to the diode terminals through metallic vias. Lumped inductors are articulately placed in the design to restrict the RF signal while allowing the DC to pass through. Two terminals are designated in layer 1: terminal 1 connects to the positive side of  $PD_1$  through the central cross-dipole bias line, whereas terminal 2 connects to the negative side via the diagonal cross-dipole. Similarly, p-i-n diodes ( $PD_2$ ) are mounted on the bottom side of layer 2, with bias lines engraved on both the top and

bottom sides. The square loop geometry on the top side is connected to the anode of  $PD_2$  through shared vias, while the diagonal lines on the bottom side are connected to the cathode. Terminals 3 and 4 are joined with the top square loop and the bottom diagonal line, respectively, providing direct connections to the diodes in layer 2. Since the bias lines from one unit cell are connected to their adjacent unit cells through the parallel circuit, applying a single DC voltage at one end of the structure will simultaneously activate the corresponding operations across the entire periodic geometry.

Therefore, the diodes in layers 1 and 2 can be independently regulated by applying a supply voltage of  $V_{21}$  between terminals 1 and 2, and a supply voltage of  $V_{43}$  between terminals 3 and 4, respectively. For various operating modes, the voltages across the diodes can be suitably adjusted to achieve the desired EM responses. For example, in the OFF–OFF case, the supply voltages across both diodes ( $PD_1$  and  $PD_2$ ) are maintained below their respective threshold voltages ( $V_{21} < V_{th1}$ ,  $V_{43} < V_{th2}$ ), ensuring that each diode operates in reverse bias. Conversely, in the ON–ON state, the supply voltages are set above the threshold levels ( $V_{21} > V_{th1}$ ,  $V_{43} > V_{th2}$ ), allowing both diodes to function in forward bias conditions. The other operational states are similarly achieved according to their supply voltage requirements. Figure 5.10(e) illustrates the required voltage ranges for different conditions.

### 5.4.2 Fabrication of 1-D Prototype

The conceptual analysis of the proposed geometry is corroborated by fabricating a one-dimensional (1-D) prototype consisting of 15 unit cells arranged in a single row. Each of the top and bottom layers is separately manufactured on FR4 substrates using the PCB etching technique with an overall dimension of  $190 \times 10$  mm<sup>2</sup>. P-i-n diodes BAR 64-02 V [118] and BAR 65-02 V [119] from Infineon Technologies are used on the top side of layer 1 ( $PD_1$ ) and the bottom side of layer 2 ( $PD_2$ ), respectively, enabling the realization of four distinct operating states. A lumped resistor of  $30 \Omega$  from KOA Speer Electronics [131] is mounted on the top side of layer 1 to obtain the desired absorption characteristic. Since the resistor is connected in parallel to diode  $PD_1$ , a short-circuit path is created between the diode terminals, potentially disrupting its switching behavior. To mitigate this issue, a 10 pF lumped

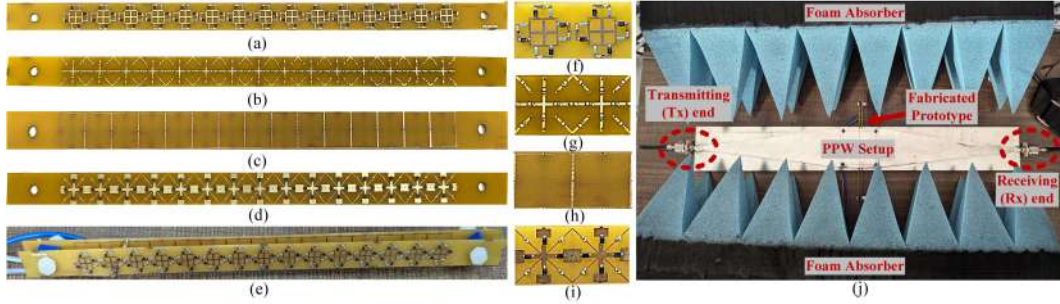


Figure 5.11: Fabricated prototype and measurement setup photographs of the proposed wideband RFSS geometry: (a)–(d) individual layer photographs, (e) overall sample photographs, (f)–(i) enlarged views of the unit cell, and (j) PPW experimental setup for  $S_{11}$  and  $S_{21}$  characteristics.

capacitor from Murata is inserted between the diode and the resistor, effectively breaking the short-circuit condition while maintaining RF signal flow. Finally, two sets of inductors, valued at 3.3 nH and 10 nH with self-resonating frequencies of 6 GHz and 3.2 GHz, respectively, are sourced from Multicomp Pro and strategically positioned to restrict the RF signal from the bias lines. The fabricated RFSS sample, along with detailed photographs of its individual layers, is presented in Figures 5.11(a)–(i).

### 5.4.3 PPW Measurement Setup

To mitigate the high manufacturing costs associated with the 2-D fabricated prototypes required for conventional free-space measurement setups, a similar PPW setup, as used in the previous chapters, has been utilized to characterize the fabricated 1-D prototype. The waveguide is made using two parallel metallic (aluminium) sheets, with the top plate tapered at both ends to facilitate impedance matching and connector soldering, while the bottom sheet is rectangular in shape. The width and height of the central section are specifically determined based on the dimensions of the proposed 1-D RFSS geometry, while the other parameters are carefully optimized to ensure the propagation of the fundamental mode (TEM) through the waveguide. The required spacing between the plates is maintained by using Teflon screws. Figure 5.11(j) illustrates the proposed PPW setup comprising the waveguide and surrounding pyramidal foam absorbers. One VNA (Anritsu S820E) is connected to the two opposite terminals (Tx terminal and Rx terminal) of the waveguide, and

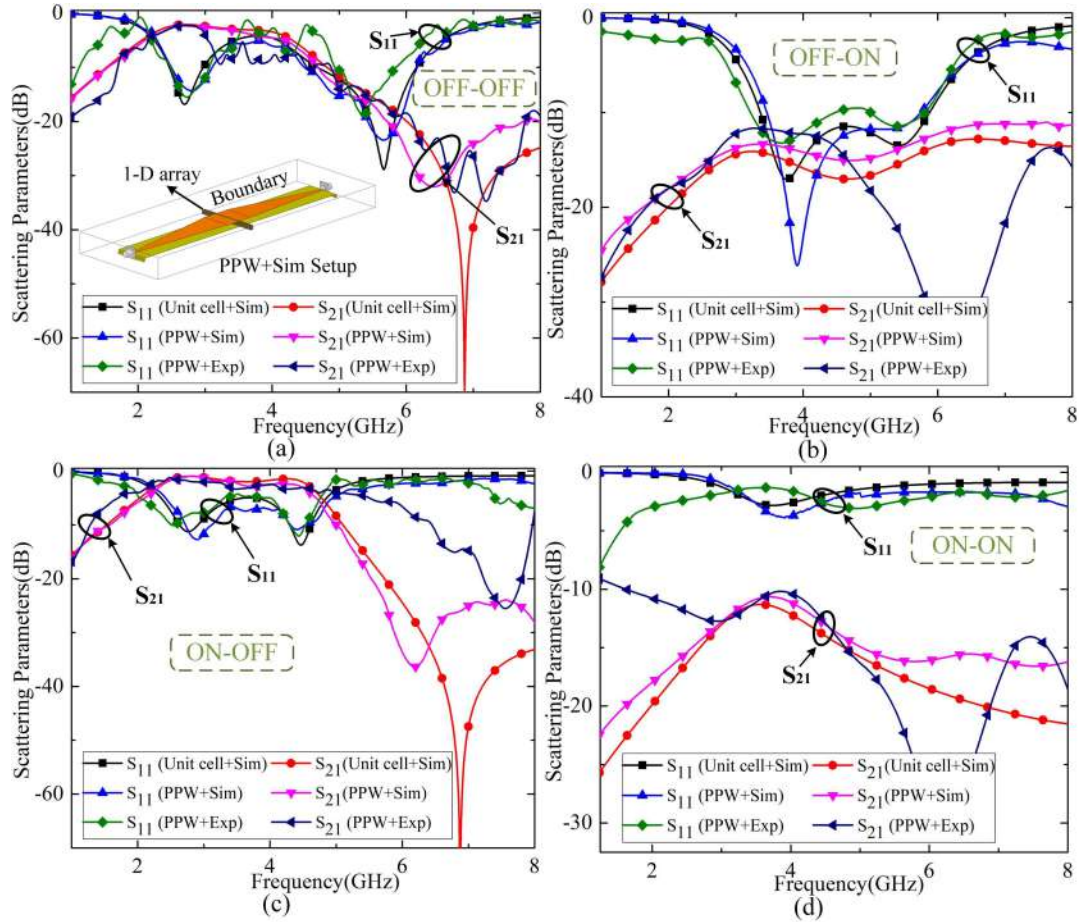


Figure 5.12: Comparison of measured responses with unit-cell simulation results and 1-D array PPW simulation setup results for the proposed wideband RFSS geometry: (a) transmission-absorption (T-A) mode, (b) absorption mode, (c) transmission mode, and (d) reflection mode. The inset figures show the simulation and experimental PPW setups.

two separate DC power supplies are used to regulate the diodes mounted on layers 1 and 2 ( $PD_1$  and  $PD_2$ ).

Initially, the PPW has been calibrated to eliminate the propagation loss in the setup. The  $S_{11}$  has been normalized by placing a metallic sheet of identical size at the center of the waveguide, whereas the  $S_{21}$  has been standardized by measuring the response between the two ends of the waveguide without any sample in between. After calibration, the prototype has been positioned at the center of the waveguide, and the required voltages have been applied across the p-i-n diodes to observe the EM responses under different operating states. The actual responses have been obtained by subtracting the calibrated results from those of the measured results.

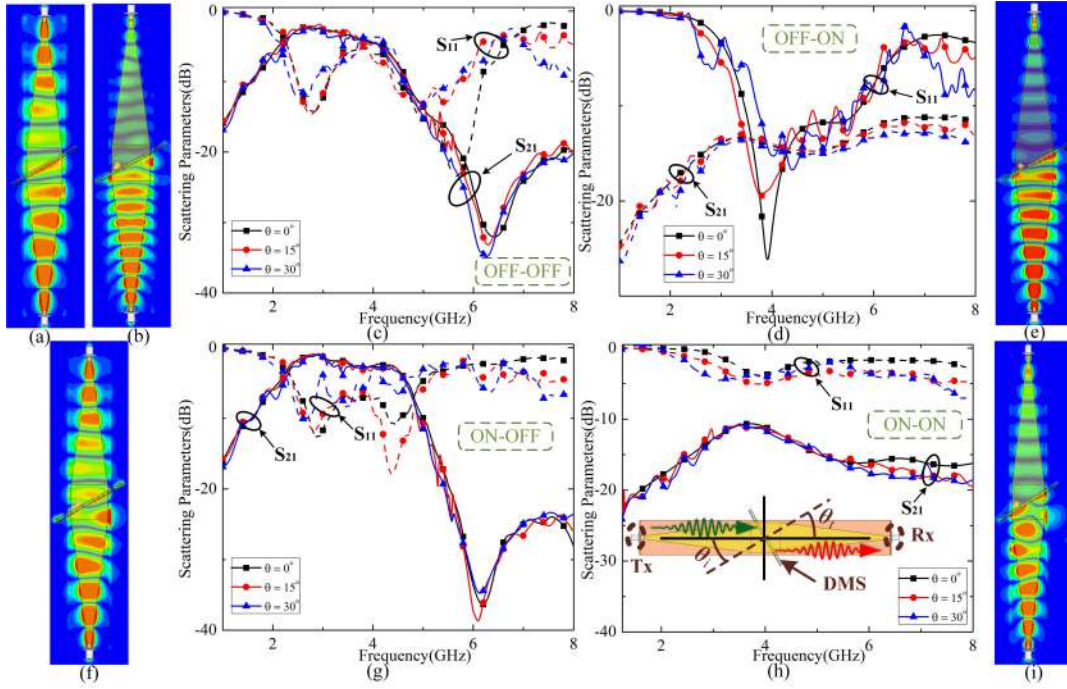


Figure 5.13: Oblique incidence responses and electric field distribution of the proposed wideband RFSS geometry in the PPW setup: rasorber mode – E-field at (a) 2.75 GHz and (b) 5 GHz, and (c) scattering parameters; absorption mode – (d) scattering parameters and (e) E-field at 4 GHz; transmission mode – (f) E-field at 4 GHz and (g) scattering parameters; reflection mode – (h) scattering parameters and (i) E-field at 3.85 GHz. The inset shows the oblique incidence setup in the PPW device.

The pyramidal foam absorbers are installed on both sides of the PPW setup to minimize the edge diffraction and scattering effects, thereby further improving the measurement accuracy.

#### 5.4.4 Validation of Measurement Results

The fabricated prototype has been tested by applying DC voltages across the p-n diodes  $PD_1$  and  $PD_2$ . Two different voltage levels, viz. 1 V and 0 V, have been provided to operate the diodes under forward and reverse bias conditions, respectively, allowing for independent regulation of all four operating states. In the OFF–OFF state, where 0 V is applied across both diodes, the measured response displays a rasorber behavior with an insertion loss of 2.21 dB at 2.77 GHz and an absorption bandwidth of 21.61% from 4.91–6.1 GHz, as presented in Figure 5.12(a). In the next state (OFF–ON mode), with  $PD_1$  biased at 0 V and  $PD_2$  at 1 V,

a wideband absorption response has been observed having an  $> 80\%$  absorptivity bandwidth of  $68.62\%$  ranging from 3.13 to 6.4 GHz, as shown in Figure 5.12(b). During the third case (ON–OFF state), where  $PD_1$  is biased at 1 V and  $PD_2$  at 0 V, a wide transmission characteristic is achieved from 2.32 to 4.06 GHz, with an insertion loss of 2 dB and a fractional bandwidth of  $54.54\%$ , as depicted in Figure 5.12(c). Finally, in the ON–ON state, both diodes are biased at 1 V, resulting in a complete reflective behavior with  $S_{11} < -2.85$  dB across the entire operating range, as observed in Figure 5.12(d). These measured responses from the fabricated samples have been compared with those of the unit cells arranged under periodic boundary conditions as well as a 1-D array designed in a PPW setup. The plots for all four cases are presented in Figure 5.12, showing close agreement despite minor deviations due to parasitic elements, limited fabrication size, and manual setup imperfections.

To further validate the oblique-incidence response of the proposed RFSS geometry, the same PPW approach has been used, which has already been discussed in the Chapter 3. The angular stability of a periodic structure is typically evaluated by rotating the transmitting (Tx) and receiving (Rx) antennas to a specific angle ( $\theta$ ) in a free-space measurement setup. However, a PPW device has fixed end ports, thereby restricting conventional oblique-incidence analysis. A promising solution has been devised by tilting the RFSS structure itself to the required angle ( $\theta$ ) instead of adjusting the port ends. When the TEM wave generated in the PPW setup interacts with the tilted structure at an angle ( $\theta$ ), the transmitted wave refracts in the opposite direction at the same angle and finally reaches the receiver end without distortion. Thus, the configuration ensures an accurate measurement of the  $S_{21}$  under oblique incidence. The  $S_{11}$  response can also be measured using the same setup, where a portion of the reflected wave returns to the excitation port. The PPW setup is illustrated in the inset of Figure 5.13, along with the electric-field distributions at different frequencies. Figures 5.13(a) and 5.13(b) depict the  $E$ -field distributions in the absorber mode (OFF–OFF state) at 2.75 GHz and 5.0 GHz, respectively, confirming wave propagation in the corresponding directions. The attenuation of the  $E$ -field at 4 GHz is presented in Figure 5.13(e) for the absorber mode (OFF–ON state). The remaining field-distribution plots validate the oblique-incidence concept in the PPW setup, correlating with their respective operating modes. Consequently,

Table 5.2: Comparison with other Existing Designs

References	Number of operating modes	Operating functions	IL (dB) or AB (%) or RA (dB)/ Frequency range (GHz)	Operating bandwidths (%)	Polarization	Biasing circuitry	Angular stability (deg)	Unit cell dimensions/ thickness ( $\lambda$ )
[78]	2	Rasorber [A-T-A] Absorber	IL: 3 / 3.47-4.51 LAB: > 80 / 1.18-2.16 UAB: > 80 / 5.15-6.93 AB: > 90 / 1-6.22	40%, 58.7%, 29.5% 144.6%	Dual	Series-Parallel	45 (UC)/ 45 (FS)	28 mm (0.093 $\lambda$ )/ 46 mm (0.013 $\lambda$ )
[84]	2	Rasorber [A-T-A] Rasorber [A-T]	IL: 0.45 / 5.8 LAB: > 80 / 2.9-5.4 UAB: > 80 / 6.3-8.2 AB: > 80 / 2.85-8.11	90.14% 92.6%	Dual	Parallel	50 (UC)/ 45 (FS)	20 mm (0.19 $\lambda$ )/ 6.5 mm (0.14 $\lambda$ )
[94]	3	Transmission Absorption Reflection	IL: 0.82 / N.A. AB: 94 / N.A. RA: > -0.5 / N.A.	~0% ~0% ~0%	Single	Parallel	45 (UC)/ N.A. (FS)	6.5 mm (0.22 $\lambda$ )/ 1 mm (0.03 $\lambda$ )
[95]	3	Transmission Absorption Reflection	IL: < 1 / 0.9-2 / 10-4 AB: > 90 / 6.0-11.9 RA: > -1 / 8.9-10.7	~12.24% ~49.37% ~18.37%	Dual	Series	N.A. (UC)/ N.A. (FS)	36 mm (0.60 $\lambda$ )/ 7.8 mm (0.26 $\lambda$ )
[102]	2	Transmission Transmission	IL: < 1 dB / 1.49-3.45 IL: < 1 dB / 3.4-4.85	79.35% 35.15%	Single	Parallel	70 (UC)/ 70 (FS)	10 mm (0.049 $\lambda$ )/ 0.508 mm (0.002 $\lambda$ )
This Work	4	Rasorber [T-A] Transmission Absorption Reflection	IL: 2.1 / 2.77, AB: > 80 / 4.76-6.34 IL: < 2 / 2.41-4.49 AB: > 80 / 3.25-6.05 RA: > -2.8 / 2-8	28.5% 60.28% 60.21% 120.0%	Dual	Parallel	45 (UC)/ 30 (PPW)	10 mm (0.083 $\lambda$ )/ 6 mm (0.05 $\lambda$ )

Note: N.A.: Not applicable; LAB: Lower absorption bandwidth; UAB: Upper absorption bandwidth;  $\lambda$ : Wavelength corresponding to lowest operating frequency;  
 IL: Insertion loss (in dB); AB: Absorption magnitude (in %); RA: Reflection amplitude (in dB); 0% corresponds to no tuning operation; UC: Unit cell simulation;  
 FS: Free space.

the  $S$ -parameters have been derived under different incident angles ( $0^\circ$ ,  $15^\circ$ , and  $30^\circ$ ) across all four operational modes, reinforcing the effectiveness of the proposed approach. It is noteworthy that the PPW setup can be used to measure the oblique incidence responses for TE polarization only; since the signal propagation direction cannot be altered in the PPW, no TM polarization can be carried out using this setup.

## 5.5 Conclusion

This chapter presents a polarization-insensitive RFSS by utilizing a multilayer topology, resistive components, and diode-based switching to achieve broadband absorption, wideband rasorber (T-A) behavior, broadband transmission, and wideband reflection within a single structure. The proposed configuration utilises two FR4 layers separated by an air spacer, along with modified square-loop metallic patterns and symmetrically placed p-i-n diodes, to achieve strong interlayer coupling and enhanced bandwidth performance. The individual layer analyses have been discussed, with only the layer 1 response, which switches between a low-pass filter and a lossy low-pass response. The integration of lumped resistors in the top layer introduces the lossy behavior in one case and broadens the absorption band and supports wideband rasorber functionality, when the switching layer 2 regulates the transition between transmission and reflection. The combination of FSSs layer 1 and layer 2 allows the overall structure to maintain stable wideband behavior under various switching states, which is essential for wide-spectrum EM platforms and modern multifunctional systems.

An equivalent circuit model is developed to interpret the key operating mechanisms of the multilayer structure. The model captures the contributions of resistive elements, metallic patterns, and switching paths, and explains the interaction between the two layers that determines wideband characteristics. The close match between the circuit responses and full-wave HFSS simulations validates the overall behavior of the proposed structure. The geometry has been analyzed for the polarization-insensitive behavior and angular stability characteristics under TE and TM polarizations. Finally, a 1-D prototype has been fabricated and evaluated us-

ing standard PCB processes and the PPW measurement setup developed in this thesis, which allows reliable characterization under normal and oblique incidence. The measured scattering parameters show excellent agreement with the simulated results, validating the wideband rasorber response, wideband absorption, broadband reflection and transmission states. The angular stability of the structure has been tested using the PPW setup under different incidence angles. These results verify that the proposed RFSS maintains wideband functionality while providing reliable switching performance, making it a suitable candidate for wideband radome systems, low-observable platforms, and multifunctional EM environments.

A comparison with previously reported works is also included in Table 5.2, showing that this geometry is the first proposed geometry to incorporate all four EM operations (absorption, transmission, reflection and rasorber) within a single geometry, where previous switchable RFSS structures are mostly limited to achieving a maximum of three EM states. In addition, several novel features, such as wideband EM functionalities, compact footprint, simple biasing configuration, polarization-insensitivity, and angular stability are clearly observed. Overall, this research work establishes a significant advancement over the earlier contributions by moving from narrowband and tunable multifunctional structures to a wideband reconfigurable geometry capable of simultaneous broadband absorption and rasorber behaviour together with transmission and reflection control.

This chapter, therefore, completes the design-oriented part of the thesis, demonstrating that the switching mechanisms, resistive loading, multilayer configurations, and systematic analysis can be combined to achieve wideband multifunctionality. The next chapter focuses on the experimental characterization framework that supports such multifunctional RFSSs. It introduces the development of an advanced PPW measurement setup with wide-angle capability and explains that this setup enables accurate validation of both narrowband and wideband reconfigurable structures presented across the thesis.

# Chapter 6

## Wide-Angle RFSS

## Characterization using Modified Parallel-Plate Waveguide

### 6.1 Introduction

The earlier chapters of this thesis focus on the design and development of RFSSs, beginning with simple switching concepts and progressively advancing toward multifunctional and wideband designs. These RFSSs have utilized different combinations of p-i-n diodes, varactors, resistive elements, and multilayer topologies to produce a wide range of EM functions, such as transmission, absorption, reflection, rasorber operations, along with frequency tuning behavior under different states. The responses have been simulated in full-wave electromagnetic software (Ansys HFSS) and subsequently characterized using free-space or PPW measurement procedures. However, those PPW-based measurements are mostly limited to normal incidence, because the technique used in those chapters can accurately capture only the  $S_{21}$  measurements, but is not able to measure  $S_{11}$  under oblique incidence. In this regard, the present chapter addresses this limitation by developing an innovative and compact PPW methodology that can accurately characterize both normal and oblique incidence responses for transmission as well as reflection behaviors.

Before introducing the custom-built measurement system developed in this work, it is essential to examine the commonly used experimental approaches for FSS char-

acterization. There exist three different types of characterization systems, viz. free-space measurement, rectangular waveguide measurement and PPW measurement. The free-space measurement system is widely employed due to its ability to measure transmission and reflection responses across a wide frequency span. The system uses two horn antennas (one transmitting and the other receiving), and the sample is placed in between those antennas such that the signal transmitting from one antenna interacts with the sample and finally reaches to the receiving antenna. While suitable for broadband characterization, free-space setups require a sufficiently large sample size to approximate an infinite periodic surface and demand precise mechanical alignment. They also face challenges when capturing oblique-incidence responses because both transmitting and receiving antennas must be physically rotated to specific angles, which sometimes introduces alignment errors, non-uniform illumination, and increased scattering from surrounding absorbers.

Rectangular waveguide measurements offer another standard solution, especially for retrieving material parameters. A small sample, in the dimensions of the waveguide aperture, is generally inserted inside the waveguide, and the signal is impinged on the sample by connecting the two ports of the waveguide to a network analyzer. The measurement process is low-cost, simple, repeatable, and well-controlled, but inherently band-limited due to the cutoff constraints imposed by waveguide dimensions. More importantly, rectangular waveguides support only limited modes and do not allow the evaluation of wide-angle oblique incidence. These limitations make them unsuitable for characterizing RFSS designs that must be analyzed over broad bandwidths and different incident angles.

PPW structures provide an attractive alternative of the above two methods because they support a TEM mode that closely resembles free-space plane-wave illumination. A sample comprising one or two rows of periodic unit cells is generally inserted into the waveguide, where the signal is impinged on the sample by connecting the two ports of the waveguide to a network analyzer. PPWs require significantly smaller sample sizes than free-space setups and inherently reduce diffraction and edge leakage when designed properly. Moreover, they offer stable field distribution and are highly suitable for evaluating periodic surfaces. For these reasons, PPWs are used in several earlier studies, including some of the prototypes developed in

this thesis. In those implementations, the PPW-based setups successfully measure normal-incidence responses and provide preliminary insight into oblique-incidence behavior, but the angular measurement technique is not fully optimized. Specifically, the earlier PPW arrangement produces reasonably accurate oblique-incidence transmission measurements ( $S_{21}$ ), but is less reliable for reflection measurements ( $S_{11}$ ) due to the fixed port geometry and partial signal leakage. These limitations motivate the need for a robust PPW configuration capable of accurately capturing both  $S_{11}$  and  $S_{21}$  over a wide range of incident angles.

This chapter focuses on developing a modified PPW configuration that overcomes the existing drawbacks of the previously used setups and enables accurate characterization of both transmission and reflection responses under normal as well as oblique incidence. The improved configuration introduces a low-cost, mechanically simple, easily repeatable, and structurally stable method for angular measurements. The redesigned PPW ensures uniform field confinement, reduced leakage, and stable quasi-TEM propagation, which collectively enhance the reliability of the extracted scattering parameters. The methodology aligns well with practical measurement requirements and remains compatible with periodic structures, enabling accurate and repeatable EM validation.

The construction of the modified PPW system begins with the geometrical design of the metallic plates, the selection of plate spacing, and the mechanism used to support and position the DUT inside the waveguide. The excitation and receiving sections are arranged to ensure TEM propagation, and absorbers are placed strategically to suppress unwanted reflections and maintain a reliable propagation environment. A dedicated mounting approach is incorporated to introduce controlled angular rotation, enabling stable and repeatable measurements across the required incident angles. These design considerations ensure consistent PPW behavior over the intended frequency range and form the basis for the measurement procedure adopted in this work. The normal- and oblique-incidence characterization steps include configuring the VNA, acquiring reference and sample measurements, and following specific guidelines to maintain repeatability. The results obtained using the modified PPW system demonstrate the accuracy, consistency, and stability of the measurement approach. Overall, the developed PPW methodology provides

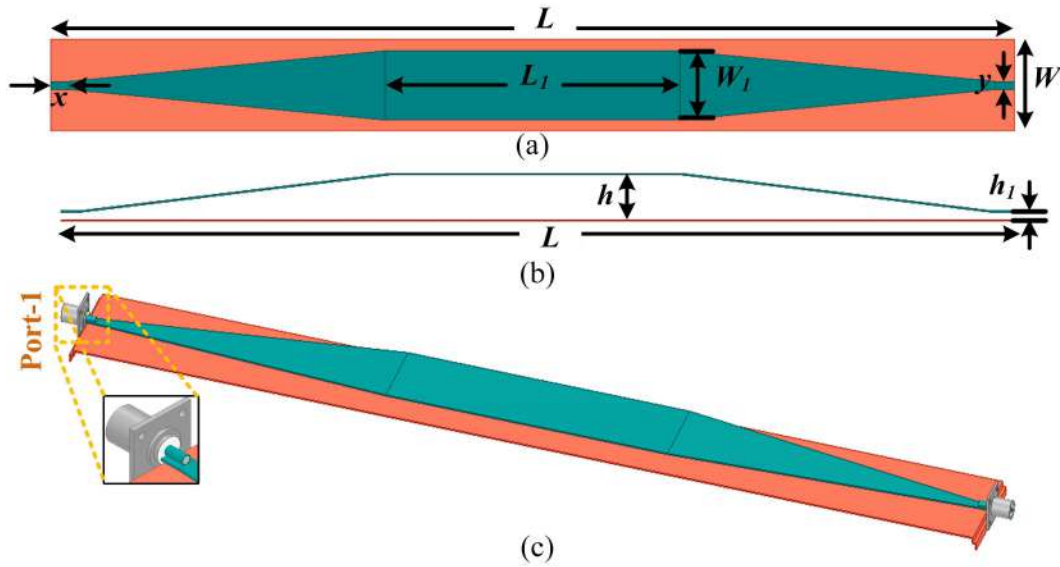


Figure 6.1: Schematic representation of the proposed PPW structure: (a) top view, (b) side view, and (c) isometric view.

a complete and reliable framework for experimentally validating periodic EM structures and consolidates the measurement strategy established throughout this thesis.

## 6.2 PPW Design and Characterization

### 6.2.1 PPW Design

The PPW structure is constructed using two metallic plates, each 1 mm thick, separated by a uniform air gap. The bottom plate is flat and rectangular, whereas the top plate is specifically engineered with tapering and bending at the feeding ends to achieve wideband impedance matching with the coaxial connectors. This tapered transition gradually transforms the characteristic impedance of the feeding ports to that of the parallel-plate region at the center, thereby minimizing reflections and enabling stable broadband operation. At the central region of the PPW, both plates remain strictly parallel so that the FSS samples can be mounted in a controlled and uniform EM environment, as illustrated in Figures 6.1(a) – (c). The PPWs generally support multi-mode operation; however, each of the modes can be regulated by appropriately designing the waveguide dimensions. In the proposed PPW, the structural parameters are optimized such that only the TEM mode will

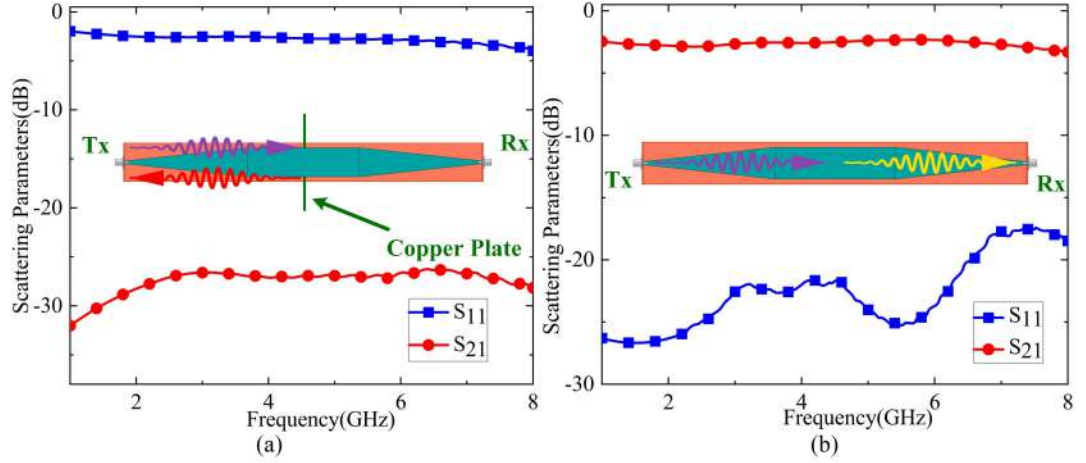


Figure 6.2: Simulated results of the PPW: (a) with a copper sheet placed at the center, and (b) without any test structure.

be propagated over 1-8 GHz range, and the higher-order modes will appear afterwards. This confirms that if any FSS structure is placed inside the waveguide, only TEM wave will be impinged on the structure, similar to the full-wave simulation condition. The final dimensions of the waveguide (in mm) are:  $L = 800$ ,  $W = 80$ ,  $W_1 = 60$ ,  $L_1 = 250$ ,  $x = 8$ ,  $y = 7$ ,  $h = 10$ , and  $h_1 = 1.5$ .

The proposed geometry is analyzed using full-wave simulations in Ansys HFSS 2025 R1. Before performing the actual device characterization, the PPW structure is calibrated in simulation to obtain accurate readings of  $S_{11}$  and  $S_{21}$ . For reflection calibration, a copper plate is inserted precisely at the center of the PPW, as shown in Figure 6.2(d). Under this condition, the structure exhibits  $S_{11} < -3$  dB and  $S_{21} > -25$  dB across the 1–8 GHz band, confirming that the majority of the incident energy is reflected back toward the input port and only a very small portion propagates to the output. This verifies that the PPW behaves as an effective short-circuit termination during the reflection calibration step.

Subsequently, the copper plate is removed to assess the transmission response of the empty PPW. In this case, a nearly uniform transmission characteristic is obtained, with  $S_{21} > -3$  dB and  $S_{11} < -20$  dB across the entire frequency range, as presented in Figure 6.2(e). These results confirm that the PPW introduces negligible insertion loss and minimal back-reflection when no sample is inserted. Minor amplitude variations are mainly attributed to small geometric nonlinearities caused by the tapering and bending of the top plate, as well as unavoidable discontinuities

at the feeding interfaces. Overall, the calibration method confirms the suitability of the proposed PPW setup for accurate and reliable FSS characterization.

### 6.2.2 FSS unit cell designs and simulation results

To verify the reliability of the in-house PPW setup, three representative FSS prototypes, each exhibiting a distinct EM behavior are designed, simulated, and experimentally analyzed. The geometries of these structures are shown in Figure 6.3, and their corresponding scattering responses are presented in Figure 6.4. Together, these design span bandstop filtering, wideband absorption, and reconfigurable absorption/transmission, thereby providing a comprehensive validation of the PPW system.

#### Design-1: Bandstop Filtering Structure

Design-1, as shown in Figure 6.3(a), consists of a simple square metallic loop printed on an FR4 substrate ( $\epsilon_r = 4.4$ ,  $\tan \delta = 0.02$ ). This structure serves as a baseline case for validating the PPW's ability to accurately capture a narrowband resonant behavior. The unit-cell geometry includes the periodicity  $a$ , inner loop length  $a_1$ , and strip width  $w$ , as labeled in the figure. The unit cell is analyzed using periodic boundary conditions (PBC) in Ansys HFSS, and the simulated response is presented in Figure 6.4(a), which exhibits a bandstop characteristic near 4.5 GHz. At this frequency, the transmission coefficient  $S_{21}$  drops below  $-40$  dB, and the reflection coefficient  $S_{11}$  remains less than  $-3$  dB.

#### Design-2: Wideband Absorber with Lumped Resistor Loading

Design-2 involves a multilayer geometry incorporating lumped resistive elements. As illustrated in Figures 6.3(b)–(c), the proposed design consists of a lossy patterned top metallic layer on an FR4 substrate, a bottom ground plane, and an intermediate air spacer of height  $t_{\text{air}}$ . The metallic pattern features a modified square loop with four symmetrically placed dipole arms, each loaded with a surface-mounted resistor and a capacitive strip. These form four parallel  $RC$  branches, introducing ohmic losses responsible for wideband absorption. The unit cell simulation is carried out using periodic boundary conditions in Ansys HFSS, and the simulated reflection

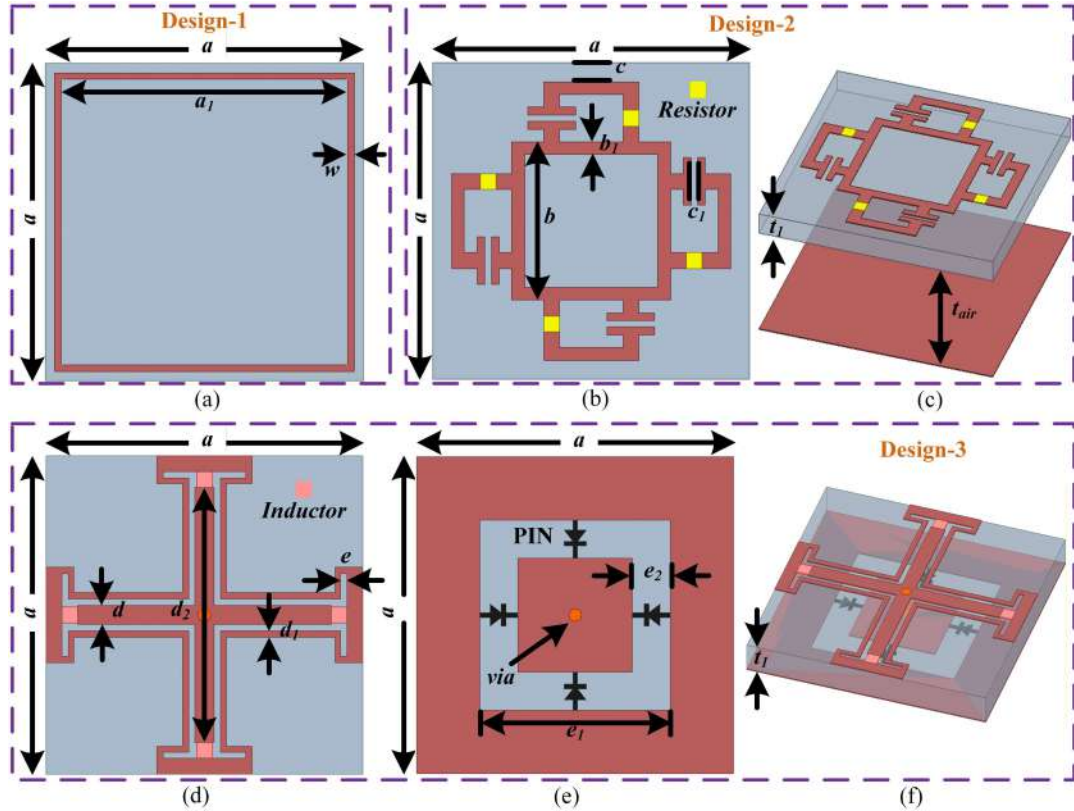


Figure 6.3: Unit cell designs. Design-1: (a) top view. Design-2: (b) top view, and (c) isometric view. Design-3: (d) top view, (e) bottom view, and (f) isometric view. The optimized dimensions (in mm) are:  $a = 10$ ,  $a_1 = 9$ ,  $w = 0.2$ ,  $b = 5$ ,  $b_1 = 0.4$ ,  $c = d = 0.6$ ,  $c_1 = 0.2$ ,  $t_1 = 1$ ,  $t_{\text{air}} = 4$ ,  $d_1 = e = 0.25$ ,  $d_2 = 8$ ,  $e_1 = 6$ , and  $e_2 = 1.2$ .

response in Figure 6.4(b) shows that  $S_{11}$  remains below  $-10$  dB over 4.38–8.00 GHz, corresponding to an absorptivity exceeding 80% across the band. The backside of the geometry is a complete plane, indicating no transmission across the design.

### Design-3: Reconfigurable Narrowband Transmission/Absorption FSS

Design-3, as shown in Figures 6.3(d)–(f), corresponds to the RFSS structure discussed in Chapter 2. Unlike the passive bandstop and absorber configurations discussed earlier, this design incorporates electronically controlled diode elements to exhibit a reconfigurable EM behavior. The geometry consists of two metallic layers printed on opposite sides of an FR4 substrate. The top layer features a Jerusalem-cross-inspired configuration with a central dipole, while the bottom layer integrates four p–i–n diodes. A central via and surface-mounted inductors form the DC biasing network. Depending on the diode bias conditions, under the OFF state, the diodes

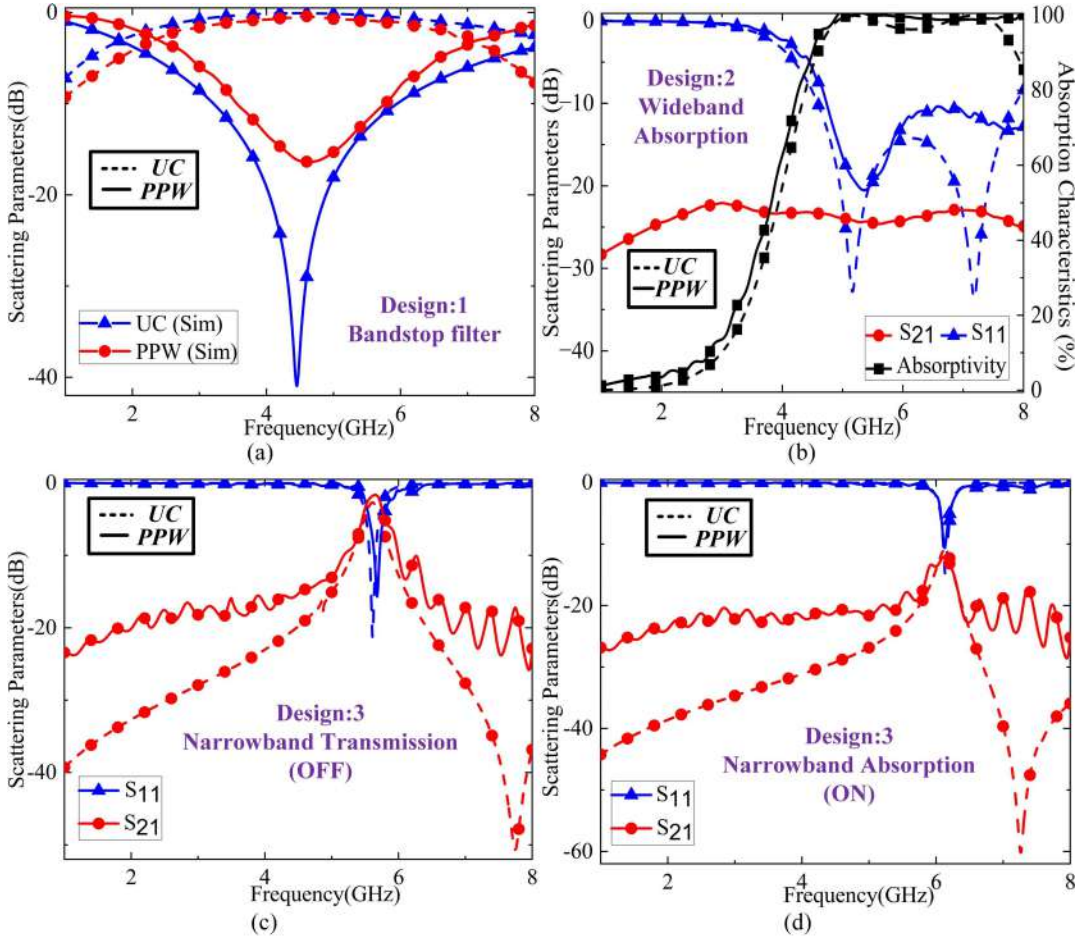


Figure 6.4: Comparison of unit cell (UC) and PPW simulations under normal incidences of the proposed designs: (a) bandstop filter, (b) wideband absorber, and RFSS: (c) OFF case, (d) ON case.

behave as capacitive elements, preventing the current flow. The structure exhibits a narrowband transmission, with the unit-cell simulation, showing an insertion loss of approximately 1.2 dB at 5.68 GHz. Under the ON state, the diodes act as a short circuit path, forming a conductive loop that resembles a ground plane. This produces narrowband absorption indicating more than 95% absorption near 6.05 GHz. Figures 6.4(c) and 6.4(d) exhibit the unit cell simulated responses under the OFF state and the ON state, respectively, of the proposed structure.

### Comparison of Unit-Cell (PBC) and PPW Simulation Results

For each prototype, the FSS sample is placed at the center of the PPW where the fields are uniform and normally incident. The calibration is performed using the

reference characterization described earlier:  $S_{11}$  is corrected using the copper-plate insertion response, while  $S_{21}$  is normalized using the empty-PPW transmission.

Each of the configurations is first simulated using PBC and later analyzed in the PPW setup, and their scattering parameters are compared in each case. The calibrated PPW responses for all three structures, shown in Figures 6.4(a)–(d), exhibit excellent agreement with their periodic HFSS simulations. The PPW reproduces all critical EM features, including bandstop filter (Design–1), wideband absorption (Design–2), and switchable narrowband transmission/absorption characteristics (Design–3). Overall, these results confirm that the proposed PPW setup serves as a robust, repeatable, and cost-effective alternative to conventional free-space measurement systems for accurate characterization of diverse FSS geometries.

### 6.3 Modified PPW for Oblique Incidence

While the initial PPW configuration enables reliable FSS characterization under normal incidence, its major limitation lies in the inability to support oblique-angle measurements. To overcome this constraint, the PPW structure is redesigned by integrating two identical sections with different aperture geometries, as illustrated in Figures 6.5(a) and 6.5(b). The two PPW sections are mechanically coupled at the center such that one section remains stationary while the other is capable of rotating about its longitudinal axis. This arrangement allows continuous angular variation between  $30^\circ$  and  $150^\circ$ , offering a flexible platform for incident-angle-dependent EM characterization.

In this modified configuration, the desired oblique incidence is achieved by adjusting both the FSS tilt angle and the rotation of the movable PPW section. For example, a  $15^\circ$  incidence angle can be produced by tilting the FSS by  $15^\circ$  and rotating the second PPW by  $30^\circ$ . Under such a configuration, an incident wave launched from Port 1 interacts with the tilted structure and is redirected toward Port 3, thereby enabling accurate reflection measurement. For transmission characterization, the TEM wave impinges on the FSS at an angle  $\theta$  and refracts at  $-\theta$  upon exiting, ultimately reaching the receiving port (Port 2) without distortion, as conceptually shown in Figures 6.5(c) and 6.5(d). The other ports remain matched

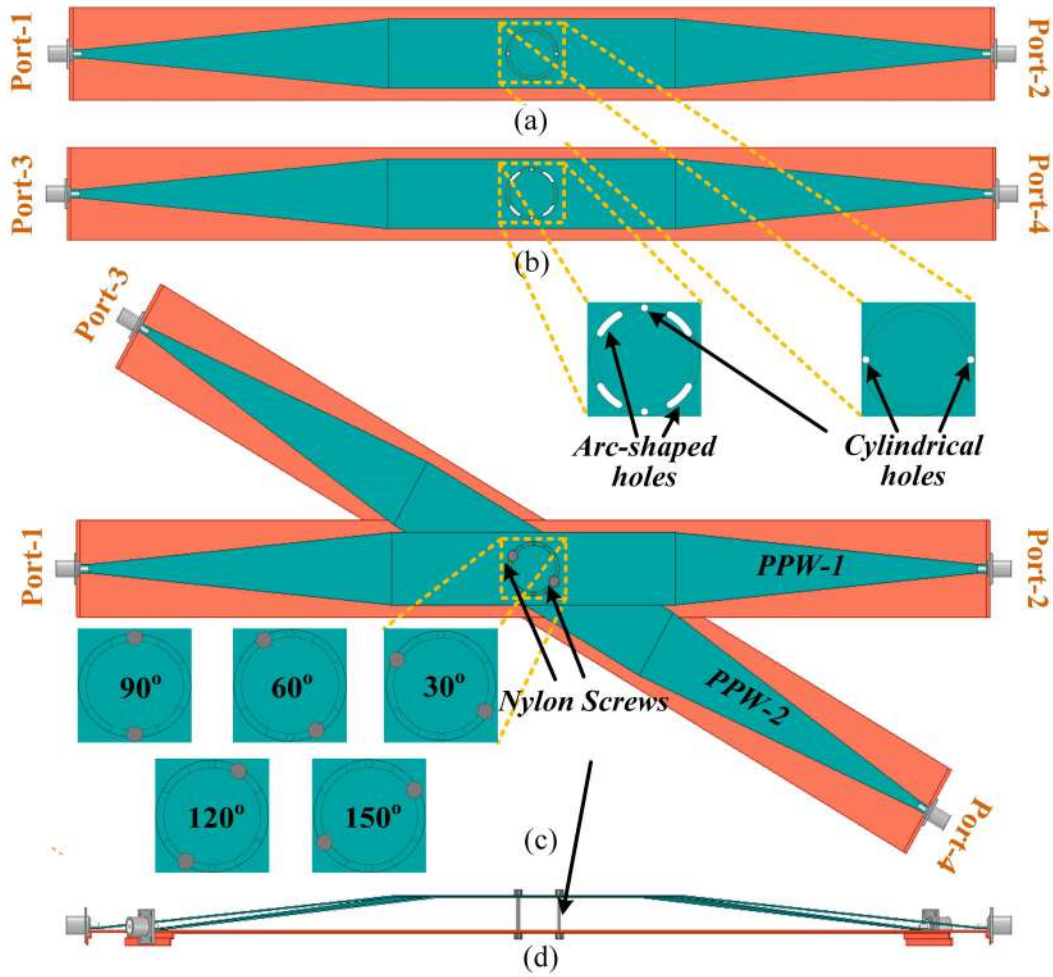


Figure 6.5: Modified PPW configuration for oblique incidence measurement: (a) PPW-1 (with cylindrical apertures); (b) PPW-2 (with both cylindrical and arc-shaped apertures). Combined measurement setup integrating both PPWs: (c) top view and (d) side view.

during the measurement; i.e., Ports 2 and 4 are matched during the reflection measurement, while Ports 3 and 4 are matched during the transmission measurement. This ensures that both  $S_{11}$  and  $S_{21}$  are extracted correctly even under oblique incidence.

### 6.3.1 Calibration of the Modified PPW Setup:

To ensure the accurate extraction of scattering parameters under oblique incidence, the modified PPW is characterized using two reference scenarios:

1. **Reflection reference:** A copper plate is placed at the center of the structure

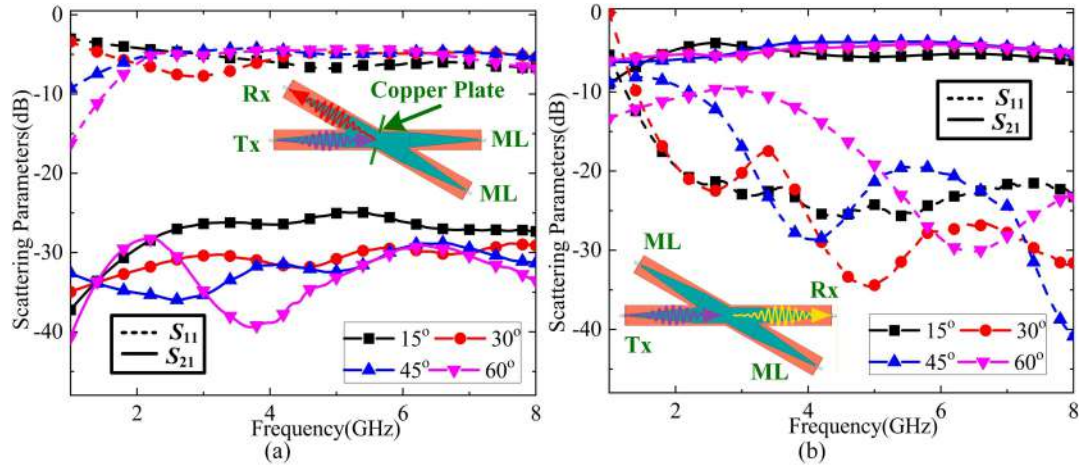


Figure 6.6: Simulated results of the modified PPW: (a) with a copper sheet placed at the center, and (b) without any test structure. ML: Matched Load.

and tilted to various angles ( $15^\circ$ ,  $30^\circ$ ,  $45^\circ$ , and  $60^\circ$ ). The simulated responses have been recorded at two different ports (Port 3 for  $S_{11}$  and Port 2 for  $S_{21}$ ) for various incident angles, which demonstrate that  $S_{11}$  consistently lies between  $-6$  dB and  $-8$  dB, while  $S_{21}$  remains around  $-30$  dB across the 1–8 GHz band, as shown in Figure 6.6(a).

2. **Transmission reference:** With no sample inserted, the insertion loss of the system is evaluated under oblique incidence. The simulated  $S_{21}$  varies between  $-5$  dB to  $-7$  dB with almost no reflection, as illustrated in Figure 6.6(b). The slightly higher insertion loss compared with the single-section PPW is attributed to the additional transitions introduced by the extended structure, but the loss remains within acceptable limits for accurate FSS measurements.

### 6.3.2 Comparison of Unit-Cell (PBC) and PPW Simulation Results for Modified PPW Setup

To evaluate the angular performance of the proposed FSS geometries, all three designs are analyzed under oblique incidence using the modified PPW configuration. For each design, a 1-D array is placed at the center of the PPW, and the signal is made incident from different ports of the device. The responses obtained from the FSS-loaded PPW model are then normalized by subtracting the corresponding

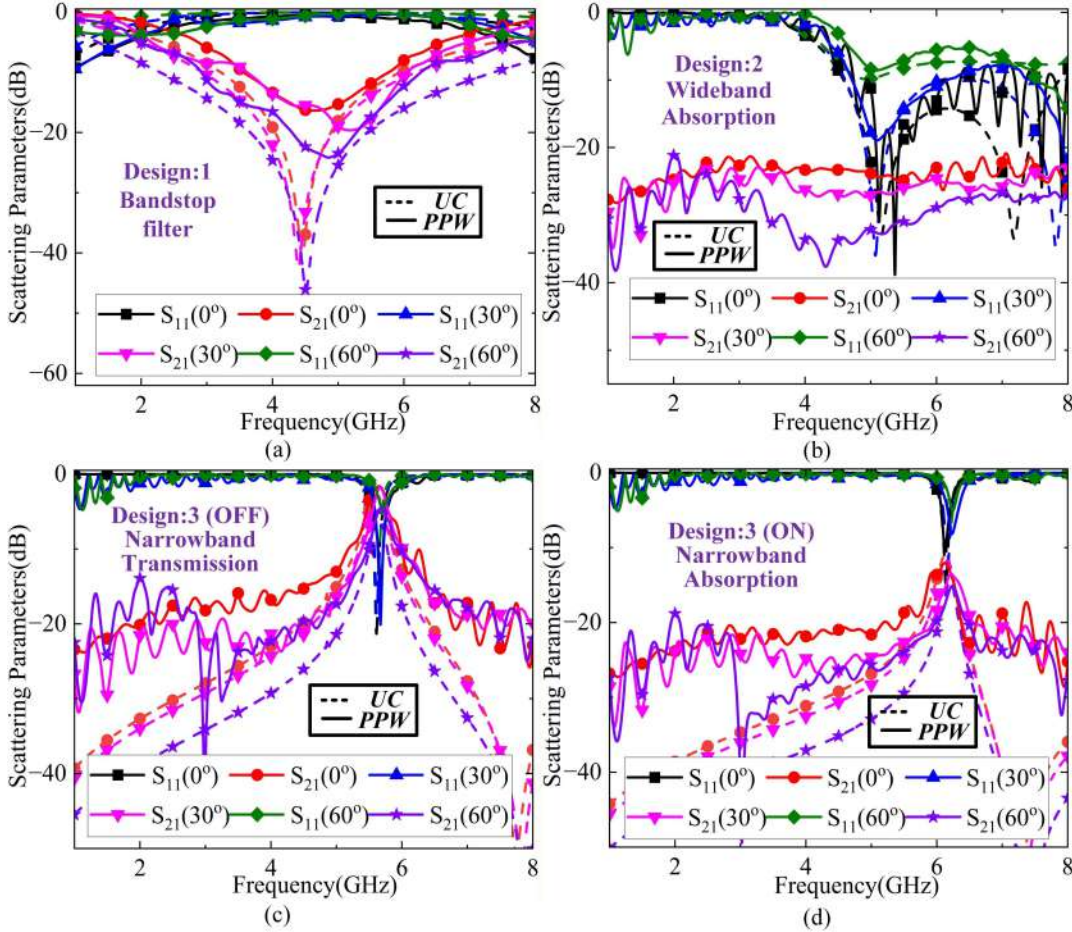


Figure 6.7: Comparison of unit cell and full wave PPW simulations under normal and oblique incidences of the proposed designs: (a) bandstop filter, (b) wideband absorber, and RFSS: (c) OFF case, (d) ON case.

reference results, thereby obtaining the actual scattering parameters of the FSS samples under oblique incidence.

The PPW simulated responses for all three designs demonstrate strong agreement with their respective unit cell simulations, as shown in Figure 6.7. The simulated data in both cases,  $S_{11}$  and  $S_{21}$ , remain consistent across incident angles up to  $60^\circ$ , with only minor discrepancies arising from edge effects, finite-array truncation, and the non-ideal field distribution inherent to the PPW geometry. Overall, this comparison confirms that the designed PPW structure is capable of accurately emulating oblique-plane-wave excitation within a full-wave simulation framework, thereby serving as a reliable tool for angular characterization of diverse FSS geometries prior to experimental validation.

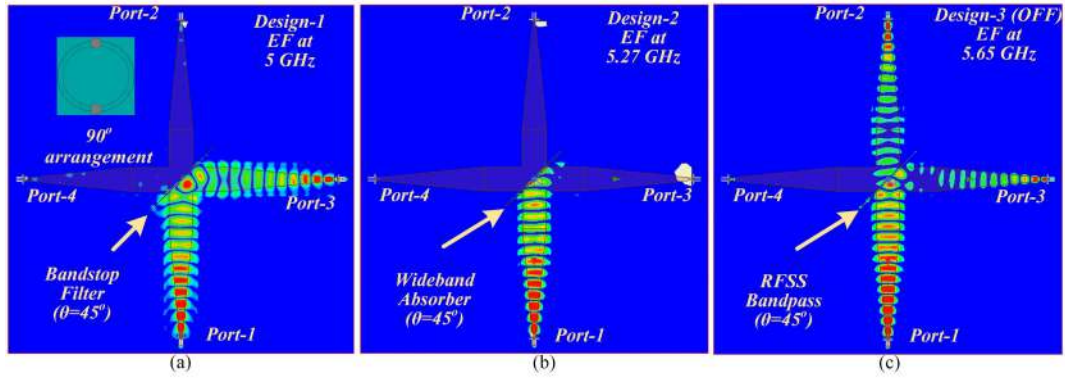


Figure 6.8: Electric field distributions of the proposed designs in the modified PPW simulations for the  $90^\circ$  configuration: (a) bandstop filter at 5.00 GHz, (b) wideband absorber at 5.27 GHz, and (c) RFSS at 5.68 GHz under OFF state.

### 6.3.3 Electric Field Distribution Analysis

To further visualize the EM behavior inside the modified PPW, electric field (E-field) distributions for different designs at representative frequencies are shown in Figure 6.8. These distributions correspond to three different functional behaviors:

- Design-1 (Reflection Band at 5.00 GHz):** The field pattern in Figure 6.8(a) clearly illustrates strong reflection by the bandstop filter geometry at 5.00 GHz, with the incident wave impinging from Port 1 and redirecting toward Port 3. Almost no energy is transmitted toward Port 2, confirming the bandstop nature of the structure.
- Design-2 (Absorption Band at 5.27 GHz):** Figure 6.8(b) shows that the EM energy is predominantly dissipated within the lossy structure, with negligible energy detected at either of the output ports (Port 2 or 3). This confirms the wideband absorption functionality of the proposed design.
- Design-3 (Transmission Band at 5.68 GHz):** As shown in Figure 6.8(c), the RFSS structure exhibits the transmission behavior from Port 1 to Port 2 with minimal reflection toward Port 3, demonstrating the switching between transmission and absorption responses regulated by the p-i-n diode network.

These field plots, extracted using HFSS full-wave simulations for a  $90^\circ$  PPW arrangement (equivalent to  $45^\circ$  oblique incidence), provide a clear understanding of

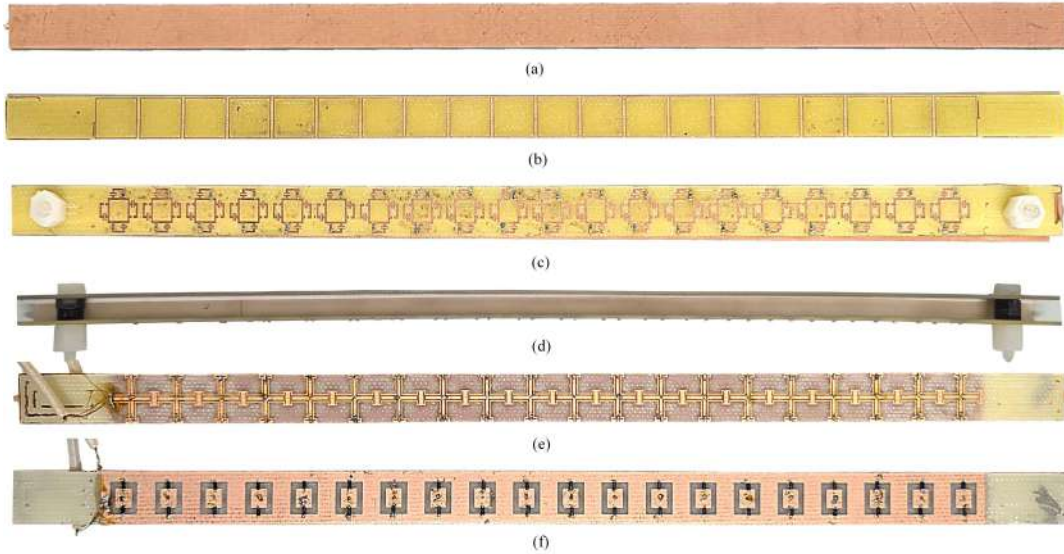


Figure 6.9: FSS prototypes and modified PPW experimental setup for  $60^\circ$  arrangement: (a) copper with the same dimensions as FSS samples, (b) bandstop filter (Design-1), wideband absorber (Design-2): (c) top view, (d) side view, and RFSS (Design-3): (e) top view, (f) bottom view.

wave propagation and confirm the operation of each FSS design inside the modified PPW environment.

## 6.4 Fabrication and Experimental Setup

### 6.4.1 Fabrication of FSS Prototypes

To experimentally validate the proposed concept, the modified PPW structure as well as the 1-D prototypes of all three FSS designs are fabricated using in-house facilities. Each FSS prototype consists of a linear array of 15 unit cells with an overall size of  $150 \text{ mm} \times 10 \text{ mm}$ . All metallic patterns are realized using an LPKF Protomat S104 PCB prototyping machine, ensuring high fabrication accuracy and repeatability for the multilayer geometries.

For the wideband absorber (Design-2),  $30 \Omega$  lumped resistors from KOA Speer Electronics [131] are mounted on the top surface using standard surface-mount technology, providing the required resistive loading for broadband absorption. The switchable RFSS geometry (Design-3) incorporates BAR 64-02V p-i-n diodes from Infineon Technologies [118], along with  $3.8 \text{ nH}$  inductors. The photographs of the

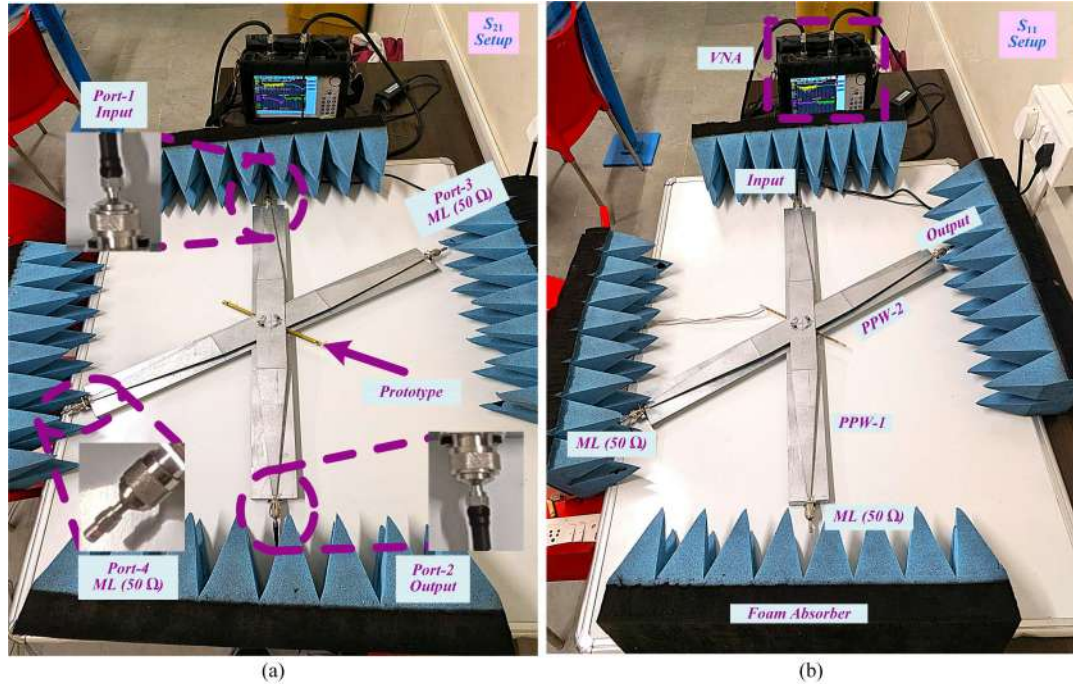


Figure 6.10: Modified PPW measurement setup for: (a)  $S_{21}$ , (b)  $S_{11}$ .

fabricated FSS prototypes are shown in Figures 6.9(a)–(f).

#### 6.4.2 Fabrication of the Modified PPW Setup

The modified PPW device is also fabricated in-house using standard sheet-metal processing tools. Two aluminum plates of thickness 1 mm are used for constructing the top and bottom sections. The required outlines of both plates are first marked on the metal sheets and then manually cut using a metal shear. The tapered regions on the top plate are formed by carefully bending the sheet using a bench vise and a rubber mallet, achieving the desired bending angles of approximately  $3^{\circ}$ – $5^{\circ}$ . These tapered transitions ensure broadband impedance matching with the coaxial feed connectors. The central portion of the top plate remains planar to maintain a uniform propagation region for the FSS samples.

The bottom plate is fabricated as a flat rectangular sheet without tapering, offering a stable reference surface for guided-wave propagation. To enable oblique incidence measurements, cylindrical and arc-shaped apertures are created on both PPW sections, allowing controlled rotation of one plate relative to the other while maintaining proper height alignment and ensuring reliable electrical contact between

surfaces. The two PPW sections (PPW-1 and PPW-2) are assembled using nylon screws to prevent unwanted EM interference and to maintain structural stability. The final PPW device, along with the complete measurement setup, is shown in Figures 6.10(a) and 6.10(b).

### 6.4.3 Measurement Setup

Before performing measurements, the PPW device is calibrated for  $S_{11}$  and  $S_{21}$  measurements using two different configurations: (i) a copper plate of identical size for  $S_{11}$  calibration and (ii) an empty PPW for  $S_{21}$  calibration. For reflection measurements ( $S_{11}$ ), Ports 1 and 3 serve as the transmitter (Tx) and receiver (Rx), respectively, while Ports 2 and 4 are terminated with  $50\ \Omega$  matched loads. For transmission ( $S_{21}$ ), Ports 1 and 2 act as Tx and Rx, respectively, with the remaining ports terminated likewise.

A VNA (Anritsu S820E) is used to capture the scattering parameters across the operating band. For the RFSS sample (Design-3), two programmable DC power supplies are employed to bias the p-i-n diodes into either forward or reverse states. The complete measurement arrangement, including the PPW device, VNA connections, and surrounding pyramidal absorbers, is illustrated in Figures 6.10(a) and 6.10(b).

### 6.4.4 Measured Results

The fabricated FSS prototypes are evaluated under both normal and oblique incidences using the calibrated PPW device. Design-1 exhibits a clear bandstop behavior centered around 5 GHz. Design-2 demonstrates wideband absorption exceeding 80% over the 4.5–8.0 GHz range. For the switchable RFSS (Design-3), a narrow-band absorption peak appears at approximately 6.23 GHz under forward bias of the diodes, whereas a bandpass response at 5.98 GHz with low insertion loss is generated under the reverse bias.

The measured S-parameters, as shown in Figures 6.11(a)–(d), exhibit strong agreement with the full-wave simulation results obtained using the modified PPW geometry. A small frequency offset of about  $\pm 0.2$  GHz is observed, which primarily arises from the finite length of the fabricated prototypes, fabrication tolerances, and

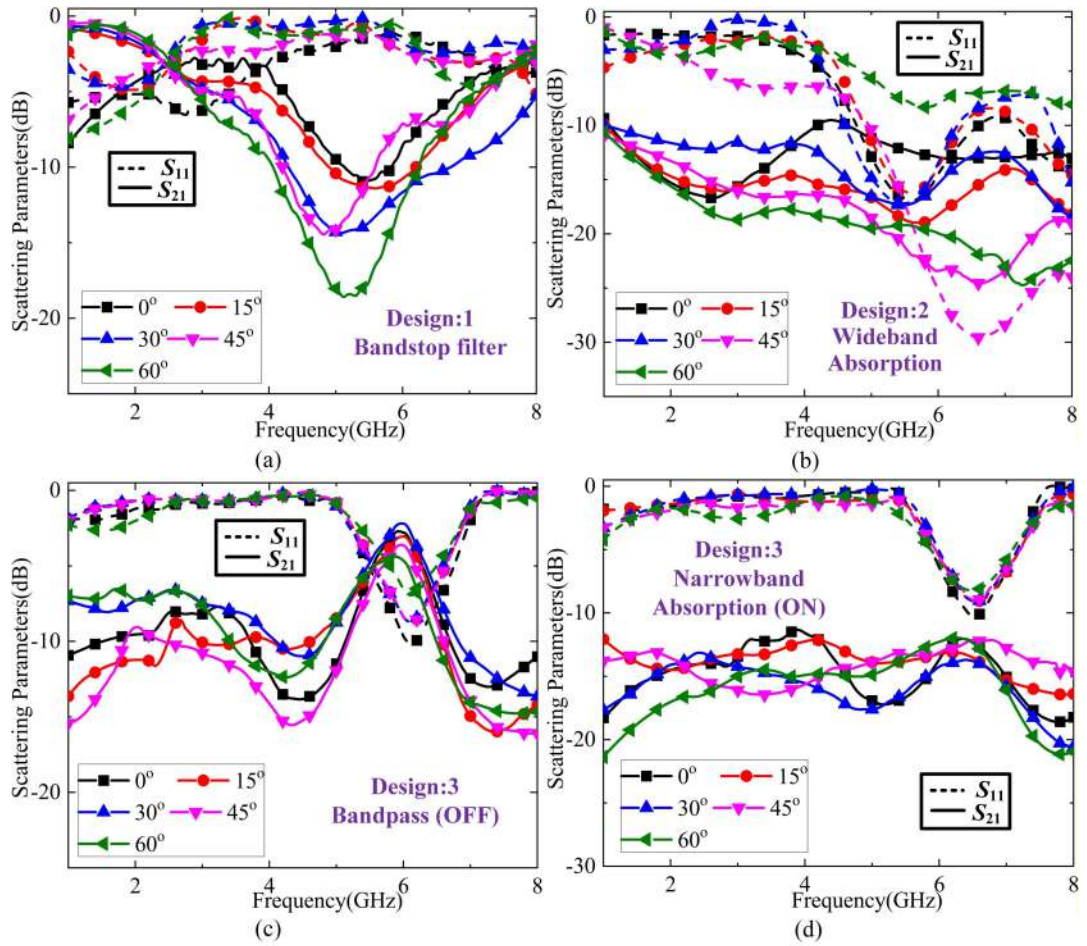


Figure 6.11: Measured responses in the modified PPW setup under normal and oblique incidences of the proposed designs: (a) bandstop filter, (b) wideband absorber, and RFSS: (c) OFF case, (d) ON case.

parasitic effects from surface-mount components and interconnects. Overall, the close correspondence between simulation and measurement confirms the effectiveness of the modified PPW device for accurate characterization of diverse FSS structures under both normal and oblique incidence conditions.

## 6.5 Conclusion

This chapter presents the development of a modified PPW measurement framework that addresses the limitations of conventional PPW-based characterization techniques. While the previous chapters of this thesis focus on the design, analysis, and validation of various RFSS geometries, their experimental verifications are constrained by the limited measurement capabilities of the PPW system, particularly

Table 6.1: Comparison with Existing Literature

Ref.	Functionality	Frequency range	Calibration losses ( $S_{11}/S_{21}$ )	Measurement limitations
[92]	Switching (RAS/A)	2–14 GHz	High/High	PPW ( $0^\circ$ ) / Unit cell simulation (Ob. In.)
[102]	T	1–6 GHz	N.R./N.R.	PPW ( $0^\circ$ ) / FSM (Ob. In.)
[115]	A	1–6 GHz	Low/N.R.	PPW ( $0^\circ$ ) / No Ob. In.
[132]	T	1–8 GHz	N.R./Low	PPW ( $0^\circ$ ) / No Ob. In.
<b>This Work</b>	<b>R, A, T, Switching (A/T)</b>	<b>1–8 GHz</b>	<b>Low/Low</b>	<b>PPW (<math>0^\circ</math>) / PPW (Ob. In.)</b>

*Note:* A: Absorption, T: Transmission, R: Reflection, RAS: Rasorber, Ob. In.: Oblique incidence, FSM: Free-space measurement, N.R.: Not reported.

its inability to obtain reliable oblique-incidence reflection ( $S_{11}$ ) responses. The work presented in this chapter, therefore, focuses on the improvement of the measurement system, establishing a complete, accurate, and robust PPW methodology suitable for characterizing various types of FSSs under both normal and oblique incidence.

Initially, this chapter explains that free-space, rectangular waveguide, and earlier PPW-based measurement techniques provide useful characterization capabilities; however, each suffers from limitations related to sample size, bandwidth, angular incidence, or measurement reliability. These constraints motivate the development of a redesigned PPW structure capable of supporting stable TEM propagation and enabling accurate, repeatable full S-parameter ( $S_{11}$  and  $S_{21}$ ) characterization under oblique incidence.

Based on the above observations, the chapter first examines the conventional PPW configuration, which is shown to be primarily effective for normal-incidence characterization. The periodic unit-cell geometries, including a bandstop FSS, a wideband absorber, and a reconfigurable FSS, are analyzed using both PBC simulations and PPW simulations under normal incidence, demonstrating good agreement between the two approaches. Building on these results, a modified PPW configuration is subsequently developed to extend the measurement capability to oblique incidence by incorporating improved angular adjustability, controlled mechanical rotation, enhanced aperture shaping, and optimized plate spacing to maintain stable TEM propagation. The effectiveness of the redesigned PPW is validated through electric-field distribution analysis, confirming accurate EM behavior and improved reliability in capturing both reflection and transmission responses under oblique incidence. Using the enhanced PPW system, all periodic structures are characterized,

with the extracted  $S_{11}$  and  $S_{21}$  exhibiting excellent agreement with unit-cell and full-wave simulations and stable performance up to  $60^\circ$  incidence.

In addition to validating the measurement accuracy, the chapter highlights practical considerations, including plate alignment, rotational tolerances, absorber placement, and finite-array effects that influence measurement consistency. Despite minor amplitude variations and slight frequency offsets caused by fabrication tolerances and prototype dimensions, the modified PPW system consistently produces reliable experimental results. A comparative summary of PPW capabilities with the existing literature is also included in Table 6.1, clearly demonstrating that the proposed methodology provides wider angular coverage and improved measurement facility compared to previously reported configurations.

Overall, this chapter concludes the technical developments of the thesis by establishing a comprehensive measurement approach that complements the wideband multifunctional RFSS designs introduced earlier. Together, the design methodologies, equivalent circuit analyses, switching techniques, and the modified PPW measurement system form a cohesive body of work that advances both the synthesis and experimental validation of multifunctional EM surfaces. This integrated framework paves the way for future research involving adaptive radome systems, reconfigurable EM platforms, and wideband steerable FSS technologies, and represents a significant step toward the practical deployment of next-generation RFSS and MRFSS architectures.



# Chapter 7

## Conclusion and Future Scope

### 7.1 Summary of Research

Over the past few decades, FSSs have evolved into vital components for stealth platforms, radar systems, EMI shielding, and multifunctional EM architectures. However, conventional FSS designs remain limited to a single, fixed EM behavior, which restricts their applicability in modern dynamic scenarios where adaptive transmission, reflection, and absorption characteristics are required in real time. To address these functional constraints and expand the operational versatility of FSS structures, this thesis systematically investigates reconfigurable FSS (RFSS) technologies through a progressive sequence of contributions—advancing from fundamental switching, to multimode operation, then combined switching–tuning, followed by wideband multifunctionality, and finally concluding with experimental innovations through a modified PPW measurement system. This structured progression forms the backbone of the entire thesis and the conclusions summarized below, providing a coherent transition from basic conceptual developments to fully engineered practical solutions. Each stage builds upon the limitations identified in the previous one, ultimately presenting a unified framework for designing compact, versatile, and experimentally validated RFSS structures suited for next-generation EM platforms.

The research begins by addressing a key limitation in existing switchable RFSS designs: their inability to simultaneously maintain polarization insensitivity, single-layer compactness, and dual-mode operation without complex biasing. **Chapter 2** presents a single p-i-n–diode–based absorptive/transmissive RFSS, where a

Jerusalem-cross-loaded dipole on the top layer and a square-slot geometry with four symmetrically placed diodes on the bottom layer collectively enable narrowband switching between high absorption and bandpass transmission modes. In the ON state, the unit cell achieves 93.51% absorption at 6.93 GHz, and under the OFF state it supports a 5.62 GHz transmission band with minimal insertion loss. A carefully embedded bias network ensures polarization-insensitive operation up to  $60^\circ$ , and the equivalent circuit analysis provides physical insight into how the diode alters the *RLC* behavior of the surface. The design is experimentally validated using an in-house PPW setup, confirming excellent agreement between simulated and measured responses. Although this single-layer configuration successfully demonstrates basic dual-mode switching, it remains limited to only two functionalities and requires manual diode control, making it unsuitable for real-time systems. This limitation directly motivates the development of a structure capable of multiple distinct operating states with automated biasing, leading to **Chapter 3**.

Building on the fundamental switching concept, **Chapter 3** presents a more sophisticated RFSS architecture by integrating two independently biased p-i-n diode sets placed on opposite sides of a single FR4 substrate. The top layer employs a meander-line connected to a dipole, while the bottom layer utilizes an outer square loop coupled to a rotated inner square patch. This configuration enables four diode states (OFF–OFF, OFF–ON, ON–OFF, and ON–ON), each producing a distinct EM response, thereby realizing three major functionalities within the same structure. In the OFF–OFF mode, the unit cell supports a narrowband transmission window, whereas the OFF–ON mode yields strong absorption exceeding 90% around 5.2 GHz. The ON–OFF and ON–ON combinations introduce partial and full reflection characteristics, respectively, extending up to 8 GHz. A key advancement in this design is the integration of an FPGA-based automatic biasing controller, which facilitates real-time and dynamic switching among all operational states, effectively overcoming the limitations of manual tuning encountered in the previous chapter. The full-wave simulations, equivalent circuit modeling, and PPW-based measurements further validate the multifunctional behavior, demonstrating robust polarization insensitivity and angular stability. However, despite the expanded functionality, the resonant frequencies associated with each operational state remain fixed, limiting

adaptability in scenarios requiring frequency-agile responses. This inherent restriction naturally motivates the progression toward introducing continuous tunability alongside switching, which forms the focus of **Chapter 4**.

While **Chapter 3** demonstrates multiple operating states, its static resonance limits practical deployment in scenarios requiring frequency tunability. **Chapter 4** overcomes this limitation by integrating p-i-n diodes for discrete mode switching together with varactor diodes for continuous frequency tuning within a single-layer topology, thereby creating a multifunctional reconfigurable FSS (MRFSS) capable of both switching and tuning. Utilizing a meander-loaded dipole on the top layer and a centrally connected patch with diode elements on the bottom layer, the structure achieves four programmable states, each exhibiting its own tunable resonant response. In this configuration, the design supports a tunable transmission band spanning 1.68–2.56 GHz, a tunable absorption band extending from 1.84–2.85 GHz, and the tunable selective and full reflection characteristics for the entire operating band. A compact biasing scheme requiring only four terminals further simplifies implementation compared with conventional RFSS architectures. A  $20 \times 20$  unit-cell array is fabricated to realize a large two-dimensional periodic surface representative of the designed MRFSS. The subsequent free-space measurements performed on this prototype validate the tunable behavior across all operational states, clearly demonstrating its advancement beyond the fixed-frequency and narrowband limitations of the previous designs. Nevertheless, despite achieving both switching and tuning capabilities, all operational responses remain narrowband, thereby motivating the transition toward wideband multifunctionality, which is subsequently explored in **Chapter 5**.

To overcome the bandwidth limitations inherent in previously discussed single-layer designs, **Chapter 5** introduces a two-layer wideband RFSS separated by an air gap. In this geometry, the incorporation of lumped resistors together with multi-layer metallic patterns enables four distinct wideband EM functionalities. The structure supports multiple wideband EM functionalities across its different diode states. In the OFF–OFF mode, it operates as a rasorber, exhibiting a transmission window around 2.67 GHz followed by a 28.5% absorption bandwidth. The OFF–ON configuration realizes a wideband absorption response with a 60.21% fractional

bandwidth. In the ON–OFF state, the structure provides broadband transmission covering 2.41–4.49 GHz, while the ON–ON state yields a wideband reflective characteristic extending across the entire operating region. The multilayer topology further ensures polarization insensitivity and angular stability up to  $45^\circ$ , as verified through equivalent circuit modeling and full-wave simulations. The experimental validation, using a fabricated 1-D prototype measured with a PPW setup, confirms the wideband, multifunctional performance of the proposed RFSS design. In summary, the developments presented in **Chapters 2 to 5** collectively establish a comprehensive set of RFSS designs, progressing from single-layer switchable structures to multilayer wideband multifunctional configurations. Despite these design advancements, most of the proposed designs rely on a PPW measurement setup that is inherently limited to normal incidence characterization, restricting accurate evaluation of oblique-incidence behavior, an essential requirement for practical FSS validation. In view of this limitation, the thesis transitions from design-oriented investigations to the development of an improved measurement approach, which is addressed in **Chapter 6** through the introduction of a modified wide-angle PPW system.

Building upon this transition toward improved measurement methodologies, **Chapter 6** provides a detailed exploration of the modified wide-angle PPW system introduced in the preceding discussion. The practical evaluation of reconfigurable and wideband FSS structures benefits from measurement setups that minimize sample size and simplify the testing environment. The PPW approach offers these advantages by allowing 1-D sample testing within a confined structure, making it far more cost-effective for rapid prototyping and controlled experimentation than conventional free-space systems. Therefore, **Chapter 6** presents a modified PPW setup composed of two mechanically adjustable sections connected through cylindrical and arc-shaped apertures, enabling controlled wide-angle incidence ranging from  $30^\circ$  to  $150^\circ$  while preserving TEM-mode propagation. The effectiveness of this configuration is demonstrated through measurements performed on multiple fabricated prototypes, including a bandstop filter, a two-layer wideband absorber, and a switchable absorber/transmitter RFSS, thereby establishing the versatility of the proposed setup. The close agreement between simulated and measured results confirms the accuracy of the modified system, positioning it as a compact and cost-

effective alternative to traditional measurement approaches. By providing a robust experimental framework capable of evaluating RFSS structures under realistic angular conditions, this final chapter reinforces and supports all design developments presented earlier in the thesis.

Throughout this thesis, the evolution of reconfigurable FSS technology has been explored through a carefully structured sequence of developments that progressively extend the functional boundaries of conventional FSS designs. Beginning with the establishment of fundamental switching mechanisms and advancing through multi-mode reconfiguration, frequency-tunable operation, and wideband multifunctional behavior, each contribution has been designed to address the limitations identified in the preceding chapters. This systematic progression ultimately leads to the formulation of an improved experimental methodology based on a modified wide-angle PPW system, ensuring reliable validation of the proposed RFSS structures under practical EM conditions. Overall, the progression establishes a comprehensive framework for the design, realization, and characterization of advanced RFSS architectures, enabling their use in next-generation applications, including stealth systems, adaptive radomes, EMI-shielding solutions, and intelligent wireless platforms.

## 7.2 Scope of Future Work

In this thesis, various types of RFSS structures have been developed to realize multifunctional EM responses suited for next-generation applications. Beginning with single-layer switchable designs based on p-i-n diodes, the work progresses through multifunctional configurations capable of exhibiting absorption, transmission, and reflection within a single geometry, followed by tunable FSS structures integrated with varactor diodes to achieve continuous frequency tunability. These contributions are further extended to multilayer wideband RFSS designs that demonstrate absorber, broadband absorption, transmission, and reflection characteristics within a single architecture. All proposed structures exhibit polarization-insensitive and angularly stable behavior, with their performances thoroughly validated through conventional and modified PPW measurement setups. The designs reported here show significant improvements over earlier RFSS structures in terms of multifunctionality,

compactness, and experimental realizability. However, despite these advancements, several open challenges and opportunities remain in the broader domain of RFSS technology. Based on the observations made throughout this thesis, the following points outline potential directions for future research:

1. One potential extension of the present research is the development of a compact sensing–communication module that can be seamlessly integrated with the proposed reconfigurable FSS structures. While the RFSS designs presented in this thesis are capable of dynamically switching among absorption, transmission, and reflection states, they are operated by manual intervention, where the biasing conditions need to be regulated manually to exhibit different EM states. In practical scenarios, however, intelligent EM platforms require surfaces that can not only reconfigure their response but also detect, classify, and react to incoming signals in real time. To achieve such functionality, an additional sensing layer comprising sensing antennas, band-selective filters, rectifying circuits, low-power RF detectors, or FPGA-based digital control modules may be incorporated into the RFSS architecture. The integration of these components into a compact and co-designed platform would allow the surface to autonomously sense the incident waveform, determine the required EM function, and trigger the appropriate switching or tuning state without external intervention. Developing such a compact, self-aware sensing–communication system represents a natural progression of the thesis and would transform the proposed RFSS designs from manually-operated reconfigurable structures into fully adaptive surface architectures capable of real-time decision-making.
2. Another promising direction for future research lies in exploring reconfiguration mechanisms that can offer improved robustness for deployment in demanding operational environments. The electronically controlled RFSS structures presented in this thesis rely primarily on p–i–n diodes and varactor diodes, which, although effective for laboratory-scale demonstrations, pose challenges when integrated into large platforms such as aircraft, high-altitude vehicles, or harsh outdoor installations. In such environments, factors like mechanical vibration, air pressure variation, temperature cycling, and long-term material fatigue can compromise the reliability of discrete semiconductor components, potentially leading to de-

tachment, performance drift, or premature failure. To address these limitations, future work may investigate alternative reconfiguration strategies that can embed tunability directly into the EM material or surface structure, thereby minimizing the reliance on fragile soldered components. Approaches based on adaptive materials, distributed tuning elements, or structurally integrated control mechanisms could provide enhanced mechanical stability while still supporting dynamic EM functionality. Advancing RFSS technology toward such material-level or mechanically resilient reconfiguration schemes would significantly broaden its applicability, enabling reliable operation in aerospace, defense, and other high-stress environments where conventional electronic switching elements are difficult to maintain.

3. A further extension of this work involves exploring RFSS designs that can efficiently operate on conformal platforms. All RFSS prototypes developed in this thesis are implemented on planar substrates, which greatly simplifies fabrication, component placement, and bias routing. However, many practical applications, especially in aerospace, vehicular, and wearable EM systems, require surfaces that conform to curved radomes or structural contours. Integrating discrete components such as p-i-n diodes, varactors, resistors, and biasing networks onto non-planar geometries introduces significant challenges related to mechanical reliability, solder joint integrity, and non-uniform current distribution. Furthermore, achieving stable multifunctional responses, such as switchable absorption, transmission, or reflection, becomes substantially more complex when the unit-cell geometry is distorted by curvature. Addressing these issues would require the development of conformal-based unit-cell designs, flexible substrates, or distributed control mechanisms that can maintain EM performance under bending or deformation. Thus, advancing RFSS technology toward conformal implementations represents a valuable research direction with strong relevance to real-world deployment scenarios.
4. Another significant avenue for future research is the integration of phase-controlled reconfigurability to extend the present RFSS designs toward fully functional reconfigurable intelligent surfaces (RIS). The multifunctional RFSS structures developed in this thesis primarily control the amplitude characteristics of incident

EM waves, enabling switchable absorption, transmission, and reflection under various states. However, in these configurations, the reflected or transmitted wave generally follows the angle of incidence, limiting the ability to steer or redirect energy in arbitrary directions. In contrast, RIS technologies achieve dynamic wavefront manipulation by imparting spatially varying phase shifts across the surface, thereby enabling functionalities such as anomalous reflection, beam steering, wave focusing, and signal redirection—all of which are essential for next-generation wireless communication and sensing systems. Future research could therefore explore geometries that jointly engineer both amplitude and phase responses, enabling multifunctional RIS structures capable of not only steering reflected or transmitted beams but also selectively absorbing unwanted interference or enabling controlled transmission through the surface. Developing such multifunctional RIS architectures would represent a substantial advancement, merging the strengths of conventional RFSS technologies with the emerging capabilities of intelligent surfaces for adaptive EM environments.

5. Another compelling direction for future research is the incorporation of transistor-based active elements into reconfigurable FSS architectures. The structures explored in this thesis rely primarily on p-i-n diodes and varactor diodes, which act as passive switching or tuning components and do not contribute additional gain to the incident electromagnetic wave. In contrast, RF transistors—such as MOSFETs, HEMTs, or bipolar devices—offer the possibility of realizing active RFSS unit cells capable of amplifying, shaping, or conditioning incoming signals before reflection, absorption, or transmission. Embedding such active devices within the metallic pattern of the FSS may enable functionalities such as gain-enhanced reflection, loss-compensated transmission, adaptive filtering, or localized signal boosting, thereby overcoming the inherent passive loss mechanisms observed in conventional diode-based designs. Although integrating transistor circuits onto periodic surfaces introduces challenges related to power distribution, thermal stability, and biasing complexity, successful implementation would extend reconfigurable FSS technology into an entirely new class of active, gain-adaptive surfaces with promising applications in communication front-ends, sensing receivers, and intelligent electromagnetic platforms.

# References

- [1] T. K. Wu, *Frequency Selective Surface and Grid Array*. 1st ed. New York, NY, USA: Wiley, 1995.
- [2] J. C. Vardaxoglou, *Frequency Selective Surfaces: Analysis and Design*. 1st ed. New York, NY, USA: Wiley, 1997.
- [3] B. A. Munk, *Frequency Selective Surfaces: Theory and Design*. 1st ed. New York, NY, USA: Wiley, 2005.
- [4] F. Bayatpur, *Metamaterial-Inspired Frequency-Selective Surfaces*. PhD thesis, University of Michigan, 2009.
- [5] B. Chambers and K. Ford, “Tunable radar absorbers using frequency selective surfaces,” in *IEEE Eleventh International Conf. Antennas Propag.*, vol. 2, 2001, pp. 593–597.
- [6] P. S. Taylor, E. A. Parker, and J. C. Batchelor, “An active annular ring frequency selective surface,” *IEEE Trans. Antennas Propag.*, vol. 59, no. 9, pp. 3265–3271, 2011.
- [7] B. Sanz-Izquierdo and E. Parker, “Dual polarized reconfigurable frequency selective surfaces,” *IEEE Trans. Antennas Propag.*, vol. 62, no. 2, pp. 764–771, 2013.
- [8] J. A. Bossard *et al.*, “Tunable frequency selective surfaces and negative-zero-positive index metamaterials based on liquid crystals,” *IEEE Trans. Antennas Propag.*, vol. 56, no. 5, pp. 1308–1320, 2008.
- [9] B. Schoenlinner, A. Abbaspour-Tamijani, L. C. Kempel, and G. M. Rebeiz,

- “Switchable low-loss RF MEMS Ka-band frequency-selective surface,” *IEEE Trans. Micro. Theory Tech.*, vol. 52, no. 11, pp. 2474–2481, 2004.
- [10] S. Ghosh and S. Lim, “A multifunctional reconfigurable frequency-selective surface using liquid-metal alloy,” *IEEE Trans. Antennas Propag.*, vol. 66, no. 9, pp. 4953–4957, 2018.
- [11] S. N. Azemi, K. Ghorbani, and W. S. Rowe, “A reconfigurable FSS using a spring resonator element,” *IEEE Antennas Wireless Propag. Lett.*, vol. 12, pp. 781–784, 2013.
- [12] A. Munir and V. Fusco, “Frequency selective surface with dual band switchable reflection and transmission characteristics,” *Microw. Opt. Technol. Lett.*, vol. 51, no. 9, pp. 2059–2061, 2009.
- [13] W. Li, Y. Wang, S. Sun, and X. Shi, “An FSS-backed reflection/transmission reconfigurable array antenna,” *IEEE Access*, vol. 8, pp. 23 904–23 911, 2020.
- [14] S. Celozzi, R. Araneo, and G. Lovat, *Electromagnetic Shielding*. 1st ed. New York, NY, USA: Wiley, 2008.
- [15] D. F. Sievenpiper, *High-impedance electromagnetic surfaces*. PhD thesis, University of California, Los Angeles, 1999.
- [16] S. Ghosh, S. Bhattacharyya, D. Chaurasiya, and K. V. Srivastava, “An ultrawideband ultrathin metamaterial absorber based on circular split rings,” *IEEE Antennas Wireless Propag. Lett.*, vol. 14, pp. 1172–1175, 2015.
- [17] F. Costa, A. Monorchio, and G. Manara, “Analysis and design of ultra thin electromagnetic absorbers comprising resistively loaded high impedance surfaces,” *IEEE Trans. Antennas Propag.*, vol. 58, no. 5, pp. 1551–1558, 2010.
- [18] Y. Shang, Z. Shen, and S. Xiao, “Frequency-selective rasorber based on square-loop and cross-dipole arrays,” *IEEE Trans. Antennas Propag.*, vol. 62, no. 11, pp. 5581–5589, 2014.

- 
- [19] A. Motevasselian and B. L. G. Jonsson, "Design of a wideband rasorber with a polarisation-sensitive transparent window," *IET Microw. Antennas Propag.*, vol. 6, no. 7, pp. 747–755, 2012.
- [20] F. Costa and A. Monorchio, "A frequency selective radome with wideband absorbing properties," *IEEE Trans. Antennas Propag.*, vol. 60, no. 6, pp. 2740–2747, 2012.
- [21] A. Sharma, M. Saikia, S. Malik, S. Ghosh, and K. V. Srivastava, "A polarization-insensitive broadband rasorber with in-band transmission response," *Microw. Opt. Technol. Lett.*, vol. 62, no. 12, pp. 3668–3676, 2020.
- [22] W. F. Bahret, "The beginnings of stealth technology," *IEEE Trans. Aerospace Elect. Sys.*, vol. 29, no. 4, pp. 1377–1385, 2002.
- [23] R. Mittra, C. H. Chan, and T. Cwik, "Techniques for analyzing frequency selective surfaces-a review," *Proceedings of the IEEE*, vol. 76, no. 12, pp. 1593–1615, 1988.
- [24] R. S. Anwar, L. Mao, and H. Ning, "Frequency selective surfaces: A review," *Applied Sciences*, vol. 8, no. 9, p. 1689, 2018.
- [25] R. Panwar and J. R. Lee, "Progress in frequency selective surface-based smart electromagnetic structures: A critical review," *Aerospace Science and Technology*, vol. 66, pp. 216–234, 2017.
- [26] G. M. Coutts, R. R. Mansour, and S. K. Chaudhuri, "Microelectromechanical systems tunable frequency-selective surfaces and electromagnetic-bandgap structures on rigid-flex substrates," *IEEE Trans. Micro. Theory Tech.*, vol. 56, no. 7, pp. 1737–1746, 2008.
- [27] B. Ma, S. Liu, X. Kong, Y. Jiang, J. Xu, and H. Yang, "A novel wide-band tunable metamaterial absorber based on varactor diode/graphene," *Optik*, vol. 127, no. 5, pp. 3039–3043, 2016.
- [28] X. Kong, X. Wang, X. Jin, W. Lin, L. Kong, S. Jiang, and L. Xing, "Liquid based wideband and switchable 3-D frequency-selective rasorber," *IEEE Trans. Electromag. Comp.*, vol. 65, no. 1, pp. 88–95, 2022.

- [29] D. R. Smith, W. J. Padilla, D. C. Vier, S. C. Nemat-Nasser, and S. Schultz, “Composite medium with simultaneously negative permeability and permittivity,” *Phys. Rev. Lett.*, vol. 84, no. 18, p. 4184, 2000.
- [30] T. Chang, R. J. Langley, and E. A. Parker, “Frequency selective surfaces on biased ferrite substrates,” *Electron. Lett.*, vol. 30, no. 15, pp. 1193–1194, 1994.
- [31] C. Mias and J. H. Yap, “A varactor-tunable high impedance surface with a resistive-lumped-element biasing grid,” *IEEE Trans. Antennas Propag.*, vol. 55, no. 7, pp. 1955–1962, 2007.
- [32] B. Sanz-Izquierdo, E. A. Parker, and J. C. Batchelor, “Dual-band tunable screen using complementary split ring resonators,” *IEEE Trans. Antennas Propag.*, vol. 58, no. 11, pp. 3761–3765, 2010.
- [33] F. Bayatpur and K. Sarabandi, “Design and analysis of a tunable miniaturized-element frequency-selective surface without bias network,” *IEEE Trans. Antennas Propag.*, vol. 58, no. 4, pp. 1214–1219, 2010.
- [34] H. Zahra, S. Rafique, M. F. Shafique, and K. P. Esselle, “A switchable frequency selective surface based on a modified jerusalem-cross unit cell,” in *European Conf. Antenna Propag. (EuCAP)*. IEEE, 2015, pp. 1–2.
- [35] C. Yang, H. Li, Q. Cao, and Y. Wang, “Switchable electromagnetic shield by active frequency selective surface for LTE-2.1 GHz,” *Microw. Opt. Technol. Lett.*, vol. 58, no. 3, pp. 535–540, 2016.
- [36] J. Zhu, D. Li, S. Yan, Y. Cai, Q. H. Liu, and T. Lin, “Tunable microwave metamaterial absorbers using varactor-loaded split loops,” *Euro. Phy. Lett.*, vol. 112, no. 5, p. 54002, 2015.
- [37] D. Yang, Y. Xi, H. Zhai, and C. Liu, “Multifunctional active reconfigurable frequency selective surface,” in *Asia-Pacific Conf. Antennas Propag. (APCAP)*. IEEE, 2020, pp. 1–2.
- [38] A. de Lustrac, B. Ratni, G.-P. Piau, Y. Duval, and S. N. Burokur, “Tri-state metasurface-based electromagnetic screen with switchable reflection, trans-

- mission, and absorption functionalities,” *ACS Applied Electronic Materials*, vol. 3, no. 3, pp. 1184–1190, 2021.
- [39] M.-Y. Yoo and S. Lim, “Switchable electromagnetic metamaterial reflector/absorber,” in *Asia-Pacific Microw. Conf. Proceedings*. IEEE, 2012, pp. 445–447.
- [40] P. Kong, X.-W. Yu, M. Zhao, Y. He, L. Miao, and J. Jiang, “Switchable frequency selective surfaces absorber/reflector for wideband applications,” *J. Electromag. Waves App.*, vol. 29, no. 11, pp. 1473–1485, 2015.
- [41] H. Li, F. Costa, Y. Wang, Q. Cao, and A. Monorchio, “A wideband multifunctional absorber/reflector with polarization-insensitive performance,” *IEEE Trans. Antennas Propag.*, vol. 68, no. 6, pp. 5033–5038, 2019.
- [42] M. Saikia, S. Ghosh, and K. Srivastava, “Switchable reflective metamaterial polarisation rotator,” *Electron. Lett.*, vol. 52, no. 12, pp. 1030–1032, 2016.
- [43] W. Zhang, J. Li, G. Yang, and J. Xie, “Broadband window-type circular polariser based on frequency selective surfaces,” in *IEEE Intern. Symp. Antennas Propag. USNC/URSI Nat. Radio Science Meeting*. IEEE, 2017, pp. 687–688.
- [44] Y. Li, Q. Cao, and Y. Wang, “A switchable reflection-type linear/circular polarizers based on active metasurface,” in *IEEE Intern. Symp. Antennas Propag. USNC-URSI Radio Science Meeting*. IEEE, 2019, pp. 447–448.
- [45] S. Kitagawa, R. Suga, K. Araki, and O. Hashimoto, “Active absorption/transmission fss using diodes,” in *IEEE Intern. Symp. Electromag. Comp. (EMC)*. IEEE, 2015, pp. 1538–1541.
- [46] C. Huang, B. Zhao, J. Song, C. Guan, and X. Luo, “Active transmission/absorption frequency selective surface with dynamical modulation of amplitude,” *IEEE Trans. Antennas Propag.*, vol. 69, no. 6, pp. 3593–3598, 2020.
- [47] G. Marconi, “Reflector for use in wireless telegraphy and telephony,” *U. S. Patent 1,301,473*, 1919.

- [48] M. I. Skolnik *et al.*, *Introduction to radar systems*. McGraw-hill New York, 1980, vol. 3.
- [49] R. Ulrich, “Far-infrared properties of metallic mesh and its complementary structure,” *Infrared Physics*, vol. 7, no. 1, pp. 37–55, 1967.
- [50] S.-W. Lee, G. Zarrillo, and C.-L. Law, “Simple formulas for transmission through periodic metal grids or plates,” *IEEE Trans. Antennas Propag.*, vol. 30, no. 5, pp. 904–909, 1982.
- [51] Accessed, “The royal navy during the second world war A24893,” [https://commons.wikimedia.org/wiki/File:The\\_Royal\\_Navy\\_during\\_the\\_Second\\_World\\_War\\_A24893.jpg](https://commons.wikimedia.org/wiki/File:The_Royal_Navy_during_the_Second_World_War_A24893.jpg).
- [52] Available, “Bundesarchiv bild 141-2732, radargeräte würzburg-riese and freya,” [https://commons.wikimedia.org/wiki/File:Bundesarchiv\\_Bild\\_141-2732,\\_Radarger%C3%A4te\\_%22W%C3%BCrzburg-Riese%22\\_und\\_%22Freya%22.jpg](https://commons.wikimedia.org/wiki/File:Bundesarchiv_Bild_141-2732,_Radarger%C3%A4te_%22W%C3%BCrzburg-Riese%22_und_%22Freya%22.jpg).
- [53] S. Ghosh, *Studies on Multi-band and Broadband Absorbers based on Passive/Active Frequency Selective Surfaces*. PhD thesis, Indian Institute of Technology Kanpur, 2017.
- [54] J. Lee and S. Lim, “Bandwidth-enhanced and polarisation-insensitive metamaterial absorber using double resonance,” *Electron. Lett.*, vol. 47, no. 1, pp. 8–9, 2011.
- [55] Y. Liu, S. Gu, C. Luo, and X. Zhao, “Ultra-thin broadband metamaterial absorber,” *Applied Physics A*, vol. 108, no. 1, pp. 19–24, 2012.
- [56] W. S. Arceneaux, R. D. Akins, and W. B. May, “Absorptive/transmissive radome,” Mar. 21 1995, US Patent 5,400,043.
- [57] Y. Yu, Z. Shen, T. Deng, and G. Luo, “3-D frequency-selective absorber with wide upper absorption band,” *IEEE Trans. Antennas Propag.*, vol. 65, no. 8, pp. 4363–4367, 2017.

- [58] A. Sharma, S. Malik, S. Ghosh, and K. V. Srivastava, "A miniaturized frequency selective rasorber with independently regulated selective dual-transmission response," *IEEE Antennas Wireless Propag. Lett.*, vol. 21, no. 2, pp. 257–261, 2021.
- [59] Accessed, "Geodesic radomes at the misawa security operations center, misawa, japan," <https://commons.wikimedia.org/wiki/File:Navy-Radome.jpg>.
- [60] Y.-X. Che, S.-J. Wu, M. Li, and Y.-L. Ban, "Research progress on FSS stealth radome," *Electronics*, vol. 14, no. 6, p. 1132, 2025.
- [61] X. Chen, J. Tan, L. Kang, F. Tang, M. Zhao, and N. Kato, "Frequency selective surface toward 6G communication systems: A contemporary survey," *IEEE Commun. Surveys Tuts.*, vol. 26, no. 3, pp. 1635–1675, 2024.
- [62] J. Li, J. Jiang, Y. He, W. Xu, M. Chen, L. Miao, and S. Bie, "Design of a tunable low-frequency and broadband radar absorber based on active frequency selective surface," *IEEE Antennas Wireless Propag. Lett.*, vol. 15, pp. 774–777, 2015.
- [63] L. Zhang, G. Yang, Q. Wu, and J. Hua, "A novel active frequency selective surface with wideband tuning range for EMC purpose," *IEEE Trans. Mag.*, vol. 48, no. 11, pp. 4534–4537, 2012.
- [64] X.-G. Huang, Z. Shen, Q. Feng, and B. Li, "Tunable 3-D bandpass frequency-selective structure with wide tuning range," *IEEE Trans. Antennas Propag.*, vol. 63, no. 7, pp. 3297–3301, 2015.
- [65] H. Li, Q. Cao, L. Liu, and Y. Wang, "An improved multifunctional active frequency selective surface," *IEEE Trans. Antennas Propag.*, vol. 66, no. 4, pp. 1854–1862, 2018.
- [66] M. Li, B. Yu, and N. Behdad, "Liquid-tunable frequency selective surfaces," *IEEE Microw. Wireless Compon. Lett.*, vol. 20, no. 8, pp. 423–425, 2010.
- [67] A. G. D'Aloia, M. D'Amore, and M. S. Sarto, "Adaptive broadband radar absorber based on tunable graphene," *IEEE Trans. Antennas Propag.*, vol. 64, no. 6, pp. 2527–2531, 2016.

- [68] S. Ghosh and S. Lim, “Fluidically reconfigurable multifunctional frequency-selective surface with miniaturization characteristic,” *IEEE Trans. Micro. Theory Tech.*, vol. 66, no. 8, pp. 3857–3865, 2018.
- [69] J. Kim, H.-K. Jang, J. Oh, and J. Park, “A rational design procedure for absorbers of square-loop-shaped resistive frequency selective surface placed on glass/epoxy laminate,” *IEEE Trans. Electromag. Comp.*, vol. 65, no. 1, pp. 104–113, 2022.
- [70] S.-H. Wang, X.-X. He, and Y. Yang, “An active tunable frequency selective surface based on the rotatable magnet,” in *Cross Strait Radio Science & Wireless Tech. Conf. (CSRSWTC)*. IEEE, 2020, pp. 1–3.
- [71] G. I. Kiani, K. L. Ford, L. G. Olsson, K. P. Esselle, and C. J. Panagamuwa, “Switchable frequency selective surface for reconfigurable electromagnetic architecture of buildings,” *IEEE Trans. Antennas Propag.*, vol. 58, no. 2, pp. 581–584, 2009.
- [72] S. Ghosh and K. V. Srivastava, “Broadband polarization-insensitive tunable frequency selective surface for wideband shielding,” *IEEE Trans. Electromag. Comp.*, vol. 60, no. 1, pp. 166–172, 2017.
- [73] Q. Guo, Z. Li, J. Su, J. Song, and L. Y. Yang, “Active frequency selective surface with wide reconfigurable passband,” *IEEE Access*, vol. 7, pp. 38 348–38 355, 2019.
- [74] S. Ghosh and K. V. Srivastava, “Polarization-insensitive single-and broadband switchable absorber/reflector and its realization using a novel biasing technique,” *IEEE Trans. Antennas Propag.*, vol. 64, no. 8, pp. 3665–3670, 2016.
- [75] H. Jeong and S. Lim, “Broadband frequency-reconfigurable metamaterial absorber using switchable ground plane,” *Sci. Rep.*, vol. 8, no. 1, p. 9226, 2018.
- [76] J. Yuan, S. Liu, B. Bian, X. Kong, H. Zhang, B. Ma, Z. Mao, and B. Wang, “A novel tunable dual-band microwave metamaterial absorber based on split ring resonant.” in *PIERS Proceedings*, 2014.

- [77] S. Ghosh and K. V. Srivastava, “A dual-band tunable frequency selective surface with independent wideband tuning,” *IEEE Antennas Wireless Propag. Lett.*, vol. 19, no. 10, pp. 1808–1812, 2020.
- [78] H. Jiang, Y. Zhang, Y. Wu, B. Jiang, S. Liao, and Q. Xue, “Reconfigurable bandpass frequency-selective raserber with perfect elliptic filtering response,” *IEEE Trans. Micro. Theory Tech.*, 2024.
- [79] B. Chambers and K. Ford, “Topology for tunable radar absorbers,” *Electron. Lett.*, vol. 36, no. 15, pp. 1304–1306, 2000.
- [80] A. Tennant and B. Chambers, “A single-layer tuneable microwave absorber using an active FSS,” *IEEE Microw. Wireless Compon. Lett.*, vol. 14, no. 1, pp. 46–47, 2004.
- [81] J. Zhao, Q. Cheng, J. Chen, M. Q. Qi, W. X. Jiang, and T. J. Cui, “A tunable metamaterial absorber using varactor diodes,” *New Journal of Physics*, vol. 15, no. 4, p. 043049, 2013.
- [82] S. Ghosh and K. Srivastava, “Polarisation-independent tunable absorber with embedded biasing network,” *Electron. Lett.*, vol. 53, no. 17, pp. 1176–1178, 2017.
- [83] L. Wu, S. Zhong, J. Huang, and T. Liu, “Broadband frequency-selective raserber with varactor-tunable interabsorption band transmission window,” *IEEE Trans. Antennas Propag.*, vol. 67, no. 9, pp. 6039–6050, 2019.
- [84] S. C. Bakshi, D. Mitra, and S. Ghosh, “A frequency selective surface based reconfigurable raserber with switchable transmission/reflection band,” *IEEE Antennas Wireless Propag. Lett.*, vol. 18, no. 1, pp. 29–33, 2018.
- [85] S. C. Bakshi, D. Mitra, and F. L. Teixeira, “Multifunctional frequency selective raserber with dual mode and continuous tunability,” *IEEE Trans. Antennas Propag.*, vol. 69, no. 9, pp. 5704–5715, 2021.
- [86] B. Zhu, Y. Feng, J. Zhao, C. Huang, and T. Jiang, “Switchable metamaterial reflector/absorber for different polarized electromagnetic waves,” *Appl. Phys. Lett.*, vol. 97, no. 5, 2010.

- [87] Y. Han, W. Che, X. Xiu, W. Yang, and C. Christopoulos, "Switchable low-profile broadband frequency-selective rasorber/absorber based on slot arrays," *IEEE Trans. Antennas Propag.*, vol. 65, no. 12, pp. 6998–7008, 2017.
- [88] M. Yoo and S. Lim, "Switchable electromagnetic reflector/absorber with electric-field-coupled LC resonator," *Electromagnetics*, vol. 34, no. 5, pp. 421–429, 2014.
- [89] J. Yuan, X. Kong, X. Wang, S. Jiang, and L. Kong, "Polarization-independent reconfigurable frequency selective rasorber/absorber with low-insertion loss," *Microw. Opt. Technol. Lett.*, vol. 63, no. 5, pp. 1339–1345, 2021.
- [90] X. Kong *et al.*, "Design of switchable frequency-selective rasorber with A-R-A-T or A-T-A-R operating modes," *IEEE Antennas Wireless Propag. Lett.*, vol. 22, no. 1, pp. 69–73, 2022.
- [91] S. C. Bakshi, D. Mitra, and F. L. Teixeira, "Wide-angle broadband rasorber for switchable and conformal application," *IEEE Trans. Micro. Theory Tech.*, vol. 69, no. 2, pp. 1205–1216, 2021.
- [92] A. Parameswaran, D. K. Sahoo, H. S. Sonaliker, D. Kundu, and A. Patnaik, "PSO-assisted design of a dual-polarized broadband switchable rasorber/absorber," *IEEE Trans. Electromag. Comp.*, vol. 65, no. 5, pp. 1309–1319, 2023.
- [93] H. Li, Q. Cao, and Y. Wang, "A novel 2-B multifunctional active frequency selective surface for LTE-2.1 GHz," *IEEE Trans. Antennas Propag.*, vol. 65, no. 6, pp. 3084–3092, 2017.
- [94] R. Phon, S. Ghosh, and S. Lim, "Novel multifunctional reconfigurable active frequency selective surface," *IEEE Trans. Antennas Propag.*, vol. 67, no. 3, pp. 1709–1718, 2018.
- [95] M. Zhao, H. Li, J. Shi, and Q. Cao, "A polarization-independent multifunctional active frequency selective surface with compound modes of absorption, transmission, and reflection," *IEEE Antennas Wireless Propag. Lett.*, vol. 23, no. 4, pp. 1291–1295, 2024.

- [96] C. Mias, “Varactor-tunable frequency selective surface with resistive-lumped-element biasing grids,” *IEEE Microw. Wireless Compon. Lett.*, vol. 15, no. 9, pp. 570–572, 2005.
- [97] F. Costa, A. Monorchio, and G. P. Vastante, “Tunable high-impedance surface with a reduced number of varactors,” *IEEE Antennas Wireless Propag. Lett.*, vol. 10, pp. 11–13, 2011.
- [98] A. Ebrahimi, Z. Shen, W. Withayachumnankul, S. F. Al-Sarawi, and D. Abbott, “Varactor-tunable second-order bandpass frequency-selective surface with embedded bias network,” *IEEE Trans. Antennas Propag.*, vol. 64, no. 5, pp. 1672–1680, 2016.
- [99] F. Bayatpur and K. Sarabandi, “Tuning performance of metamaterial-based frequency selective surfaces,” *IEEE Trans. Antennas Propag.*, vol. 57, no. 2, pp. 590–592, 2009.
- [100] H. Yuan, B. Zhu, and Y. Feng, “A frequency and bandwidth tunable metamaterial absorber in X-band,” *J. Appl. Phys.*, vol. 117, no. 17, 2015.
- [101] H. Wang, P. Kong, W. Cheng, W. Bao, X. Yu, L. Miao, and J. Jiang, “Broadband tunability of polarization-insensitive absorber based on frequency selective surface,” *Sci. Rep.*, vol. 6, no. 1, p. 23081, 2016.
- [102] L.-M. Zhang, X. Ding, and M. Bozzi, “Passband tunable reconfigurable frequency-selective surface with wide tuning range,” *IEEE Trans. Micro. Theory Tech.*, vol. 72, no. 9, pp. 5167–5178, 2024.
- [103] R. Phon, S. Ghosh, and S. Lim, “Active frequency selective surface to switch between absorption and transmission band with additional frequency tuning capability,” *IEEE Trans. Antennas Propag.*, vol. 67, no. 9, pp. 6059–6067, 2019.
- [104] Z. Wu, Q. Zhou, P. Liu, and M. Lin, “Active frequency selective raserber with switchable transmission band and tunable absorption band,” *IEEE Microw. Wireless Tech. Lett.*, vol. 33, no. 8, pp. 1247–1250, 2023.

- [105] S. C. Bakshi, D. Mitra, and F. L. Teixeira, "FSS-based fully reconfigurable rasorber with enhanced absorption bandwidth and simplified bias network," *IEEE Trans. Antennas Propag.*, vol. 68, no. 11, pp. 7370–7381, 2020.
- [106] F. Bayatpur and K. Sarabandi, "Single-layer high-order miniaturized-element frequency-selective surfaces," *IEEE Trans. Micro. Theory Tech.*, vol. 56, no. 4, pp. 774–781, 2008.
- [107] P. Zhao, C. H. Chan *et al.*, "Design and analysis of a high-selectivity frequency-selective surface at 60 GHz," *IEEE Trans. Micro. Theory Tech.*, vol. 64, no. 6, pp. 1694–1703, 2016.
- [108] S. Ghosh, S. Bhattacharyya, and K. V. Srivastava, "Design, characterisation and fabrication of a broadband polarisation-insensitive multi-layer circuit analogue absorber," *IET Microw. Antennas Propag.*, vol. 10, no. 8, pp. 850–855, 2016.
- [109] A. Monorchio, G. Manara, U. Serra, G. Marola, and E. Pagana, "Design of waveguide filters by using genetically optimized frequency selective surfaces," *IEEE Microw. Wireless Compon. Lett.*, vol. 15, no. 6, pp. 407–409, 2005.
- [110] C. Zhao, C.-F. Wang, and S. Aditya, "Power-dependent frequency-selective surface: Concept, design, and experiment," *IEEE Trans. Antennas Propag.*, vol. 67, no. 5, pp. 3215–3220, 2019.
- [111] L. Zhou, L. Liu, and Z. Shen, "High-performance energy selective surface based on the double-resonance concept," *IEEE Trans. Antennas Propag.*, vol. 69, no. 11, pp. 7658–7666, 2021.
- [112] Y. Shang, Z. Shen, and S. Xiao, "On the design of single-layer circuit analog absorber using double-square-loop array," *IEEE Trans. Antennas Propag.*, vol. 61, no. 12, pp. 6022–6029, 2013.
- [113] Y. Han and W. Che, "Low-profile broadband absorbers based on capacitive surfaces," *IEEE Antennas Wireless Propag. Lett.*, vol. 16, pp. 74–78, 2016.

- [114] M. Hossain, N. Nguyen-Trong, A. S. Alqadami, and A. M. Abbosh, “Calibrated broadband measurement technique for complex permittivity and permeability,” *IEEE Trans. Micro. Theory Tech.*, vol. 68, no. 8, pp. 3580–3591, 2020.
- [115] M. I. Hossain, N. Nguyen-Trong, and A. M. Abbosh, “Calibrated parallel-plate waveguide technique for low-frequency and broadband absorptivity measurement,” *IEEE Antennas Wireless Propag. Lett.*, vol. 19, no. 9, pp. 1541–1545, 2020.
- [116] S. Sheikh, “Miniaturized-element frequency-selective surfaces based on the transparent element to a specific polarization,” *IEEE Antennas Wireless Propag. Lett.*, vol. 15, pp. 1661–1664, 2016.
- [117] O. Luukkonen and Others, “Simple and accurate analytical model of planar grids and high-impedance surfaces comprising metal strips or patches,” *IEEE Trans. Antennas Propag.*, vol. 56, no. 6, pp. 1624–1632, 2008.
- [118] Accessed, “BAR 64-02 V p-i-n diode datasheet,” <https://www.infineon.com/cms/en/product/rf/rf-diode/rf-pin-diode/antenna-switch/bar64-02v/>.
- [119] Available, “BAR 65-02 V p-i-n diode datasheet,” <https://www.infineon.com/cms/en/product/rf/rf-diode/rf-pin-diode/antenna-switch/bar65-02v/>.
- [120] Online, “Basys 3 Artix-7 FPGA trainer board,” <https://digilent.com/shop/basys-3-amd-artix-7-fpga-trainer-board-recommended-for-introductory-users/>.
- [121] G. Engen and C. Hoer, “Thru-reflect-line: An improved technique for calibrating the dual six-port automatic network analyzer,” *IEEE Trans. Micro. Theory Tech.*, vol. 27, no. 12, pp. 987–993, 1979.
- [122] T. Hong, M. Wang, K. Peng, Q. Zhao, and S. Gong, “Compact ultra-wide band frequency selective surface with high selectivity,” *IEEE Trans. Antennas Propag.*, vol. 68, no. 7, pp. 5724–5729, 2020.
- [123] X. Ma, Y. Wang, F. Bai, and C. Guo, “A metasurface with switchable reflection, transmission and absorption functionalities,” in *Photonics & Electromagnetics Research Symposium (PIERS)*, 2024, pp. 1–6.

- [124] X. Song and Others, “Switchable metasurface for nearly perfect reflection, transmission, and absorption using PIN diodes,” *Opt. Express*, vol. 29, no. 18, pp. 29 320–29 328, Aug 2021.
- [125] Y. Liu, L. Dong, J. Zheng, M. F. Mohd Sabri, N. A. Majid, and S. Ibrahim, “Switchable absorbing, reflecting, and transmitting metasurface by employing vanadium dioxide on the same frequency,” *Superlattices and Microstructures*, vol. 162, p. 107109, 2022.
- [126] M. Borgese and F. Costa, “A simple equivalent circuit approach for anisotropic frequency-selective surfaces and metasurfaces,” *IEEE Trans. Antennas Propag.*, vol. 68, no. 10, pp. 7088–7098, 2020.
- [127] F. Mesa, R. Rodríguez-Berral, M. García-Vigueras, F. Medina, and J. R. Mosig, “Simplified modal expansion to analyze frequency-selective surfaces: An equivalent circuit approach,” *IEEE Trans. Antennas Propag.*, vol. 64, no. 3, pp. 1106–1111, 2016.
- [128] Accessed, “BAR 50-02 V p-i-n diode datasheet,” <https://www.infineon.com/part/BAR50-02V>.
- [129] Available, “BB 857-02 V varactor datasheet.” <https://www.infineon.com/assets/row/public/documents/24/49/infineon-bb837-bb857series-ds-en.pdf?fileId=db3a304313d846880113d97339a9011a>.
- [130] A. Rashidian, L. Shafai, D. Klymyshyn, and C. Shafai, “A fast and efficient free-space dielectric measurement technique at mm-wave frequencies,” *IEEE Antennas Wireless Propag. Lett.*, vol. 16, pp. 2630–2633, 2017.
- [131] Available, “KOA resistor datasheet.” <https://www.koaspeer.com/products/resistors/general-purpose/rk73h/>.
- [132] X. Wang, X. Kong, S. Jiang, L. Kong, and J. Yuan, “Wideband transverse electromagnetic cell design and its application in frequency selective surface measurement,” *Intern. J. RF and Microw. Computer-Aided Engineer.*, vol. 31, no. 7, p. e22690, 2021.

# List of Publications

## Journals

1. **P. Megh Sainadh** and S. Ghosh, “A reconfigurable metasurface for real-time dynamic control of EM wave in microwave systems,” accepted for publication in *IEEE Microwave and Wireless Technology Letters*, March. 2026.
2. **P. Megh Sainadh** and S. Ghosh, “A modified parallel plate waveguide for wide-angle characterization of frequency selective surfaces,” accepted for publication in *IEEE Antennas and Wireless Propagation Letters*, Feb. 2026.
3. **P. Megh Sainadh** and S. Ghosh, “Wideband polarization-insensitive switchable FSS-based rasorber/absorber/transmitter/reflector,” *IEEE Antennas and Wireless Propagation Letters*, vol. 24, no. 12, pp. 4735-4739, Dec. 2025.
4. **P. Megh Sainadh** and S. Ghosh, “A multifunctional reconfigurable frequency-selective surface with simultaneous switching and tuning capability,” *IEEE Transactions on Antennas and Propagation*, vol. 72, no. 10, pp. 7700–7709, Oct. 2024.
5. **P. Megh Sainadh**, A. Sharma, and S. Ghosh, “Polarization-insensitive absorptive/transmissive reconfigurable frequency selective surface with embedded biasing,” *IEEE Antennas and Wireless Propagation Letters*, vol. 22, no. 1, pp. 164–168, Jan. 2023.

## Conferences

1. **P. Megh Sainadh** and S. Ghosh, “Oblique incidence analysis of FSS using a dual-section parallel plate waveguide,” *2025 IEEE Microwaves, Antennas, and Propagation Conference (MAPCON)*, Kochi, India, 2025, pp. 1-4.

2. **P. Megh Sainadh** and S. Ghosh, “A narrowband polarization insensitive multifunctional frequency selective surface,” *2024 IEEE Microwaves, Antennas, and Propagation Conference (MAPCON)*, Hyderabad, India, 2024, pp. 1–4.
3. **P. Megh Sainadh**, S. K. James, and S. Ghosh, “A parallel plate waveguide measurement technique for characterizing frequency selective surfaces,” *2024 International Symposium on Antennas and Propagation (ISAP)*, Incheon, Korea, 2024, pp. 1–2.
4. **P. Megh Sainadh** and S. Ghosh, “A polarization-insensitive reconfigurable frequency selective surface switching and tuning among absorption, transmission, and reflection,” *2024 IEEE International Symposium on Antennas and Propagation and INC/USNC-URSI Radio Science Meeting*, Firenze, Italy, 2024, pp. 263–264.
5. **P. Megh Sainadh** and S. Ghosh, “A wideband reconfigurable frequency selective surface switching among transmission, absorption, reflection, and rasorber operations,” *2024 4th URSI Atlantic Radio Science Meeting (AT-RASC)*, Meloneras, Spain, 2024, pp. 1–4.
6. **P. Megh Sainadh** and S. Ghosh, “A switchable and tunable multifunctional reconfigurable frequency selective surface,” *2024 4th URSI Atlantic Radio Science Meeting (AT-RASC)*, Meloneras, Spain, 2024.
7. **P. Megh Sainadh** and S. Ghosh, “A reconfigurable frequency selective surface switching between absorption, transmission, and reflection, along with frequency tunability,” *IEEE Microwave Antennas and Propagation Conference (MAPCON) 2023*, held in Ahmedabad, India, 11–14 Dec 2023.
8. **P. Megh Sainadh** and S. Ghosh, “Reconfigurable frequency selective surface switching between absorption and transmission band,” *2022 IEEE Wireless Antenna and Microwave Symposium (WAMS)*, India, 2022.

# List of Publications in Collaboration with Other Group Members

## Journals

1. Mishra P., Gouda A., **P. Megh Sainadh**, and S. Ghosh, “Wideband high-gain beam-steerable reflectarray for millimeter-wave non-terrestrial networks,” *Physica Scripta*, vol. 100, no. 10, p. 105509, 2025.
2. S. Ghosh, **P. Megh Sainadh**, A. Sarkhel, and S. Ghosh, “Wideband superstrate-loaded metasurface-based multifunctional polarization converters,” *IEEE Antennas and Wireless Propagation Letters*, vol. 24, no. 6, pp. 1337–1341, June 2025.
3. D. Laxmikant, **P. Megh Sainadh**, A. Juin, S. Shrey Anant, G. Saptarshi, and M. Nipuni Kumar, “Direction independent broad-band wide angle metamaterial absorber for “K” band applications,” *Frequenz*, vol. 78, no. 1–2, 2024, pp. 9–20.
4. L. Dewangan, **P. Megh Sainadh**, J. Acharjee, Y. Solunke, S. Ghosh, N. Kumar Mishra, “Broadband metamaterial absorber for stealth applications at K-band,” *AEU - International Journal of Electronics and Communications*, vol. 170, 2023, 154828.
5. **P. Megh Sainadh**, Laxmi Banoth, Aditi Sharma, Kumar Vaibhav Srivastava, and Saptarshi Ghosh, “A frequency selective rasorber with wideband absorption and in-band transmission using resistive ink,” *Microwave and Optical Technology Letters*, vol. 64, no. 9, pp. 1544–1552, 2022.

## Conferences

1. S. Yadav, M. Aziz, A. Gouda, **P. Megh Sainadh** and S. Ghosh, "Broadband 3D-printed honeycomb absorber integrated on wing structure for RCS reduction," *2025 IEEE Microwaves, Antennas, and Propagation Conference (MAPCON)*, Kochi, India, 2025, pp. 1-4.
2. G. Sricharani, **P. Megh Sainadh** and S. Ghosh, "A 2-bit reconfigurable intelligent surface with wide beam steering angles," *2024 IEEE Microwaves, Antennas, and Propagation Conference (MAPCON)*, Hyderabad, India, 2024, pp. 1-4.
3. M. Aziz, A. Gouda, **P. Megh Sainadh**, A. Shukla and S. Ghosh, "A lightweight flexible microwave absorber using 3-D printed honeycomb structure," *2024 IEEE International Symposium on Antennas and Propagation and INC/USNC-URSI Radio Science Meeting (AP-S/INC-USNC-URSI)*, Firenze, Italy, 2024, pp. 1697-1698.
4. A. Rastogi, **P. Megh Sainadh**, and S. Ghosh, "A miniaturized polarization-insensitive reconfigurable intelligent surface for beam steering applications," *IEEE Microwave Antennas and Propagation Conference (MAPCON) 2023*, held in Ahmedabad, India, 11-14 Dec 2023.
5. A. Rastogi, **P. Megh Sainadh**, and S. Ghosh, "A polarization-insensitive reconfigurable intelligent surface for beam steering applications," *2022 IEEE Microwaves, Antennas, and Propagation Conference (MAPCON)*, Bangalore, India, 2022, pp. 1388-1392.

## About the Author

**Patinavalasa Megh Sainadh** was born in Andhra Pradesh, India, on August 14, 1996. He has received the B.Tech. degree in Electronics and Communication Engineering from *University College of Engineering, JNTU, Kakinada*, Andhra Pradesh, India, in 2017, and the M.Tech. degree in Communication Engineering from *National Institute of Technology, Surathkal*, Karnataka, India, in 2020. He has joined the Ph.D. degree program with the Department of Electrical Engineering, IIT Indore, Indore, Madhya Pradesh, India. His current research interests include multifunctional reconfigurable frequency selective surfaces, reconfigurable intelligent surfaces, and microwave absorbers.

He is a recipient of the IEEE AP-S Fellowship Award for graduate students in 2023. In 2024, he has received the Young Scientist and Student Paper Competition Awards from URSI AT-RASC and the C. J. Reddy Travel Grant from APS-URSI.